

Meteorological Satellite Instrumentation and Data Processing

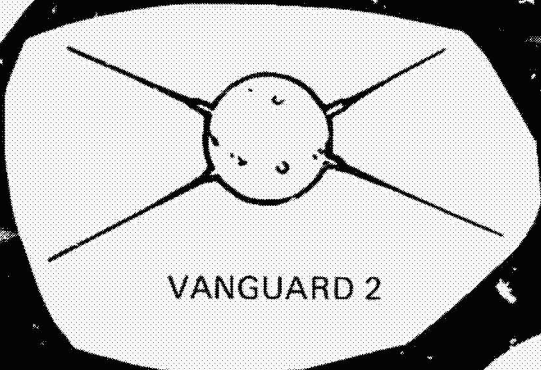
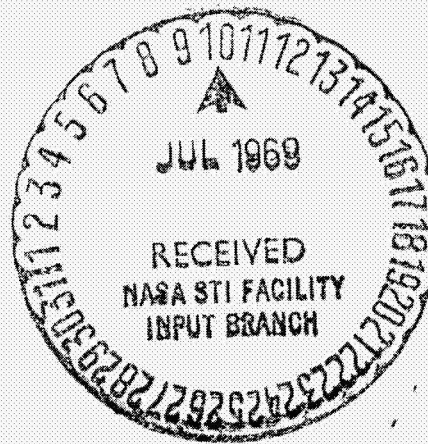
Final Scientific Report on NASw-65 1958-1968

Department of Meteorology

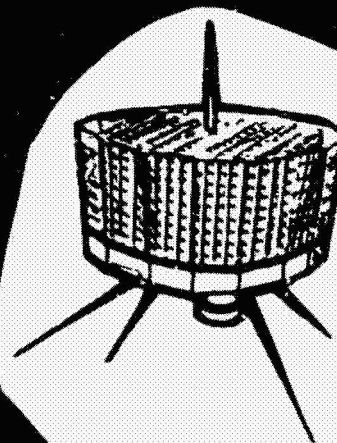
The University of Wisconsin

Madison, Wisconsin

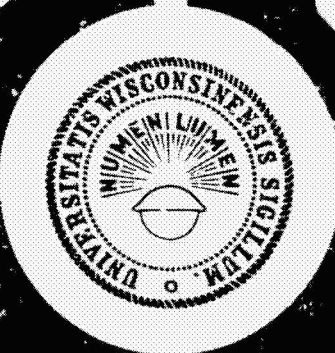
December 1968


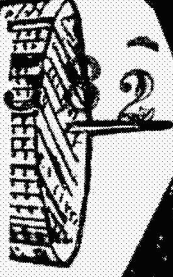


VANGUARD 2



TIROS



	
N 69 - 33576	N 69 - 33
(ACCESSION NUMBER)	(THRU)
198	1
(PAGES)	(CODE)
CR-103678	20
(NASA CR OR TMX OR AD NUMBER)	(CATEGORY)

ATIS-C

Department of Meteorology
The University of Wisconsin
Madison, Wisconsin

**METEOROLOGICAL SATELLITE INSTRUMENTATION
AND DATA PROCESSING**

Final Scientific Report

on

NASw-65

1958 - 1968

**The research reported in this document has been supported, in whole or in part,
by the National Aeronautics and Space Administration.**

December 1968

300-2.59

PRINCIPAL INVESTIGATORS

Verner E. Suomi
Robert J. Parent

Project Supervisor: T. H. Vonder Haar

CONTRIBUTIONS BY

T. D. Damon
I. Dirmhirn
K. J. Hanson
F. F. Hauth
F. B. House
N. Levanon
L. P. Merritt
R. J. Parent

S. A. Rossby
W. C. C. Shen
J. O. Siebers
B. B. Sparkman
V. E. Suomi
T. H. Vonder Haar
J. A. Weinman
M. Weinstein

University of Wisconsin

PREFACE

This publication covers most of the work performed under Contract NASw-65 from 1958 through 1968. Due to the multiplicity of activities pursued during this period, the report does not contain all scientific papers completed. We feel, however, that the two sections of this report—(1) technical articles, and (2) abstracts—provide an adequately comprehensive view of the past ten years' activities. All papers not contained in this publication have been previously issued in special contract reports or published as theses or papers.

PRECEDING PAGE BLANK NOT FILMED.

CONTENTS

	Page	
INTRODUCTION	vii	
<u>Technical Articles</u>		
1. Determination of the Sea Surface Slopes Distribution and Wind Velocity Using Sun Glitter Viewed from a Synchronous Satellite	1	✓
2. Investigation of Clouds Above Snow Surfaces Utilizing Radiation Measurements Obtained from the Nimbus II Satellite	16	✓
3. Variations of the Earth's Radiation Budget	31	✓
4. The Reflection of Sunlight and Absorption by the Earth and Atmosphere over the United States During Spring, 1962	108	✓
5. Radiation Analysis of a Subtropical High	125	✓
6. On the Interpretation of Long-wave Radiation Data from Explorer VII Satellite	151	✓
ABSTRACTS	165	
APPENDIX	171	

PRECEDING PAGE BLANK NOT FILMED.

INTRODUCTION

This contract, over the last ten years, has been as varied and interesting as the development of meteorological satellite sensors and applications. Many individuals at the University of Wisconsin, NASA, and other agencies have participated and cooperated in our research efforts. All of these efforts and the related expenditures have provided:

1. The first radiation measurements from a meteorological satellite (Weinstein and Suomi)
2. The first application of these data to studies of atmospheric energetics (Shen and Suomi)
3. The first measurements of the earth's planetary albedo and radiation budget during a seasonal period (House)
4. The first multi-annual study of the earth's radiation budget for all seasons (Vonder Haar).

All of these results, and many others, were possible because of the excellent engineering and data reduction support provided by my co-investigator, Professor Robert J. Parent, and his staff. To these individuals and to my students and colleagues in the Department of Meteorology, I extend my thankful appreciation.

V. E. Suomi

N 69 - 33577

DETERMINATION OF THE SEA SURFACE SLOPES DISTRIBUTION
AND WIND VELOCITY USING SUN GLITTER
VIEWED FROM A SYNCHRONOUS SATELLITE

by

N. Levanon

CONTENTS

	Page
Introduction	1
The Synchronous Satellite as the Observer	2
The Satellite, The Points of Reflection, and The Sun Subpoint	3
The Geometry of Reflection	5
Slope Probability and Light Intensity	7
Background Light	8
The Slope Distribution	9
Results	11
Conclusion	12
References	12

Introduction

The use of sun glitter to study the slope statistics of the sea was suggested and explored by Cox and Munk [1, 2]. Their basic idea can be summarized as follows. If the sea surface were entirely calm, then an overhead observer would see a single, mirror-like reflection of the sun at the horizontal specular point.

The sea, of course, is never mirror flat, but due to the short wavelength of light, can be considered as constructed from many small facets, each with its own inclination. The farther a facet is from the horizontal specular point, the greater is the inclination required to reflect light toward the observer. The location of the reflected light source can therefore be interpreted as a certain sea slope, and the average intensity of the light coming from this location can be interpreted as the frequency with which this particular slope occurs.

Cox and Munk estimated sea-slope distributions using sun glitter photographs taken from an aircraft. They also suggested an empirical relation between the variance of the slopes and the surface wind velocity.

With the advent of the ATS-1 synchronous satellite, the sun glitter has appeared as a major phenomenon on the photographs received daily from the spin-scan camera.

The purpose of the present work is to adapt the Cox-Munk technique to pictures taken from a much larger altitude, by a synchronous satellite. The main modification involves the use of a sequence of photographs of a limited area (taken over a time period) rather than a single photograph of the whole sun glitter area.

Such data from the satellite were used to calculate the slope distribution, and from it the wind velocity, for the locations of Palmyra, Fanning and Christmas Island, on the 16th and 19th of April, 1967. The calculated values were compared to direct wind measurements obtained at these locations during the "Line Island Experiment" [3].

Utilizing the data from the scanning type electronic camera, it was possible to by-pass the highly degrading photographic and photometric processes and to do all the quantitative work on the received video signal.

The Synchronous Satellite as the Observer

In their work, Cox and Munk photographed the sun glitter from aircraft altitudes, and studied the slope distribution from a single photograph. This was done by identifying each location within the glitter with the specific sea slope which would cause reflection at that location.

The basic assumption involved in using different locations within a single glitter is that the statistical characteristics of the sea surface are essentially constant over the whole area of the sun glitter. When the photograph is taken from an aircraft this assumption is true. However, when the photograph is taken from synchronous altitude (35,783 km), the sun glitter covers a circle whose diameter can exceed 3000 km, and with regard to such a large area the above basic assumption is no longer plausible.

This point is brought out in Figure 1, which shows a sequence of six photographs of the same portion of the ocean (5°N - 15°N and 160°W - 230°W), taken at intervals of about 23 minutes. The sun glitter is apparent in all the frames, and its shift to the west can be clearly seen. Note the calm area of the ocean which appears as a dark area in the midst of the sun glitter in the second frame. In the third frame this area already includes the horizontal specular point of reflection, and the light intensity reflected from part of it is greater than the light scattered from the clouds. In the last frame the specular point of reflection has moved outside the calm area and the sun glitter ends sharply at its edge. Thus, Figure 1 shows that the sea roughness may vary considerably over the glitter large area. But we also note that the shape of the calm area did not change appreciably in the two-hour period between the first and the last frame. This leads to an alternative assumption, viz., that the statistical characteristics of the sea surface at a fixed point in the open ocean does not vary appreciably over a period of several hours.

Recalling that the synchronous satellite is in a fixed position relative to the earth while the horizontal specular point of reflection shifts with time from east to west, we see that this assumption allows us to adapt the Cox-Munk technique to the case of observation from a synchronous satellite. Specifically, the values of light intensity reflected towards the satellite from a fixed point at different times, can be interpreted in terms of the sea slope distribution around that point.

The Satellite, The Points of Reflection and The Sun Subpoint

The ATS-I Satellite is positioned over the equator at about 150° West Longitude. From a height of 35,783 km, its spin-scan camera [4, 5] usually observes the portion of the earth bounded by 70°W and 230°W , and by 52.5°N and 52.5°S . This area is scanned by 2018 horizontal (west to east) lines. The optical resolution is 2.0 nautical miles when the telescope is pointed straight down. The normal down scan takes 20 minutes and the retrace an additional 2 minutes. The optical system bandpass is 4750\AA to 6300\AA . The camera video output is linear within $\pm 2\%$, up to the intensity of 10,000 foot lamberts.

The data at the ground station was available in three forms: as pictures, on analog tape and on digital tape. On the digital tape, the maximum intensity was divided into 250 units, and each line into 8192 picture elements, of which the limb distance of an equatorial line occupies 7128 picture elements.

Accurate techniques were derived for navigation on the pictures [6]. This work utilized the simple method of two landmarks—Baja, California and Hawaii—which were not overcast on the specific days used for analysis. The accuracy achieved with this method was better than 50 miles.

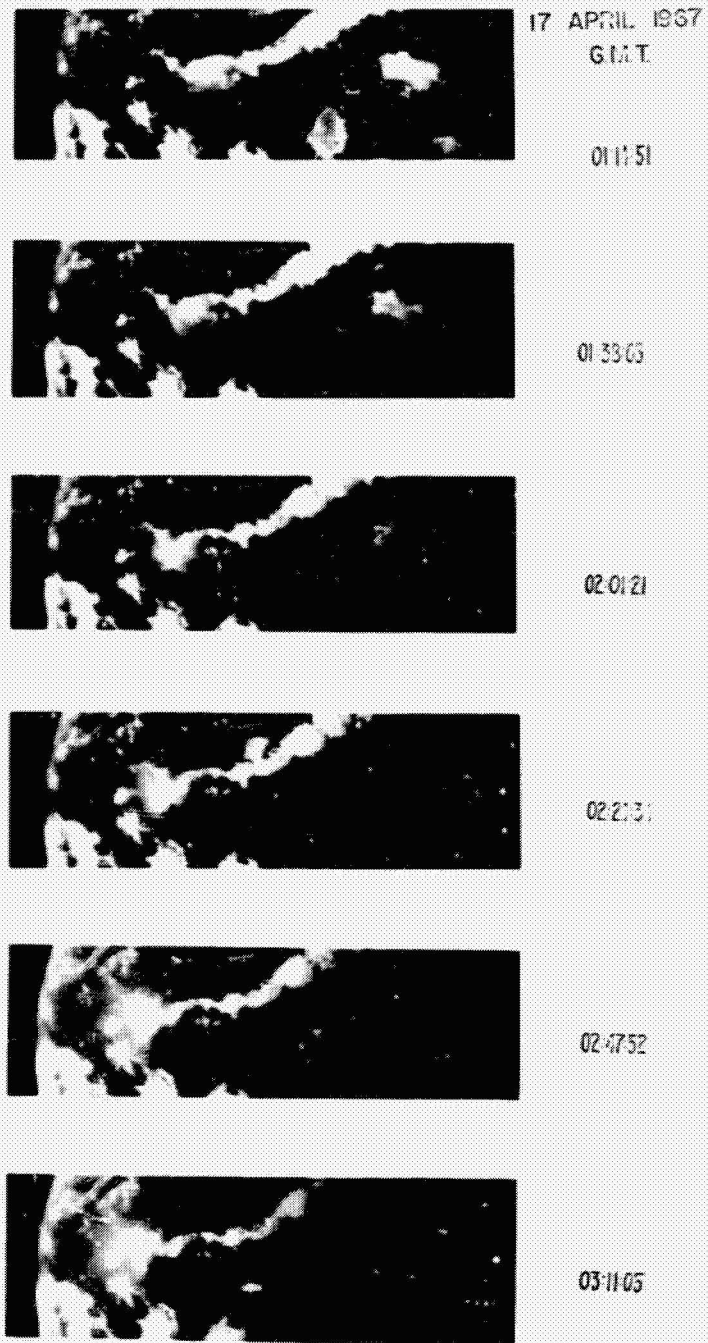


Fig. 1. The sun glitter shifts toward west over a calm area in the midst of a rough ocean.

The points of reflection in our study corresponded to Palmyra Island (50° 53'N, 162° 05'W), Fanning Island (3° 54'N, 159° 23'W), and Christmas Island (1° 55'N, 157° 20'W). Actual wind measurements were obtained on these three islands during the "Line Island Experiment."

On the 16th of April, 1967, the sun subpoint traveled along the 10°N latitude, and on the 19th of April, along the 11°N. The exact longitude and latitude of the sun subpoint as function of time, were obtained from the Air Almanac [7].

The Geometry of Reflection

To apply the method, we need an answer to the following geometrical question: given the longitude and latitude of the sun and the synchronous satellite subpoints, and of the point of reflection, what is the tilt magnitude and direction and the angle of incidence, at that point of reflection?

To derive the necessary formulae we shall use the following notation (Figure 2):

- 0 — The center of the earth
- S — The sun subpoint
- A — The synchronous satellite
- P — The point of reflection
- i — An index taking values S, R, or P
- Q_i — The point created by the surface and a vector parallel to \tilde{i} and starting at 0
- θ_i — Latitude of i (or of Q_i)
- φ_i — Longitude of A - longitude of i (or of Q_i)
- r — The radius of Earth
- h — The synchronous altitude
- \tilde{i} — Vector between the satellite and the point of reflection
- \tilde{n} — The normal required for reflection from P
- θ — The northward tilt at P
- φ — The eastward tilt at P
- β — The magnitude of the total tilt at P
- ω — The angle of incidence

An elementary manipulation of rectangular and spherical coordinates yields the formulae:

$$\phi_i = \tan^{-1} \frac{-r \cos \theta_p \sin \phi_p}{h + r(1 - \cos \theta_p \cos \phi_p)} \quad (1)$$

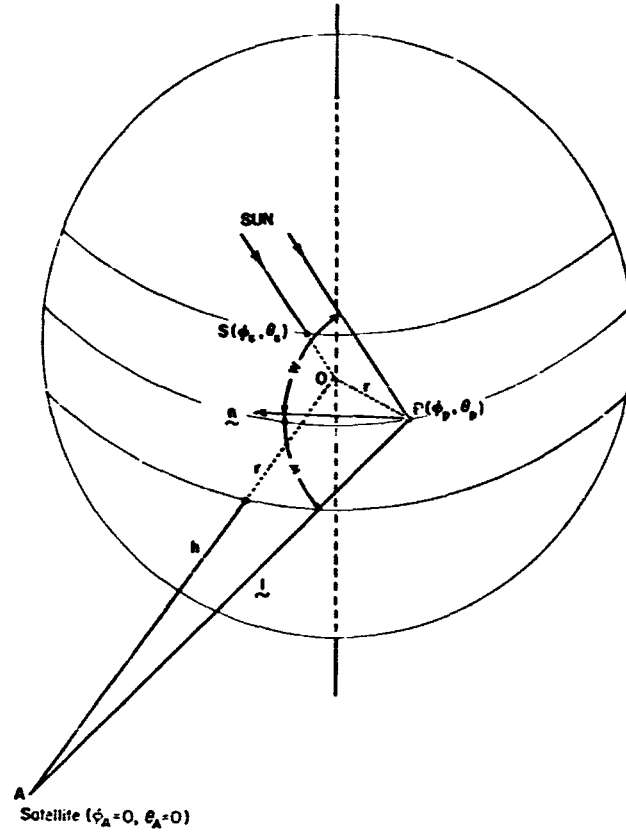


Fig. 2: The geometry of reflection

$$\theta_l = \tan^{-1} \frac{-r \sin \theta_p}{[(h+r)^2 - 2r(h+r) \cos \theta_p \cos \phi_p + r^2 \cos^2 \theta_p]^{1/2}} \quad (2)$$

and

$$\phi_n = \tan^{-1} \frac{\cos \theta_l \sin \phi_l + \cos \theta_s \sin \phi_s}{\cos \theta_l \cos \phi_l + \cos \theta_s \cos \phi_s} \quad (3)$$

$$\theta_n = \tan^{-1} \frac{\sin \theta_l + \sin \theta_s}{[\cos^2 \theta_l + \cos^2 \theta_s + 2 \cos \theta_l \cos \theta_s \cos(\phi_l - \phi_s)]^{1/2}} \quad (4)$$

At the point of reflection the tilt in the east (or ϕ) direction is given by

$$\phi = \phi_n - \phi_p \quad (5)$$

and the tilt in the north (or θ) direction by

$$\theta = \theta_n - \theta_p \quad (6)$$

Recalling that ϕ and θ are orthogonal, we get for the total tilt magnitude

$$\beta = \tan^{-1} [\tan^2 \theta + \tan^2 \phi]^{1/2} \quad (7)$$

and the angle of incidence is given by

$$\omega = \tan^{-1} [\tan^2 (\theta_n - \theta_s) + \tan^2 (\phi_n - \phi_s)]^{1/2} \quad (8)$$

If both the point of reflection and the sun subpoint are near the satellite subpoint, i. e., if all θ and ϕ values are small, the above equations can be approximated by the simplified formulae:

$$\phi \simeq \frac{\phi_s}{2} - (1 + \frac{r}{2h})\phi_p \quad (9)$$

$$\theta \simeq \frac{\theta_s}{2} - (1 + \frac{r}{2h})\theta_p \quad (10)$$

$$\beta^2 \simeq \theta^2 + \phi^2 \quad (11)$$

$$\omega^2 \simeq \frac{1}{4} (\theta_s + \frac{r}{h} \theta_p)^2 + \frac{1}{4} (\phi_s + \frac{r}{h} \phi_p)^2 \quad (12)$$

Slope Probability and Light Intensity

Cox and Munk [1, 2] and Cox [8] have shown that the probability density P of the slope (determined by the location) is related to the received intensity J , from this location, in the following manner:

$$P = (4H^{-1} \rho^{-1}(\omega) A^{-1} \cos \mu) J \cos^4 \beta \quad (13)$$

where: H — the solar energy flux per unit area of beam
 ω — the angle of incidence
 $\rho(\omega)$ — the reflection coefficient
 β — the slope magnitude
 A — the telescope effective area
 μ — the telescope tilt from nadir

They have calculated $\rho(\omega)$ for sea water to be: $\rho(\omega) = 0.020, 0.021, 0.060$ and 1.00 for (respectively) $\omega = 0^\circ, 30^\circ, 60^\circ$ and 90° .

In our system (fixed satellite and single point of reflection), the angle μ is constant. For the case of small angles, ω is less than 30 degrees and therefore $\rho(\omega)$ is also essentially constant. Therefore, the term in brackets

in Eq. (13) does not vary with time, and the only variable correction is $\cos^4 \beta$.

Background Light

In addition to the sun glitter two other sources of radiation have to be considered. Cox and Munk pointed out two of them, (1) the skylight reflected at the sea surface, and (2) the sunlight scattered by particles beneath the sea surface. Rozenberg and Mullamaa [9] pointed out another source, (3) the scattered light in the air column separating the satellite from the water surface. Undoubtedly there are more contributors to the background light.

The sources (1) and (2) were studied by Cox and Munk, who found that their contribution depends mainly on the angle between the vertical and the vector from the point under analysis to the observer. In the case of an observer on a synchronous satellite this angle is fixed.

Some idea on the contribution of the scattered light in the atmosphere (3) can be received from the maps of Sekera and Viezee [10] even though they assume the satellite's at infinity. We will use the maps calculated for the case of a planetary surface that absorbs all the incident radiation ($A = 0$); i. e., when the only return is from scattering in the atmosphere. Those maps indicate only slight variations in the intensity of the scattered light in the vicinity of the satellite subpoint, as the sun subpoint shifts away, as long as the angular distance between the sun and the satellite is smaller than about 40 degrees. For our small angles case, we can therefore assume this contribution to be constant.

The above indicates that the background light can be estimated by measuring the radiation received from the point when it is outside the sun glitter limits.

The camera on the ATS-3 Satellite [11] has three channels: Blue (.38-.48 micron), Green (.48-.58) and Red (.55-.63); the respective background intensities were related to each other as 5:6:2, when calibrated for equal reflection from cloud tops. Thus, for reducing the background light, the red channel data is the best choice.

There is of course no way to study the sun glitter in the case of overcast. However, in the case of scattered clouds, our method (since it is based on measurements at a single point) can be used to study the wind velocity in any neighborhood within which a clear area of the size of the telescope resolution can be found.

The Slope Distribution

Cox and Munk found that the slope distribution is "almost" like a two-dimensional Gaussian (normal) distribution, the "almost" standing for peakedness at the probabilities of the small slopes, and skewness toward the upwind directed slopes. To simplify our discussion we will assume the slope distribution to be Gaussian and with zero mean. Thus if c is the slope toward the crosswind direction and u toward the upwind direction, their probability density is given by

$$f(c, u) = \frac{1}{2\pi \sigma_c \sigma_u (1-r^2)^{1/2}} \exp \left[-\frac{1}{2(1-r^2)} \left(\frac{c^2}{\sigma_c^2} - \frac{2rcu}{\sigma_c \sigma_u} + \frac{u^2}{\sigma_u^2} \right) \right] \quad (14)$$

where $\sigma_c \sigma_u$ are the standard deviations of c and u , and r is their correlation coefficient.

Cox and Munk found that r is close to zero, i. e., c and u are approximately independent. In this case the c and u axes are the principal axes of the ellipses of constant density (Fig. 3). However, they will not in general coincide with the north (θ) and east (ϕ) axes, i. e., θ and ϕ will be jointly normal but correlated.

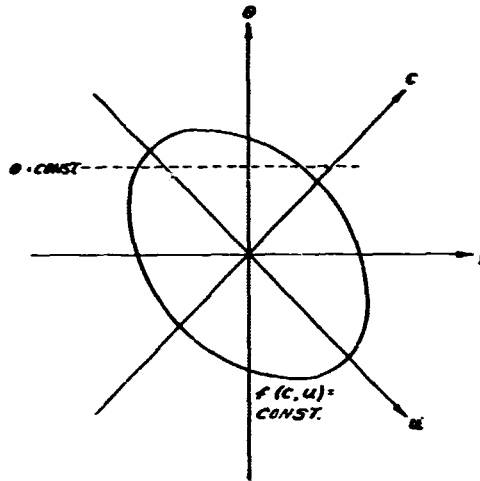


Fig. 3: The probability space of the two dimensional normal distribution of the waves slope.

- C — slope in the cross wind direction
- u — slope in the upwind direction
- φ — slope in the East direction
- θ — slope in the North direction

The sun glitter scan over a fixed point in the ocean may be considered equivalent to traversing the slope probability plane along a certain path. Note that in equations (9) and (10) the only variable (with time) is the longitude of the sun subpoint ϕ_S . For the small angles case, we see that only ϕ varies with time while θ remains constant. Our path in the slope probability plane is therefore a line $\theta = \text{const.}$ and the density P measured using (13) is (up to a constant) the conditional probability density

$$f(\phi|\theta = \text{const.}) \quad (15)$$

This density is also normal, with the mean

$$E(\phi|\theta) = \frac{r \sigma_\phi}{\sigma_\theta} \theta \quad (16)$$

and the standard deviation

$$\sigma_{\phi|\theta} = \sigma_\phi (1-r^2)^{1/2} \quad (17)$$

where r is the correlation coefficient of ϕ and θ .

Cox and Munk found linear relations between the wind velocity W and the variances as follows:

$$\sigma_c^2 = 0.003 + 1.92 \times 10^{-3} W \pm 0.002; \quad (18)$$

$$\sigma_u^2 = 0.000 + 3.16 \times 10^{-3} W \pm 0.004; \quad (19)$$

$$\sigma_c^2 + \sigma_u^2 = 0.003 + 5.12 \times 10^{-3} W \pm 0.004; \quad (20)$$

where σ is in radians and W is the mean wind in meters per second (measured 41 feet above the sea surface). Other relations of this type by Cox and Munk for sea covered by slicks, have received support from other works [12].

It can be shown (ignoring the anomaly of $\sigma_c \neq \sigma_u$ at no wind) that

$$|r| < \frac{\sigma_u^2 - \sigma_c^2}{2\sigma_c^2} \quad (21)$$

Using (18), (19) and (21) we get that $r < 0.2$ up to average winds of 10 m/sec. (This was the case 99.67% of the time, on the three islands during March and April.) This and the small θ rules out any chance to use (16) as a clue for the wind direction. It also means that (17) will reduce to:

$$\sigma_{\phi|\theta} \approx \sigma_\phi \quad (22)$$

Equation (22) indicates that as could be seen intuitively at the beginning of this section, our method estimates the distribution of slopes in the East-West direction. We do not usually know whether this direction coincides with the upwind or crosswind direction, or with any other direction between the two. We, therefore, cannot use only one of Cox and Munk's linear relations between the wind velocity and the variance (Eqs. (18), (19)) but we must use the two of them together. This is done in Figure 4 where the lines represent the two linear relations and their uncertainty boundaries. The lack of knowledge about the wind direction expands the range of possible wind velocities for each value of the slopes variance.

Results

The comparison between the calculated scalar winds and actual wind measurements were made on two dates (the 16th and 19th of April, 1967) for each of the three islands (Palmyra, Fanning and Christmas).

The process of calculating the scalar wind involved the following steps:

- (1) Plotting those scan lines which include the sun glitter, from a sequence of consecutive pictures.
- (2) Navigating on each picture to find which line and picture element represent each island location. (There were apparent variations in the line number, between consecutive pictures, because of the spacecraft variable pitch.)
- (3) Plotting the intensity J as a function of time.
- (4) Converting time to corresponding East directed tilt ϕ , using Eq. (9).
- (5) Subtracting the background light.
- (6) Finding β from (11), and applying the corrections $\cos^4\beta$ (13), to get values of the probability P (up to a constant). (This correction was significant only in cases where the latitude of the reflecting point was far from the latitude of the horizontal specular line of reflection.)
- (7) Finding the standard deviation of the probability curve.
- (8) Finding the range of possible wind velocities from Figure 4.

In Figure 5, some of these steps are illustrated for two cases: Palmyra and Fanning, 16 April 1967. The records on the right side of Figure 5 are 8 scan lines over the latitude of Fanning Island, taken in intervals of 23 minutes, the longitude of the island is marked by the vertical line. These 8 intensities yield the normal curve shown in the middle. Similar procedure is shown also for Palmyra Island.

The calculated standard deviation results are plotted against actual wind measurements, as points, in Figure 4. The numbers in brackets near those points indicate the measured wind direction relative to the east west direction.

Except for one of the c points which is only 5 degrees from the E-W direction and therefore should have been closer to the σ_u^2 line, all other points are within the limits suggested by Cox and Munk.

Conclusion

Our work shows the feasibility of studying the east-west component of the waves' slope distribution from a synchronous satellite by using the sun as the radiation source with its movement, relative to the earth, as a scanning mechanism.

Using Cox and Munk's [1, 2] linear relation between the variance of the waves' slope and the wind velocity, it was possible to calculate scalar wind velocities in the area of the sun glitter and to compare them to actual wind measurement taken on the ocean. These comparisons revealed that the enormous height of the observer did not degrade the accuracy of the observation. When the wind direction is given, the accuracy of the calculated wind velocity is as good as if the sun glitter is studied from aircraft altitude, i. e., ± 1 m/sec.

In the course of this work, it became more and more evident that the sun glitter is a strong and reliable source of radiation that should be studied instead of being avoided. In addition to the geometry of the sea and surface wind velocity, much can be learned about the atmosphere above the sea, since this radiation has crossed the whole atmosphere twice, and the trip is recorded in its spectrum.

References

1. Cox, C., and W. Munk, 1954: Measurement of the Roughness of the Sea Surface from Photographs of the Sun's Glitter. Jour. Optical Soc. Am. **44** (11) 838-850.
2. Cox, C. and W. Munk, 1954: Statistics of the Sea Surface Derived from Sun Glitter. Jour. Marine Res. **13**(2) 198-227.

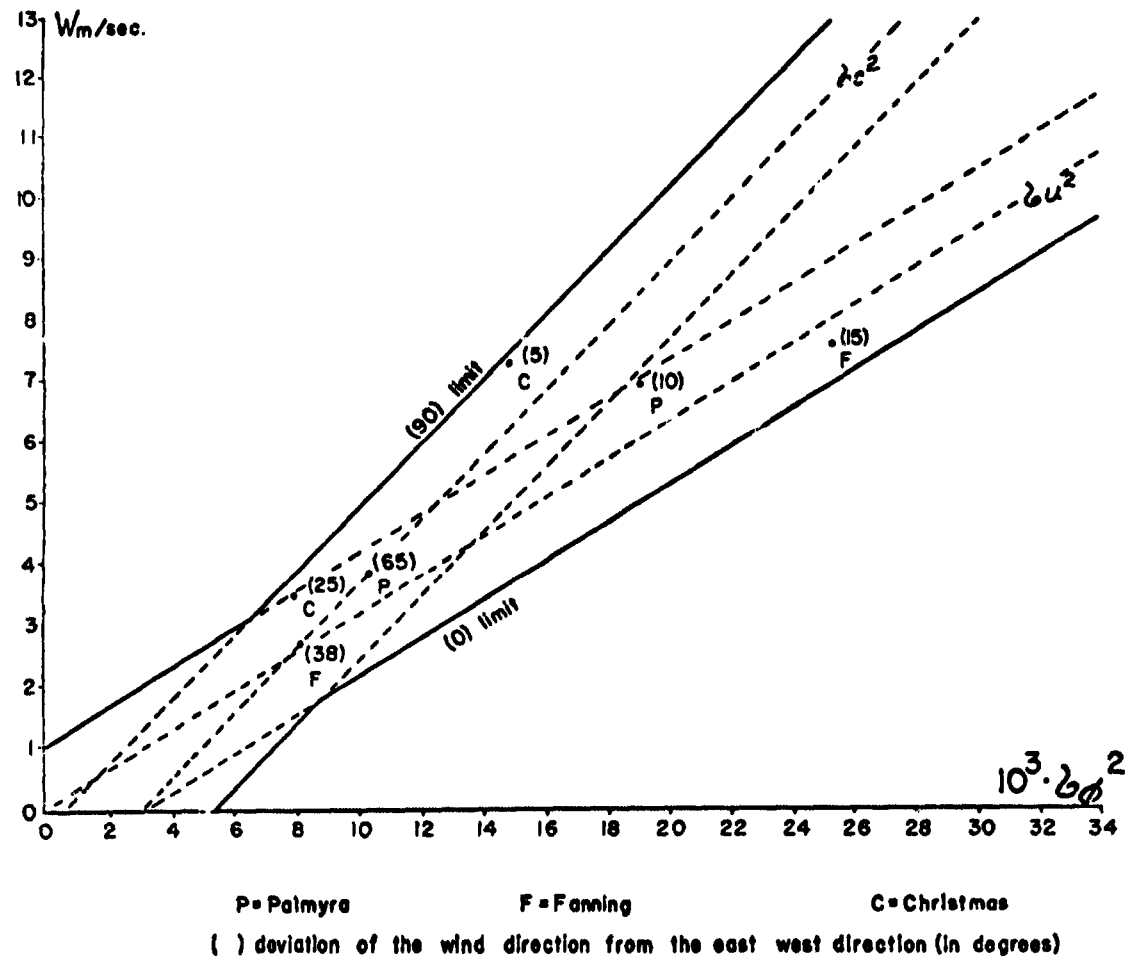


Fig. 4: The linear relation between the waves slope variance and the wind velocity (after Cox and Munk), compared to six points represented by variance calculated from the satellite data, and actual wind measurements.

PALMYRA ISLAND

FANNING ISLAND

11:31

APR. 16, 1967

LOCAL TIME

11:54



12:17

12:40

13:04

13:27

13:50

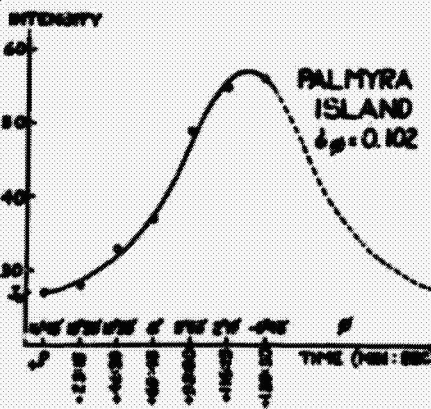
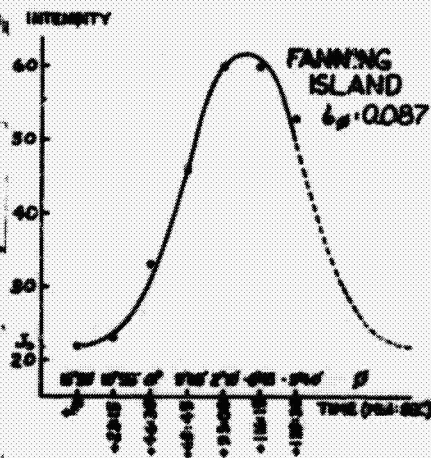


Fig. 5: Some of the steps involved in reducing the satellite data, to the standard deviation of the waves' slope.

3. Zipser, E. J., and R. C. Taylor, 1968: A Catalogue of Meteorological Data Obtained During the Line Islands Experiment February-April 1967. NCAR-TN-35.
4. Santa Barbara Research Center and University of Wisconsin, 1967: ATS Spin-Scan Cloud Camera and Prelaunch Calibration Procedure. Ann. Report 1966, Dept. of Meteorology, The University of Wisconsin, Madison, Wisconsin.
5. Sunderlin, W. S., 1967: The Spin Scan Camera System on Application Technology Satellite - 1. ATS-1 Volume.
6. Hanson, K., T. Vonder Haar and F. Nicholson, 1968: ATS-1 Navigation. ATS-1 Volume.
7. United States Naval Observatory and Her Majesty's Stationery Office, 1966: The Air Almanac 1967 January - April.
8. Cox, C., 1965: The Relation of Backscattered Radiation to Wind-Stress at the Sea Surface. Presented at the AGU-AMS International Symposium on Electromagnetic Sensing of the Earth from Satellites. Miami, 1965.
9. Rozenberg, G.V. and Yu. A. R. Mullamaa, 1965: Some Possibilities of Determining Wind Speed Over an Ocean Surface Using Observations from Artificial Earth Satellites. Izv. Atmospheric and Oceanic Series, Vol. 1, No. 3, pp. 282-290, translated by P. A. Keehn.
10. Sekera, Z. and W. Viezee, 1961: Distribution of the Intensity and Polarization of the Diffusely Reflected Light Over a Planetary Disk. The RAND Corporation Report R-389-PR November 1961.
11. Santa Barbara Research Center, 1966: Multicolor Spin-Scan Cloud Camera, Proposal SM 75/66 for the University of Wisconsin.
12. Kinsman, B., 1965: Wind Waves, Their Generation and Propagation on the Ocean Surface. Prentice-Hall, Inc. (See chapters 7 and 8.)

N 69 - 33578

INVESTIGATION OF CLOUDS ABOVE SNOW SURFACES UTILIZING RADIATION MEASUREMENTS OBTAINED FROM THE NIMBUS II SATELLITE

F. F. Hauth* and J. A. Weinman

CONTENTS		Page
1. Introduction		17
2. Method		17
	Data Acquisition	17
	Definitions	18
	Area Studied	18
	Data	18
3. Results and Discussion		19
	Snow Characteristics	19
	Cloud Characteristics	27
4. Conclusions		29
5. References		29

ABSTRACT

Bidirectional reflectance of solar radiation vs. scattering angles from snow and cloud surfaces are found markedly different. The variation of bidirectional reflectance with scattering angle depends on cloud thickness. Infrared temperature data obtained from the same region is used in conjunction with these observations to provide information on characteristics of clouds located above snow surfaces.

* Capt., Air Weather Service, USAF, Det. 7, Fifth Weather Squadron, APO San Francisco, California 96296.

Nimbus II Medium Resolution data from consecutive orbits over Greenland on 19 June 1966 are used to illustrate how such data provides information on clouds above snow surfaces.

Introduction

A major portion of the polar regions has only a sparse network of meteorological stations. Because these areas are often the source of weather systems that affect the middle latitudes, weather satellites, particularly the Nimbus system with its polar orbit, provide a valuable source of meteorological data. Previous research (Popham and Samuelson (1965)) has shown the feasibility of employing satellites for the acquisition of meteorological information from polar areas.

One of the problems encountered by the analyst interpreting photographs obtained from weather satellites over polar regions is the determination of clouds above a snow or ice background. The use of multi-channel medium resolution radiation data from a single orbit offers a partial solution to the problem, a more complete solution is rendered feasible if data from the same region is obtained from several orbits.

The purpose of this case study is to illustrate how bidirectional reflectance of solar radiation taken in conjunction with long wave radiation emitted by the surface and clouds permits one to differentiate clouds from snow or ice backgrounds. Furthermore this procedure also permits inferences to be drawn regarding the type of clouds observed, and their approximate altitude and thickness.

Method

Data Acquisition

The Medium Resolution Infrared Radiometer (MRIR) on board the Nimbus II satellite is designed to measure radiation emitted and reflected by the earth and its atmosphere. The following channels provided data employed in this study:

Channel 2 (10 to 11 microns)—This channel measures surface or near-surface temperatures over clear portions of the atmosphere; it also provides cloud cover information.

Channel 5 (0.2 to 4.0 microns)—This channel yields information on the intensity of the solar energy reflected from the earth and its atmosphere (Nimbus II Users Guide (1966)).

Definitions

The quantity measured by channel 5 of the radiometer is the solar radiance reflected from the earth. The bidirectional reflectance, ρ' , i.e., fraction of radiation incident from direction (θ_0, ϕ_0) which is reflected in the direction (θ, ϕ) , can be derived from such measurements by letting:

$$\rho' = \pi \int_{0.2\mu}^{4.0\mu} N_{\lambda}(\theta, \phi) \cdot \Phi_{\lambda} \cdot d\lambda / \cos \theta_0 \int_{0.2\mu}^{4.0\mu} H_{s\lambda}(\theta_0, \phi_0) \cdot \Phi_{\lambda} \cdot d\lambda \quad (1)$$

where $N_{\lambda}(\theta, \phi)$ is the reflected spectral radiance in units, watts cm^{-2} sterad $^{-1}$ micron $^{-1}$, $H_{s\lambda}(\theta_0, \phi_0)$ is solar spectral irradiance with units, watt cm^{-2} micron $^{-1}$ and Φ_{λ} is the spectral response of channel 5 of the radiometer. Bartman (1967) has presented an extensive discussion of the measurement and interpretation of bidirectional reflectance obtained from Nimbus II sensors. The bidirectional reflectance depends on the scattering angle, β , defined by

$$\cos \beta = \sin \theta_0 \cdot \sin \theta \cdot \cos(\phi - \phi_0) - \cos \theta_0 \cdot \cos \theta \quad (2)$$

where θ_0 is the zenith angle and ϕ_0 is the azimuth angle, measured counterclockwise from north, for the incident radiation. The zenith and azimuth angles of the reflected radiation are θ and ϕ respectively.

Area Studied

In order to illustrate how bidirectional reflectance and temperature data obtained from satellites can be analyzed, a polar area covered fairly homogeneously with snow and a variety of clouds was required. It was also necessary that data be available for the same region from two successive orbits. Since radiation data was available for only the summer months, the Greenland area was selected.

An ice cap covers 85% of Greenland; only a narrow zone around the coast remains uncovered. Snow is received throughout the year on the higher portions of the ice cap. Surface melting takes place at elevations below 2000 meters (Project Mint Julep (1954)), however most of the ice cap expanse is above this altitude. The ice cap therefore serves as a homogeneous surface which reflects solar radiation and emits terrestrial radiation.

Data

Gridded maps of digital data from MRIR channels 2 and 5 employed in this study of Greenland were obtained from Nimbus II orbits 468 and 469 which occurred on 19 June 1966 (Nimbus II Data Catalog: Volume I (1966)). For orbit

468 the data time period was 1115 to 1123 GMT, whereas for orbit 469 it was 1300 to 1309 GMT. The data obtained from orbit 468 and 469 by sensor channel 5 are shown in Figure 1 and 2, respectively. Since data obtained from channel 2 during the two orbits was virtually identical, it is sufficient to show the infrared temperatures obtained during orbit 468 in Figure 3. The shaded areas shown in Figure 4 are believed to be cloud-covered for reasons cited in a later section.

Results and Discussion

Snow Characteristics

In order to compare bidirectional reflectance observed from a satellite to measurements obtained nearer the ground, the role of the intervening atmosphere must be considered. The optical thickness of the atmosphere attributable to molecular scattering, τ_R , and aerosol scattering, τ_M , for wavelengths 0.26 to 4.0 μ were obtained from Elterman (1965). These values were then multiplied by the weighting functions $H_{s\lambda}$ and Φ_λ such that a mean optical depth of the atmosphere is

$$\tau' = \frac{\int_{0.2\mu}^{4.0\mu} (\tau_R + \tau_M) \cdot H_{s\lambda} \cdot \Phi_\lambda \cdot d\lambda}{\int_{0.2\mu}^{4.0\mu} H_{s\lambda} \cdot \Phi_\lambda \cdot d\lambda} \quad (3)$$

$$= .02$$

where these quantities are defined in Eq. (1).

The tables of Coulson et al. (1960) were employed to determine the variation of bidirectional reflectance with the zenith angle of observation, θ , the solar zenith angle θ_0 and optical thickness τ' for an atmosphere of Rayleigh scattering particles. This procedure is somewhat inaccurate because the aerosol does not scatter radiation by Rayleigh's law; however, no tabulation comparable to that of Coulson et al. is available for an aerosol-laden atmosphere.

Utilizing the solar zenith angle, $\theta_0 = 53^\circ$, and azimuth angle of observation, $(\phi - \phi_0) = 90^\circ$, simulating those actually encountered in this case study, and surface albedo $A = .80$, (the largest A considered by Coulson et al.) values of bidirectional reflectance above the atmosphere obtained for various radiometer zenith angles, θ , are shown in Figure 5. It can be seen from these curves that when $0 < \tau' < .02$, variations of bidirectional reflectance due to variations in optical thickness are less than 0.1%.

The computed bidirectional reflectance, $\rho' = .48$, differs from the bidirectional reflectances measured over snow surfaces, $\rho' = .64$. This difference can be attributed to the approximations employed in these computations: Only

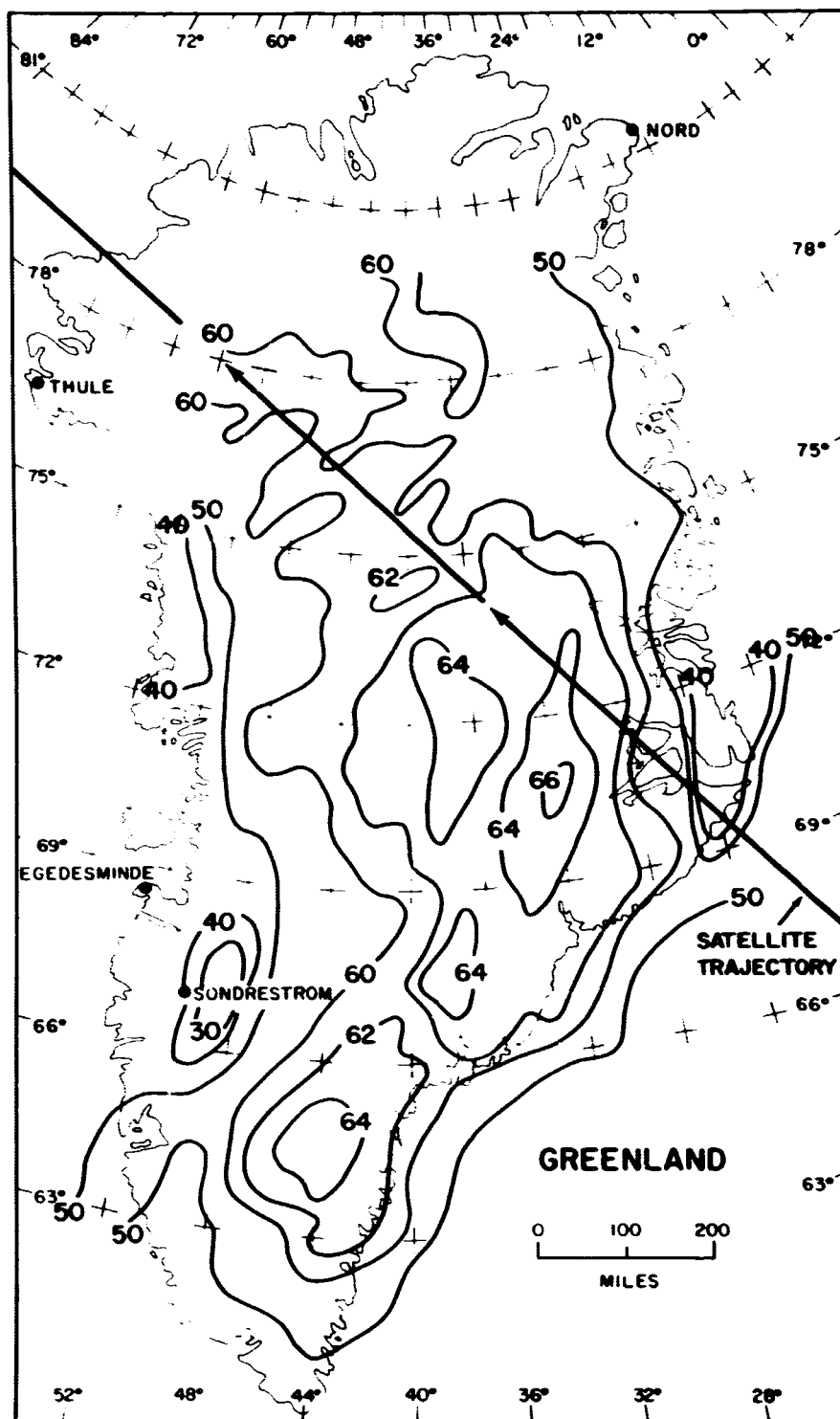


Fig. 1. Nimbus II M.R.I.R. channel 5 bidirectional reflectance (%) for orbit 468 (June 19, 1966: 1115 to 1123 GMT).

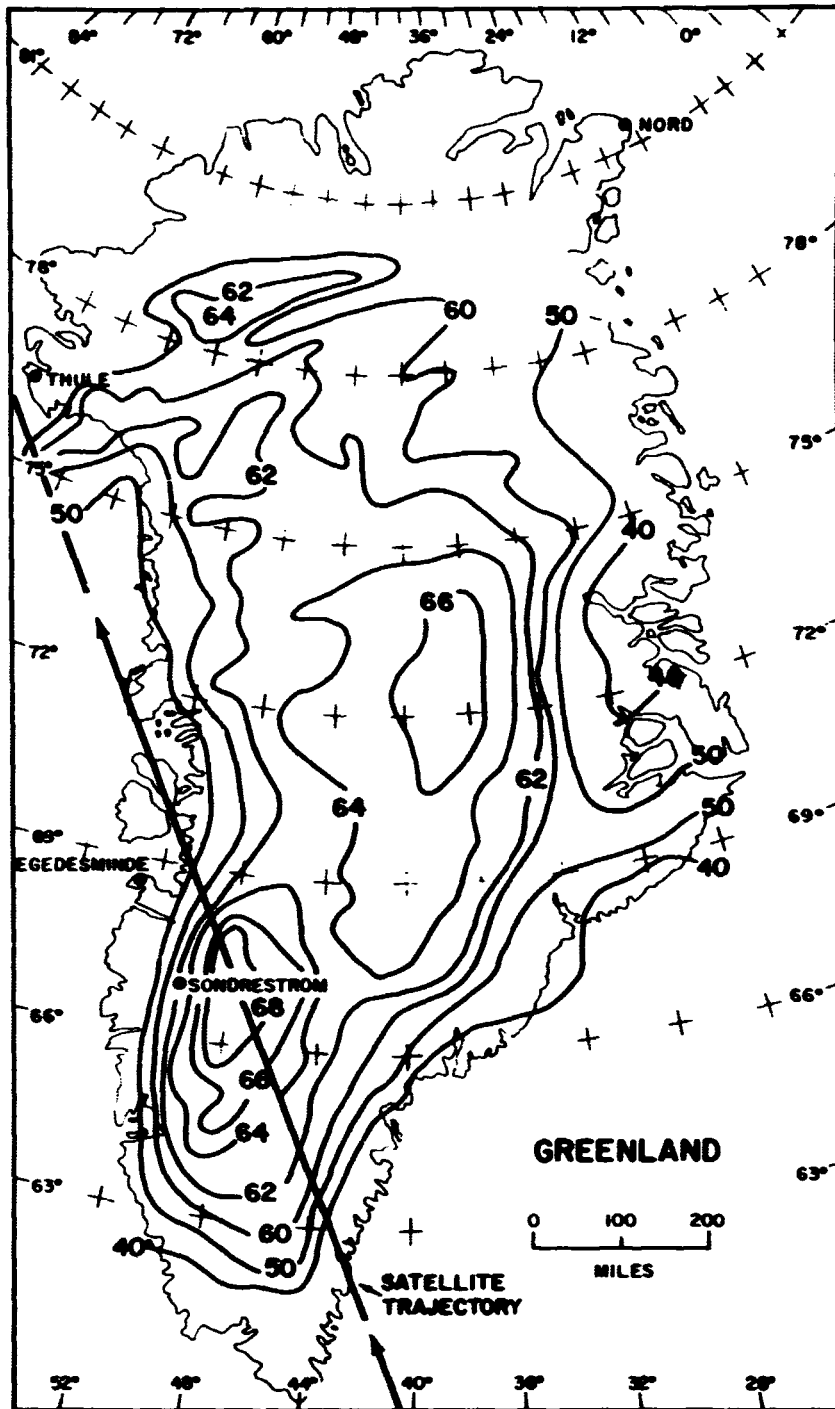


Fig. 2. Nimbus II M.R.I.R. channel 5 bidirectional reflectance (%) for orbit 469 (June 19, 1966: 1300 to 1309 GMT).

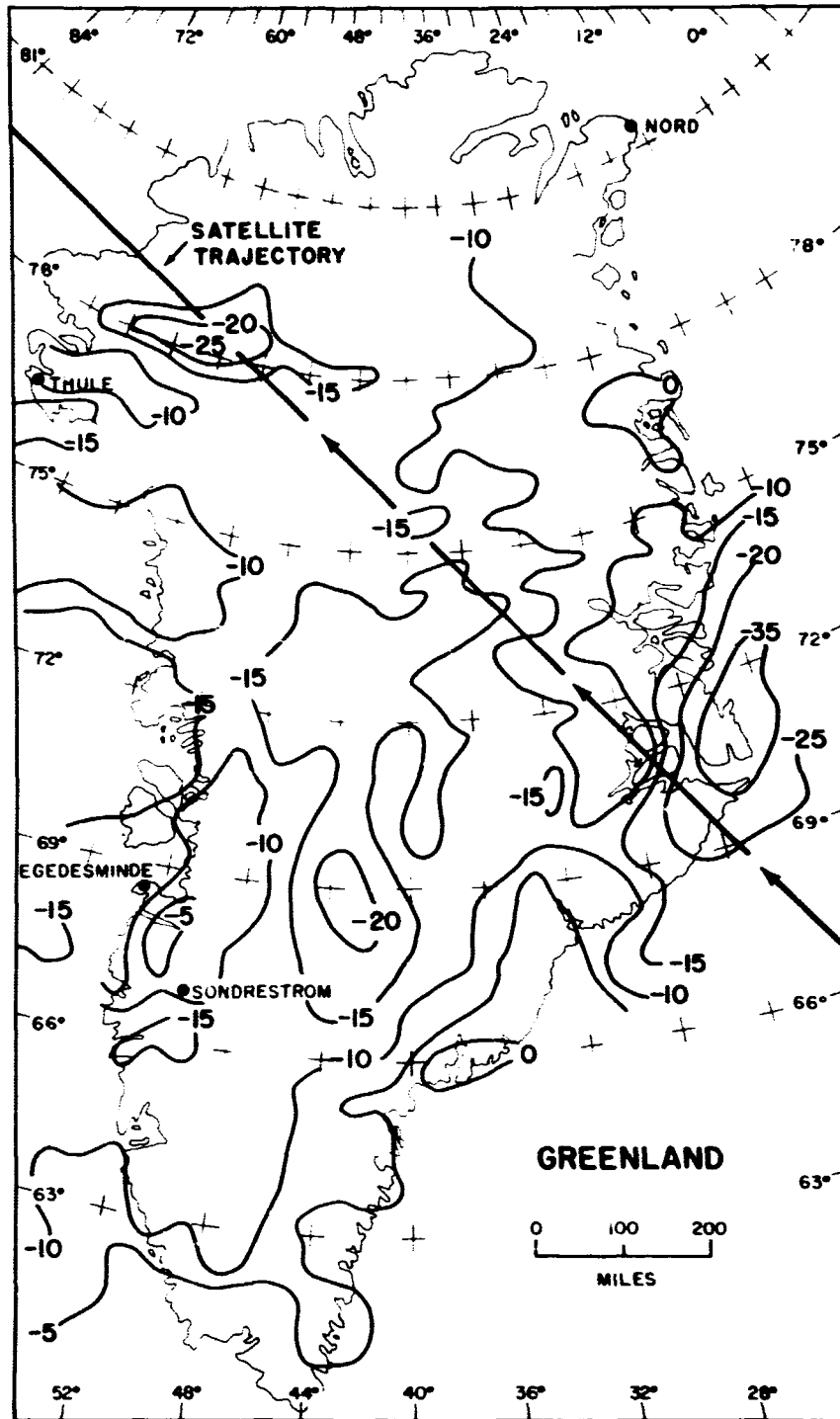


Fig. 3. Nimbus II M.R.I.R. channel 2 infrared temperatures ($^{\circ}$ C) for orbit 468.

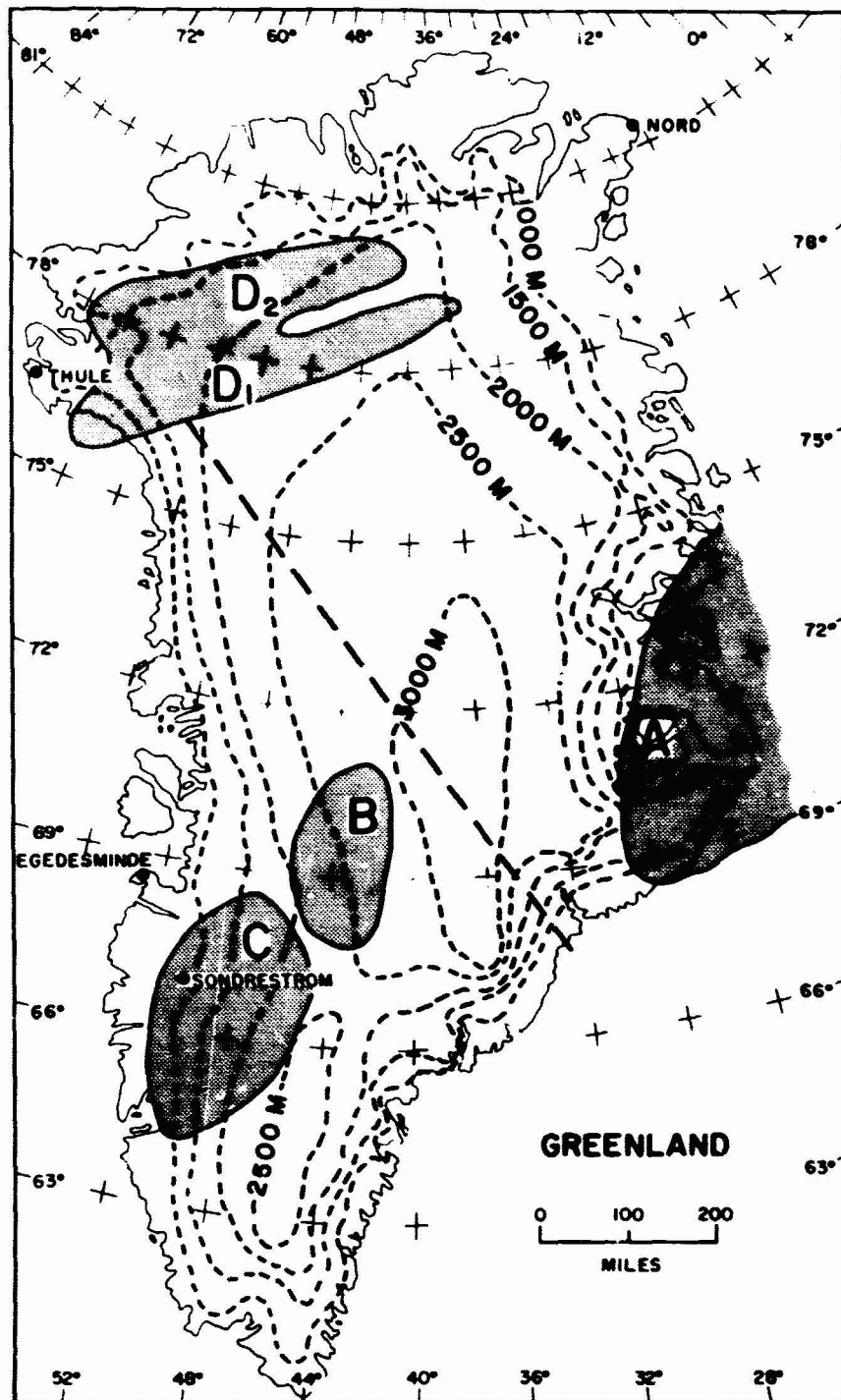


Fig. 4. Height contours of Greenland in meters with cloud area shaded. The dashed line is the locus of points for which β has the same value for both orbits.

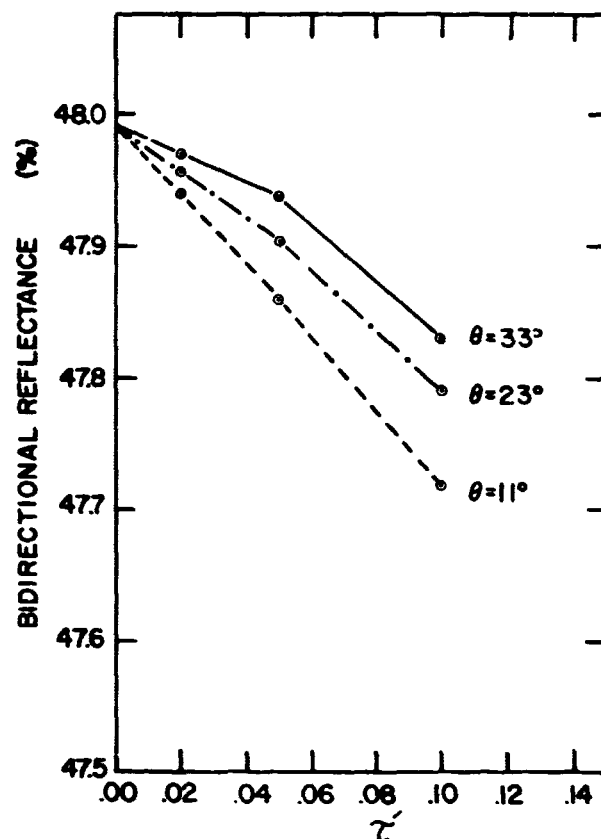


Fig. 5. Theoretical bidirectional reflectance (%) as a function of optical thickness (τ) for various observational zenith angles (θ). Solar zenith angle ($\theta_0 = 53^\circ$), observational azimuth angle ($\phi - \phi_0 = 90^\circ$), and surface albedo, $A = .80$. (Coulson *et al.* (1960))

calculated radiances for pure Rayleigh atmospheres were available. The tables of Coulson *et al.* only presented data for an albedo $\leq .80$; this albedo is less than that measured over relatively fresh snow surfaces (Project Mint Julep: Part II (1955)). The surface was assumed to be Lambertian by Coulson *et al.* (1960), whereas aged snow surfaces are somewhat specular reflectors.

From this exercise it is concluded that the angular dependence of bidirectional reflectance is probably characteristic of the reflecting surface and not of the intervening cloudless atmosphere.

The bidirectional reflectance of the ice cap depends on the surface composition. The Mint Julep Project showed that bidirectional reflectance has maximum values over the fresh snow surfaces with values decreasing slowly down the ice cap slopes as more ablation occurs. Minimum values occur at the coastal regions where tundra and rock are exposed during the summer season.

The effect of surface inclination on bidirectional reflectance values is evident in both Figures 1 and 2. The satellite approaches the eastern and southern Greenland coasts respectively with its MRIR scanning perpendicular to the satellite orbit; the corresponding solar azimuth angles are $\phi_0 = 57^\circ$ and 33° respectively. Scrutiny of these figures shows that the bidirectional reflectance isopleths tend to follow the height contours in regions other than those shaded in Figure 4.

The dashed line of Figure 4 traces areas from which solar radiation is reflected to both satellite orbits by the same angle β namely $110^\circ \leq \beta \leq 112^\circ$. The gradients of the ice cap elevation, determined from Air Force Operational Navigation Charts, were measured at points of the dashed line of Figure 4 in the directions which bisect the azimuthal separation between the incident and reflected radiation, i. e., $(\phi - \phi_0)/2$. Positive gradients are those inclined toward the satellite orbit and the sun, negative gradients are those inclined in the opposite sense. The effect of surface inclination on bidirectional reflectance is shown in Figure 6. The dashed lines connect data obtained from the same

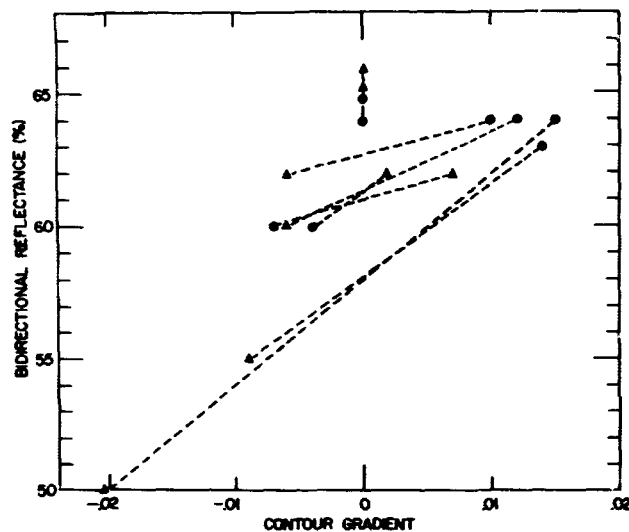


Fig. 6. Variation of bidirectional reflectance as a function of the elevation gradient measured in the direction which bisects the angle between the solar azimuth and MRIR scanning azimuth. Negative gradients are inclined away from the incident solar intensity and MRIR. Points obtained from the same area are connected by dashed lines: orbit 468 (●), orbit 469 (▼).

area as it was received at the two satellite orbits under consideration. It is evident that the bidirectional reflectance is lowest when the ice cap is inclined away from the sun and the satellite. These results are consistent with data cited by Kondrat'yev (1965). The dependence of the bidirectional reflectance on the known inclination of the ice cap aids in the identification of cloud covered regions.

The bidirectional reflectance values from three typical horizontal snow areas are shown in Figure 7 as a function of the scattering angle β defined in Eq. (2). These values are in the 60% to 66% range and show little variation with scattering angle for $110^\circ < \beta < 135^\circ$. Although these data extend over only a limited range of zenith angles of observation, Bartman (1967) found that fresh snow surfaces exhibit relatively constant bidirectional reflectance over this range of scattering angles.

In agreement with climatological data, Figure 3 shows that the temperature of the snow surfaces exhibit the tendency to follow the topographic features of the ice cap and coastal areas. The infrared temperatures measured by the channel 2 sensor range from -15°C in the central portion of the ice cap to -5°C near the edges.

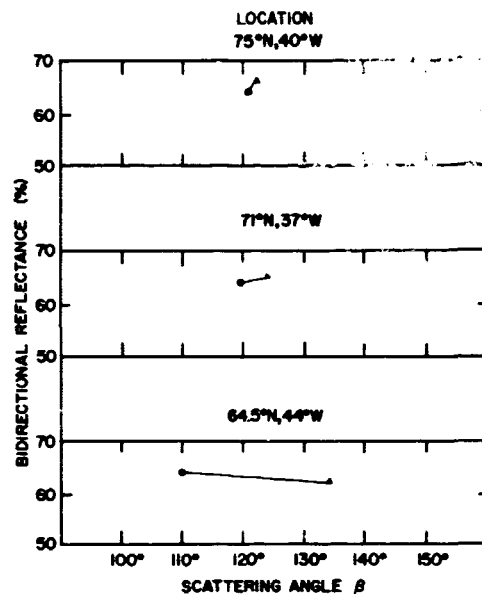


Fig. 7. Bidirectional reflectance vs. scattering angle: orbit 468 (●), orbit 469 (▲).

Cloud Characteristics

The shaded areas of Figure 4 are believed to be cloud covered for reasons cited below:

The bidirectional reflectance values of cloud area A shown in Figure 1 range from 38% in the central portion of the cloud mass to 60% near the edges. Unfortunately bidirectional reflectance data for most of this cloud area were not available from orbit 469 shown in Figure 2.

Infrared temperatures are in the -30°C to -35°C range for the central portion of the cloud mass increasing gradually to -10°C to -15°C near the edges. The structure of the underlying surface is such that decreasing bidirectional reflectances and increasing temperatures would be expected from the ice cap toward the coast. The opposite sequence is observed, suggesting that this cloud area is high and relatively thick (cirrus).

The bidirectional reflectance of cloud area B ranges between 55% and 60% in Figure 1 and 62% to 64% in Figure 2. This cloud occurs above a portion of the ice cap where the surface is tilted away from the incident solar radiation during both orbits. Because the bidirectional reflectance values continue to decrease down the slope of the ice cap, the inference is made that the surface characteristics show through the cloud. Figure 8 shows that the bidirectional reflectance values of cloud B increase only slightly with scattering angle in the "fogbow" region ($120^{\circ} < \beta < 160^{\circ}$). The bidirectional reflectance variation approaches that of the underlying snow surface; the clouds in area B are therefore assumed to be thin or scattered in coverage.

Figure 3 shows that the temperatures for this cloud area are 5°C to 10°C colder than those of the snow surface. Because these temperatures are a blend of surface and cloud temperatures, this cloud area is most probably scattered to thin broken cirrus.

The surface below cloud area C extends from the higher elevations of the snow-covered ice cap to the coastal region where exposed rock and tundra areas predominate. The bidirectional reflectance values of Figure 2 seem consistent with the assumption of cloudfree conditions and a tundra surface. However, the values observed during orbit 469 differ markedly from those observed in orbit 468: Whereas a minimum zone of 30% bidirectional reflectance was observed during orbit 468, a maximum zone of 68% is observed during orbit 469. The change in bidirectional reflectance is consistent with the observations of Bartman shown in Fig. 8. This measurement suggests that the clouds in area C are sufficiently thick so that the reflectance of the underlying surface is not apparent.

Figure 3 shows that the temperature patterns of cloud area C are about 5°C to 10°C colder than would be expected under clear-sky conditions. The

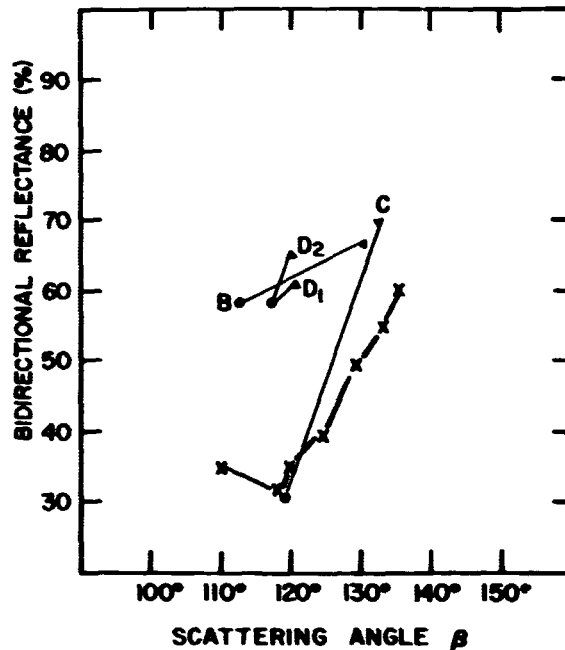


Fig. 8: Bidirectional reflectance from cloud areas vs. scattering angle: orbit 468 (●), orbit 469 (▲), measurements by Bartman (1967) (x). Letters refer to cloud area designation in Fig. 4.

bidirectional reflectance indicates that this cloud layer is relatively thick; therefore this is probably a middle type cloud (alto cumulus); a blend of thin cirrus with middle clouds below could produce a similar temperature pattern.

Conventional data verify that the latter situation exists. Sondrestrom Air Base, located under the western portion of cloud area C, reported a broken cloud deck based at an estimated 9000 feet with broken cirrus above at the time of orbit 468. A radiosonde ascent in this area at 1200 GMT indicated a temperature of -12°C at the 590 mb inversion top, this agrees with the infrared measurements near Sondrestrom shown in Figure 3. A temperature dew point spread of 8°C to 10°C was maintained to 400 mbs.

The surface underlying cloud area D is snow-covered ice cap sloping toward the west and northwest away from the incident solar radiation. With cloudless skies the bidirectional reflectance values from orbit 468 should slowly decrease toward the coastal regions. Bidirectional reflectance data from orbit 468 is missing along the northwest coast, and from both orbits north of 80°N . However, the remaining data show that the bidirectional reflectance increases with latitude; this is contrary to what would be expected from snow

surfaces inclined away from the incident solar intensity. The southern cloud area D_1 had bidirectional reflectance varying in alternating bands from 58% to 62% in orbit 468 and 60% to 63% in orbit 469. The bidirectional reflectance variation with scattering angle of region D_1 in Figure 8 is similar to that characteristic of snow surfaces.

Little contrast is noted in the temperature patterns of the cloud area D_1 shown in Figure 3. There is a tendency for the temperature and bidirectional reflectance values to align in bands parallel to the contours; this suggests that these clouds are solid and low rather than high and broken. The northern cloud area D_2 exhibits a somewhat greater bidirectional reflectance variation with scattering angle and colder temperatures than the southern area D_1 . This suggests that the low clouds extend inland from the Baffin Bay area in a north-easterly direction, becoming thicker toward the northern coast. This conclusion was confirmed by Thule's report of status and fog to the south of their station at the time of orbits 468 and 469.

Conclusions

Figure 8 shows that for cloud areas where bidirectional reflectance data from consecutive orbits were available, the bidirectional reflectance exhibited changes in the "fogbow" region which are proportional to the cloud thickness. The bidirectional reflectance of snow shown in Fig. 7 is relatively independent of scattering angle over the range of angles encountered in this study. Because of this difference, the analysis of bidirectional reflectance data from consecutive orbits in conjunction with temperature data permits inferences to be drawn concerning characteristics of clouds above snow surfaces.

Acknowledgment

This research was supported by funds from NSF Grant GA 1020 and NASA Contract NASW-65.

References

1. Bartman, F. L., 1967: "The Reflectance and Scattering of Solar Radiation by the Earth," Department of Aerospace Engineering High Altitude Engineering Laboratory Technical Report, ORA Project 05863, University of Michigan, Ann Arbor, Michigan, 257 pp.
2. Coulson, K. L., J. V. Dave and Z. Sekera, 1960: Tables Related to Radiation Emerging from a Planetary Atmosphere with Rayleigh Scattering, University of California Press, Berkeley and Los Angeles, 548 pp.

3. Elterman, L., 1965: In Handbook of Geophysics and Space Environments, edited by Shea Valley, McGraw-Hill Book Company, Inc., New York, pp. 7-1 to 7-2, and 7-14 to 7-35.
4. Kondrat'yev, K. Ya., 1965: Actinometry, Translation of "Aktinometriya," Gidrometeorologicheskoye Izdatel'stvo, Leningrad, NASA TT F-9712, N66 10158, Clearinghouse for Federal Scientific and Technical Information, Springfield, Virginia. 675 pp.
5. Nimbus II Data Catalog: Volume I, 1966: Goddard Space Flight Center, Greenbelt, Maryland, 439 pp.
6. Nimbus II Users Guide, 1966: Goddard Space Flight Center, Greenbelt, Maryland, 229 pp.
7. Popham, R. W. and R. E. Samuelson, 1965: "Polar Exploration with Nimbus Meteorological Satellite," Arctic, Vol. 18, pp. 246-255.
8. Project Mint Julep, Part II, 1955: Arctic Construction and Frost Effects Laboratory, New England Division, Boston, Massachusetts, 90 pp.
9. Project Mint Julep, Part IV, 1954: Arctic Construction and Frost Effects Laboratory, New England Division, Boston, Massachusetts, 77 pp.

N 69 - 33579

VARIATIONS OF THE EARTH'S RADIATION BUDGET

by

Thomas H. Vonder Haar

CONTENTS

	Page
INTRODUCTION	33
1. The Radiation Budget: A Component of the Energy Budget	35
1.1 Radiation Budget of the Earth-Atmosphere System	36
2. Available Satellite Data	37
2.1 The Radiation Sensing Systems	37
2.11 Low Resolution Sensors	37
2.12 Medium Resolution Sensors	39
2.2 Special Characteristics of the Satellite Data	39
2.21 Coverage in Time and Space	40
2.22 Data Adjustments	41
3. Accuracy of the Radiation Data	42
3.1 Albedo and Longwave Radiation Accuracy Estimates	43
3.11 Random Error	43
3.12 Bias Error	43
3.13 Accuracy Tests	45
3.2 Net Radiation Error Analysis	48
3.21 Effect of Albedo and Longwave Radiation Accuracy	48
3.22 Effect of Uncertainty in the Solar Constant	49
3.3 Error Analysis Summary	50
4. Radiation Budget Results	51
4.1 Geographical Variations	52
4.11 Mean Seasonal Budgets	52
4.12 Mean Annual Budgets	65
4.2 Budgets of Latitudinal Zones	70
4.21 Mean Meridional Profiles	70
4.22 Time-Latitude Sections	73
4.23 Budgets of Selected Zones	77

4.3	Global and Hemispheric Budgets	79
4.31	Temporal Variations	79
4.32	Mean Annual and Seasonal Values	81
5.	Energy Budget Results and Required Transports	86
5.1	The Energy Budget of the Earth-Atmosphere System	86
5.2	Mean Seasonal Energy Budgets	88
5.3	The Mean Annual Case	92
6.	Summary	98
	REFERENCES	100
	APPENDIX — Satellite Observations of The Solar Constant	103

ABSTRACT:

More than 40 months of radiometric measurements from the first generation meteorological satellites are used to describe the radiation budget of the earth-atmosphere system. The geographical and temporal variation of the energy exchange between the earth and space is examined with the aid of mean annual and seasonal maps, zonal averages and mean global values.

Maps of the radiation budget components show that the lower latitudes are characterized by radiation patterns which depart considerably from the zonal mean value. These maps mark persistent features of the atmospheric circulation during each season which should be included in numerical models that simulate atmospheric conditions. Radiation budgets of latitudinal zones, including the polar regions, are used to note areas where changing surface and atmospheric conditions modify the large-scale radiation budget, even though the dominant effect is due to seasonal changes in incident solar energy. On a hemispheric scale, the measurements show that, despite the difference in surface features, the northern and southern hemispheres have nearly the same radiation budget over the course of one year. The mean annual planetary albedo was found to be 29% and the equivalent radiation temperature of the earth-atmosphere system is 252°K. Over all time periods for which measurements were available, the net radiation budget of the earth showed a small net gain, although the value is close to the limit of error in the measurements. When these new radiation budget data are combined with estimates of the other energy budget terms the net poleward heat transport required by balance considerations is derived.

The study includes a complete error analysis and the satellite measurements compare well with the few available independent obser-

variations. The same sensors used to obtain most of the radiation budget data were used to derive a magnitude of the solar constant equal to $1.99 \pm 0.03 \text{ cal} \cdot \text{cm}^{-2} \cdot \text{min}^{-1}$.

INTRODUCTION

Radiant energy exchange across the upper boundary of our earth-atmosphere system is the primary forcing function of large-scale atmospheric and oceanic circulations. For this reason, atmospheric scientists have for many years sought more knowledge about the magnitude of this energy exchange and its variations with time and location. The significance of such information has recently been demonstrated by House (1965). Using satellite observations, he has shown that because of a lower planetary albedo in the tropical regions, the required poleward energy transport may be as much as 40 percent greater than was estimated from earlier studies. More observations of this type will give us a better indication of the driving force responsible for large-scale weather variations.

In the past, studies of the earth's radiative budget were based on theoretical calculations of the transfer of radiant energy through the atmosphere whose mean state and constituents were defined by available climatological data. One of the major difficulties that hindered these theoretical studies, the problem of radiative transfer in a cloudy atmosphere, still exists today. A critical synopsis on the earliest work of this kind was summarized by Lettau (1954) and some of the more recent studies are discussed by Budyko and Kondratiev (1964) and House (1965).

An immediate need for information about the earth's radiation budget has arisen because of the rapid development of numerical models of the atmosphere's circulation. These models do not require radiation observations as input parameters, but any model that properly describes the variations of atmospheric conditions must contain a method to account for radiant energy transfer. Thus, such a model can yield computed values of the radiation budget at the top of the atmosphere over various intervals of time and for different locations. Because measurements from satellite provide observed values of this same budget, average values of the observations, particularly of the net radiation, are a good control for the developing numerical models. With this in mind, the Committee on Atmospheric Sciences of the ICSU/IUGG¹ listed as one of five special areas of research to be emphasized in preparation for a Global Atmospheric Research Program (GARP) "... studies of the global distribution of radiation balance (net

¹ICSU/IUGG, Second Report of the IUGG Commission on Atmospheric Sciences, 15 September 1966.

flux)...² A more recent report² reiterated this need by assigning a high priority to the task of obtaining a new radiation climatology.

The purpose of the present study is to use an extended time series of satellite radiation measurements to determine the mean radiative budget of the earth-atmosphere system at various locations and for different time periods, and to investigate variation from the mean state.

Late in 1959, the first successful observations of one component of the radiation budget (the infrared radiation from the earth) were obtained from sensors carried on the Explorer VII satellite (Suomi (1958), House (1965)). Several years later, sensors flown on some of the TIROS satellites obtained measurements of both infrared and reflected solar radiation from the earth-atmosphere system. These data were used by House (1965), Bandeen *et al.* (1965), Rasool and Prabhakara (1967), Winston (1967) and others to investigate the radiation budget over limited periods of time. Even during these time periods the data sampling was often quite limited and in most cases absolute values of the solar radiation budget parameters could not be obtained.

In the present study some of the TIROS data will be combined with additional satellite measurements in order to describe the earth's radiation budget as observed from our first generation of meteorological satellites. Thus, for the first time we will be able to examine more than 40 months of satellite observations in a single study. Because there were occasions when more than one satellite was operating over the same areas at the same time, it is possible to intercompare these data to check on the absolute accuracy of the measurements.

The available data may be separated into two time periods:

- a) a period of intermittent observation: December 1959 - June 1963
- b) a period of continuous observations: June 1963 - November 1965.

Excluding the Explorer VII values, all of the measurements will be used to derive mean values of net radiation, planetary albedo, and emitted longwave radiation on various spatial scales ranging from global mean values to averages over a 10×10 degree latitude-longitude region. The lower limit was necessary since most of the radiation data were obtained from sensors with low areal resolution. Because of the large data sample now available, mean values of the radiation budget parameters will be presented for each of the four seasons and

² ICSU/IUGG, WMO, COSPAR, Global Atmospheric Research Programme (GARP), Report of the Study Conference held at Stockholm, 28 June - 11 July 1967.

for the annual case. This is possible because every portion of the year was observed in at least two different calendar years. In addition, selected averages that represent the radiation budget during specific years, seasons and months will be discussed and compared with the mean values.

The present study will determine the various spatial and temporal scales of the earth's gain in energy from the sun and its loss of longwave radiation to space. These results are derived from observations from near-earth satellites. As such, they represent only the first stage of a continuous program now underway that should vastly improve our understanding of the energy exchange between our planet and space, and of the response of our earth-atmosphere system to variations in that exchange.

1. THE RADIATION BUDGET: A COMPONENT OF THE ENERGY BUDGET

Energy transfer by radiation is only one component of the total energy budget of the entire earth-atmosphere system. The principle of energy conservation requires that the total energy budget must balance at every location and over all time periods, but the radiative portion of any such budget need not do so. It is precisely this radiative imbalance which can be measured from a satellite that is meteorologically important on various spatial and temporal scales.

Consider a column of unit cross-sectional area extending from the top of the atmosphere to a level beneath the surface (either land or ocean) where all energy exchange is assumed negligible. Starr (1951) and others have developed the detailed expressions for the energy budget of such a system. In a qualitative form these expressions may be represented by the concept of an energy balance equation where:

$$\begin{array}{l} \text{ENERGY SOURCES} \\ \text{(or SINKS)} \end{array} + \begin{array}{l} \text{ENERGY STORAGE} \\ \text{(or RELEASE)} \end{array} + \begin{array}{l} \text{ENERGY EXPORT} \\ \text{(or IMPORT)} \end{array} = 0 .$$

Such a balance equation validly depicts the energy budget of any portion of the earth-atmosphere system. It does not, of course, represent the total energetics of the column since terms that describe the transformations (conversions) between the various forms of energy are not explicitly included.

The qualitative expression does demonstrate that any imbalance in the source and sink term must be compensated by a change in the total energy content of the column and/or by lateral energy exchange with neighboring columns. One portion of the total source (sink) term is the radiative exchange across the upper boundary of the column. The present study provides new results about this one energy transfer term.

1.1 The Radiation Budget of the Earth-Atmosphere System

A sketch of the radiation budget of the earth-atmosphere system is shown in Figure 1. The balance or imbalance of this budget on any space or time scale is given by the value of the net radiation RN_{EA} . Positive values show a net gain of energy across the top of the atmosphere by radiative processes and the total radiation budget can be written as:

$$RN_{EA} = I_0(1-A) - H_L \quad (1)$$

where:

I_0 = direct solar irradiance ($\text{cal}/\text{cm}^2 \text{ min}$)

A = the planetary albedo (%)

H_L = infrared radiation from the earth-atmosphere system ($\text{cal}/\text{cm}^2 \text{ min}$)

The first term on the RHS of Eq. (6) equals the amount of solar energy absorbed in the earth-atmosphere system (i. e., $I_0(1-A) = H_a$). Note also that the product $I_0A = H_r$, the amount of solar energy reflected and scattered back to space from the earth's surface and the constituents of the atmosphere.

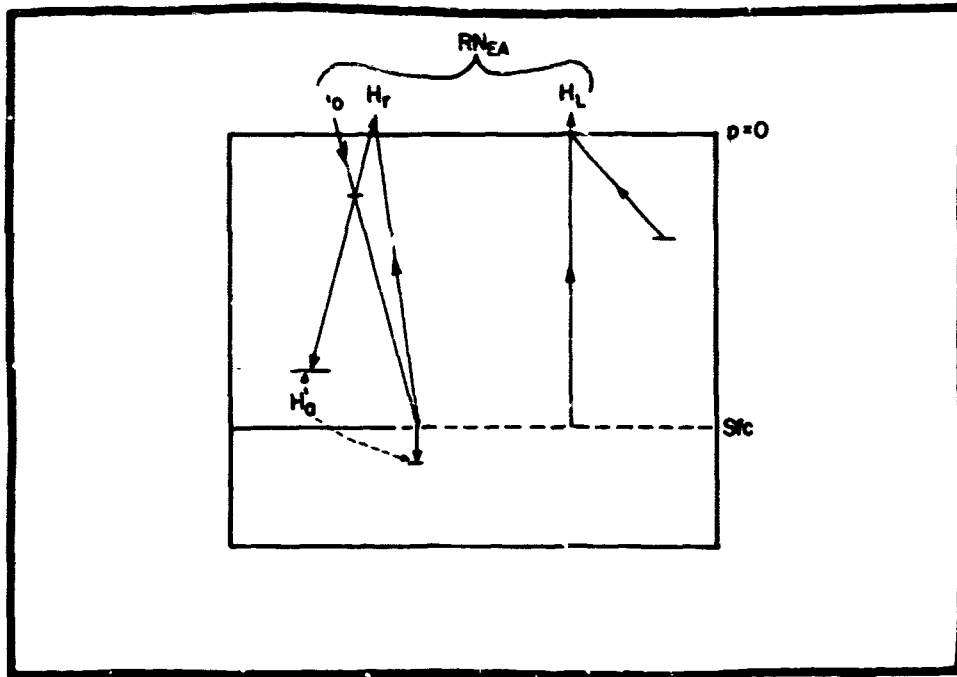


Fig. 1. The radiation budget of the earth-atmosphere system.

2. AVAILABLE SATELLITE DATA

Although more than 40 months of satellite observations are used in the present study, they were obtained from three types of sensing systems:

- a) low resolution hemispheric sensors
- b) low resolution flat sensors
- c) medium resolution scanning radiometers.

As seen in Figure 2, low resolution sensors provided most of the data (approximately 30 months). They were flown on Explorer VII, Tiros IV and VII and on experimental satellites. In order to investigate a continuous time series of satellite radiation data commencing in June of 1963, this study also includes 12 months of data from NASA's medium resolution, five-channel scanning radiometer carried onboard TIROS VII.

2.1 Radiation Sensing Systems

2.11 Low Resolution Sensors

The principles of the low resolution radiation budget sensors were first formulated by Suomi (1958). On Explorer VII and on the TIROS satellites, black and white hemispheres mounted on aluminized mirrors comprised the sensing system. The design and construction of these sensors has been detailed by B. Sparkman (1964) and House (1965). Through the years the basic principles of this experiment have been applied to different types of sensors, although the physical construction has been changed to meet the requirements of various spacecraft and to provide more accurate measurements. The experimental satellites carried a heat budget system consisting of black and white flat disc sensors. Improved versions of flat sensors are now being used onboard the ESCA operational satellites.

Radiation budget parameters (longwave radiation, albedo, and net radiation) are derived from the low resolution sensors by measuring the temperatures of the black and white sensors approximately every thirty seconds. These temperatures are used in energy balance equations that equate all gains and losses of energy to the sensors. The gains of energy by the sensors that are caused by direct solar radiation, solar radiation reflected from the earth-atmosphere system, and infrared radiation emitted by the underlying earth and atmosphere are obtained by solution of the energy balance equations. These sensor energy gains are reduced to effective irradiance values at a standard level (30 kilometers) by applying the appropriate geometrical relationships between the sensors and the radiation source(s). The techniques have been developed in detail by

SATELLITE RADIATION DATA

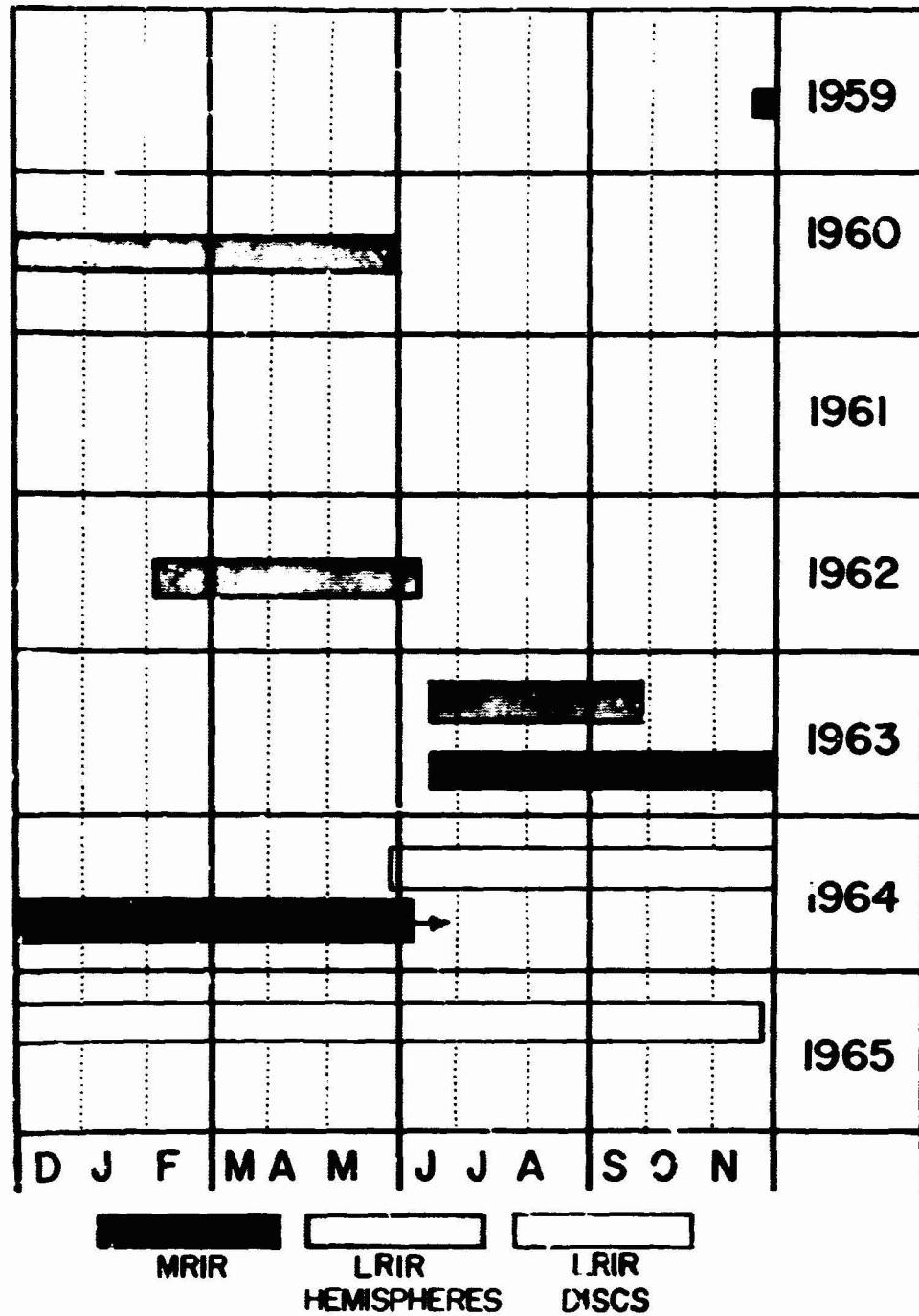


Fig. 2. Summary of satellite radiation data (other MRIR observations during 1961 and after June, 1964 were not included in this study).

House and Suomi, et al. (1967). Low resolution sensors can be calibrated against the sun after launch. This is a significant advantage and is done each time the satellite passes in or out of the earth's shadow. It is used both as a check for degradation of the sensors' responses with time and to supplement laboratory calibration data needed to deduce the irradiance terms. These "in-flight calibration" procedures are also explained in the two references mentioned above.

2.12 Medium Resolution Sensors

A complete description of the medium resolution scanning radiometer is given by the NASA Staff Members (1964). This "beam" instrument had been flown on three satellites prior to TIROS VII and, unlike the LRIR, was not designed primarily as a radiation budget sensor since its real resolution was sufficient for even mesoscale investigations and imagery.

Data from this instrument were obtained from NASA in the form of grid-point maps. These map values were smoothed and used to form seasonal averages of diffuse albedo (reflectance) and longwave radiation in a manner similar to that described by Bandeen et al. (1965). The most important exception to their technique was that the MRIR albedo data were not adjusted by a factor needed to obtain global radiative equilibrium on an annual basis (see Section 2.22).

2.2 Special Characteristics of the Satellite Data

Although the data set used in the present study is the most extensive available at the present time, it differs substantially from an optimum system for measuring the earth's radiation budget as discussed by Godson (1958) and others. Ideally, measurements of the earth's radiation budget should be made by continuously recording, accurate solar and thermal radiation sensors positioned over all locations at the "top of the atmosphere." In practice, the data used in this study were obtained from several sensors flown on different types of satellites, each having different viewing geometries (Figure 3) and orbital characteristics (Table 1).

The results of this study and their intercomparison with future studies are related to the special characteristics of the types of data that were used. For this reason, the following sections contain a discussion of the coverage in space and time of the satellite observations and the adjustments applied to some of the data.

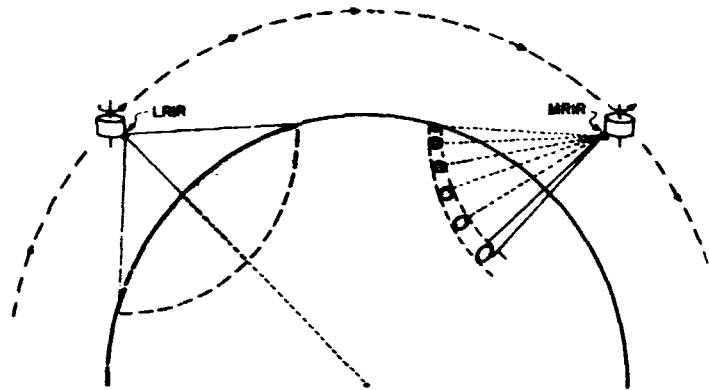


Fig. 3. Simplified viewing geometries of the low and medium resolution TIROS radiation sensors.

Table 1

<u>Satellite</u>	<u>Exp. VII</u>	<u>TIROS IV</u>	<u>TIROS VII</u>	<u>Disc LRR</u>
Latitudinal coverage	$\pm 50^\circ$	$\pm 50^\circ$	$\pm 60^\circ$	$\pm 85^\circ$
Longitudinal coverage	sporadic	360° with gaps	360° with gaps	360°
Local time coverage	24 hr*	24 hr*	24 hr*	0900-2100 LT

*Approximate orbital synodic cycles for Explorer VII, TIROS IV, and TIROS VII were 65, 60 and 75 days, respectively.

2.21 Coverage in Time and Space

Data sampling distribution in space and time varied for each of the satellites. Some knowledge of this sampling pattern is necessary in order to interpret our results. Rados (1967) and Widger (1967) have recently discussed these problems in detail for the TIROS satellites. Within the operational lifetime of any radiation sensing system, spatial coverage is restricted:

- a) in latitudinal extent by the inclination of the satellite's orbit to the equator

b) over some regions by a combination of onboard data storage capacity and ground station readout frequency

c) over other areas because data recording was not possible during the time of ground station readout.

Local-time sampling over a given location will vary if a satellite's orbit had a nodal precession that departs from -1.0 degrees per day (i.e., departs from the rate and direction of the earth's course around the sun). This departure was a common characteristic of the earlier satellite's orbits and as a result measurements at a location were obtained at all local times only during the course of one orbital synodic period.

The sampling constraints mentioned thus far apply specifically to measurements of the infrared irradiance which are obtained during both day and night. Albedo measurements, and the net radiation values derived in part from them, were obtained only when the satellites were over the solar-illuminated portion of the earth. Thus, an additional constraint was placed on the albedo calculations in order to insure adequate illumination of the area viewed; no calculations were made if the local solar zenith angle was greater than 70 degrees.

All of the spatial sampling problems noted above are evident on the maps of the radiation parameters obtained from this study. Restrictions on the gross temporal coverage can be noted by comparing the albedo (daytime data) and infrared (day and night) maps. The sampling problems discussed above can be summarized with reference to Table 1 as follows:

a) Spatial sampling was limited primarily in the north-south direction by the inclination of each satellite's orbit. However, in all cases measurements were made between $\pm 50^\circ$ latitude and 18 months of pole-to-pole data are used.

b) The available satellite data represent the two extremes of sampling in time. On one hand, the satellites in moderately inclined orbits sampled over all local times, but only during the course of a finite time period never less than 60 days. At the other extreme, some data obtained from a near polar orbit was confined, over most of the earth, to only two local times.

In section 3 the effect of imperfect sampling on the accuracy of the results is considered.

2.22 Data Adjustments

The MIRIR albedo data from TIROS VII were the only values used in this study to which special adjustments were applied after normal data reduction had been completed. This was necessary because these data have a history of

uncertainty arising from post-launch sensor deterioration (NASA Staff Member (1964)) and because the "albedo" sensor measured only that portion of reflected solar radiation from 0.55 - 0.75 microns. Two adjustments were made:

- a) one so that the data were more representative of the total (0.3 - 3 micron) albedo
- b) a second adjustment so that the absolute magnitudes of the MRIR albedo values agreed with the albedo values obtained from the LRIR data when the sensors were viewing the same areas at the same time.

In this study the MRIR albedo data were obtained from NASA. The correction for degradation suggested by the NASA Staff Members (1964) was applied to all the albedo (reflectance) values. However, the factor 1.60 used by Bandeen *et al.* (1965) to adjust the albedo data so that global net radiation equaled zero was not used in the present study. Instead, adjustment (a), based on the work of Bartman (1967) was applied to the "red" MRIR (0.55 - 0.75 micron) albedo values to account for that portion of the reflected and scattered radiation (mostly in the blue region) not viewed by the sensor. The adjustment was limited to the lower range of albedo values (i.e., to relatively cloud-free regions); and the largest adjustment increased the MRIR albedo values by a factor of 1.30.

These adjusted MRIR measurements were compared with LRIR albedo values obtained over the same regions during the same time periods. It was found that to force the LRIR and MRIR values to agree, each MRIR value had to be multiplied by the factor 1.18. Both Bartman (1967) and Solomonson (1966) have suggested that a factor of this size may account for the error in the MRIR albedo data due to the isotropic assumption implicit in the data reduction technique.

3. ACCURACY OF THE RADIATION DATA

Before we can discuss the radiation budget results, the accuracy of the albedo, longwave radiation and net radiation values must be established. The "first generation" satellite sensors that provide the measurements summarized in this paper were relatively simple instruments. The satellites did not carry active onboard calibration equipment and none of the sensors were recovered for recalibration in a laboratory. However, most of the data used in this study were obtained from low resolution sensors (LRIR) which were designed so that an inflight calibration against the sun was possible twice each orbit. By using these special measurements as well as pre-launch laboratory tests and comparisons with independent measurements made over the same areas at the same times it was possible to obtain accuracy estimates for the albedo and infrared radiation measurements. Thus, the complete error analysis proceeded as follows:

1. Accuracy estimates were derived for the disc LRIR measurements.
2. The MRIR data were examined by comparing them with disc LRIR data obtained over the same regions at the same time.
3. Error estimates obtained by House (1965) were used for the hemispheric LRIR values.

3.1 Albedo and Longwave Radiation Accuracy Estimates

3.11 Random Error

The effect of random error is negligible because the results presented in this study are values averaged over space and time. The smallest sample used to obtain an average (i. e., the mean albedo of a 10×10 degree region during one specific season) was about 400 measurements. The largest amount of data (5×10^8 observations) were combined to obtain the mean annual net radiation budget of the entire earth. Because only such large samples were used, any random error arising from quantization of the satellite signal, noisy data, etc., has been removed from the results.

3.12 Bias Error

A special kind of bias error may occur in satellite radiation data. It is caused by deterioration of some part of the experiment due to exposure to the environment of space. In the case of the disc LRIR such an error can be caused by a drift in the electronics, by a change in the spectral characteristics of the sensors, or by physical damage to the experiment. Fortunately, these sensors' long-term stability can be checked each time the satellite passes in and out of the earth's shadow by observing their response to the (constant) step function of direct solar radiation. The disc LRIR data used in the present study were periodically checked in this manner and no apparent degradation of the black sensors was observed. The white sensors did change response with time but the data reduction technique described by Suomi *et al.* (1967) was used to remove the effect of this degradation from the measurements used in this study. Thus, no bias error due to sensor degradation should be present in the disc LRIR data.

Additional bias errors that affect the albedo and longwave radiation measurements may be categorized as:

- a) determinate bias error (i. e., an error whose magnitude and direction can be evaluated with good confidence, and
- b) indeterminate systematic error (i. e., an error whose magnitude and direction can only be inferred indirectly by referring to some independent standard, if one exists).

Two kinds of determinate bias errors may occur in the disc LRIR albedo and infrared radiation values; they are:

- a) error in the original temperature calibration of the instruments;
- b) error due to inaccurate determination of sensor calibration constants.

Each of these errors can act in a positive or a negative direction. A quantitative estimate of the bias error introduced into the radiation budget parameters by these errors was made by using a technique analogous to that of House (1965). This straightforward scheme uses reasonable estimates of the inaccuracies of the sensor temperature measurements and calibration constants to evaluate differentiated forms of the albedo and longwave radiation equations. Results showed that the most probable bias errors in the albedo and longwave radiation data were $\pm 1\%$ and $\pm 0.01 \text{ cal} \cdot \text{cm}^{-2} \cdot \text{min}^{-1}$.

The most probable error is derived quantitatively by assigning a reasonable magnitude and direction to various possible errors. In this way compensating effects (i. e., arising from differences in two quantities, each having a bias error with the same magnitude and direction) are allowed in the error analysis. (This method may be contrasted with a maximum absolute error estimate which would not include compensating effects.) For example, we assume that all sensor temperature measurements may be either too high or too low since there is no reason to expect a sign change after launch. Indeed, if the thermistors had a drift of calibration due to the effects of high energy radiation in space, each would drift in the same direction since each thermistor is fabricated from the same material. Similarly, if the materials from which the sensors were fabricated deteriorated due to the space environment one would expect that these changes would also have the same sign. For these reasons, the most realistic view is to assume that any additional bias error arising from sensor characteristics may add to the magnitude of the errors already evaluated but should not change their directions.

The albedo and longwave radiation measurements may contain additional, indeterminate, systematic error. Examples are:

- a) errors due to the sampling in time and space;
- b) errors due to the isotropic assumption.

Point (a) arises from the sampling constraints discussed in a previous section, and (b) results from the data reduction requirements. We can obtain an estimate of the magnitude and direction of these possible bias errors by considering several other studies.

Spatial sampling by these LRIR sensors was quite good. All areas were viewed and when zonal and global averages were formed, each region or zone was weighted equally in forming the mean. The temporal sampling problem is

worse because, over most of the earth, disc LRIR data were obtained at local times near 0900 and 2100 hours. A first approximation to information about the diurnal variation of globally averaged albedo and longwave radiation data has been presented by Astling and Horn (1964) and by Vonder Haar and Hanson (1967). These studies show general agreement and results from the latter are shown in Figure 4. Both of the studies contain spatial sampling problems of their own and are representative of limited time periods (26 and 90 days, respectively). When Figure 4 is considered, it is apparent that albedo and infrared measurements made only near 0900 and 2100 may contain bias errors of $+ 0.015 \text{ ly} \cdot \text{min}^{-1}$ and -2% since the values that represent these times in the figure differ by these amounts from the daily average.

The anisotropic nature of the radiation measured by the satellites, especially the reflected and scattered solar radiation, causes difficulties in the use of the MRIR satellite radiation data for many purposes (see Bartman (1967)). Estimates of the error involved by neglecting the anisotropic effect on these data for radiation budget studies have been made by Ruff *et al.* (1967). They conclude that average values of absorbed solar energy (H_a) derived from MRIR albedo values would not be in error by more than 5%. Bignell (1962) has discussed the same problem for the hemispheric sensors. Based on his results, House (1965) states that albedo and longwave radiation averages obtained from these sensors may be in error by 1 or 2%, even if persistent anisotropic conditions (i. e., limb brightening and darkening) occur. Since the flat disc sensors give less weight to limb radiation than hemispheres, bias error arising from such effects should be even less.

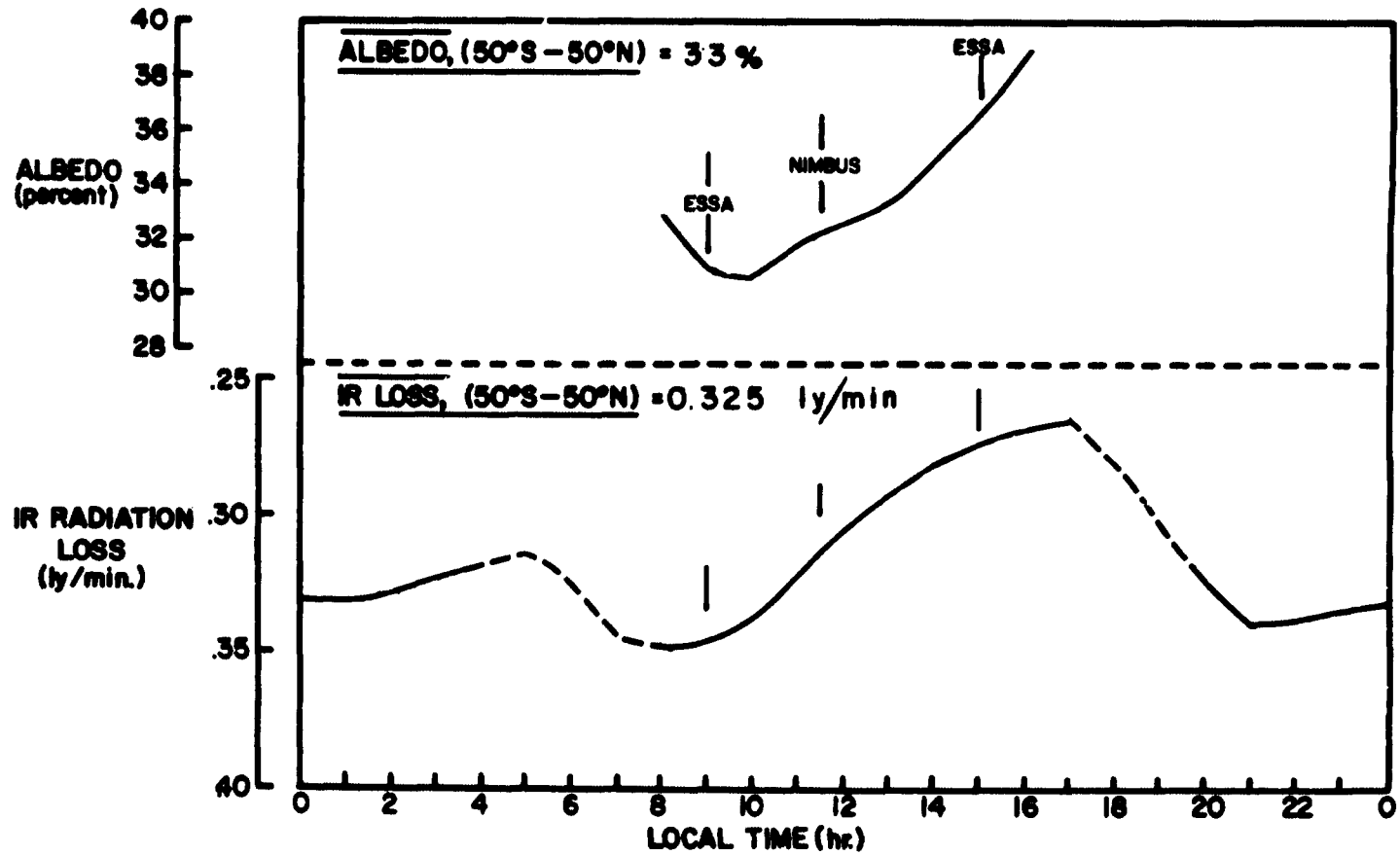
The above discussion of possible indeterminate bias error in our results shows that we have no firm basis for raising (or lowering) the bias error estimates derived from an evaluation of determinate bias error. It is important to note that a correction for bias error would require that all absolute values of a given quantity would be raised or lowered the same amount and in the same direction.

An additional fact concerning any LRIR error analysis has been discussed by House (1965) and Suomi *et al.* (1967). They have shown that albedo and longwave radiation values from LRIR experiments are interdependent in a manner that causes any bias error in either of them to have an opposite effect on the other (i. e., if the albedo is too high the longwave values are too low). In section 3.22 it is shown that this effect is important in minimizing the error in net radiation values derived from LRIR measurements.

3.13 Accuracy Tests

In order to check the accuracy limits determined above, two tests were performed. They consist of comparisons between disc LRIR measurements and independent observations. The tests were essentially limited by the scarcity of reliable independent data.

DIURNAL VARIATION



46

Fig. 4. Diurnal variation of planetary albedo and outgoing longwave radiation based on TIROS IV measurements.

During the southern hemisphere winters of 1964 and 1965, disc LRIR measurements of outgoing radiation were made over the dark polar regions. At the same time, balloon-borne radiometers launched from several locations in the Antarctic measured the total upward longwave radiation from the earth-atmosphere system. The following winter, 1966, the first radiation budget measurements from the second generation satellites were obtained from a MRIR sensor on NIMBUS II. In the table following, they are compared with the LRIR data.

AVERAGE LONGWAVE RADIATION FROM THE REGION 70-90 S. DURING
JUNE-JULY-AUGUST

<u>Data</u>	<u>Source</u>	<u>Date</u>	<u>H_L (cal · cm⁻² · min⁻¹)</u>
Disc LRIR	present study	1964 and 1965	0.175 ± 0.01
Radiometersonde	Kuhn and Cox (1967)	1964 and 1965	0.18
Nimbus MRIR	Raschke <u>et al.</u> (1967)	1966 (June and July)	0.18

The comparisons agree remarkably well and serve as a good test for our LRIR accuracy estimates. They do not, however, give information about day-time LRIR measurements nor about the diurnal sampling problem. To test the LRIR values over all time periods and over many locations, they were compared with MRIR measurements made over the same regions during the same time periods. In Figure 5 a scatter diagram of zonal averages of LRIR longwave radiation values vs. concurrent MRIR values is displayed. These values depart from a one-to-one relationship by less than ± 0.02 cal · cm⁻² · min⁻¹. Although the MRIR data are not of high accuracy, this agreement between two completely independent data sets is very encouraging. A similar test of albedo data was not possible because the original MRIR values were erroneous (see 2.22).

In summary, tests of the disc LRIR measurements against independent observations show that these data have absolute accuracies within the error limits assigned to them. Apparently the local time sampling problem does not introduce significant indeterminate bias error at least on the area scale of a latitudinal zone. Because of the interdependence of the LRIR albedo and infrared values already mentioned, the tests performed on the infrared data also imply that the LRIR albedo values do not contain large bias errors. A third, though somewhat indirect, accuracy check is provided in Appendix A where the disc LRIR sensors were used to derive a very reasonable value of the solar constant.

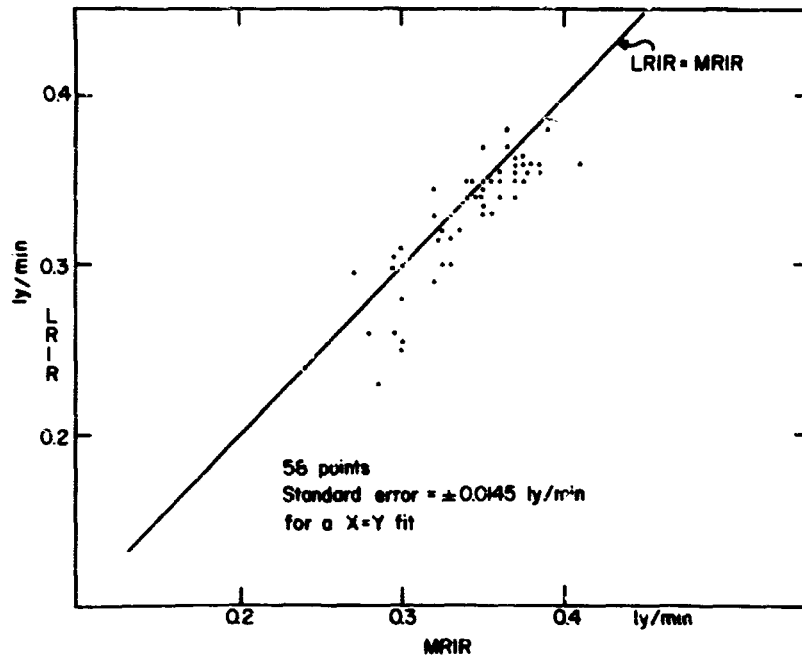


Fig. 5. Comparison of zonally averaged longwave radiation measurements obtained from LRIR and MRIR sensors during the same time periods.

3.2 Net Radiation Error Analysis

Values of net radiation used in the present study were derived from Eq. (1) by using albedo and infrared radiation measurements together with incident solar radiation values computed by assuming a magnitude of the solar constant.

3.2.1 Effect of Albedo and Longwave Radiation Accuracy

Before deriving the most probable error in the net radiation data, it will be helpful to illustrate the effect of various albedo and infrared radiation bias errors on the accuracy of a typical net radiation value. By differentiating Eq. (1), we obtain:

$$dRN_{EA} = dI_0 - I_0 dA - AdI_0 - dH_L \quad (2)$$

We assume the solar constant is known perfectly ($dI_0 = 0$) and equals $2.00 \text{ cal} \cdot \text{cm}^{-2} \cdot \text{min}^{-1}$. Using representative values of $I_0 = 0.5 \text{ cal} \cdot \text{cm}^{-2} \cdot \text{min}^{-1}$, $A =$ and $H_L = 0.33 \text{ cal} \cdot \text{cm}^{-2} \cdot \text{min}^{-1}$, we have determined dRN_{EA} for different magnitudes and directions of the possible errors dA and dH_L . The results are shown in Figure 6 as a nomogram. In the first and third quadrants of this figure the net radiation bias errors are minimized. This results when

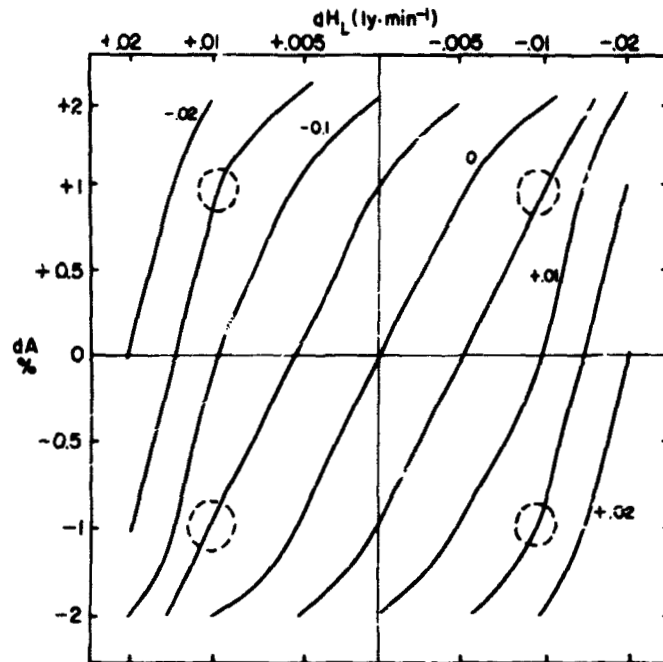


Fig. 6. Nomogram showing the absolute error in net radiation ($\text{cal} \cdot \text{cm}^{-2} \cdot \text{min}^{-1}$) resulting from albedo and longwave radiation measurement errors.

albedo and longwave radiation errors are in opposing directions. When the inverse is true, the resulting difference between two large numbers can cause errors that are twice as large.

Figure 6 is useful in considering the effect of our A and H_L error estimates on net radiation values derived from them. This nomogram shows that errors $dA = \pm 0.01$ and $dH_L = \pm 0.01$ would result in net radiation errors of ± 0.005 or $\pm 0.015 \text{ cal} \cdot \text{cm}^{-2} \cdot \text{min}^{-1}$ (dashed circles), depending on the direction of these albedo and longwave radiation errors. As mentioned in 3.12, the LRIR observations which comprise 80% of the data used in this study do in fact have inversely related albedo and infrared bias errors that would make the smaller value ($\sim \pm 4 \text{ watts/m}^2$) the reasonable choice, if the solar constant were known perfectly.

3.22 Effect of Uncertainty in the Solar Constant

Recently, Drummond *et al.* (1967) have reported some preliminary results from an experiment designed to measure the solar constant from a high altitude aircraft. They obtained a value of $1.95 \text{ ly} \cdot \text{min}^{-1}$ which may have an uncertainty of less than 2%. Until these data became available, most recent studies have used the values of $2.00 \pm .04$ (Johnson (1954)) or 1.98 ± 0.1 (Nicolet

(1951)) derived from measurements made at the earth's surface. Because the absolute magnitude and the possible error of the solar constant is important to the present radiation budget study, satellite observations from the disc LRIR sensors were also used to derive a value of this parameter. The results of this first measurement of the solar constant from a satellite yielded a magnitude of $1.99 \text{ ly} \cdot \text{min}^{-1} \pm 0.03$ ($\pm 1.5\%$). After considering each of the measurements mentioned above, a value of 2.00 ± 0.03 was chosen for use in the present study.

Because of the uncertainty in I_0 , our net radiation error estimate cannot be obtained from Figure 6. Rather, it is necessary to reevaluate Eq. (2) with typical radiation budget values and their associated absolute errors.

The following data were used:

<u>Parameter</u>	<u>Value</u>	<u>Percent Error</u>	<u>Absolute Error</u>
insolation (I_0)	0.5 ly/min	1.5%	$\pm 0.0075 \text{ ly/min}$
Longwave radiation (H_L)	0.33 ly/min	3%	$\pm 0.01 \text{ ly/min}$
albedo (A)	30 (percent)	3.5%	± 1.0 (percent)

From this evaluation we obtain a most probable bias error for net radiation ($dRNEA$) of $\pm .01 \text{ cal} \cdot \text{cm}^{-2} \cdot \text{min}^{-1}$ ($\sim \pm 7 \text{ watts/m}^2$). This error results in equal measure from uncertainties in the solar constant and from the inaccuracy of the albedo and longwave radiation measurements, when the latter errors are inversely related.

3.3 Error Analysis Summary

The error analysis presented in this chapter has been directed primarily toward the disc LRIR data even though 40% of the measurements used in this study were obtained from two other sensing systems. However, the MRIR longwave radiation values are shown in 3.13 to have an accuracy comparable to the disc LRIR data and in 2.22 the medium resolution sensor's albedo measurements were adjusted to agree with the LRIR data, this forcing their accuracies to be the same. In addition, House (1965) has provided an error analysis for zonal averages of hemispheric LRIR data and his estimates fall within the error limits derived in this section.

For these reasons, all the data used in this study were assigned the following most probable bias errors:

Longwave radiation (H_L)	$\pm 0.01 \text{ cal} \cdot \text{cm}^{-2} \cdot \text{min}^{-1}$
albedo (A)	± 1.0 percent
net radiation (RN_{EA})	$\pm 0.01 \text{ cal} \cdot \text{cm}^{-2} \cdot \text{min}^{-1}$

Because of large data samples, no random error should influence these results. These error limits are valid only if no large indeterminate bias error influenced the measurements, but tests using independent observations did not suggest the presence of such errors. Over a typical range of averaged observations these absolute errors yield percentage errors of 3 - 5% and 2 - 8% for longwave radiation and albedo data respectively. Of course, when two regions have the same albedo, the error in reflected shortwave radiation (H_r) is less where the incoming solar radiation is greater.

These error estimates affect the various questions treated in this study to different degrees. Because all random error has presumably been removed by averaging over space and time, and because all apparent sensor degradation bias has been resolved, relative values of the radiation parameters can be considered without concern. Of course, the relative error in the net radiation results will be less over regions where the earth-atmosphere system has a large radiation imbalance. Thus, the tropical latitudes and the winter polar regions can be observed more accurately. Indeed, these regions are most important from an energy budget viewpoint. One problem that requires great accuracy cannot be considered in the present study; it is the longterm (climatological) warming or cooling of the earth-atmosphere system. We can, within the absolute accuracy of our measurements, examine the balance or imbalance of the radiation budget over different areas at various time periods, locate the primary radiation sources and sink regions, compute required energy transports and investigate other similar radiation budget problems with an extended time series of observational data.

4. RADIATION BUDGET RESULTS

The exceedingly large amount of albedo and longwave radiation measurements (5×10^8) obtained from the satellite experiments were used to form averages over different spatial and temporal scales. We begin our discussion of these results by considering maps of albedo, longwave radiation and net radiation which show the geographical variations of the radiation budget. After that, the scale of spatial averaging is increased to form the budgets of individual latitudinal zones, hemispheres and the entire earth.

The observations used to form averages for any time period (i. e., a season) are shown in Figure 2 although none of the Explorer VII data were included in the results presented in this section. Mean albedo values were

obtained by averaging reflected solar radiation and insolation values separately and deriving a mean albedo from their ratio. The average insolation for different locations and time periods was computed based on a solar constant of $2.00 \text{ cal} \cdot \text{cm}^{-2} \cdot \text{min}^{-1}$.

4.1 Geographical Variations

The satellite observations used in this study include measurements during each of the four seasons obtained in at least two calendar years. Thus, for the first time, we can derive mean seasonal and annual maps of the radiation budget parameters.* Such mean maps are useful for examining regions within latitudinal zones where the radiation budget differs significantly from the zonal mean value. For this reason, "high" and "low" regions noted on the maps were chosen relative to the average for that time period and zone rather than to some absolute magnitude. A 10×10 degree latitude-longitude grid was used to construct the maps since the low resolution sensor data requires this limit on the spatial resolution. Thus, the maps show sufficient detail for a study of the radiation budget of large areas, but cannot be used to examine the budget at a specific location.

Spatial and temporal sampling problems were discussed in section 2.21 and some of the constraints mentioned there are evident on the maps. All the maps contain both solid and dashed isolines and the dashed lines cover regions where the number of satellite observations at a grid point was approximately 25% less than the number of grid points analyzed with solid lines. Isolines of albedo, longwave radiation and net radiations were drawn at intervals greater than the error limits of the data discussed in section 3.3. The map values for regions where a strong diurnal variation of cloudiness may be expected must be interpreted with care since more than one-half of our observations were obtained near 0900 and 2100 local times. This problem is discussed in sections 2.21, 3.12 and 6.0.

A complete set of maps (about 200) describing the radiation budget for all time periods (months, seasons and years) observed by the first generation satellites will be presented in a separate atlas of the earth's radiation budget.

4.11 Mean Seasonal Budgets

(a) Longwave Radiation. Mean seasonal maps of the longwave radiation (H_L) from the earth-atmosphere system are shown in Figures 7 and 8. Such

* Others (Rasool (1964), Winston and Taylor (1967)) have used TIROS radiation data to obtain maps for selected months and seasons and recently Raschke and Pasternak (1967) have done the same with several months of NIMBUS data.

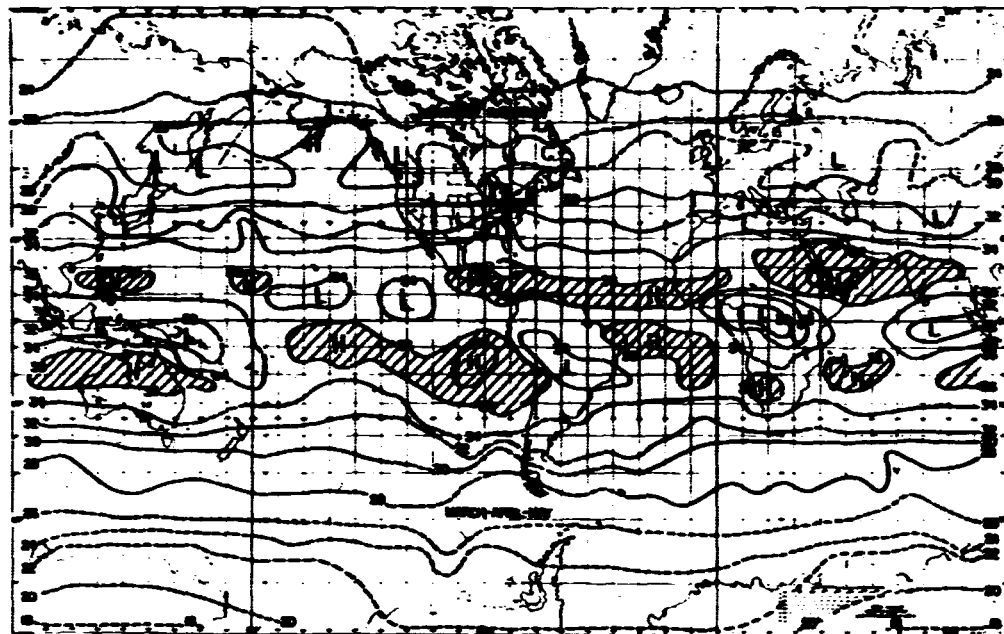


Fig. 7. Mean values of outgoing longwave radiation from the earth-atmosphere system (H_L) during Dec. -Jan. -Feb. and Mar. -Apr. -May. Units are $10^{-2} \text{ cal} \cdot \text{cm}^{-2} \cdot \text{min}^{-1}$ and regions of $H_L > 0.36 \text{ cal} \cdot \text{cm}^{-2} \cdot \text{min}^{-1}$ are shaded.

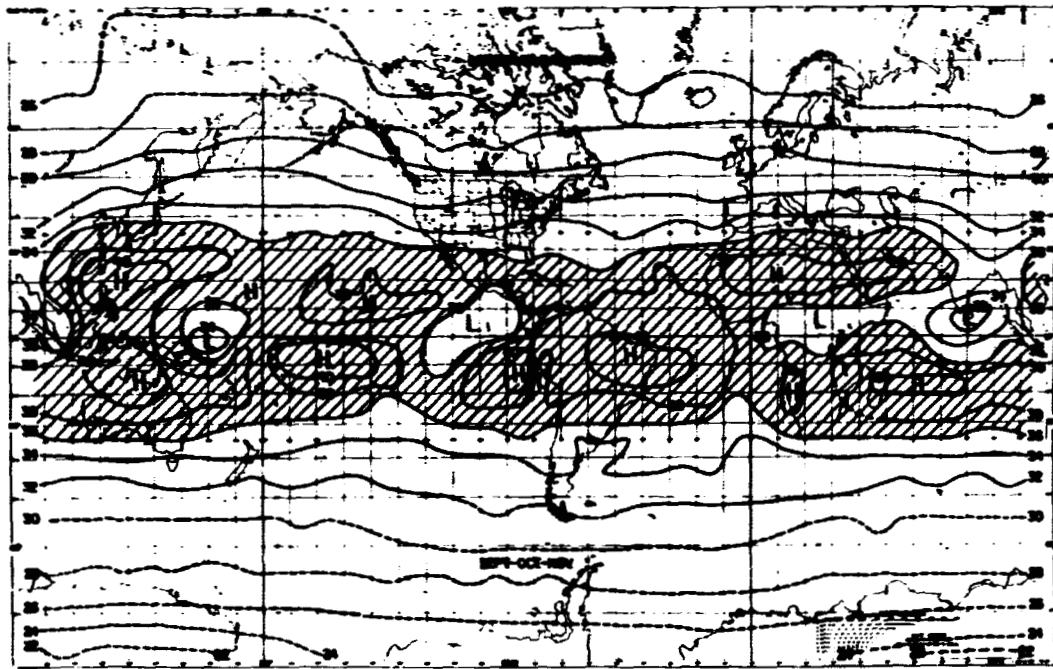
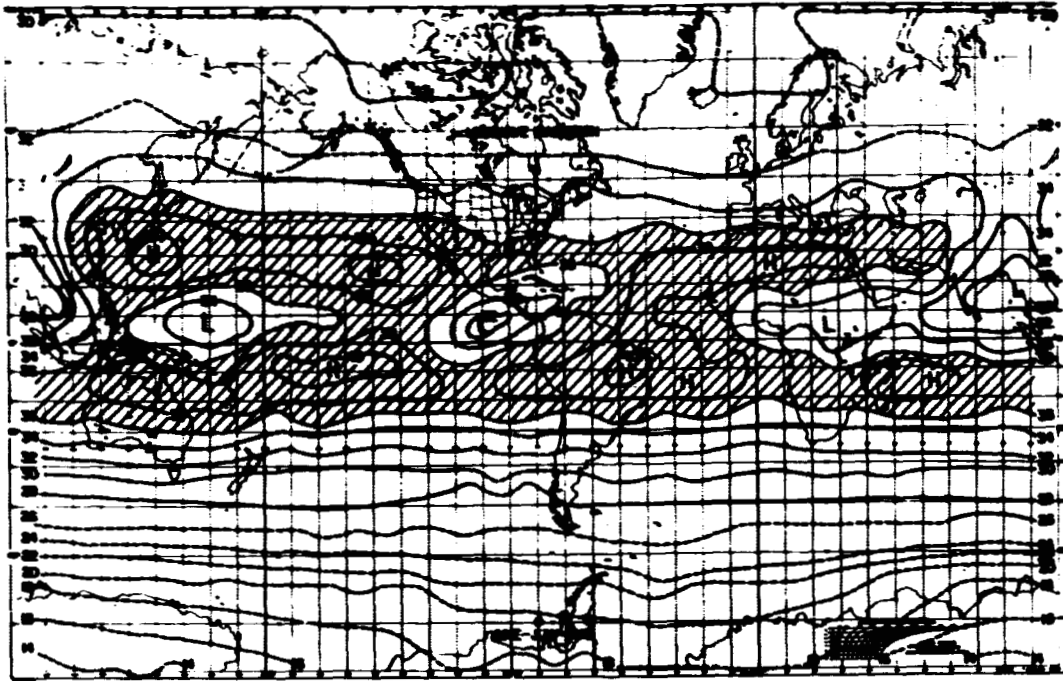


Fig. 8. Same as Figure 7 for June-July-Aug. and Sept.-Oct.-Nov.

maps are a good indication of atmospheric conditions because clouds play a dominant role in determining the magnitude of the outgoing infrared energy. In the absence of clouds, the temperature and moisture content of the atmosphere and the local surface temperature strongly influence values of H_L .

The most significant feature common to all four seasons is the contrast between the zonal pattern of isolines in the higher latitudes of both hemispheres and the presence of many local regions of high and low outgoing radiation in the tropics and subtropics. In these seasonal maps the zonal patterns result from many observations obtained over both clear and cloudy regions in the latitudes where migratory storm systems dominate the circulation pattern. The highs and lows found at lower latitudes show persistent features of the earth-atmosphere system during the respective seasons. In each hemisphere the boundary between these two types of radiation patterns moves north and south in phase with the seasonal path of the sun and from winter to summer both boundaries range from twenty to forty-five degrees respectively, thus marking the equatorward intrusion of storm tracks each season. The east-west continuity of the boundaries is quite strong but some breaks do occur. These breaks show as weakened north-south gradients of outgoing longwave radiation (i. e., the south-central Pacific, south Atlantic and the region near 20° N, 140° W during DJF; the region of the summer monsoon and near the Caribbean during JJA). Winston (1967) has already demonstrated that variations in this gradient are related to the mid-latitude circulation pattern in the northern hemisphere, thus pointing out a good application of these maps for regions where the circulation pattern is not well known.

Within the regions where the outgoing longwave radiation decreases toward the poles at all longitudes, the effect of the distribution of land and ocean is noticeable, especially in the northern hemisphere. Thus in DJF the isolines of H_L drop southward over the continents which are colder than oceans at the same latitude. In the southern hemisphere lower values of outgoing radiation are observed over the Antarctic continent than over nearby ocean regions. Seasonal variations in the mean temperature of the earth and atmosphere at mid-latitudes are also evident in the poleward gradients of longwave radiation. These gradients are strongest during the winter seasons and weakest during summers. With the exception of the zone near 50° N during MAM, seasonal averages of longwave radiation from the earth-atmosphere system poleward of 40° latitude can be well represented by zonal mean values when the continentality effect is considered.

On the other hand, these maps show that zonal averages of outgoing radiation over one-half the earth (30° N - 30° S) would give only a rough approximation to the true value at most longitudes. This is due to the pronounced nonzonal, sometimes even meridional, orientation of the regions of high and low outgoing radiation. An elementary climatological view of these regions would mention a northern and southern subtropical zone (warm, dry and cloudless) broken by a tropical convergence region (warm, wet and cloudy). We will discuss the

major departures from this simple picture as seen in the seasonal H_L maps.

High values of emitted infrared energy that mark the northern subtropical zone show definite seasonal variations at most longitudes. Near $140^\circ W$, for example, lower values of H_L indicate cloudy conditions during the winter and spring but a strong high covers the same region for the other six months. The entire band is strongest during the summer and least well-defined in MAM. The regions of maximum outgoing radiation have values greater than $0.40 \text{ cal} \cdot \text{cm}^{-2} \cdot \text{min}^{-1}$ and the only maxima that is observed near the same longitude during all four seasons occurs at $120^\circ E$.

In recent years continuous photographic and radiometric observation of the tropical regions has shown that earlier ideas regarding the position and intensity of cloudiness associated with the convergence zone require modification (i.e., Kornfield, *et al.* (1967)). Lower values of outgoing radiation from this region identify it on the mean seasonal H_L maps. Within the spatial resolution of the radiation sensors, the maps show that this cloudy belt is definitely discontinuous and marked by persistent regions of low outgoing radiation at preferred locations each season. Low regions with a meridional orientation ($120^\circ W$ during DJF and MAM, $90^\circ E$ in MAM) may correspond to the double-ITC areas noted by Kornfield *et al.* In several seasons the radiation maps show the presence of cloudy regions extending from the convergence zone across the subtropics and into the mid-latitudes. As a whole, the convergence zone is strongest during MAM and most discontinuous in SON. Four primary H_L minima (20° , 90° and $160^\circ E$; $110^\circ W$) remain near the same longitudes each season and the cloudy belt is not well-defined in the Atlantic sector except during MAM. The lowest values of outgoing radiation in this zone ($0.30 \text{ cal} \cdot \text{cm}^{-2} \cdot \text{min}^{-1}$) are found over the summer monsoon.

In the southern hemisphere the subtropical region of high outgoing radiation is best defined during Spring. Primary maxima, exceeding $0.40 \text{ cal} \cdot \text{cm}^{-2} \cdot \text{min}^{-1}$, persist near 40° and $130^\circ E$, 90° and $150^\circ W$. Lower values of H_L denote major breaks in the zone over the west central Pacific and east of South America, particularly during the summer and fall. Along with its northern counterpart and the tropical convergence zone, this subtropical belt has a seasonal latitudinal displacement in phase with the solar declination.

(b) Albedo. Mean seasonal albedo maps (Figures 9 and 10) were also obtained from the satellite measurements. These maps are less representative of atmospheric conditions than the infrared data since the effects of snow, ice and deserts emphasize land versus ocean differences better than thermal effects. In fact, the mean albedo data provide more information about the type of surface in view (and in the case of clouds, the persistence of cloudiness) than about the shortwave energy budget. However, since incident solar radiation varies only as a function of latitude across these mean maps, values of reflected and absorbed solar energy can be inferred from them.

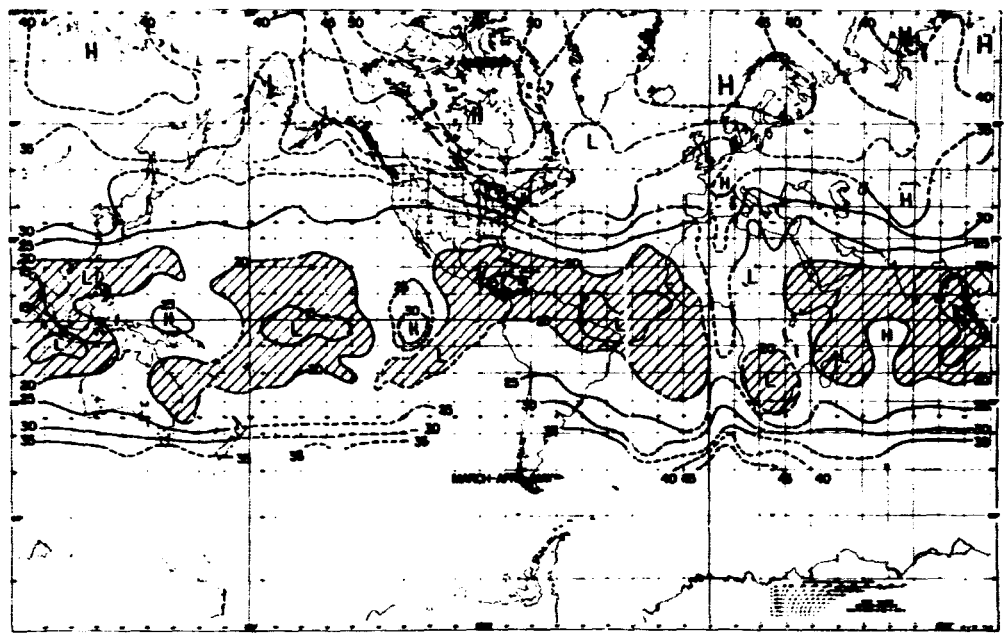
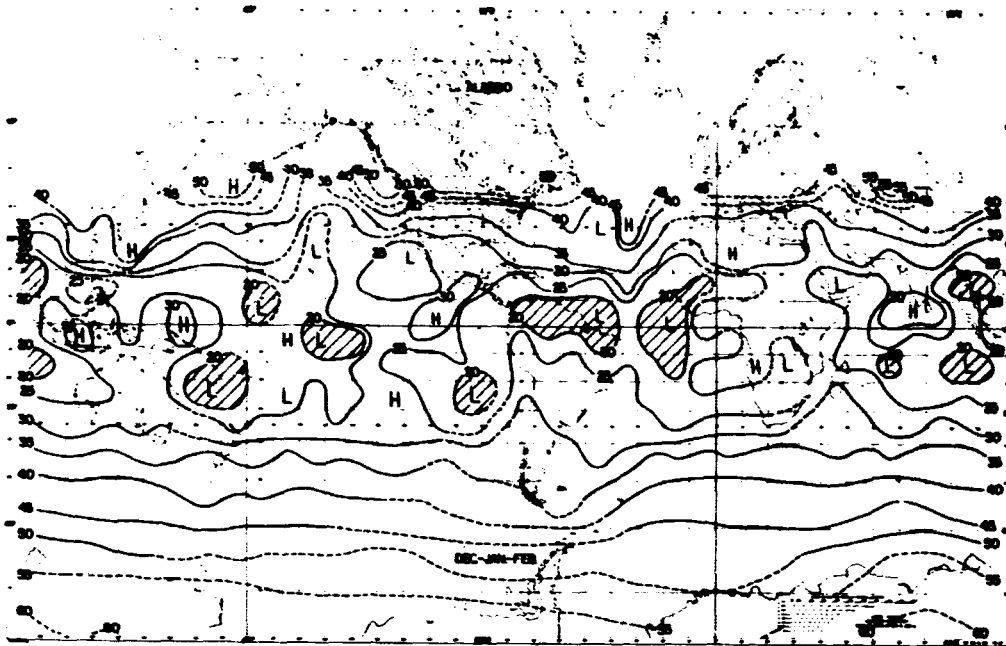


Fig. 9. Mean values of planetary albedo (A) during Dec.-Jan.-Feb. and Mar.-Apr.-May. Regions of $A < 20\%$ are shaded.

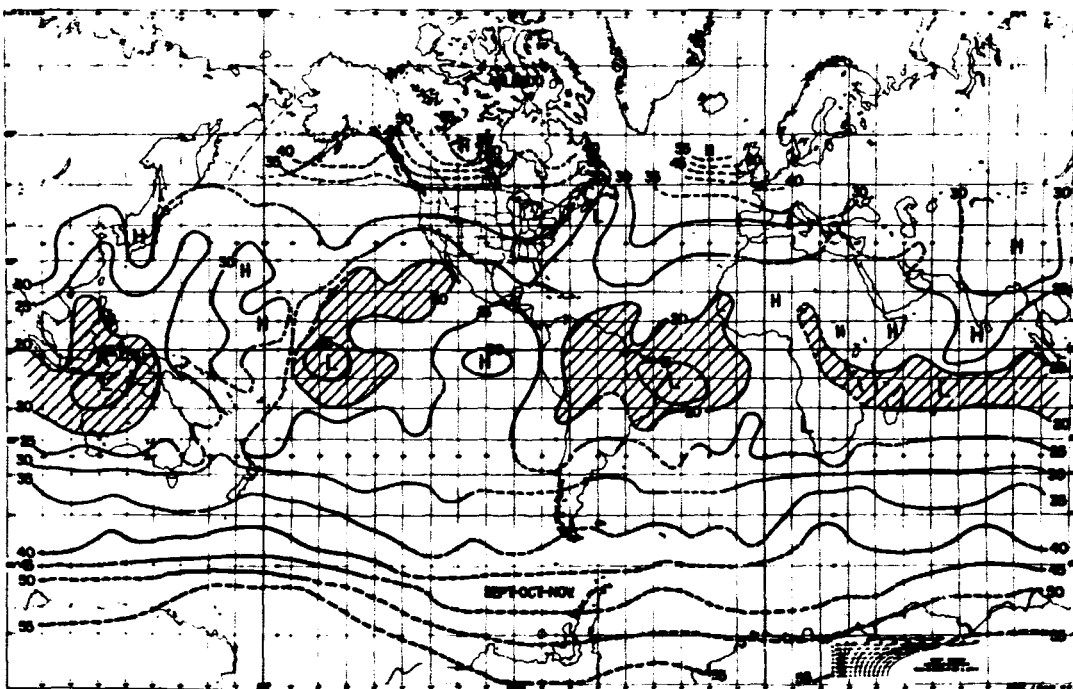
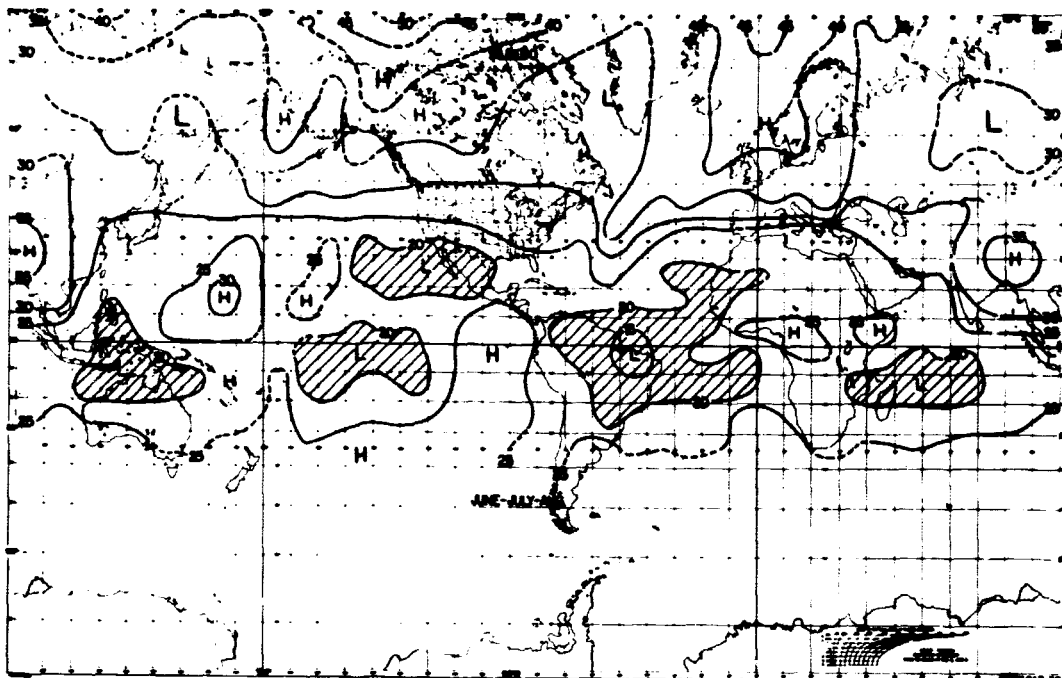


Fig. 10. Same as Figure 9 for June-July-Aug. and Sept.-Oct.-Nov.

In general, the albedo and longwave radiation maps show the expected inverse relation between the two quantities. Within the tropics and subtropics most regions of high outgoing longwave radiation have mean albedo values less than twenty percent. In the south-central Pacific and near the east coast of Brazil the measured albedos were less than 15% during all seasons except DJF. Low values of H_L near the equator correspond with albedo values of more than 30%. In the subtropical regions an exception to this inverse relation is found over the deserts of Australia and Africa which have both high albedos and high values of infrared energy.

The departures from mean zonal values examined with the aid of the longwave radiation maps apply also to the albedo data within $30^\circ\text{N} - 30^\circ\text{S}$ if the desert effects are considered. In higher latitudes, however, the effect of ocean-land contrasts is much more striking when albedo maps are examined. For example, during the northern hemisphere Spring and Summer the oceanic regions near $40^\circ - 60^\circ\text{N}$ have a zonal pattern but the continents contain bright and dark areas primarily because of the influence of snow and vegetation. Near Hudson Bay and eastern Canada the albedo difference of 15% from MAM to JJA is probably due as much to changes at the surface as to changing atmospheric conditions. The absence of land in the same latitudes of the southern hemisphere causes more zonal albedo patterns in the corresponding seasons since these mean values are obtained from many observations of clear and cloudy regions in the migratory storm belt.

The highest mean seasonal albedo values observed over a large area in the northern hemisphere were 55% over central Canada during Spring and Fall. Undoubtedly there are higher values over small areas, but the low resolution sensors cannot define them especially if they are surrounded by darker regions. In the southern hemisphere the albedo isolines show a gradual increase toward the pole, and the border of the Antarctic continent seen on these maps has a mean albedo greater than 55%.

(c) Net Radiation. The geographical distribution of mean seasonal albedo and longwave radiation data were combined with incident solar energy values to derive the net radiation maps shown in Figures 11 and 12. These maps are most valuable for an energy budget study because they show the geographical variation of the net energy gain or loss between portions of the earth-atmosphere system and space.

Two features of these maps are of special interest. One is the north-south movement of the zero isolines which mark the latitudes where the earth-atmosphere system is in radiative equilibrium at its upper boundary. Except during MAM these isolines have a zonal orientation in both hemispheres and they move in phase with seasonal variations of solar declination. The range in latitudinal location is more than sixty degrees in the northern hemisphere but less (about 50°) in the southern hemisphere. This occurs because, unlike

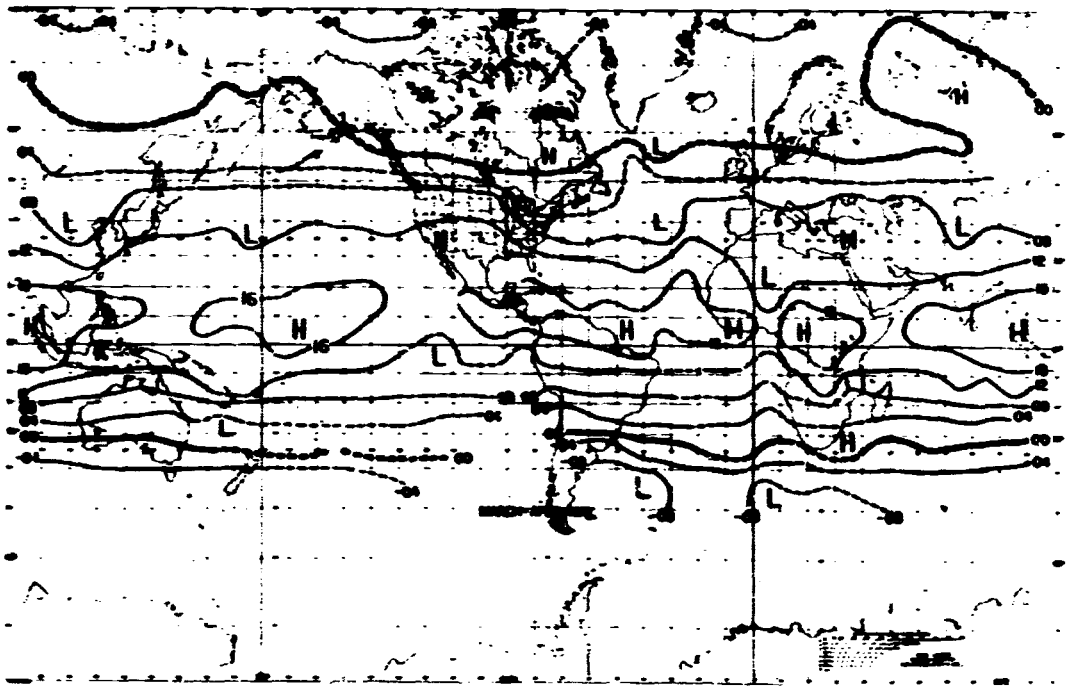
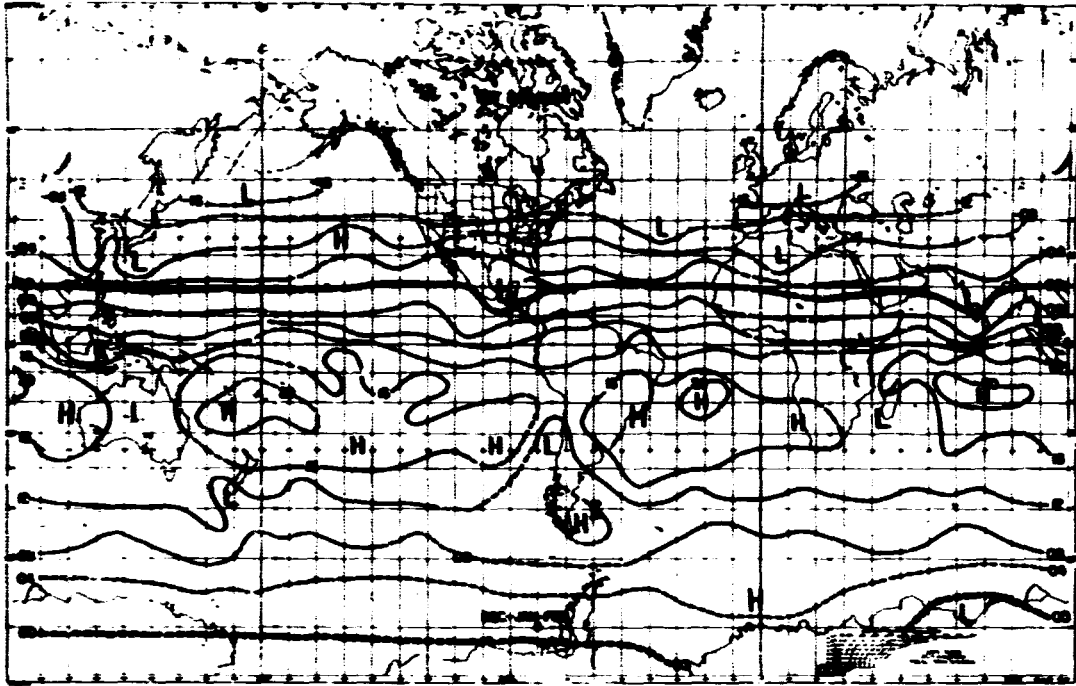


Fig. 11. Mean values of the net radiation budget of the earth-atmosphere system (R_{NEA}) during Dec.-Jan.-Feb. and Mar.-Apr.-May. Units are $\text{cal} \cdot \text{cm}^{-2} \cdot \text{min}^{-1}$ and isolines of $R_{NEA} = 0.0$ are double-width.

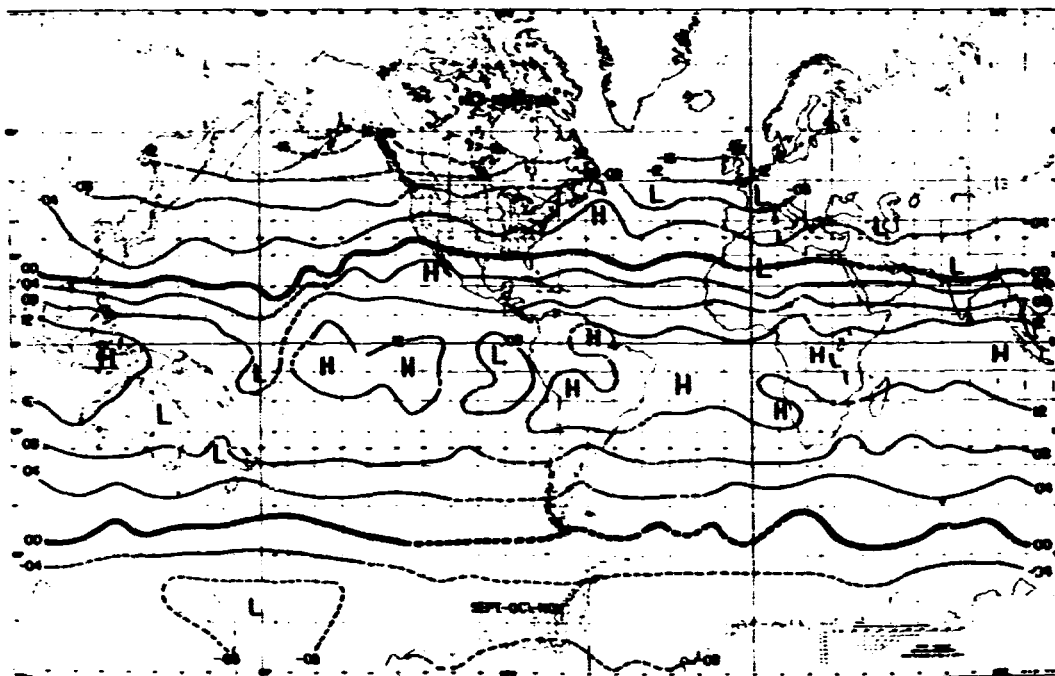
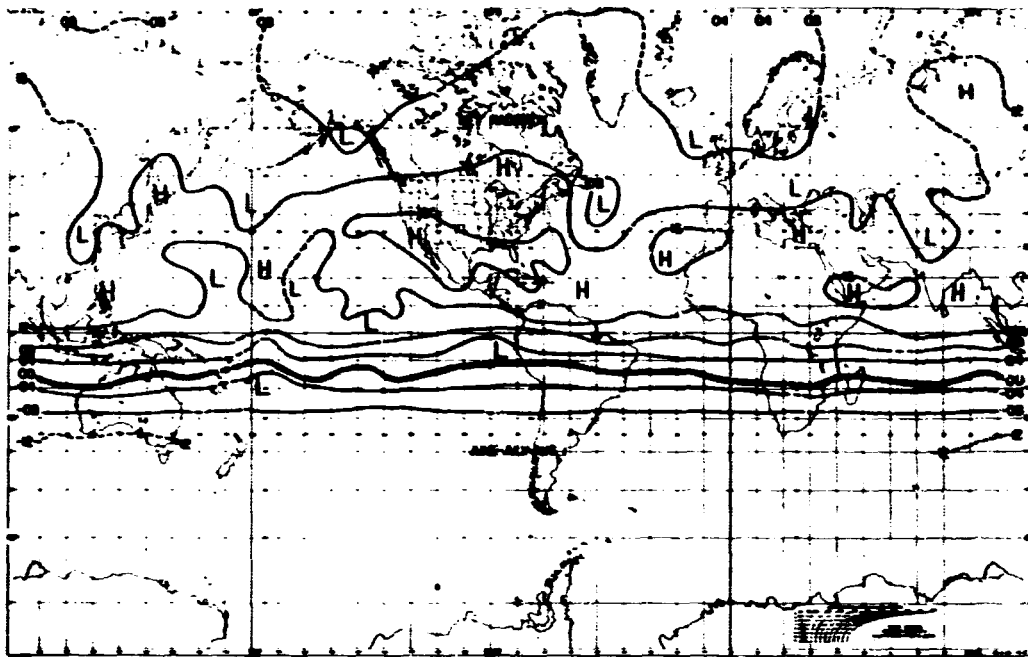


Fig. 12. Same as Figure 11 for June-July-Aug. and Sept.-Oct.-Nov.

the northern polar regions, the Antarctic is a net energy sink during all seasons.

These maps also show that within the broad zonal belts of net energy gain and loss there are definite highs and lows that mark departures from the zonal mean. The location of these regions changes with season in response primarily to differences in atmospheric conditions. For example, within the region of net energy gain ($25^{\circ}\text{N} - 25^{\circ}\text{S}$), the principal areas of energy input to our system are located east of Australia, in the Atlantic and over the Indian Ocean during DJF. At these locations the net radiation values exceed $+0.20 \text{ cal} \cdot \text{cm}^{-2} \cdot \text{min}^{-1}$. In other seasons the highs shift to different longitudes and their intensities drop to $+0.16$ or $+0.12 \text{ cal} \cdot \text{cm}^{-2} \cdot \text{min}^{-1}$. Note that in JJA the Indian monsoon region gains more than $+0.12 \text{ cal} \cdot \text{cm}^{-2} \cdot \text{min}^{-1}$; here the large amount of reflected solar energy is more than compensated by the decreased outgoing longwave radiation. Within the tropics and subtropics there are also areas of relatively low net radiation over the deserts of Africa and Australia in the spring and summer and over the stratus-covered oceanic desert west of South America. Such areas have high albedos and high values of outgoing longwave energy.

During the warmer months of the northern hemisphere the important non-zonal features in upper latitudes include highs over central Asia and regions of lower than average net radiation in the north Atlantic, near Alaska and in northern China.

(d) Winter-Summer Differences. As an example of the seasonal variation of the radiation budget at different locations, maps showing these changes from winter to summer are shown in Figures 13 and 14. The differences were obtained as JJA minus DJF and they ranged from zero to $\pm 0.10 \text{ cal} \cdot \text{cm}^{-2} \cdot \text{min}^{-1}$ and ± 20 percent for longwave radiation and albedo respectively.

The albedo and longwave maps show large changes that are caused by the summer monsoon and the seasonal movement of the Bermuda high pressure region. Over the Sahara the increased winter albedo must result from cloudiness associated with storms moving into this region from the north and west. An interesting feature west of central America has a longwave radiation difference similar to the summer monsoon but the albedo change is much less. This implies that the amount of clouds did not vary greatly from winter to summer, but that many more middle and high clouds occur during the summer. Smaller changes in the albedo and infrared maps can be associated with the seasonal movement of the tropical cloudy and subtropical clear regions discussed previously.

Winter-Summer differences of net radiation depend on changes in atmospheric conditions as well as the seasonal variation of incident solar radiation. The extreme zonal orientation of the isolines of net radiation difference shows

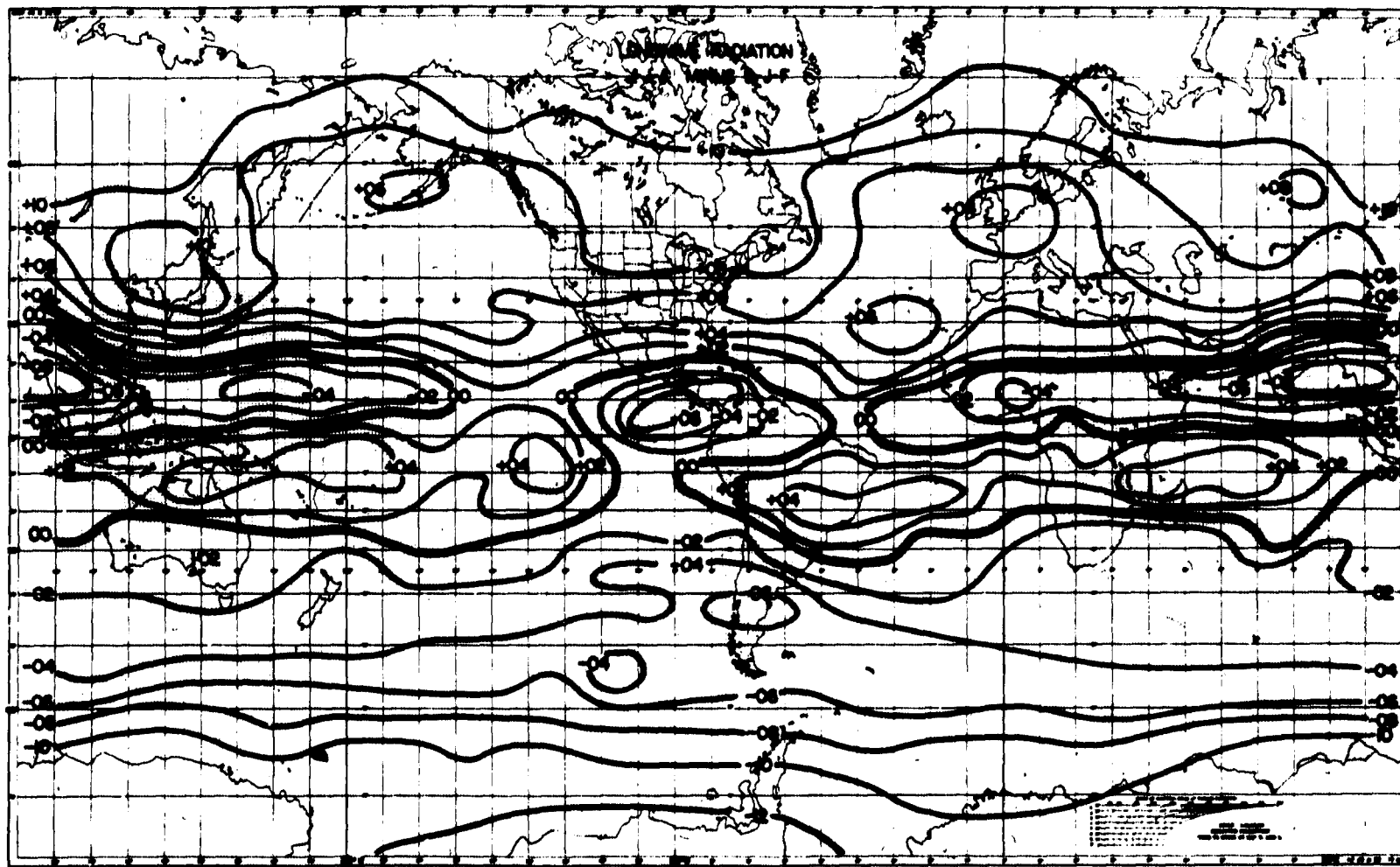


Fig. 13. Winter-summer differences in outgoing longwave radiation expressed as JJA minus DJF ($\text{cal} \cdot \text{cm}^{-2} \cdot \text{min}^{-1}$).

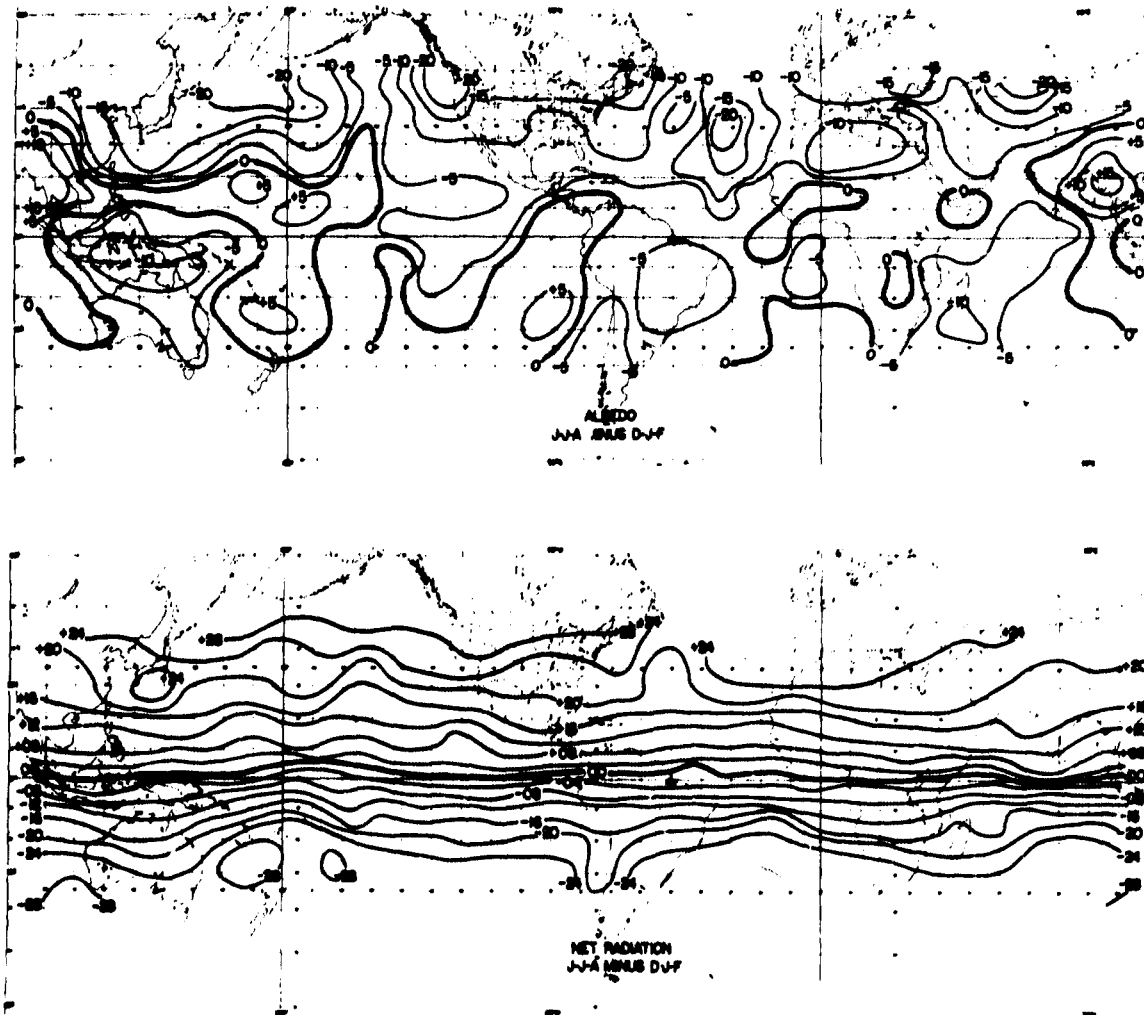


Fig. 14. Same as Figure 13 for net radiation and planetary albedo.

that despite large changes in the albedo and infrared fields the seasonal range of net radiation at a latitude is highly dominated by changes in incident solar energy. This results when differences in albedo and longwave radiation have compensating effects on the local radiation budget. In the winter-summer example only a few regions do not follow this normal pattern and they cause deviations from the zonal field. For example, the area south of Japan has higher than average net radiation during the summer and a low value during winter, thus amplifying the seasonal range. On the other hand, subtropical regions in the North Atlantic and near the coast of Chile have normal (low) winter values but also low values in summer which combine to reduce the winter-summer range of net radiation.

In this section the primary purpose has been to describe the observed radiation patterns on the mean seasonal maps. When combined with a suitable amount of cloud cover data and available meteorological information (real or simulated), a thorough investigation of the meteorological cause and feedback effect will be possible. Obviously ocean-continent differences are not the only cause of zonal anomalies and while some of the local patterns (i.e., the monsoon effect) were expected, others (in the east Pacific and over the Atlantic) cannot be simply explained. Continuous cloud observations from the ATS and ESSA satellites will be a great aid to further research in this area.

4.12 Mean Annual Budgets

The geographical variations of mean annual values of albedo, longwave radiation and net radiation are shown in Figures 15 - 17. In order to obtain a true representation of the annual case, the maps were derived from mean seasonal data. Mean albedos were obtained by weighting each seasonal value by the incident solar radiation for that time period and thus at higher latitudes the summer situation has the greatest influence on the mean annual albedo.

As in the mean seasonal maps, isolines of longwave radiation have a zonal orientation over the poleward half of each hemisphere. At these latitudes lower values of H_L are observed over the continents, especially central Asia and Antarctica. The region $10^\circ - 30^\circ N$ contains a zone of generally high outgoing longwave radiation with maxima centered over the western Pacific and the Sahara.

A band of lower H_L values results from cloudiness and the high water vapor concentrations near the intertropical convergence zone. At most longitudes this feature is centered near $5^\circ N$ on the mean annual map although it cannot be seen over the Atlantic. Principal minima ($H_L < 0.34 \text{ cal} \cdot \text{cm}^{-2} \cdot \text{min}^{-1}$) are found south of India, over equatorial Africa and east of New Guinea. Near $110^\circ W$ in the northern hemisphere and near New Guinea in the south lower values of H_L extending into the mid-latitudes may mark the regions of persistent interaction between the lower and higher latitude circulation patterns.

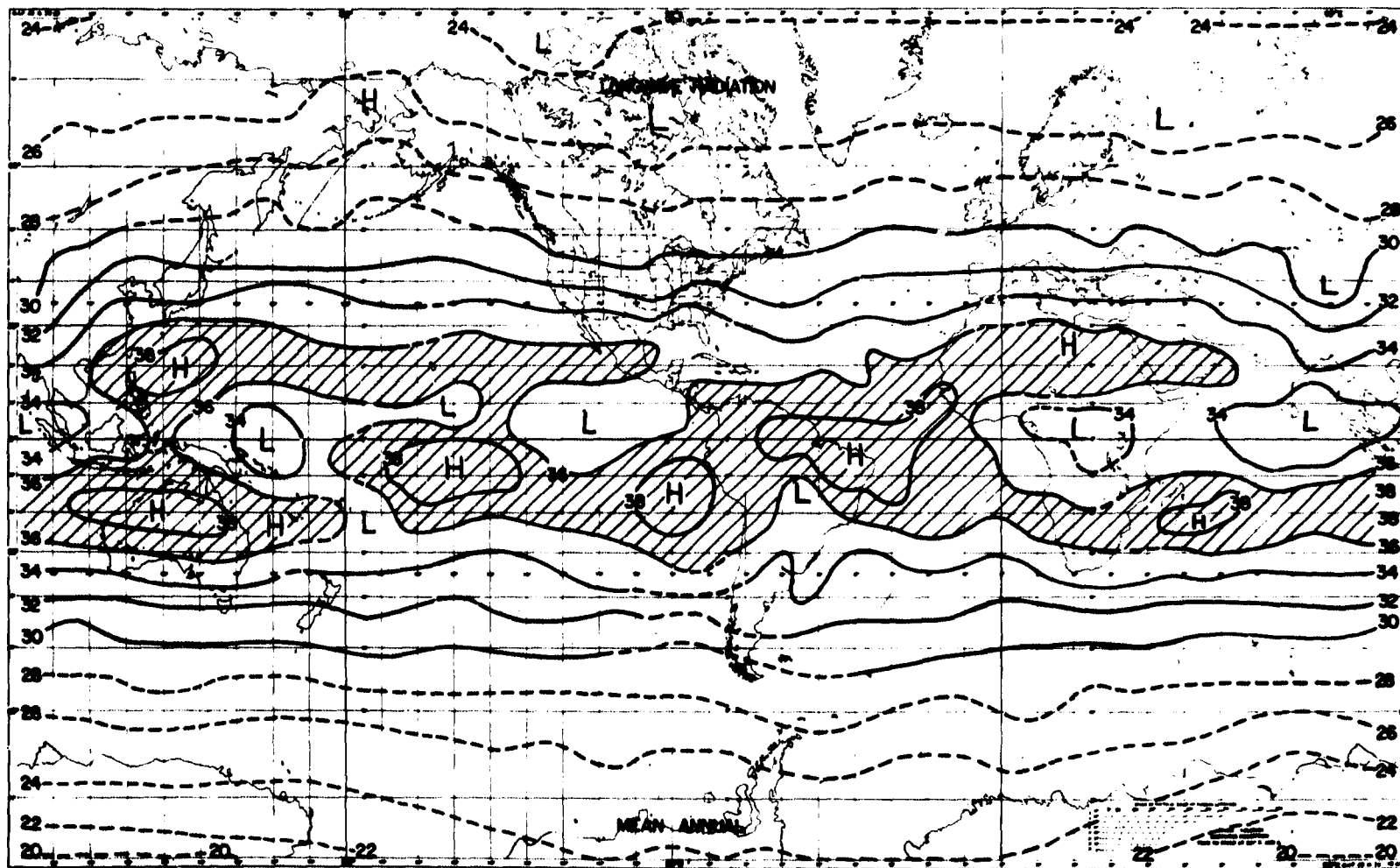


Fig. 15. Mean annual values of longwave radiation from the earth-atmosphere system: (H_L). Units are 10^{-2} $\text{cal} \cdot \text{cm}^{-2} \cdot \text{min}^{-1}$ and regions of $H_L > 0.36$ are shaded.

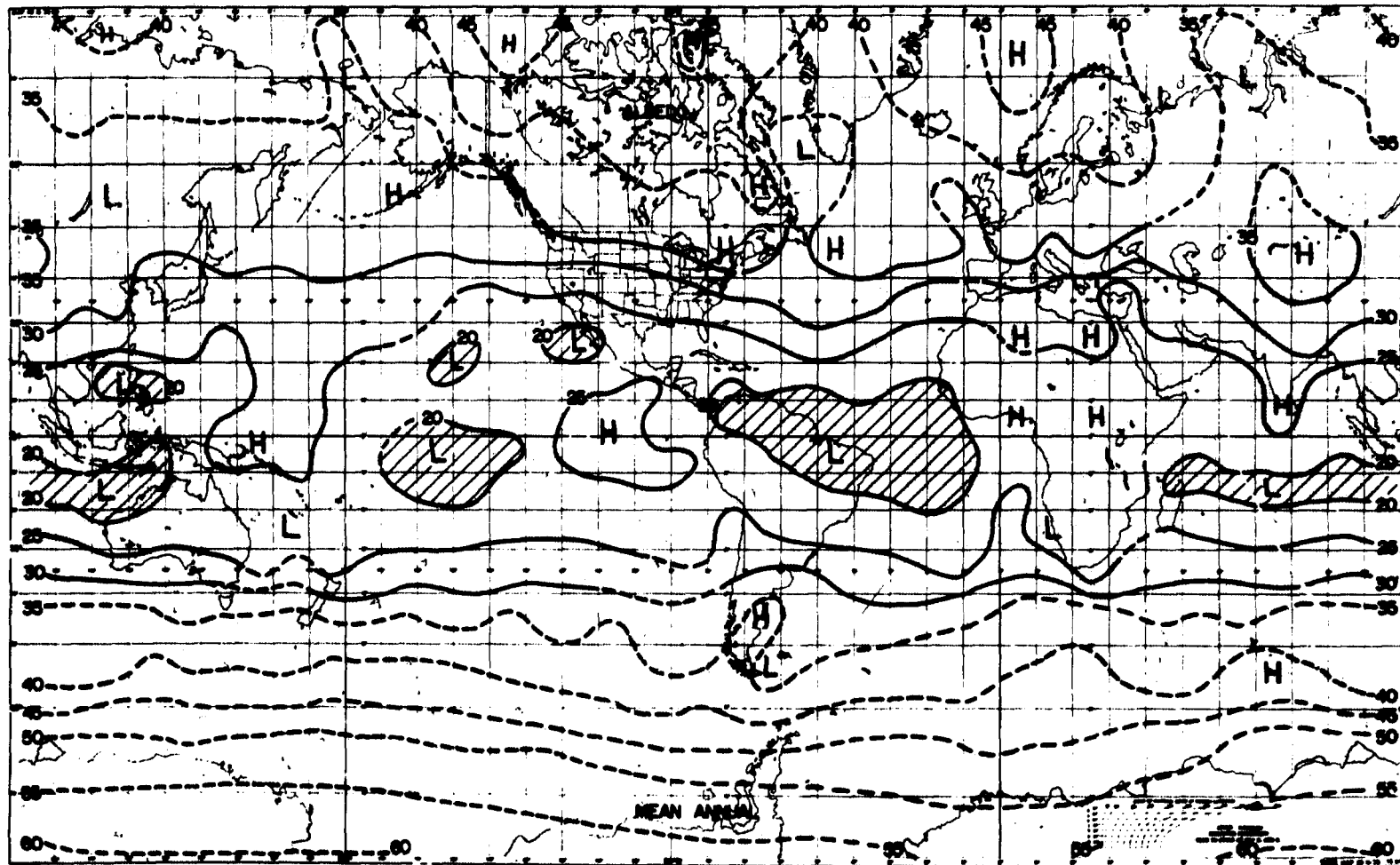


Fig. 16. Mean annual values of planetary albedo (A) in percent. Shaded areas have $A < 20\%$.

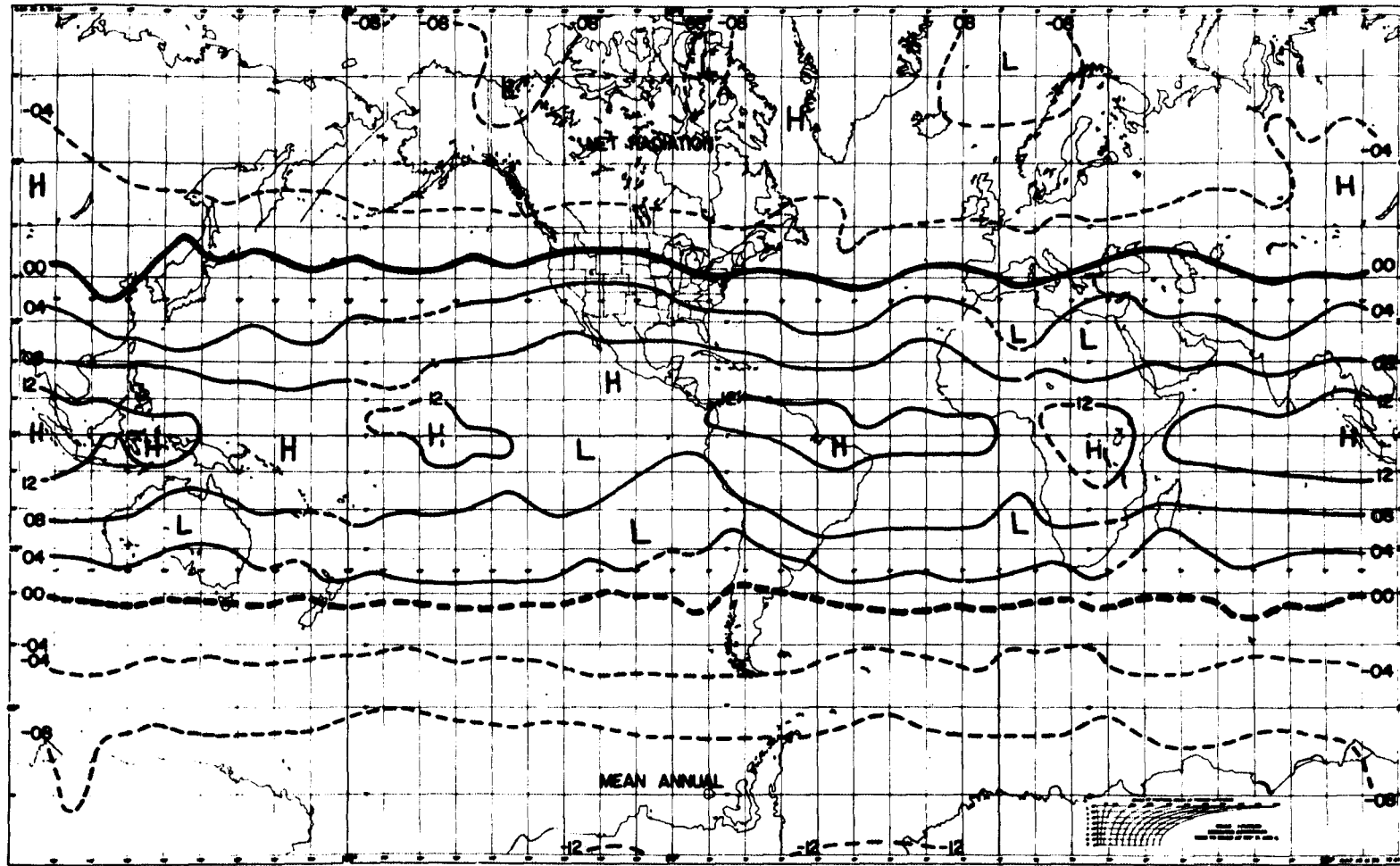


Fig. 17. Mean annual values of the net radiation budget of the earth-atmosphere system (R_{NEA}). Units are $10^{-2} \text{ cal} \cdot \text{cm}^{-2} \cdot \text{min}^{-1}$.

In the southern hemisphere the subtropical regions of high outgoing infrared energy contain two maxima (east of South America and in the central Pacific) that have a mean annual location very near the equator. Other maxima in this zone, over northwest Australia, west of South America and near Madagascar, are found at 20°S. When all of these areas are considered, the southern hemisphere region of high outgoing radiation has a greater mean annual intensity than its northern hemisphere counterpart.

Many areas on the mean annual albedo map have high and low values that are inversely related to the patterns of longwave radiation. This occurs at locations where bright cold clouds or warm dark regions persist during most of the year. Examples are over the central Pacific and east of New Guinea. Some albedo values that do not follow this pattern are highly influenced by surface characteristics (i. e., the land masses at higher latitudes in the northern hemisphere and the Sahara region). Other departures from an inverse pattern could be caused by warm (low) clouds (i. e., west of Peru) or the presence of much cirrus cloudiness.

The most extensive region of low albedo (less than 20%) is found over northern South America and the Central Atlantic. Near 70°S a combination of clouds with ice and snow yields mean annual albedos near 60%. Similar latitudes in the northern hemisphere have maximum values greater than 45%.

The geographical distribution of net radiation has a very zonal nature on the mean annual map which emphasizes the dominant role of incident solar energy in the radiation budget at any location. In the higher latitudes of the northern hemisphere the regions of maximum net energy loss by the earth-atmosphere system correspond to locations with the highest albedo. However, near the Antarctic continent where the albedo is uniformly high, net radiation values of $-0.12 \text{ cal} \cdot \text{cm}^{-2} \cdot \text{min}^{-1}$ are found over the relatively warmer regions where the outgoing longwave radiation exceeds the zonal mean. In both hemispheres the earth-atmosphere system is in radiative equilibrium with space near forty degrees of latitude.

Near the equator, the zonal pattern of net radiation gain is disrupted by maxima that occur because the longwave radiation is low (near Sumatra and over tropical Africa) or because the absorbed solar radiation is very high (east of South America). Relative minima are found over warm bright regions such as the land and oceanic deserts and over cold bright regions where the reflected solar energy plays a major role (i. e., 110°W at the equator).

These mean annual maps were derived from measurements obtained from the first generation of meteorological satellites. As such, they represent the first stages of a global radiation climatology that can be extended when other observations become available. Like the mean cloudiness maps being compiled from photographic data, these radiometric averages provide new information

about the global pattern of atmospheric conditions. However, the quantitative nature of the radiation budget data extends their usefulness much further. They can be used as a control for numerical models and provide information about the variation of the earth's brightness in the shortwave and longwave portions of the spectrum. Perhaps the most important use of these data will be in studies that not only consider the cause of the measured values but also the effect the observed energy exchange has on future atmospheric conditions at a given location.

4.2 Budgets of Latitudinal Zones

4.21 Mean Meridional Profiles

One of the most common depictions of the earth's radiation budget has always been plots of the budget components as a function of latitude only. Figure 18 presents the data of this study in such a form. Although the maps of the previous section show that these zonal averages do not properly represent the true budget at many longitudes, especially equatorward of 30° , mean meridional profiles are useful to examine gross seasonal changes forced by the variation of incident solar energy.

The solar energy absorbed in the earth atmosphere system, H_a , at any latitude is closely related to the available energy except near the summer poles and the equator. In these regions the higher albedo, especially over Antarctica, reduces the H_a values despite the large amount of incident solar radiation. The largest amount of solar radiation ($0.54 \text{ cal} \cdot \text{cm}^{-2} \cdot \text{min}^{-1}$) retained by the earth-atmosphere system is at 25°S during summer. On an annual basis the subtropical regions of the southern hemisphere absorb more energy than the same area in the north.

Zonal averages of reflected short wave radiation, H_r , show similar departures from a pattern forced by the sun. In each seasonal profile the effects of the clear, dry subtropics and the cloudy, wet tropical regions are apparent. Poleward of 40° in both hemispheres the summer averages show that reflected solar radiation increases toward the pole and this also occurs during spring in the southern hemisphere. The reflected energy exceeds $0.40 \text{ cal} \cdot \text{cm}^{-2} \cdot \text{min}^{-1}$ poleward of 70°S during DJF. Changing incident solar energy and the general increase of the planetary albedo toward the poles cause the mean annual values of H_r to be nearly the same at all latitudes. The largest annual value ($0.16 \text{ cal} \cdot \text{cm}^{-2} \cdot \text{min}^{-1}$) occurs at the south pole and other maxima are found at 5°N and 35°N .

A different view of the shortwave radiation budget is seen in the mean profiles of albedo. These data represent the latitudinal variations of the "reflecting capability" of the earth-atmosphere system. A puzzling feature on this

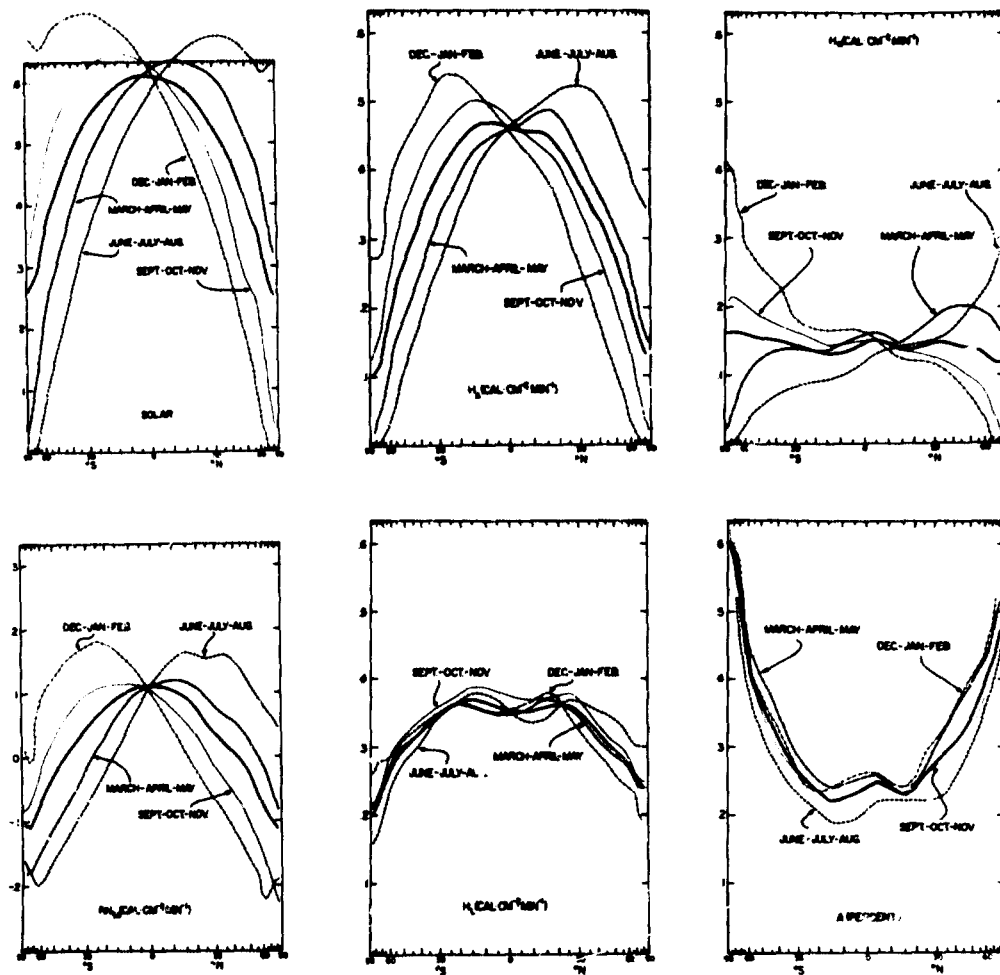


Fig. 18. Mean meridional profiles of the components of the radiation budget of the earth-atmosphere system for each season and the annual case (solid line).

plot is the significantly lower albedo of the tropics and subtropics during JJA. This effect influences the H_0 values so that the absorbed solar energy over the entire earth is nearly the same during JJA and DJF despite the changing distance from the earth to the sun. Because of this result, the effect could be interpreted as an extreme example of Simpson's hypothesis (see Rossby (1959)) of the response of a planetary system to changes in the amount of incident solar radiation by adjusting its albedo.

Zonal averages of albedo measurements also show that the darkest region overall is in the subtropics of the southern hemisphere and that the mean albedo of the Antarctic region always exceeds 60%. In the northern polar regions the albedo ranges from 45 to 55% although values for the poorly illuminated seasons are based on marginal measurements.

The other, infrared, portion of the radiation budget is notable because of the very small changes in absolute magnitude at most latitudes. Largest seasonal differences ($\pm 0.10 \text{ cal} \cdot \text{cm}^{-2} \cdot \text{min}^{-1}$) occur at the poles and, as expected, the Antarctic region has the lowest overall radiation temperature. The smallest seasonal variations are found over the oceans of the southern hemisphere and the corresponding latitudes in the north show the continental effect. When all seasons are considered, the outgoing longwave radiation is highest at most latitudes during SON. This does not correspond to the season of lowest albedo JJA, which may be explained by the presence of more bright clouds during the spring/fall season and/or more worldwide cirrus clouds during JJA. On a mean annual basis the highest region of outgoing infrared energy occurs over the subtropics of the southern hemisphere.

The total radiation budget of the earth and atmosphere at various latitudes and times is displayed by the R_{NET} curves. Near the equator the budget changes very little with season, always being about $+0.10 \text{ cal} \cdot \text{cm}^{-2} \cdot \text{min}^{-1}$. At the poles, however, the winter to summer change is very large: ± 0.20 in the south and ± 0.25 in the north. The range in the Arctic is larger because of changes in the surface albedo which actually result in a definite gain of energy during the northern summer. During both summer seasons the regions from the equator to fifty degrees latitude show net energy gains greater than $0.10 \text{ cal} \cdot \text{cm}^{-2} \cdot \text{min}^{-1}$ with maxima located near 25°S and 15° and 35°N .

Note that the net radiation deficit is greater at 60° than at the pole in the respective winters. This was also noted by Raschke *et al.* (1967) in NIMBUS measurements over the southern hemisphere and is caused by the higher values of longwave radiation at lower latitudes when the infrared component dominates the total budget. A similar reversal is found over the southern polar regions during summer and here magnitudes of albedo and incident solar energy yield a constant value of absorbed energy from $60^\circ - 90^\circ\text{S}$ and thus the infrared component decides the budget.

At all latitudes away from the equator, the net radiation budget is greatest in summer, spring, fall and winter, in that order. Thus, the total radiative forcing function is in phase with seasonal changes of incident solar radiation. Surface and atmosphere effects are most obvious in the polar regions (discussed above) and during JJA where the net energy gain at 25°N is weakened by high values of outgoing longwave radiation at this latitude.

In general, the poleward gradients of net radiation are greatest during the colder seasons of both hemispheres, although contrast between middle and high latitudes in the south during DJF is also very large. For the mean annual case the average gradient is $-0.03 \text{ cal} \cdot \text{cm}^{-2} \cdot \text{min}^{-1}$ per degree latitude poleward of 20 degrees. When all other energy budget effects are negligible these net radiation profiles represent the total forcing function that drives the atmosphere and hydrosphere. The role of these radiation budget values on the required energy transports of the total energy budget will be discussed in section 5.

4.22 Time-Latitude Sections

In order to better examine the seasonal changes of the various components of the radiation budget, time-latitude sections are displayed in Figure 19, although the data are the same as in the previous section.

It is apparent that one component of the radiation budget, the absorbed solar radiation, has a mean seasonal variation at all latitudes very similar to the changes in incident solar energy at the top of the atmosphere. Note that the region of maximum absorption ($> 0.40 \text{ cal} \cdot \text{cm}^{-2} \cdot \text{min}^{-1}$) lies along the seasonal path of the sun. Because the earth-atmosphere system absorbs energy in proportion to the amount available, the net radiation chart also shows a pattern that follows the sun. For example, the greatest seasonal change in net radiation at most middle and high latitudes occurs between summer and fall. At this time these regions change from a net energy gain to a net loss as the insolation falls off rapidly.

The time-latitude section of reflected solar radiation also shows a dependence on the available energy, particularly near the equator. This relationship is modified by atmospheric conditions when higher albedo values ($> 25\%$) coincide with periods of maximum insolation equatorward of 15°. Surface features can also influence the reflected energy pattern. For example, the region 40 - 60°N reflects more solar radiation in the spring than during summer probably because of snow on the continents at these latitudes.

On both the albedo and longwave radiation sections the seasonal movement of the two subtropical clear regions and the intervening convergence zone can be observed. The patterns are not identical because of the features noted on the mean seasonal maps. Albedo values less than 20% mark the most northern extent of the southern subtropical belt at 5°S. This low zonal value results

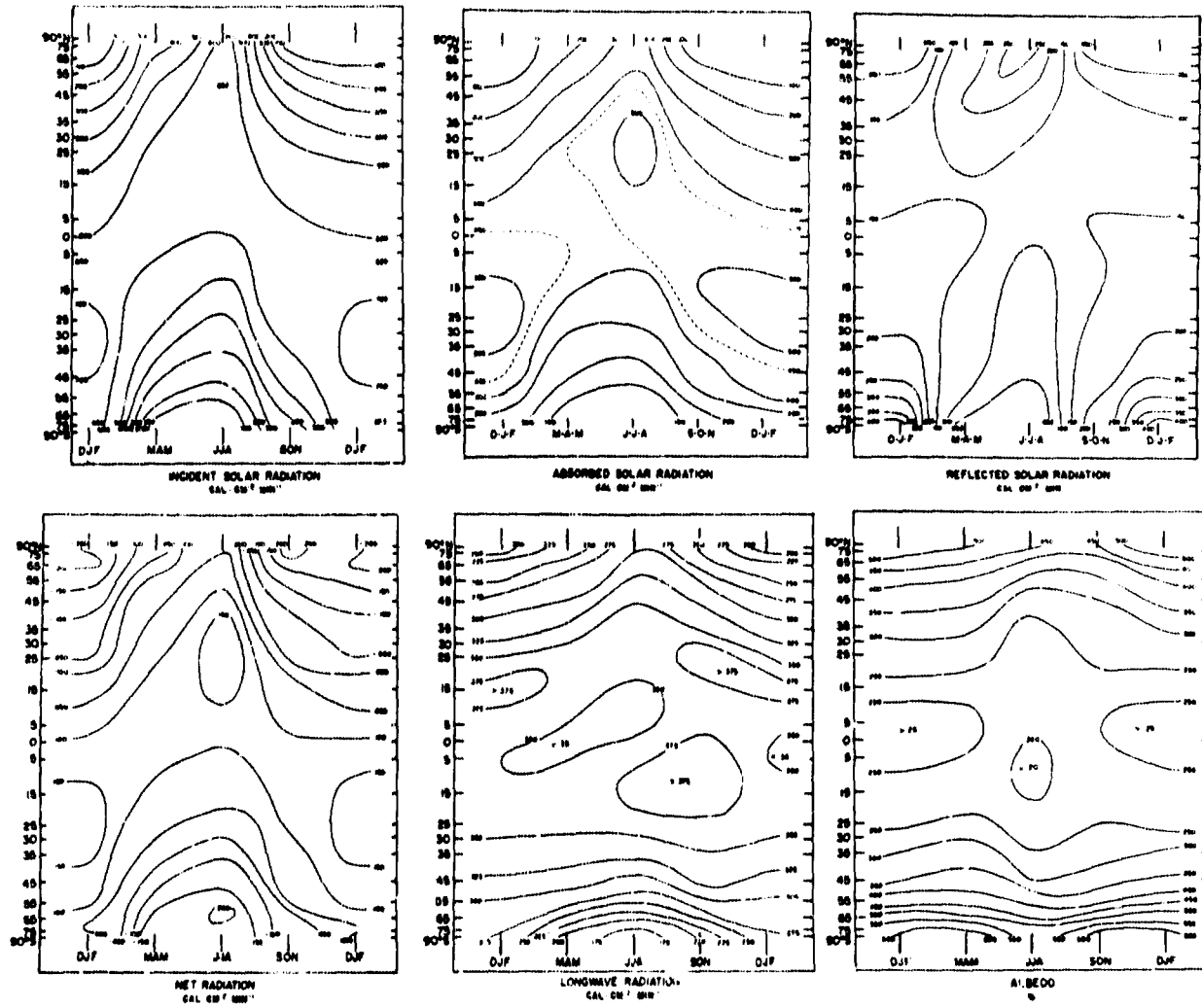


Fig. 19. Time-latitude sections showing the seasonal variations of the radiation budget components.

primarily from a region of low albedo over South America and the Atlantic. At this same time a major reason for the lower albedo values near 35°N is an extensive clear region south of California. The infrared energy from the tropical regions is lowest from March until July and the seasonal maps show that these zonal means are strongly influenced by low values near India and New Guinea.

A zone of nearly constant longwave radiation is found near 35°S and the albedo of the Antarctic, as expected, shows the smallest seasonal variation. The change in longwave radiation from one season to the next is greatest before and after winter in the south polar region.

Two minima of net radiation over the Arctic are seen on the time-latitude section. The one during SON results from relatively high longwave radiation values that counteract the weak solar absorption at this time, while the winter minimum is due to low infrared emission from the cold region. This observation, together with the reversal of net radiation near the poles in some seasons, emphasizes the importance of longwave radiation on the radiation budget of the higher latitudes.

Over all other areas it is apparent that, on a large spatial and temporal scale, changing surface and atmospheric conditions cannot override the influence of incident solar energy on the resulting radiation budget. However, with the aid of the longwave radiation and albedo sections we can examine the gross feedback effects. Over all regions except the tropical convergence zone the longwave radiation generally opposes seasonal changes of net radiation forced by the sun. Albedo values either remain the same or decrease as the incident energy increases. Thus the longwave radiation works as a negative feedback mechanism and the albedo changes act to amplify seasonal variations of net radiation. However, in the cloudy convergence zone (which moves over a range of latitudes) the higher albedo and lower infrared values act as negative and positive feedback effects, respectively.

Time-latitude sections of longwave radiation, albedo and net radiation derived from 30 consecutive months of satellite measurements are shown in Figure 20. On these charts the values poleward of 65° before June 1964 were obtained by extrapolation and reference to subsequent polar measurements. During this two and one-half year period the seasonal changes of net radiation during each year show definite similarities. Some differences do occur, however, and they must result from changes in albedo and/or the amount of outgoing longwave radiation.

The period June - November 1963 and the same interval during 1965 have a net radiation pattern that is nearly the same at all latitudes. Positive values of net radiation extend from 15°S to the north pole in JJA with maxima greater than $+0.15 \text{ cal} \cdot \text{cm}^{-2} \cdot \text{min}^{-1}$ during both years. The albedo sections for these times show low values over the tropics and subtropics of both latitudes and the generally high outgoing radiation decreased by the cloudy convergence zone

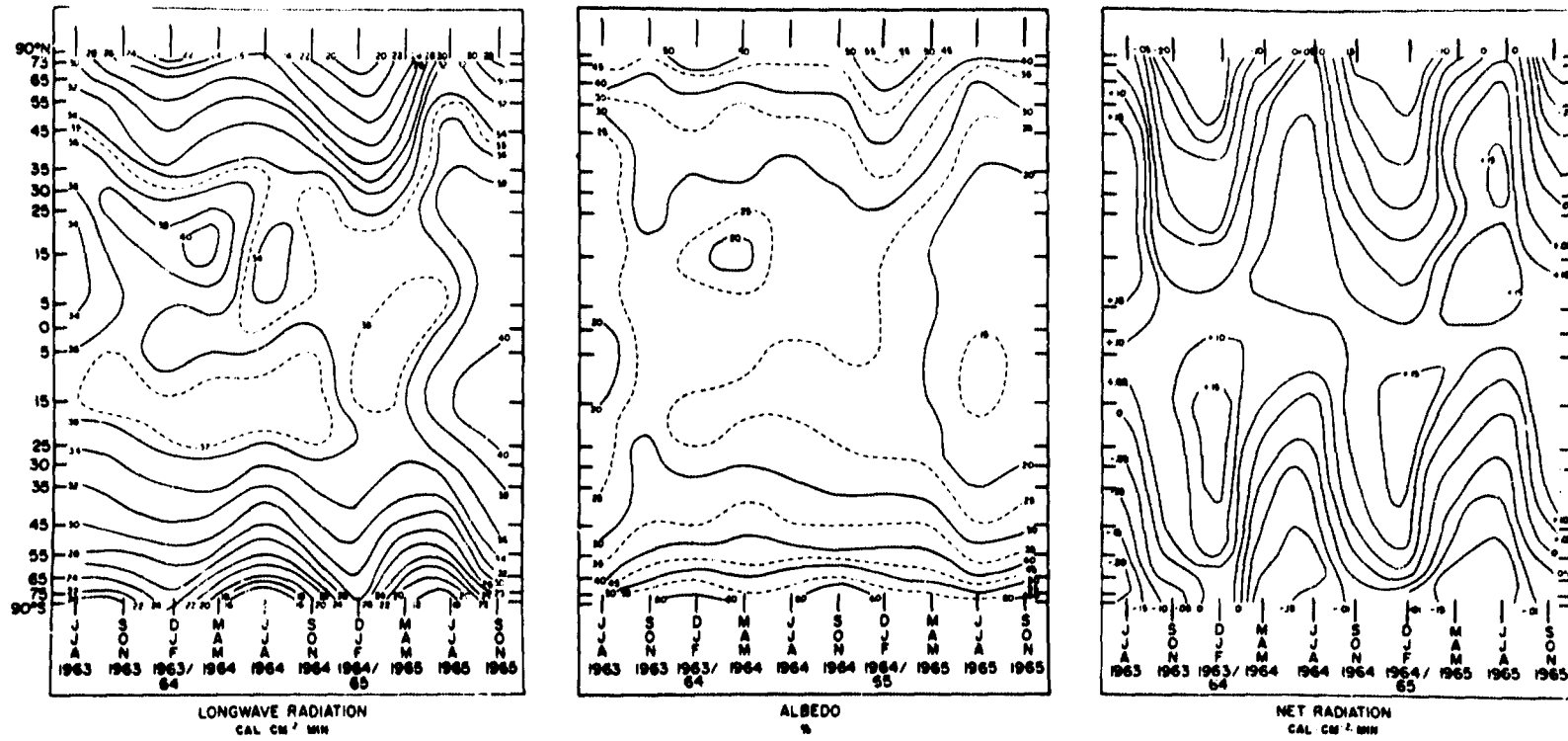


Fig. 20. Time-latitude sections of planetary albedo, outgoing longwave radiation and the net radiation budget for the period JJA, 1963 to SON, 1965.

near 15°N. During these months of 1964 the net radiation pattern is similar to the other two years in the southern hemisphere. However, the net gain of energy over the northern hemisphere is less in JJA of 1964 and results in a more moderate change of net radiation from summer to fall at 20° - 50°N. The immediate cause of this difference was a region of low outgoing radiation and higher albedo located near 15°N, the normal position of the convergence zone at this time. Along with this cloudier tropical region the entire hemisphere had lower than average values of outgoing radiation.

The two time periods between those mentioned above cover the first five months of 1964 and 1965. Although the net radiation section does show some differences in the radiation budgets at these times (i. e., in the southern polar regions), the overall patterns were rather similar. The other sections show that in the early months of 1964 both subtropical regions had high values of outgoing radiation. At the same time in 1965 the winter subtropics were apparently cloudier and the convergence zone had a larger latitudinal extent.

These charts demonstrate that noticeable differences exist between the radiation budgets of the same months in different years. With the aid of albedo and longwave radiation data, some inferences into the cause of these differences can be made. Future work should include the location of the primary features that cause a zonal anomaly and an analysis of the atmospheric conditions before and after such an occurrence.

4.23 Budgets of Selected Zones

Figure 21 shows how all the radiation budget components within some latitudinal zones change from July 1964 through November 1965.

The two polar regions have some significant differences. For example, in the south the shortwave radiation parameters are exactly in phase with seasonal changes of insolation and the reflected solar energy always exceeds the amount absorbed. In the Arctic, however, the measured albedo was greater than 50% only in March. The reduced albedo during the summer, most probably due to the melting of ice and surface puddling, shifts the maximum of the absorbed solar energy curve to July. The time of maximum energy gain thus has a one-month lag from the time of maximum insolation. In both polar regions, the outgoing infrared energy increases rapidly during the spring and decreases at a slower rate in the fall. The albedo over Antarctica stays near 60% over the entire year but at the other pole the annual range is 20%. Average net radiation values over 70° - 90°N show that the region has a net gain of energy across its upper boundary from May through August. In contrast, the southern area has only a small net gain during mid-summer.

Mid-latitudes of the northern hemisphere reflect more solar energy during spring partly because of snow on the continents. Although this albedo change shifts the H_a curve out of phase with the insolation as at 70° - 90°N, the

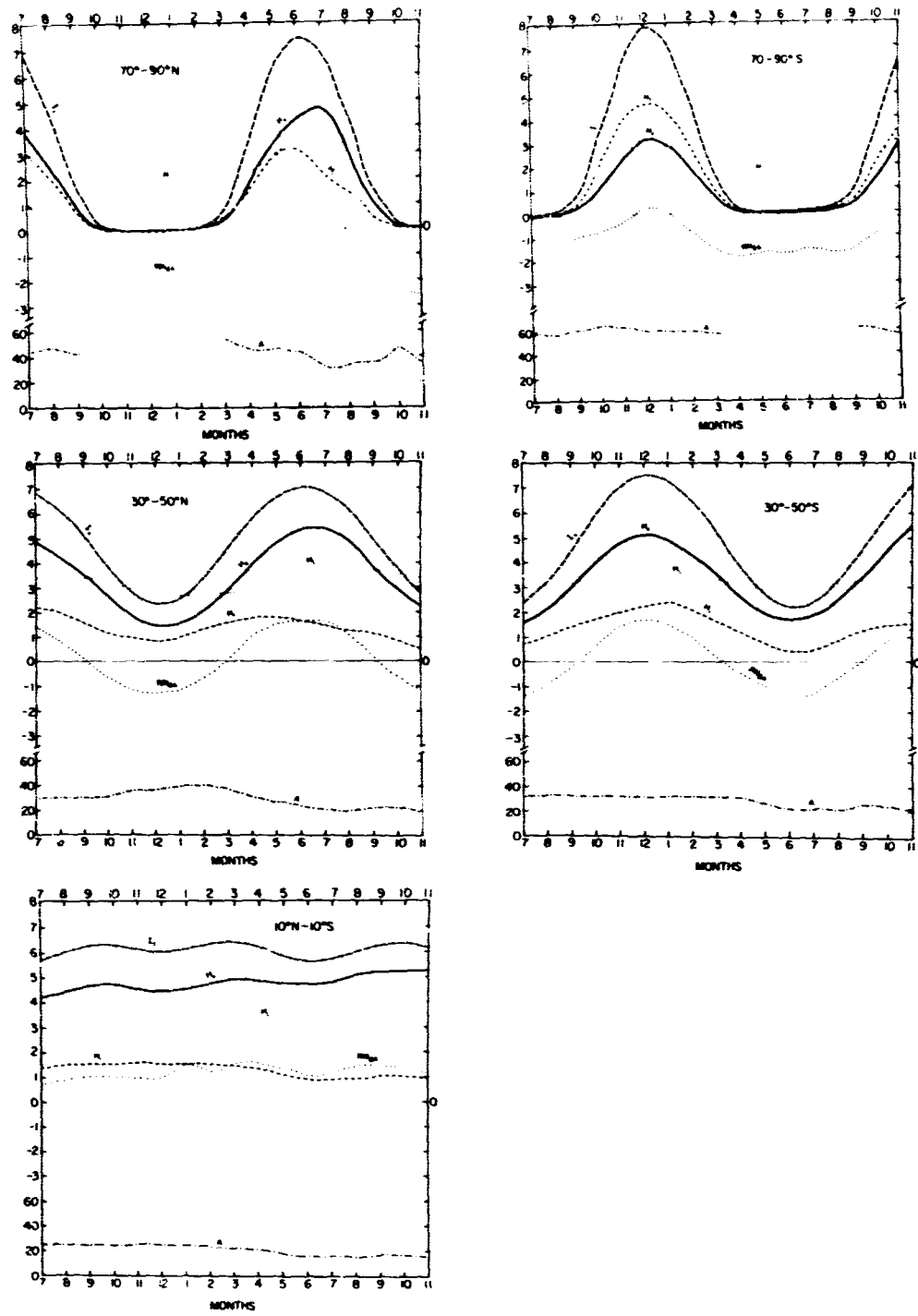


Fig. 21. The radiation budgets of selected latitudinal zones from July, 1964 through November, 1965.

increased longwave radiation during the summer counteracts this effect in the total radiation budget. The same latitudes in the other hemisphere are characterized mainly by an unchanging amount of outgoing longwave radiation.

From 10°N - 10°S the radiation budget component changes very little with time. Note, however, that the net radiation values respond to very small changes of longwave radiation and even to the slight variations of incident solar energy.

As a whole, the plots in Figure 21 show that even on a monthly time scale the budgets of large zonal areas do not show many sudden fluctuations. These first measurements of the polar radiation budgets over a long time period illustrate some important differences between the two regions.

4.3 Global and Hemispheric Budgets

4.31 Temporal Variations

In Figure 22, the measured radiation budgets of the northern and southern hemispheres and of the entire earth are shown as a function of time. Data from ten consecutive seasons are displayed beginning with JJA (season III) of 1963. The mean annual values of the radiation budget parameters are represented by horizontal dashed lines.

The radiation budgets of both hemispheres show the expected twelve-month cycle forced by the sun. Because they are six months out of phase the net radiation over the entire earth has only small temporal variations. The largest net gain of energy is found from March-August of 1965. At this time the total albedo of both hemispheres was quite low and apparently not completely compensated by increased outgoing radiation.

One naturally suspects that some instrumental problem has influenced the observations at this time but extensive data checks gave no reason to discard these measurements. In addition, some other facts preclude hasty rejection. Note that the albedo increases during the southern hemisphere spring of 1965 and that measurements during JJA of 1963 (from a different set of sensors) also show relatively low albedos for both hemispheres. An indirect indication that the sensors were returning proper values during mid-1965 was obtained when a reasonable value for the solar constant was derived partly from measurements made at this time. Another check on the satellite data was made by comparing longwave radiation values with seasonal averages of the upward infrared radiation near the top of the atmosphere derived from balloon-borne radiometers. Kuhn and Cox (1967) have summarized such measurements over Guam and Canton Islands and at Green Bay, Wisconsin. The average deviation of the balloon and satellite measurements during March-August 1965 at these locations

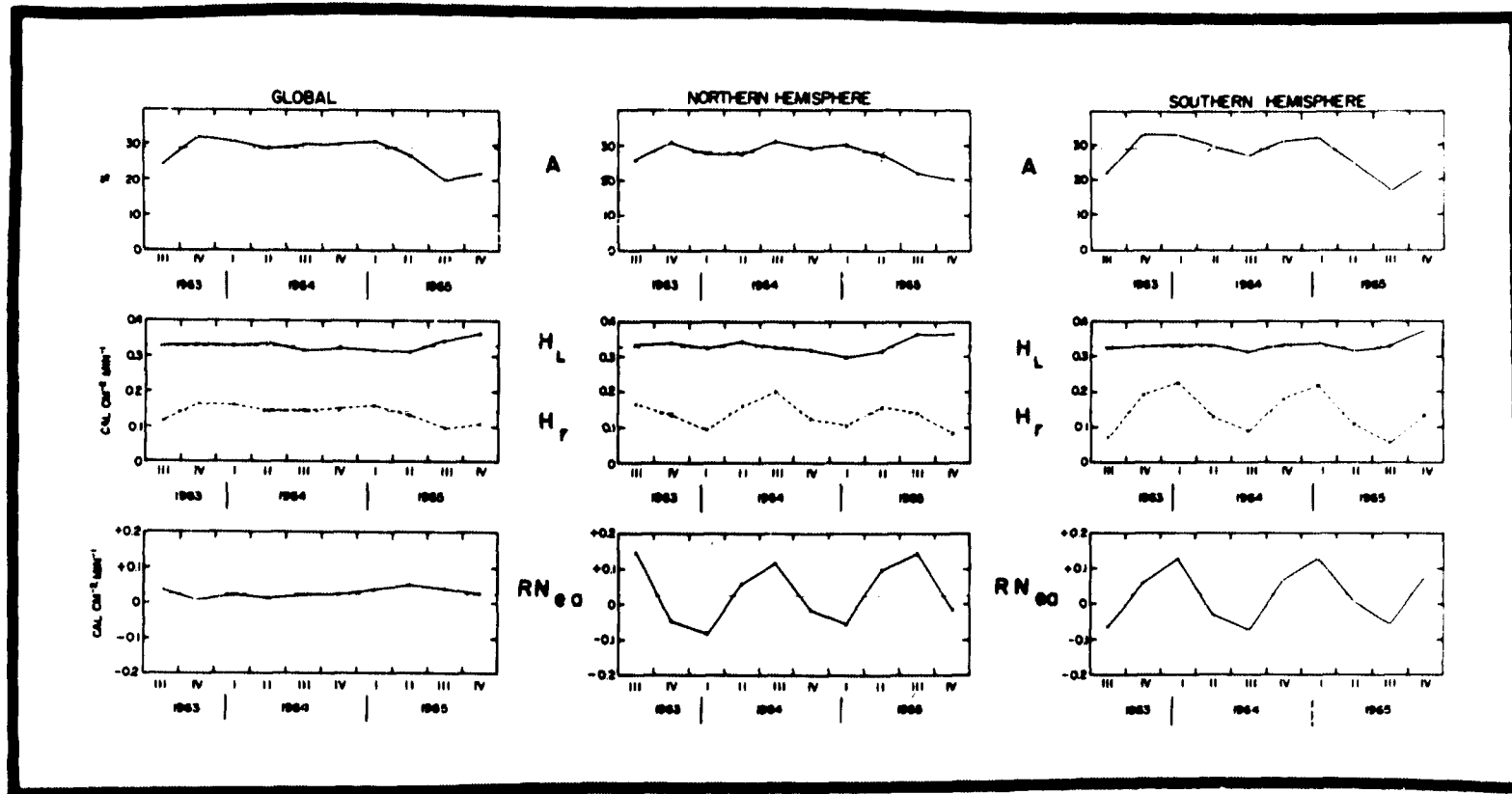


Fig. 22. Global and hemispheric averages of the radiation budget components from June, 1963 to November, 1965. Dashed lines show the mean annual values.

was less than $0.01 \text{ cal} \cdot \text{cm}^{-2} \cdot \text{min}^{-1}$, and the balloon data were slightly higher.

Of course, from only two and one-half years of data, we cannot determine if the changes in the radiation budget represents true anomalies or just some periodic phenomenon. These first measurements, thus, emphasize the need for a continuous program to observe the earth's radiation budget in order to extend this time series.

4.32 Mean Annual and Seasonal Values

Figure 23 and Table 2 present the mean annual and seasonal values of all the radiation budget measurements. In the figure the seasons are listed by number (1 = DJF) and the horizontal line shows the mean annual value.

The mean seasonal data emphasize that over these large areas all components of the shortwave radiation budget are in phase with the sun during an "average" year. In contrast, the outgoing longwave radiation has a small annual range (i. e., $0.03 \text{ cal} \cdot \text{cm}^{-2} \cdot \text{min}^{-1}$ for the northern hemisphere, even less for the southern hemisphere). The net result on the total radiation budget of each hemisphere is a seasonal variation that closely follows the sun. For example, the satellite observations indicate that the most positive net radiation value for the northern hemisphere occurs in summer and that during the winter the same region has a net radiation deficit.

Some small, second-order features of each hemisphere's budget can result from mean seasonal changes in the physical state of the earth-atmosphere system (i. e., changes in the type or amount of cloudiness or changes in the albedo of the earth's surface). On the gross time and space scale considered in this section, such departures from the overriding solar effect are difficult to observe with accuracy. However, a closer view of Figure 23 does show that in both hemispheres the albedo is larger during December-May than during June-November. An inverse relation between the longwave radiation values for these time periods is barely discernible for the northern hemisphere and there is some indication that the longwave radiation may even increase as the albedo increases in the southern hemisphere. Because we are dealing with such relatively small changes it is not realistic to enter into a discussion concerning changes in cloud cover or the heights of clouds that could account for the small variations observed. It does appear, however, that a small secondary effect on the radiation budgets of each hemisphere is caused primarily by seasonal variations of the mean reflectivity of the earth-atmosphere system. This effect acts to amplify the seasonal variations of the net radiation budget of the northern hemisphere and it reduces the variation of the same parameter in the southern hemisphere. One possible cause may be the difference in the surface albedo of the polar regions during their respective summer seasons.

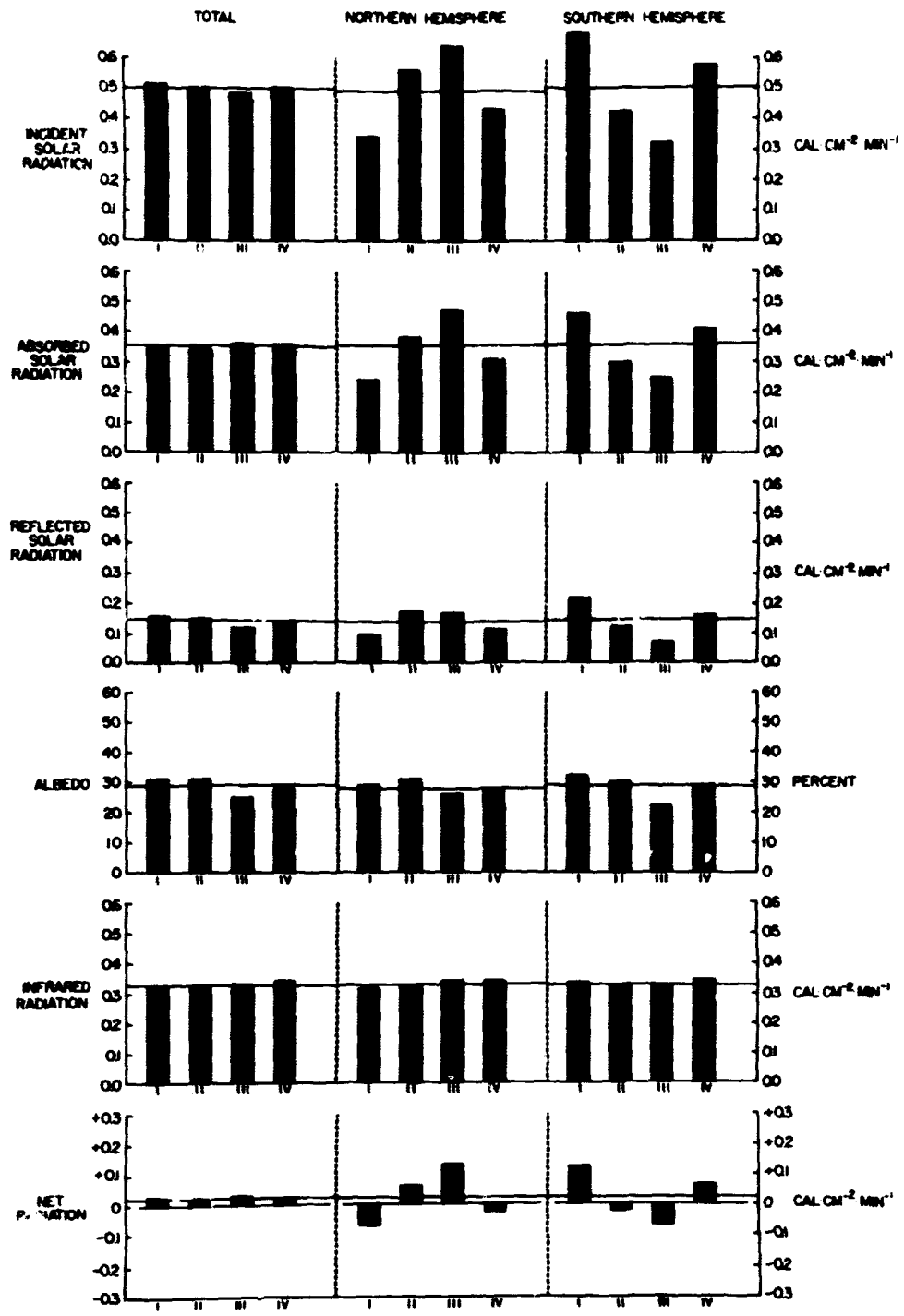


Fig. 23. The mean seasonal variation of the radiation budgets of the entire earth and each hemisphere.

TABLE 2
MEAN ANNUAL AND SEASONAL RADIATION BUDGET OF THE EARTH-ATMOSPHERE SYSTEM
OBSERVED FROM THE FIRST GENERATION METEOROLOGICAL SATELLITES

	<u>GLOBAL AVERAGE</u>					<u>NORTHERN HEMISPHERE</u>					<u>SOUTHERN HEMISPHERE</u>				
	DJF	MAM	JJA	SON	ANNUAL	DJF	MAM	JJA	SON	ANNUAL	DJF	MAM	JJA	SON	ANNUAL
I_0	.51	.50	.49	.50	.50	.34	.56	.65	.42	.50	.69	.43	.32	.58	.50
H_a	.34	.35	.37	.36	.35	.24	.39	.48	.31	.36	.46	.30	.25	.41	.35
H_r	.16	.15	.12	.14	.15	.10	.18	.17	.12	.14	.22	.13	.07	.17	.15
A	.31	.31	.25	.28	.29	.29	.31	.26	.27	.28	.32	.30	.22	.29	.29
H_L	.32	.33	.33	.34	.33	.32	.33	.34	.34	.33	.33	.32	.32	.34	.33
* RN_{EA}	.03	.02	.03	.02	.02	-.07	.06	.03	-.03	.02	.13	-.02	-.07	.06	.02

83

I_0 = incident solar radiation ($\text{cal} \cdot \text{cm}^{-2} \cdot \text{min}^{-1}$)

H_a = absorbed solar radiation ($\text{cal} \cdot \text{cm}^{-2} \cdot \text{min}^{-1}$)

H_r = reflected solar radiation ($\text{cal} \cdot \text{cm}^{-2} \cdot \text{min}^{-1}$)

A = planetary albedo (percent)

H_L = emitted infrared radiation ($\text{cal} \cdot \text{cm}^{-2} \cdot \text{min}^{-1}$)

RN_{EA} = net radiation budget of the earth-atmosphere system ($\text{cal} \cdot \text{cm}^{-2} \cdot \text{min}^{-1}$)

*Probable absolute error of $\pm 0.01 \text{ cal} \cdot \text{cm}^{-2} \cdot \text{min}^{-1}$.

When the entire earth is considered, the relative mean seasonal changes in the radiation budget are quite small. There is a slight maximum of absorbed solar energy during June-July-August, a consequence primarily of the lowered albedo of the northern hemisphere during this time. Average values of outgoing longwave radiation are particularly unchanging with season, although they increase a small amount during the last six months of each year. The entire earth is very close to radiative equilibrium during the spring-fall transition seasons, a fact noted also by House (1965).

The mean annual values of all the radiation parameters were nearly the same for each hemisphere. This emphasizes the effect of clouds, rather than surface features, on the hemispheric-scale radiation budgets. For both regions (and therefore the entire earth) the mean annual outgoing infrared radiation was $0.33 \text{ cal} \cdot \text{cm}^{-2} \cdot \text{min}^{-1}$ (corresponding to an equivalent black-body temperature of 252°K). Calculations of London (1957) and work discussed by Lettau (1954) agree with this value to within 2 or 3 percent. The shortwave portion of the budgets show each hemisphere to have a planetary albedo of approximately 29 percent, with an indication that the southern hemisphere may be slightly "brighter." On a global scale, this observed albedo value together with insolation averaging $0.5 \text{ cal} \cdot \text{cm}^{-2} \cdot \text{min}^{-1}$ requires that, in the mean, each square centimeter column of the earth-atmosphere system absorb 0.35 and reflect 0.15 calories per minute of the incident solar energy.

The planetary albedo value of 29 percent is slightly lower than any earlier estimate. Bartman (1967) has recently summarized the latest theoretical estimates and few available observations; he notes that the recent trend is toward lower values (near 30 percent). For example:

<u>Reference</u>	<u>Planetary Albedo</u>
Dines (1917)	50%
Aldrich (1919)	43
Simpson (1928)	43
Baur and Phillips (1934)	41.5
Fritz (1948)	34.7
Möller (1950)	35
Houghton (1954)	34
Lettau (1954)	34
London (1957)	35
Angström (1962)	33-38
House (1965)	35
Bandeem <u>et al.</u> (1965)	32
Vondor Haar (1968)	29 (± 1)

The earliest estimates (45 - 50%) gave way to lower values (near 35%) primarily because of new information about the albedo of clouds. The slightly lowered values obtained from global satellite observations apparently result

from a better assessment of the amount of clouds. Only the last three values were derived from satellite observations and in each of these studies the sampling in space and time was different. Raschke and Pasternak (1967) recently obtained 30% from three months of NIMBUS data.

When the albedo and longwave radiation observations are used to derive the total (net) radiation budget, we find again that each hemisphere, and the earth as a whole, has a net radiation imbalance of plus $0.02 \text{ cal} \cdot \text{cm}^{-2} \cdot \text{min}^{-1}$ for the mean annual case. This value of approximately $\pm 14 \text{ watts} \cdot \text{m}^{-2}$ is close to the absolute accuracy of the satellite sensors for measuring net radiation ($\pm 10 \text{ watts} \cdot \text{m}^{-2}$). For this reason, we can state that, within the accuracy of our measurements, the entire earth-atmosphere system was nearly in radiative equilibrium during the time of these observations. Although a small positive imbalance (i.e., warming of the earth-atmosphere system) is indicated, it must be emphasized that this applies only to the relatively short (in a climatological sense) time period for which we have data.

Note that the average solar input to our system is $349 \text{ watts} \cdot \text{m}^{-2}$ and thus the measurements used in this study allow us to examine the global radiation balance with an accuracy of $\pm 3\%$. If a solar constant of 1.95 (see 3.22) rather than $2.00 \text{ cal} \cdot \text{cm}^{-2} \cdot \text{min}^{-1}$ had been used the net radiation budget would still have a small positive imbalance.

In summary, the mean annual global and hemispheric satellite observations show that:

- a) During the time period of observations (approximately 1963-65) the entire earth-atmosphere system was in near radiative equilibrium.
- b) Despite the physical differences between the hemispheres (i.e., the larger land areas in the northern hemisphere) each had similar albedos and the same mean value of outgoing longwave radiation ($0.33 \text{ cal} \cdot \text{m}^{-2} \cdot \text{min}^{-1}$).
- c) On the average over space and time, each square meter of atmosphere and underlying surface retained 71% of the solar energy incident on it (i.e., the mean value of available solar energy was $248 \text{ watts} \cdot \text{m}^{-2}$).

Point (b) validates the assumptions made by earlier investigators when they computed the radiation budget of the northern hemisphere and used it to represent the long-period global budget.

5. ENERGY BUDGET RESULTS AND REQUIRED TRANSPORTS

Satellite measurements of the radiation budget can be combined with estimates of the other energy terms to derive the total energy budget of the earth-atmosphere system. The results show the principal regions of net energy gain or loss on various time and space scales. When the entire earth is considered, energy budgets can also be used to compute the required poleward energy transport by the atmosphere and oceans.

In order to note the major components of the energy budget and to point out the role of the radiation term, the following section presents a simple depiction of the energy budget of the earth-atmosphere system.

5.1 The Energy Budget of the Earth-Atmosphere System

The total energy budget of an earth-atmosphere column (Figure 24) can be expressed as the sum of two separate budgets, one for the surface and one for the atmosphere alone. For the earth's surface (either land or ocean) the energy balance equation can be written in schematic form* as:

$$RN_E - LE - H = G_E + \Delta F \quad (3)$$

RN_E = net radiation balance of the surface

LE = net energy removed from or added to the surface by phase transformation of water; (E = amount of water that leaves the surface and is added to the atmosphere, L = latent heat of phase transformation (600 cal/gm))

GE = subsurface storage (or release) of energy

ΔF = subsurface horizontal energy divergence (transport); (the term represents the action of ocean currents and is zero for a land surface).

Similar to (3), an energy balance equation for the atmosphere only is:

$$RN_A + LP + H = G_A + \Delta C \quad (4)$$

where:

RN_A = the net radiation budget of the atmosphere (a positive value represents a net gain of energy by the atmosphere due to radiation processes)

*The approach and notation used here closely follows that of Sellers (1966).

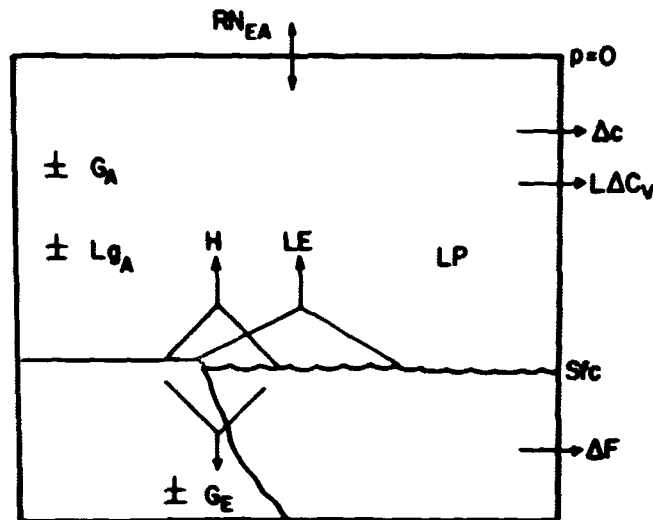


Fig. 24. Major components of the energy budget of the earth-atmosphere system.

L_P = net heat added to or removed from the atmosphere by phase transformation of water (L = latent heat of phase transformation, P = precipitation that leaves the atmosphere and arrives at the surface)

H = net energy added to or removed from the atmosphere by exchange processes at the atmosphere-surface interface

G_A = storage (or release) of energy within the atmosphere

ΔC = horizontal energy divergence (transport) in the atmosphere

Because the transport and storage as well as the transformation of latent energy in the form of water vapor are vital to the atmosphere's energy budget, Eq. (4) must be expanded by considering the water budget of an atmospheric column. It is:

$$L(E - P) = L g_A - L \Delta C_v \quad (5)$$

where:

g_A = storage (or release) of water vapor in the atmosphere

ΔC_v = transport (divergence) of water vapor.

The equation states that any difference between the water vapor added to or removed from an atmospheric column must be balanced by an appropriate storage (or release) of water vapor and/or transport of vapor in or out of the column.

Substituting (5) into (4) yields the atmosphere's balance equation when latent heat transport and storage are included. By adding the result to (3) we obtain the total schematic energy balance equation for the earth-atmosphere system:

$$RN_{EA} - G_A - G_E - L_{gA} = \Delta C + \Delta F + L\Delta C_v \quad (6)$$

This shows that the total divergence of energy (including the latent form) from a system must be balanced by the release (negative storage) of sensible and latent heat within the system and the net radiation balance of the system.

With the aid of (5) we can obtain an alternate equation:

$$RN_{EA} + L(P - E) - G_A - G_E = \Delta C + \Delta F \quad (7)$$

Here the transport and storage terms do not include latent heat, and the precipitation-evaporation difference within the system is considered as a source or sink of energy. Both (6) and (7) have been derived because they have been used in previous radiation and energy budget work and will be referenced later in the present study.

Each of these equations may be applied to a volume of the earth-atmosphere system on any space or time scale. Some of their terms may reasonably be neglected when very long time periods and/or very large areas are treated. For example, when the entire (global) earth-atmosphere budget is considered, all transport terms are zero. If the budget of any size volume is considered over long time periods, all storage terms are negligible provided no climatic change occurs. Of course, there are a few minor effects (i.e., the melting of snow and ice) that occasionally take on local importance and which have not been included in the general equation.

5.2 Mean Seasonal Energy Budgets

The information needed to evaluate the energy budget terms, other than the radiative term, on a mean seasonal basis is very limited. In particular, the geographical variation of precipitation and ocean storage is not well known. However, Rasool and Prabhakara (1966) have recently compiled mean monthly values of the energy budget terms for latitudinal zones between 60°N and 60°S. Their values of ocean storage, evaporation and precipitation were used with the mean seasonal RN_{EA} data from this study to evaluate Eq. (7). The solution gives $(\Delta C + \Delta F)$, the net non-latent energy available for transport by the

atmosphere (sensible heat + potential energy) and oceans, as a function of latitude and season.

These values, weighted by the area of each zone, were used to derive the required poleward transports during each season (Figure 25). It was assumed that (a) excess energy gained by the entire earth over a season was distributed equally by area, and (b) during the polar night the net energy loss poleward of sixty degrees is completely represented by the net radiative loss. Because of these necessary assumptions and the large uncertainty in the climatological data, the accuracy of these energy budget results is difficult to estimate.

During the spring and summer in both hemispheres, Figure 25 shows that the required transports poleward of thirty degrees are very small. Thus, in every season, one-fourth of the earth's surface area is decoupled from the remainder, in the sense that only a small net energy exchange between the two regions is required. The atmosphere and oceans move energy southward from as far north as 30°N during March-August. Maximum cross-equatorial exchange (23×10^{19} cal/day) occurs in JJA and is nearly matched by northward transport in DJF.

Despite the opposing effect of energy storage and release from the oceans, the transport from or into a hemisphere shows the similar pattern of solar dominance each season. The oceanic effect, however, is evident in the fall curves. At this time the large ocean area in the southern hemisphere continues to store energy and evaporation exceeds precipitation at the mid-latitudes. Both of these processes have a smaller magnitude in the northern fall and thus less energy must be brought poleward to compensate for the decrease in available solar energy.

During each winter season the reduced transport near thirty degrees results from a combination of annual maxima of evaporation at fifteen degrees and annual maxima of energy release by the oceans at thirty-five degrees. The polar regions require energy input during all seasons and the net radiation gain in the north during the summer apparently cannot supply all the energy needed at this time.

A time-latitude section in Figure 26 illustrates the mean seasonal variation of the required transport of non-latent energy. Note the abrupt change from northward to southward transport over the equatorial half of the earth during the first four months of each year. The radiation budget maps showed that zonal features in the subtropics were least well defined at this time and that the tropical convergence zone was strong. Together these results imply that increased atmospheric activity during this transition season may be forced by the energy requirements of the southern hemisphere oceans.

Since the transports in this study include the contribution by the ocean as

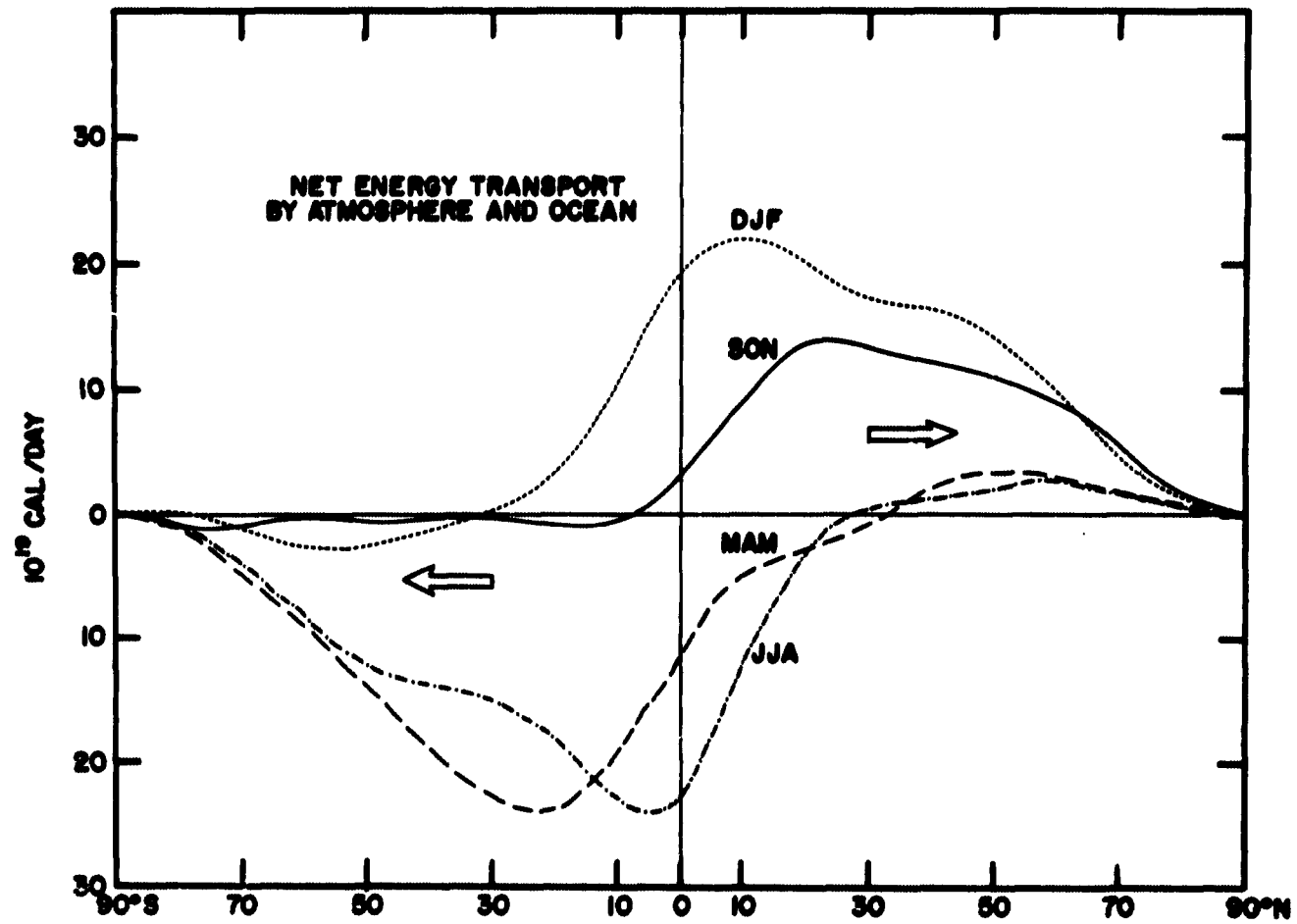


Fig. 25. Seasonal values of the required poleward energy transports by the atmosphere (sensible heat + potential energy) and the oceans. Points above the zero line represent northward transport.

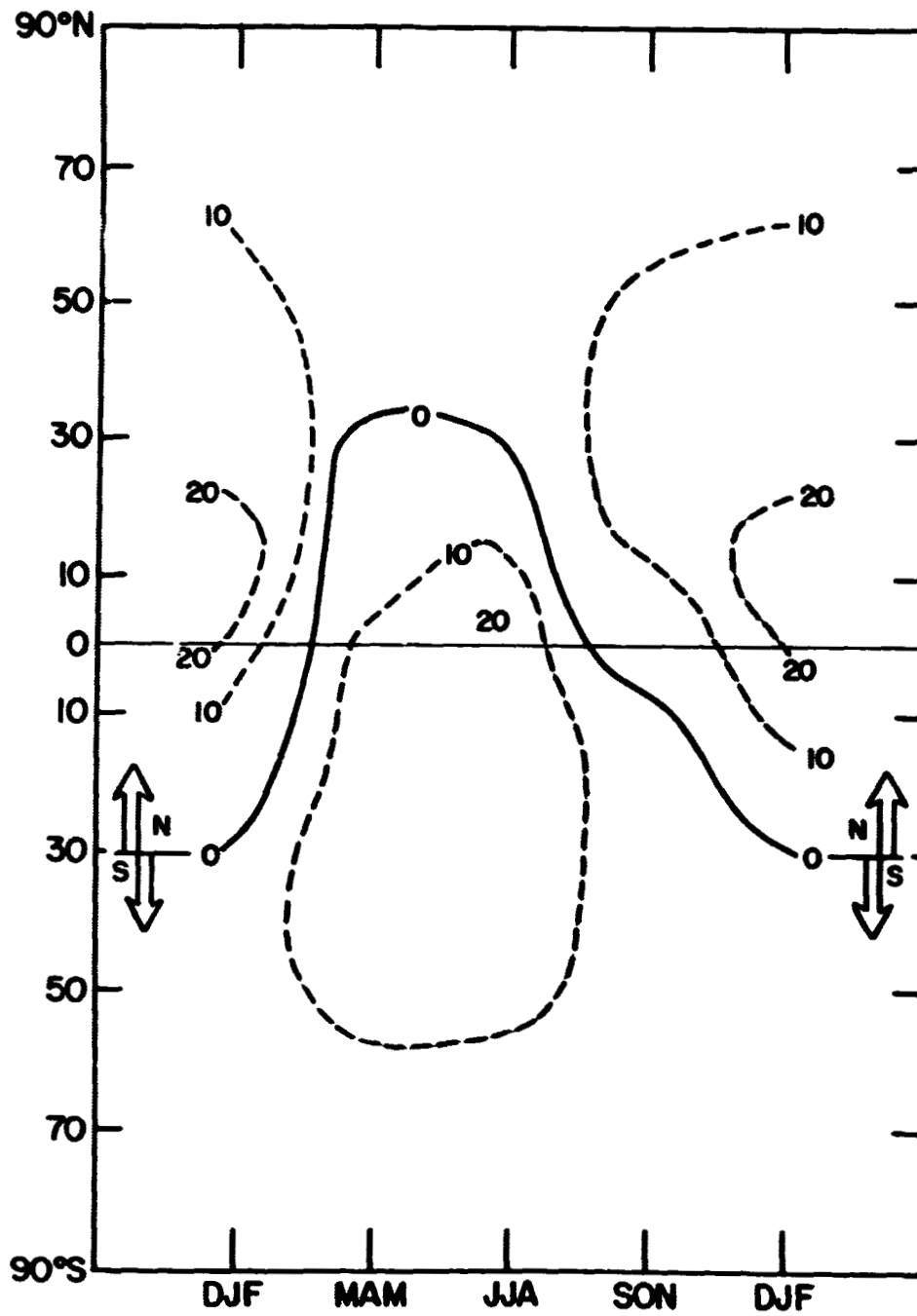


Fig. 26. Time-latitude section of the required transport of non-latent energy by the atmosphere and oceans. Units are 10^{19} cal·day⁻¹.

well as the total (sensible heat + potential energy) transport by the atmosphere, comparisons with other studies are difficult. Holopainen (1965) presented winter and summer transport values and he considered the contribution of both mean meridional circulations and eddies in the atmosphere. The shape of his curves agrees very well with those in Figure 25, but the magnitudes of his transport values averaged only 50 - 60% of those derived in this study. Some of this difference (perhaps as much as 40% according to Budyko and Kondratiev (1964)) can be attributed to oceanic transport and the remainder to computational uncertainties in both studies. He has shown that the double maxima in winter is due to peak transport values by the meridional cell near the equator and by eddies at mid-latitudes. This explains the mechanisms of transport for the available energy which is influenced by oceanic considerations noted previously.

Poleward transports of sensible heat by atmospheric eddies north of 20° N have been computed by Haines and Winston (1963). Similar seasonal transports were derived by Krueger et al. (1965) in order to infer the conversion between zonal and eddy available potential energy. Both of these studies show seasonal variations over the northern hemisphere in agreement with Figures 25 and 26.

The results most comparable with those of the present study are from Rasool and Prabhakara (1966), since we used their climatological data. We find, however, large differences ($> 10^{20}$ cal/day) in the required transport, especially during SON and DJF. Their SON values are much closer to the transports computed for the preceding six months, whereas in Figure 25 the SON and DJF curves are more similar. Such large differences result primarily from the different radiation budget data of the two studies and emphasize the importance of these data on the derived transports. An additional comparison is made in the next section.

5.3 The Mean Annual Case

A larger amount of climatological data that can be used to estimate energy budget terms is available for the mean annual case. In particular, Budyko (1963) has determined the mean annual geographical variation of evaporation, heat equivalent of precipitation, and oceanic energy divergence. Using these maps and the net radiation data of Figure 17, we derived the required net energy divergence by the atmosphere (ΔC) from Eq. (7). For this mean annual case, all storage terms are neglected. Figure 27 shows the results; the geographical distribution of regions of net sensible heat and potential energy export (D) and import (C).

The major features of this map agree well with the computations of Budyko who used empirical expressions to compute the net radiation budget of the

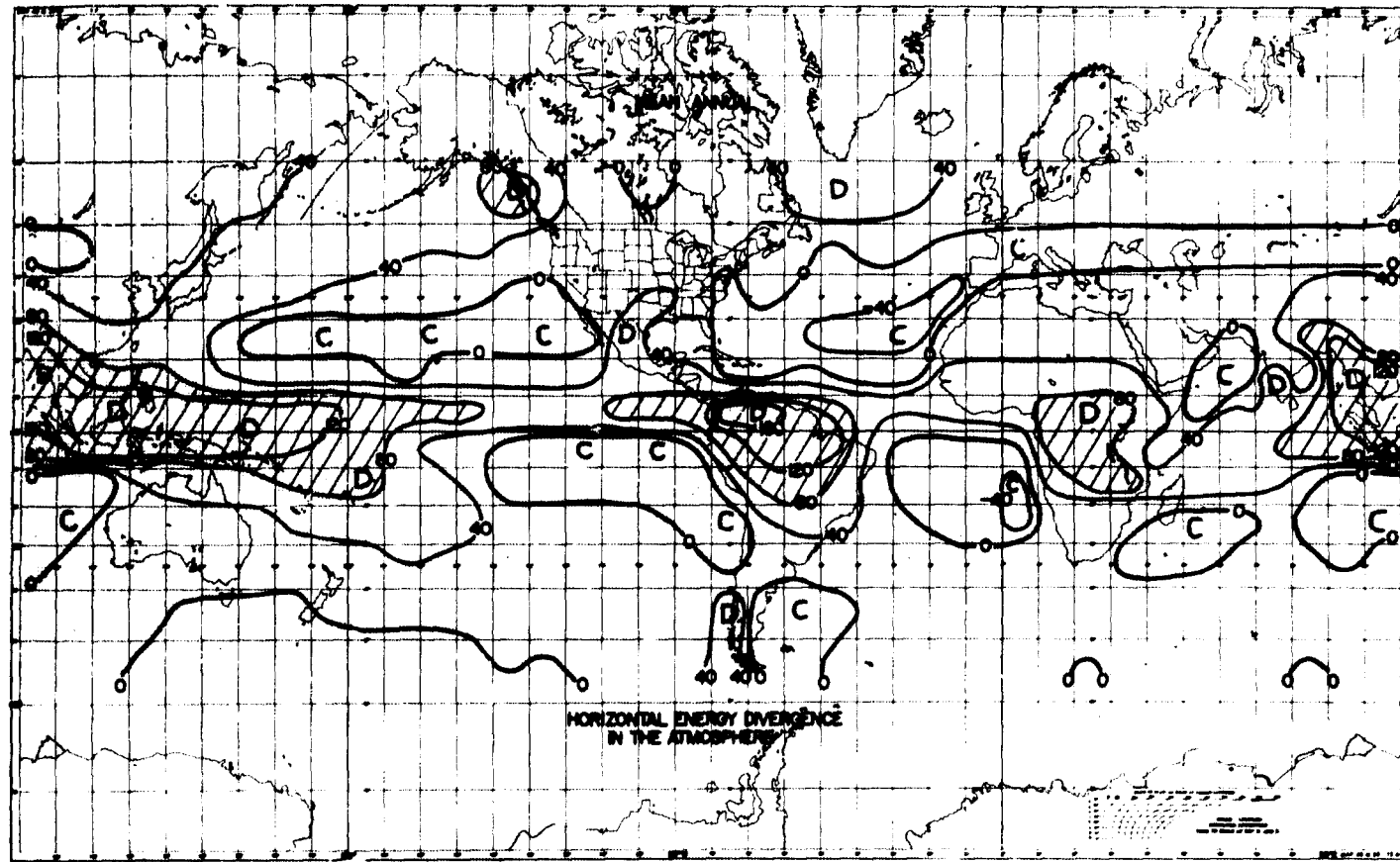


Fig. 27. Geographical distribution of required divergence of non-latent energy by the atmosphere for the mean annual case. Units are $\text{kcal} \cdot \text{cm}^{-2} \cdot \text{yr}^{-1}$ and the major energy exporting regions are shaded.

earth-atmosphere system. In general, the absolute values of energy divergence are higher, by 10 to 20 $\text{kcal} \cdot \text{cm}^{-2} \cdot \text{yr}^{-1}$ than Budyko's, especially at lower latitudes.

The regions of greatest energy export by the atmosphere are over Colombia ($160 \text{ kcal} \cdot \text{cm}^{-2} \cdot \text{yr}^{-1}$), Southeast Asia and northeast of New Guinea (> 120) and equatorial Africa (> 80). Inspection of the radiation budget maps shows that each of these regions have high values of net radiation ($> 60 \text{ kcal} \cdot \text{cm}^{-2} \cdot \text{yr}^{-1}$). Over Colombia, this results primarily from a low albedo and the other regions have moderate albedos together with low values of outgoing longwave radiation. Each of the areas also receive more than $100 \text{ kcal} \cdot \text{cm}^{-2} \cdot \text{yr}^{-1}$ from the release of latent heat. The maximum near Indonesia and Southeast Asia is decreased by 10 or 15% because of ocean energy transport from that region. Divergence minima near the equator are found over the Arabian Sea and the subtropical oceans of both hemispheres. Even though these regions have a net gain of energy across their upper boundaries, the excess of evaporation over precipitation during a year requires that the atmosphere imports energy. A notable exception is in the southwest Pacific where the cloudy band noted on the radiation maps releases enough latent heat to become a net energy source region.

At higher latitudes the continental regions of the United States, Central Asia, North Africa and Australia are very close to net energy balance in that the required mean annual atmospheric energy transports are small. Under such conditions, small changes in either the radiation or water budgets could influence the required atmospheric energy divergence.

The effects of precipitation maxima near the coasts of British Columbia and Chile are evident in the divergence centers found at these locations. Indeed the entire map of atmospheric energy export and import closely resembles the geographical distribution of precipitation (Budyko's). These results thus reaffirm the current opinion that latent heat processes must be incorporated into any model designed to simulate atmospheric conditions.

The required net energy transport by the atmosphere (sensible heat plus potential energy) and the oceans across latitudinal zones was also derived for the mean annual case. In Figure 28, three curves of $(\Delta C + \Delta F)$ are shown. The solid line and the unconnected points show the required transport that results when the radiation data of the present study are combined with estimates of the other terms in Eq. (7) derived from the data of Sellers (1966) and Rasool and Prabhakara (1965), respectively. For this annual case, the differences between the two curves result primarily from differences in the evaporation and precipitation estimates by the two studies. The relatively good agreement between the two curves occurs partly because each study used data presented by Budyko. The third (dashed) curve in Figure 28 shows the transports computed by Rasool and Prabhakara (1966) using some TIROS VII radiation data and the

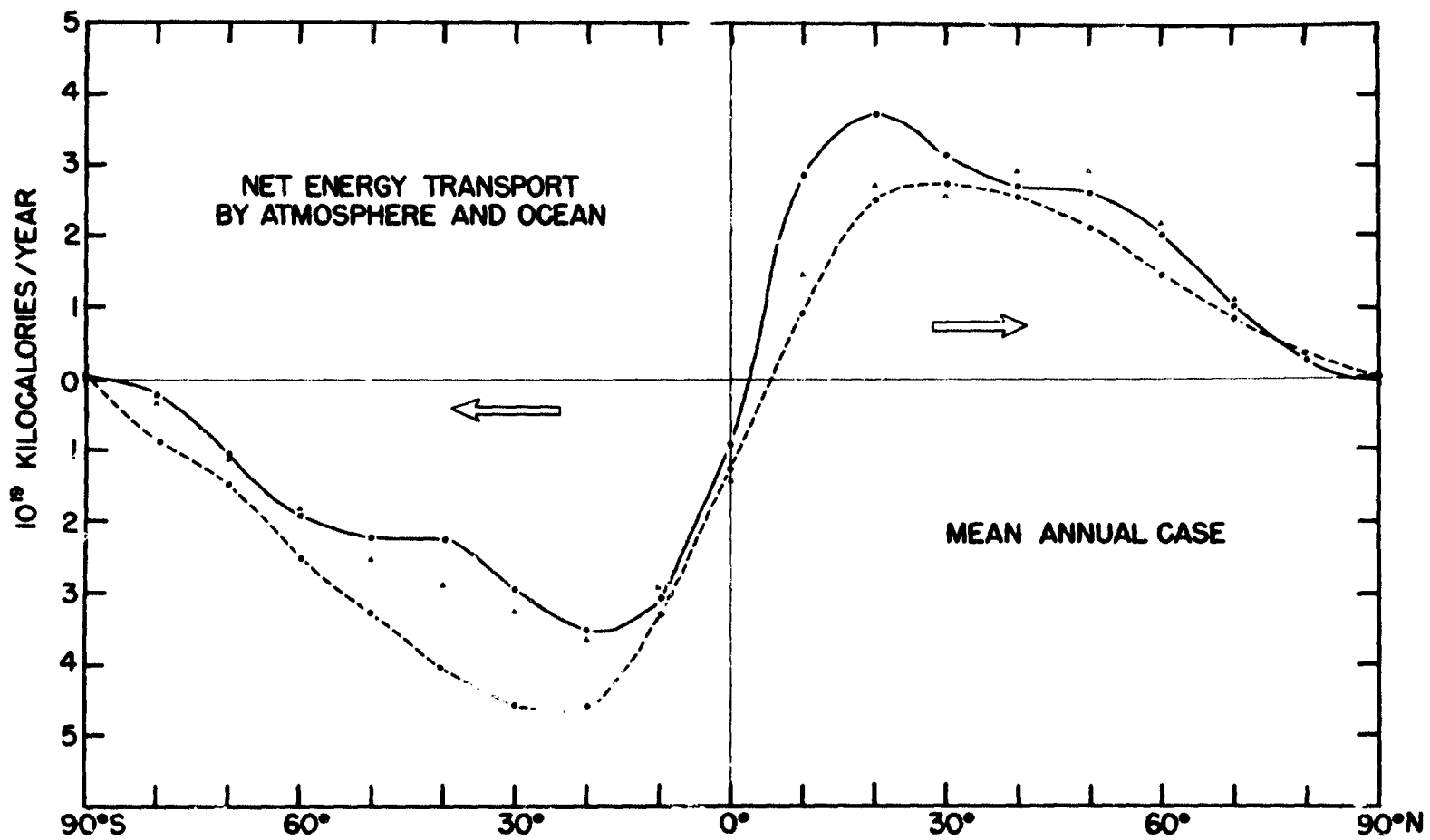


Fig. 28. Poleward transport of non-latent energy derived from the radiation data of the present study and the energy budget values of Sellers (solid line) and Rasool and Prabhakara (unconnected points). Dashed line is from Rasool and Prabhakara.

same climatological values used in our unconnected curve. Comparison of these two curves shows that the results of the present study require higher transport by the atmosphere and oceans in the northern hemisphere and lower values in the south than were derived by Rasool and Prabhakara. Some of this departure is due to differences in the radiation budget data and the remainder can be attributed to the lack of TIROS VII data poleward of sixty degrees.

These curves illustrate the best estimates at this time of the required energy transport derived from the energy budget method. All of them show that a southward transport of non-latent energy (about 10^{19} kcal · yr⁻¹) across the equator is required. Both curves derived from the radiation data of this study show that the net transport is nearly the same in each hemisphere and has a mean annual value of about 2.2×10^{19} kcal · yr⁻¹ (~ 23 watts · m⁻²). A region of zero net flux near 5°N marks the mean position of the tropical convergence zone.

The partitioning of this transport between ocean and atmosphere and the latent heat contribution is shown in Figure 29. In this illustration, each of the terms in Eq. (6) are displayed except that all storage terms are assumed to be zero for this mean annual case. The required transport (RT) derived only from the net radiation data (RNEA) is also shown. It represents the sum of the other transport terms which sometimes have opposite signs (i.e., southward transport of latent heat at 10°N versus northward transport by the other terms). House (1965) has summarized earlier estimates of RT, generally made for the northern hemisphere. The results of this study agree best with his data and those of Lettau (1954) in that the northern hemisphere region of maximum transport is $\sim 4 \times 10^{19}$ kcal · yr⁻¹ at 30°N. In the other hemisphere the radiation data show a flat maximum between 30 and 40 degrees of about the same magnitude. Because each hemisphere has the same radiation budget, the total net energy transport across the equator is zero.

The components of RT (ΔC_v , ΔF and ΔC) were obtained by using Sellers' (1966) values for the latent heat and oceanic transports and obtaining the atmosphere's contribution as a residual. Sellers describes the various sources of his data and provides a good summary of previous work. The ocean values account for 20 - 25% of the total transport in both hemispheres. Latent heat is transported both equatorward and poleward from the evaporation maxima centered near 25°N and 25°S. This moisture converges between 5 and 10 degrees north, the mean location of the ITC. More water vapor is moved from the southern hemisphere and the net northward flux across the equator ($\sim 4.5 \times 10^{16}$ gm · day⁻¹ or $\sim 10^{19}$ kcal · yr⁻¹) compensates the southward energy transport by the atmosphere (ΔC) and oceans (ΔF).

Although obtained as a residual, the mean annual meridional values of ΔC show the double maxima and other features also noted by Holopainen (1965) for the northern hemisphere. In general, the values of this study are about 15%

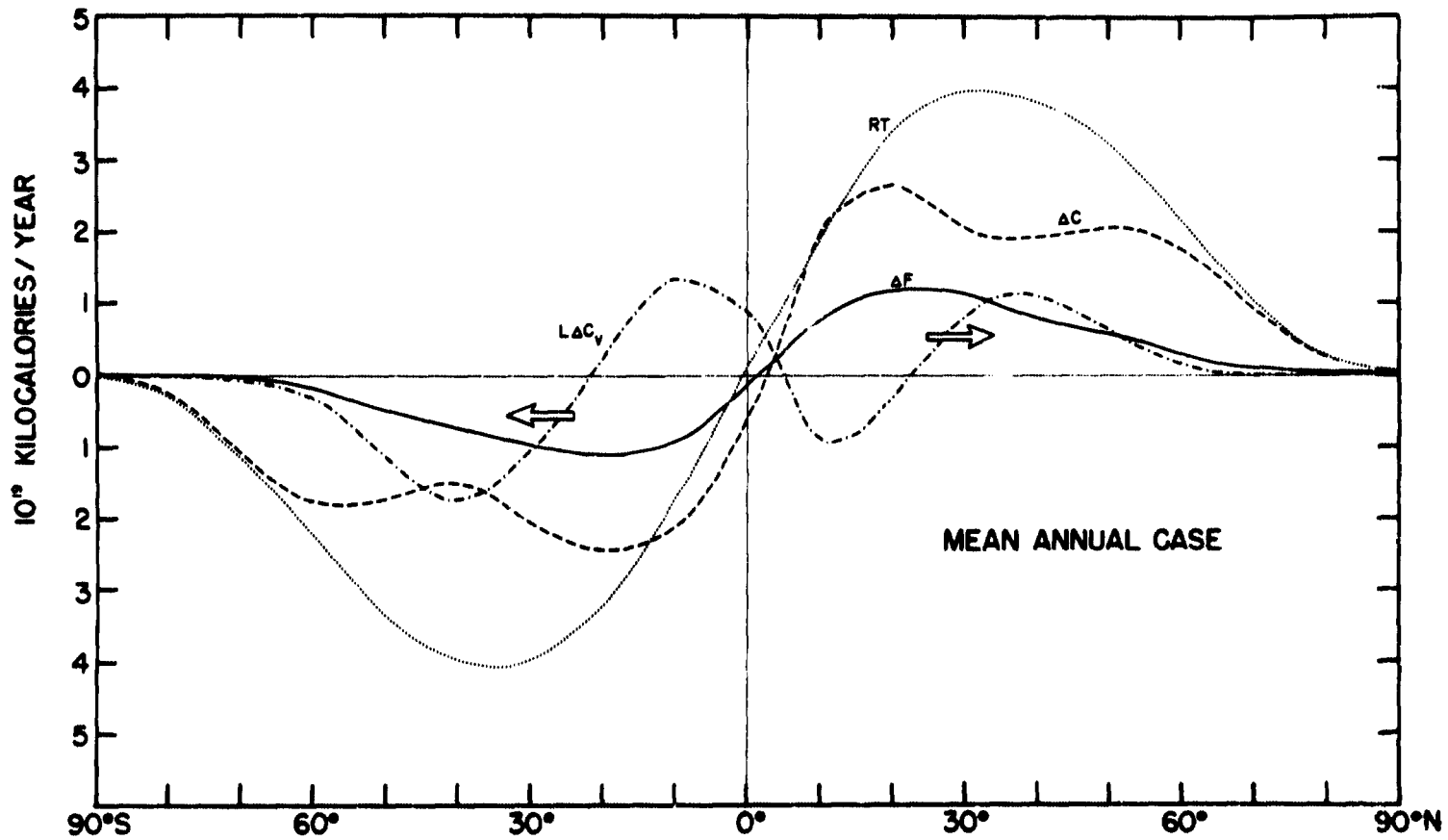


Fig. 29. The total poleward energy transport required by the radiation budget (RT) and the contributions by the oceans (ΔF), the atmosphere's transport of latent heat ($L\Delta C_v$) and sensible heat + potential energy (ΔC).

larger than his results, but in view of all the assumptions involved there is good agreement. Our southern hemisphere results show a pattern of non-latent atmospheric energy transport quite similar to that in the north.

Holopainen has also separated his data into contributions by various eddies and by the mean meridional cells. If we follow his suggestion and assign one-half of the total atmospheric energy transport to the eddies, a hemispheric average of this quantity over a year is $0.85 \times 10^{19} \text{ kcal} \cdot \text{yr}^{-1}$ ($4.4 \text{ watts} \cdot \text{m}^{-2}$). A recent evaluation of the mean annual atmospheric energy cycle by Dutton and Johnson (1967) gave $5.6 \text{ watts} \cdot \text{m}^{-2}$ as the amount of energy continually being generated and dissipated within the atmosphere. Since the transport of sensible heat by the eddies is the primary conversion mechanism between zonal and eddy available potential energy the results of this study provide an indirect check on the magnitude they derived for this portion of the energy cycle ($5.35 \text{ watts} \cdot \text{m}^{-2}$). The agreement with their computations, based in part on the energy dissipation rates of Kung (1966), is relatively good.

As a whole the energy budget data of this section compare well with various independent studies. They also point out the need for much more information on the other energy processes, now that radiation data are available on a global scale.

6. SUMMARY

The purpose of the present study has been to describe the radiation budget of the earth-atmosphere system as measured by the first generation meteorological satellites. Throughout the text some of the more noteworthy features of the observed budgets on various spatial and temporal scales have been discussed along with their meteorological implications. In the course of these discussions, the usefulness of these data for more detailed research, some of it non-meteorological, has been apparent.

Special attention should be given to the radiation budgets of the polar regions since the first extended series of measurements over them indicate that changing surface and atmospheric conditions may definitely override the normally dominant effect of incident solar radiation on the net budget. The mean seasonal and annual maps of albedo, longwave radiation and net radiation should be examined together with maps derived from specific seasons and months (to be published in atlas form).

Despite the large effect of seasonal changes in incident solar energy, time-latitude sections and budgets of selected zones have shown that the same seasons have different radiation budgets in different years. Atmospheric features that cause such changes and the response of the circulation pattern to them can be studied by using conventional meteorological data, computations of the

energetics of the atmosphere and numerical models. Indeed, one attribute of the radiation data is that they give us a vantage point midway between that which has happened and the future response of our system. From the radiation data, research efforts can proceed in either direction.

On a mean annual basis the measurements during 1963-65 show a small net gain of energy by the earth-atmosphere system of at least $0.01 \text{ cal} \cdot \text{cm}^{-2} \cdot \text{min}^{-1}$. Although this is a small percentage of the annual incident solar energy and may result from some undetected measuring problem, it may also represent part of a regular fluctuation in the energy exchange between our system and space. The addition of this energy to the mass of the atmosphere would raise the mean temperature $15^\circ\text{C}/\text{yr}$; to a 100 meter layer of the oceans, nearly $1^\circ\text{C}/\text{yr}$; and, as suggested by Rossby (1959), a 1000 meter layer of deep ocean water would be warmed at a rate of less than $0.1^\circ\text{C}/\text{yr}$.

Some of the results of this study may aid the development of numerical models that are designed to simulate atmospheric conditions. In particular, the relative distribution and absolute magnitudes of the radiation budget parameters can serve as a control for the models techniques of computing radiant energy transfer and their mean distributions of atmospheric variables that determine the radiation budget. The required poleward energy transports computed by the energy budget method in this study can be compared with those derived from the plentiful supply of data within the models. Because the mean annual location of maximum regions of required atmospheric energy divergence corresponds very well with the distribution of latent heat release, the need to include this process in the models is re-emphasized. These same areas also have a net energy gain by radiation at the upper boundary that is generally half as large as the latent heat term. Thus, the longitudinal variation of the radiation budget between 30 degrees north and south must also be considered in numerical models.

New energy budget results derived from the radiation values and climatological data compare favorably with independent studies. However, the need for more extensive and accurate information about the other energy budget parameters is very evident now that satellite measurements of the radiation budget are available on a global scale. Some information about the energy transport from the tropical regions can be obtained from geosynchronous satellite observations. Thus, the major energy exporting areas noted in this study can be examined in detail with the high spatial resolution and time sampling provided by these new satellite observations.

Even though the radiation measurements of this study agree with independent observations from balloons and some early results from the NIMBUS satellites, a considerable effort was devoted to an error analysis. The value of at least a passive means of inflight calibration of the radiation sensors cannot be overemphasized. The low resolution sensors that provided the bulk of the data for this study had this capability, but other problems remain. Some of

these can be remedied by improved technology, while others require some scientific study. All radiation budget experiments require precise knowledge of the magnitude of the solar constant and another problem is lack of information about the diurnal variation of albedo and longwave radiation. As in this study, some measurements of the solar constant can be obtained from the radiation sensors and special equipment flown on satellites may provide better data also. The diurnal problem will not be resolved if our operational satellites are always placed into similar sun-synchronous orbits, and other sensors on geosynchronous satellites may be required. Since the solar radiation terms often dominate the total budget, the current emphasis on studies of the anisotropic nature of reflected radiation should be continued.

Estimates of the accuracy of any radiation budget measurements are essential in order to compare the observations with those obtained from different sensors. Like good wine, the value of these data should improve with age, and when they have been joined by the results from the second generation satellites, we shall have just begun to properly examine the energy exchange between earth and space.

REFERENCES

- Astling, E.G., and L. H. Horn, 1964: An Analysis of Diurnal Variations in TIROS II Radiation Data. Annual Report, Grant WBG-10, Department of Meteorology, The University of Wisconsin.
- Bandeem, W.R., M. Halev, and I. Strange, 1965: A radiation climatology in the visible and infrared from the TIROS meteorological satellites, NASA TN D-2534.
- Bartman, F. L., 1967: The reflectance and scattering of solar radiation by the earth, Technical Report 05863-11-T, College of Engineering, University of Michigan.
- Bignell, K. J., 1961: Heat balance measurements from an earth satellite—An analysis of some possibilities, Quart. J. Roy. Meteor. Soc., Vol. 87, 231-244.
- Budyko, M. I. (ed.), 1963: Atlas of the heat balance of the globe (in Russian), Moscow.
- Budyko, M. I. and K. Y. Kondratiev, 1964: The heat balance of the earth, Research in Geophysics, Vol. 2: Solid Earth and Interface Phenomena, M.I.T. Press, 529-554.

- Drummond, A. J., J. R. Hickey and W. I. Scholes, 1967: Multichannel radiometer measurement of solar irradiance, J. Spacecraft and Rockets, Vol. 4, No. 9, 1200-1206.
- Dutton, J. A. and D. R. Johnson, 1967: The theory of available potential energy and a variational approach to atmospheric energetics, Advances in Geophysics, Vol. 12, Academic Press, New York, 333-436.
- Godson, W. L., 1958: Meteorological applications of earth satellites, Roy. Astron. Soc. of Canada, Vol. 52, No. 2, 49-56.
- Haines, D. A. and J. S. Winston, 1963: Monthly mean values and spatial distribution of meridional transport of sensible heat, Mon. Wea. Rev., Vol. 91, No. 7, 319-328.
- Holopainen, E. O., 1965: On the role of mean meridional circulations in the energy balance of the atmosphere, TELLUS, XVII, 3, 285-294.
- House, F. B., 1965: The radiation balance of the earth from a satellite, Ph.D. thesis, Department of Meteorology, University of Wisconsin.
- Johnson, F. S., 1954: The solar constant, J. Meteor., Vol. 11, No. 1, 431-439.
- Kornfield, J., A. F. Hasler, K. J. Hanson and V. E. Suomi, 1967: Photographic cloud climatology from ESSA III and V computer produced mosaics, Bull. Amer. Met. Soc., Vol. 48, No. 12.
- Krueger, A. F., J. S. Winston and D. A. Haines, 1965: Computations of atmospheric energy and its transformation for the northern hemisphere for a recent five-year period, Mon. Wea. Rev., Vol. 93, No. 4, 227-238.
- Kuhn, P. M. and S. K. Cox, 1967: personal communication.
- Kung, E. C., 1966: Large-scale balance of kinetic energy in the atmosphere, Mon. Wea. Rev., Vol. 94, No. 11, 627-640.
- Lettau, H. H., 1954: A study of the mass, momentum, and energy budget of the atmosphere. Archiv fur Meteorologie, Geophysik, und Bioklimatologie, Series A, Band 7, 133-157.
- London, J., 1957: A study of the atmospheric heat balance, Final Report, Contract AF 19(122)-165, Research Division, College of Engineering, New York University.
- NASA Staff Members, 1964: TIROS VII Radiation Data Catalog and Users' Manual, National Aeronautics and Space Administration, Washington.

- Nicolet, M., 1951: Sur la de'termination du flux e'nerge'tique du rayonnement extraterrestre du soleil, Archiv fur Meteorologie, Geophysik, und Bioklimatologie, Series A, Band 3, 209-216.
- Pasternak, Musa, 1967: An atlas of total outgoing long-wave radiation and of short-wave reflectances from NIMBUS II observations, Document X-622-67-500, NASA Goddard Space Flight Center.
- Rados, S. M., 1967: The evolution of the TIROS meteorological satellite operational system, Bull. Amer. Met. Soc., Vol. 48, No. 5, 326-337.
- Raschke, E. F., Möller and W. R. Bandeen, 1967: The radiation balance of the earth-atmosphere system over both polar regions obtained from radiation measurements of the NIMBUS II meteorological satellite, Document X-622-67-460, NASA Goddard Space Flight Center.
- Raschke, E. and Musa Pasternak, 1967: The global radiation balance of the earth-atmosphere system obtained from radiation data of the meteorological satellite NIMBUS II, Document X-622-67-383, NASA Goddard Space Flight Center.
- Rasool, S. I., 1964: Global distribution of the net energy balance of the atmosphere from TIROS radiation data, Science, Vol. 143, No. 3606, 567-569.
- Rasool, S. I., and C. Prabhakara, 1966: Heat budget of the southern hemisphere, Problems in Atmospheric Circulations, Spartan Books, Washington, D.C., 76-92.
- Rossby, C.-G., in The Atmosphere and the Sea in Motion (Bolin, ed.), 1959: Rockefeller Institute Press, New York, 9-50.
- Ruff, I., R. Koffler, S. Fritz, J. S. Winston, and P. K. Rao, 1967: Angular distribution of solar radiation reflected from clouds as determined from TIROS IV radiometer measurements, ESSA Technical Report NESC-38, Washington, D.C.
- Sellers, W. D., 1965: Physical Climatology, The University of Chicago Press, Chicago and London.
- Solomonson, V., 1966: Anisotropy of reflected solar radiation from various surfaces as measured with an aircraft-mounted radiometer, Research Report, Contract NASr-147, Colorado State University.
- Sparkman, Barbara B., 1964: Experimental analysis of the TIROS hemispheric sensor, M.S. thesis, Department of Meteorology, The University of Wisconsin.

- Starr, V. P., 1951: Applications of energy principles to the general circulation, Compendium of Meteorology, American Meteorological Society, Boston, 568-574.
- Suomi, V. E., 1958: The radiation balance of the earth from a satellite, Annals of the IGY, Vol. I, 331-340.
- Suomi, V. E., K. J. Hanson and T. H. Vonder Haar, 1967: The theoretical basis for low-resolution radiometer measurements from a satellite, Annual Report, Grant WBG-27, Department of Meteorology, University of Wisconsin, 79-100.
- Vonder Haar, T. H. and K. J. Hanson, 1968: A note on the diurnal variation of planetary albedo and outgoing longwave radiation, unpublished.
- Widger, W. K., 1967: Tabulations of some of the most frequently required information on individual TIROS satellites, Bull. Amer. Met. Soc., Vol. 48, No. 5, 339-346.
- Winston, J. S., 1967: Planetary-scale characteristics of monthly mean longwave radiation and albedo and some year-to-year variations, Mon. Wea. Rev., Vol. 95, No. 5, 235-256.
- Winston, J. S. and V. R. Taylor, 1967: Atlas of world maps of longwave radiation and albedo for seasons and months based on measurements from TIROS IV and TIROS VII, ESSA Technical Report NESC 43, Washington, D. C.

APPENDIX: SATELLITE OBSERVATIONS OF THE SOLAR CONSTANT

1. Purpose

Recent high-altitude aircraft observations by Drummond et al. (1967) have provided another estimate of the magnitude of the solar constant. Their value of 1.95 ly/min may have an accuracy of $\pm 2\%$ (± 0.04 ly/min) the same error limit quoted by Johnson (1954) for his value of 2.00 ly/min.

For many studies this uncertainty may be trivial, but when highly accurate albedo and longwave radiation observations are used together with an estimate of the solar constant in a study of the earth's radiation budget, the chosen value significantly affects net radiation magnitudes and the estimate absolute error of these data. (See 3.22.) In order to aid the choice of a proper value

and to estimate its accuracy a third measurement of the solar constant was derived from the observations of heat budget sensors carried on a satellite.

2. Method

Black and white flat sensors were used and the reduction of their measurements into irradiance and albedo values has been completely described by Suomi et al. (1967). Twice during each orbit these sensors pass across the terminator. Because of the satellite's altitude the sensors are exposed to direct solar radiation while still located above a dark earth. On these occasions only longwave radiation from the earth and direct solar radiation from the sun are incident on these sensors. In this study we will examine a long-time series of such measurements, remove the contribution due to IR radiation and thus obtain the solar constant as seen by the sensors (the direct solar radiation). This measurement can be used to obtain the magnitude of the solar constant if the effects of sun-sensor geometry, sensor absorptivity and earth-sun distance are removed.

3. Measured Values

Suomi et al. (1967) define two quantities that are measured each time the sensors pass from night to day. For flat spinning sensors they are:

$$D^* = (E_B - E_{W_t}) = 2I_0 r' \cos \gamma (\alpha_B' - \alpha_{W_t}')$$

$$W^* = (E_{W_t} - E_{W_N}) = 2I_0 r' \cos \gamma \alpha_{W_t}'$$

where the E values are proportional to energy loads on the black or white sensors at location t, the day side of the terminator, or N, the night side of the terminator. I_0 is the solar constant, r' the factor to account for variations in earth-sun distance, γ the angle between the solar radiation and a normal to the sensors and α' the ratio of a sensor's absorptivities for shortwave radiation. With the aid of the illustration in Figure A1, it is seen that the solar constant as seen by the sensor set is given by $(D^* + W^*) = E_{B_T} - E_{W_N}$ (i.e., the total longwave and shortwave radiation less the longwave component). In practice, both D^* and W^* were computed at point t about 2000 times and the variation of their sum with time is also shown in Figure A1.

Now

$$(D^* + W^*) = 2I_0 r' \cos \gamma \alpha_B'$$

and thus the white sensor's absorptivity ratio is eliminated from consideration. The quantity $(D^* + W^*)$ varies with time primarily because γ changes. Fortunately the effects of γ and r' are known exactly and can be removed. Thus

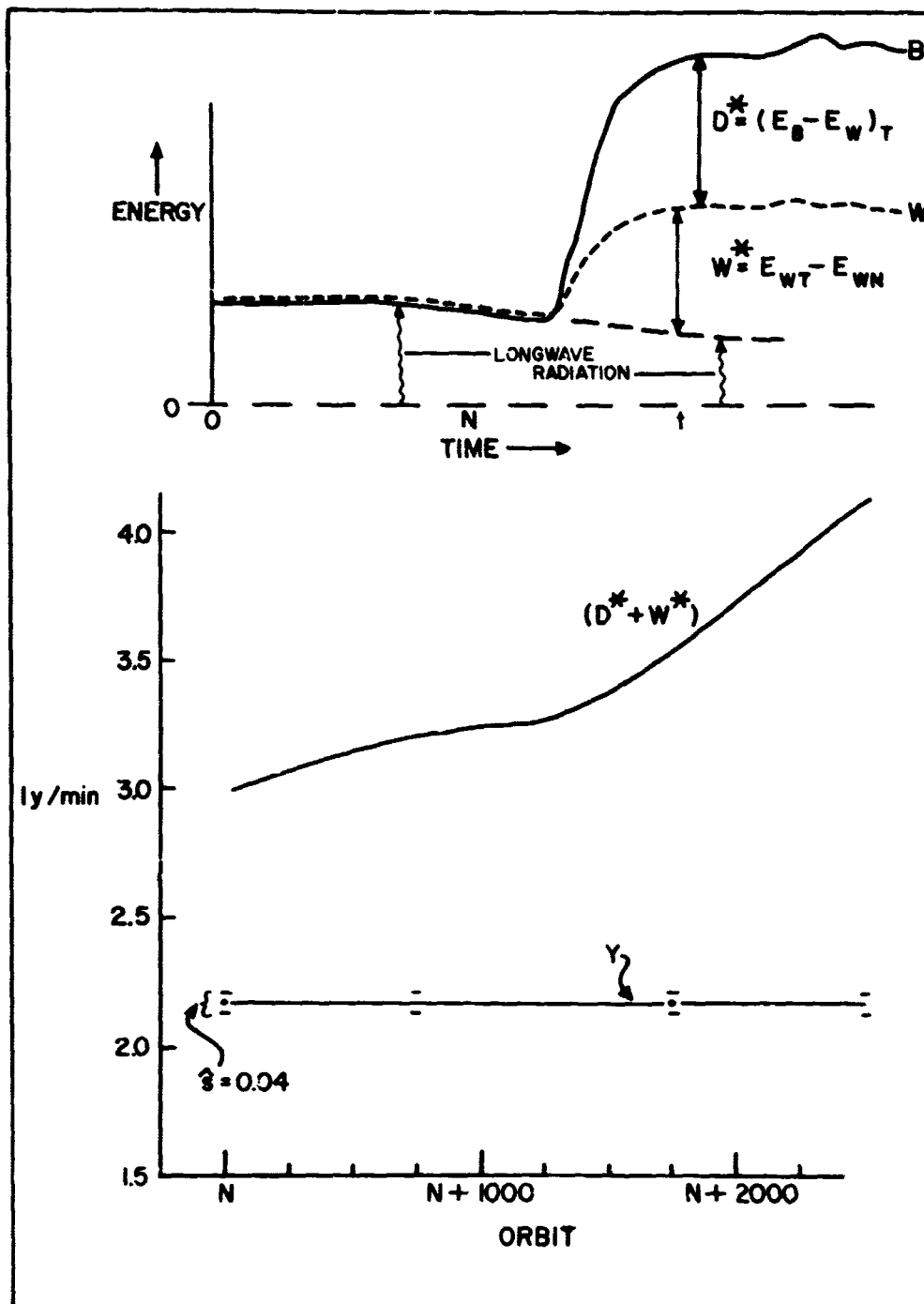


Fig. A1. Example of parameters computed at each terminator crossing (upper portion) and the variation with time of $(D^* + W^*)$ and $Y = (D^* + W^*)/2r' \cos \gamma$.

the variation of $I_0\alpha_B' = (D^* + W^*)/2r' \cos \gamma$ is also shown in Figure A1. The best fit of all the data points is a line with $Y = I_0\alpha_B' = 2.17$ ly/min. The standard error is 0.04 ly/min (1.5%) and since D^* and W^* are measured values, the $I_0\alpha_B'$ data also have a possible bias error of $\pm .02$ ly/min.

The invariance of $I_0\alpha_B'$ over a long time period is encouraging; it implies that:

- a) the absorptivities of the black sensor did not change with time (this agrees with data from similar sensors flown on other satellites);
- b) the absorptivities did not change significantly as the angle of incident solar radiation varied;
- c) the solar constant is indeed constant.

There is, of course, the possibility that any two or all of these three statements are false and that changes did occur in compensating directions, but this is improbable.

4. Necessary Laboratory Data

In order to derive an estimate of the solar constant (I_0), we must use the best value of α_B' determined before launch. Since the value apparently did not change in orbit, this laboratory estimate would be valid, barring a sudden undetected change just after launch. As mentioned

$$\alpha_B' = ((\alpha_{SW}/\alpha_{LW}))_B$$

and the two components were obtained separately for experimental reasons. The mean shortwave absorptivity was obtained by weighting precision spectrometer measurements made at Lion Research Corp. by the shape of the extra-terrestrial solar irradiance curve given by Johnson (1954); refer to House (1967).* The value for $\alpha_{B_{SW}}$ was 0.97 ± 0.01 . Absorptivity of the black sensor to infrared radiation typical of that emitted by the earth and atmosphere from the regions where the measurements were made was determined by Hanson (1966).* He used hohlraum data for the black paint provided by Shoffer (1962)* and obtained $\alpha_{B_{LW}} = 0.90$. His calculations agree to within $\pm .02$ with independent estimates by Sparkman (1964) and the author using a second set of hohlraum data for the same paint. Thus the best estimates of $\alpha_B' = 1.075$ and a reasonable bias error is $\pm .02$.

* Unpublished report

5. Results and Error Analysis

Solving for $I_0 = (I_0 \alpha_B') / \alpha_B'$ we obtain a solar constant magnitude of 2.01 ly/min from our satellite observations. A simple estimate of the possible bias error can be made if we let

$$\begin{aligned}(I_0 \alpha_B') &= Y = 2.17 \text{ ly/min} \\ dY &= \pm 0.02 \text{ ly/min} \\ \alpha_B' &= X = 1.075 \\ dX &= \pm 0.02\end{aligned}$$

and

$$dI_0 = \frac{y dx - x dy}{y^2} = \pm 0.05 \text{ ly/min}$$

for the worst absolute error and $dI_0 = \pm .017$ ly/min for the best case (a range in percent error from 2.5% to less than 1%). A small part of the possible bias error in the measurement results from slight changes of adsorbitivity at different incidence angles. The best estimate of both the magnitude and direction of this error yields a solar constant of $1.99 \pm 0.03 \text{ cal} \cdot \text{cm}^{-2} \cdot \text{min}^{-1}$.

The goal of any solar constant measurement should be at least 1% accuracy since the best estimates of the variation of this parameter are within that range. With the data of the present study, checks on the absolute magnitude of α_B' and its variation with angle will be made in order to remove some small uncertainties. Sensors now being carried on the ESSA satellites can be used to obtain more accurate measurements of $Y = \alpha_B' I_0$ since they are better isolated from the spacecraft itself. Although this improved design may pose some problems regarding the geometry of the sensing surfaces, ESSA data together with careful pre-launch study of α_B' should provide more accurate measurements of the solar constant. The addition of a relative calibration mechanism on the satellite would eliminate any uncertainty arising from degradation occurring between pre-launch tests and the start of normal operations at altitude.

N69-33580

THE REFLECTION OF SUNLIGHT TO SPACE AND ABSORPTION BY THE EARTH
AND ATMOSPHERE OVER THE UNITED STATES DURING SPRING, 1962*

by

K. J. Hanson, T. H. Vonder Haar and V. E. Suomi

CONTENTS		Page
	List of Symbols	110
1.	INTRODUCTION	111
2.	METHOD OF CALCULATION	111
	a. Irradiance at Upper Boundary	112
	b. Outward Irradiance at the Upper Boundary	113
	c. Irradiance at the Ground	113
	d. Irradiance Reflected at the Ground	113
	e. Boundary Condition	115
3.	MEASUREMENTS	115
	a. Irradiance Values	115
	b. Optical Pathlength of Atmospheric Water Vapor	115
4.	GEOGRAPHICAL DISTRIBUTION	117
	a. Reflection and Absorption of Sunlight over the United States	117
	b. Solar Heating over the United States	120
5.	ABSORPTION OF SUNLIGHT IN THE ATMOSPHERE	120
6.	REFERENCES	122

* Published, Monthly Weather Review, June 1967, 95:6, pp. 354-352.

ABSTRACT

This study describes a method for determining the reflection of sunlight to space and absorption by the earth and atmosphere, using low-resolution radiometer data from earth satellites. The method has been used with TIROS IV data together with radiation measurements at the ground to determine the reflection and absorption of sunlight over the United States during the Spring of 1962.

The results indicate that for this region and time, 40 percent of the incident sunlight at the top of the atmosphere was reflected to space, 13 percent was absorbed by the atmosphere and clouds, and the remaining 47 percent was absorbed at the earth's surface. Atmospheric absorption of the sunlight varied from over 20 percent in the moist air in southeastern United States to less than 10 percent over much of the dry mountain west and northern plains.

Atmospheric absorption values determined from this study have been compared with earlier studies of absorption in a cloudless atmosphere. There is good agreement at low values of water vapor; however, the present study gives significantly higher absorption at high values of water vapor.

An empirical relationship is determined for fractional absorption of sunlight as a function of optical pathlength of water vapor, based on the present study.

$$q_a = 0.096 + 0.045(u^*)^{1/2} \text{Log}_e(u^*)$$

The fractional absorption of sunlight, q_a , is the fraction of the total amount incident at the top of the atmosphere. The optical pathlength, u^* , is given in cm.

$$u^* = u \cdot \sec(\zeta)$$

Here, u is total precipitable water in a vertical column, given in cm, and ζ is the solar zenith angle.

LIST OF SYMBOLS

<u>Symbol</u>	<u>Meaning</u>
<u>Roman Letters</u>	
A_s/A_f	ratio: albedo snowcovered ground to albedo snow-free ground
c_p	Specific heat of air at constant pressure
d	Direct distance from point p on ground to satellite at height h
g	Acceleration of gravity at earth's surface
h	Height of satellite
I_s	Solar constant
p	Point at earth's surface
q_a	Fraction of Q_0 absorbed in the atmosphere
q_e	Fraction of Q_0 absorbed at the ground
q_g	Fraction of Q_0 incident at the ground
q_r	Fraction of Q_0 reflected to space
Q_a	Radiation absorbed in the atmosphere
Q_g	Irradiance at the ground
Q_0	Irradiance at the top of the atmosphere
Q_r	Outward Irradiance at the top of the atmosphere
Q_s	Irradiance reflected at the ground
r	Earth-sun distance
r_m	Mean earth-sun distance
u	Total precipitable water in the atmosphere
u^*	Optical pathlength of atmospheric water vapor
WF_p	Weighting factor for radiance from point p to a spherical sensor at height h above the earth
w	Mixing ratio of water vapor
<u>Greek letters</u>	
α	Surface albedo
ζ	Solar zenith angle at the subsatellite point
ϕ	Zenith angle of satellite at height h , viewed from point p

1. INTRODUCTION

The albedo is defined as the ratio of reflected to incident radiation integrated over the solar spectrum from 0.2 to 4.0 microns. The albedo of the earth and atmosphere is an important component in the global heat budget, but, unfortunately, it is a difficult component to determine. Prior to 1957, there was no possibility of making direct measurements of this component on a global scale. In the ensuing nine years since satellite measurements have become available, there has been conflicting interpretation of them. One problem in determining the albedo of the earth and atmosphere is that cloudiness, which has a strong modulating influence on the albedo, varies widely over the planet both in time and space. This, of course, causes a sampling difficulty because measurements cannot be made everywhere, all the time. Another hindrance to determining the albedo is that the scattering properties of water droplets in clouds, together with the variable solar zenith angle over the spherical earth, further complicates the sampling.

Prior to the launching of earth satellites, the only "outside" approach to determining the amount of sunlight reflected from earth was to measure the "earth-light" reflected from the shadowed side of the moon (Danjon [3]; Dubois [4]). Computations of the planetary albedo have been made from those illumination measurements (Angstrom [1]). Another approach to estimating the earth's albedo was through a knowledge of cloud distribution over the earth and estimates of the reflectivity of various cloud types (Simpson [13]; Houghton [6]; London [11]).

Recently, Fritz *et al.* [5] have described a method of combining satellite and surface radiation measurements to determine the reflection and absorption of sunlight. In that study, the data from medium-resolution radiometers of TIROS III were used. This gives the albedo of relatively small areas (50 km radius) near surface radiation stations. In comparison to Fritz, the study reported in this paper is similar in that it combines simultaneous satellite and surface data to determine reflection and absorption terms. However, it differs in that low-resolution measurements are used. Thus, the resulting albedoes are representative of larger surface areas.

The low-resolution measurements have been described by Suomi [14] and House [8].

2. METHOD OF CALCULATION

From consideration of conservation of radiant energy, it is clear that sunlight reaching the top of the atmosphere is either reflected to space or is absorbed by the earth or atmosphere. To define these relationships for the present study, we have used a notation similar to that of Fritz.

As illustrated in Fig. 1, Q_o and Q_r are the values of solar irradiance incident and reflected from the top of the atmosphere. Likewise, Q_g and Q_s are values of solar irradiance incident and reflected from the earth's surface. These irradiance terms define the absorption in the atmosphere, Q_a , as

$$(1) \quad Q_a = (Q_o + Q_s) - (Q_r + Q_g)$$

Dividing Eq. (1) by Q_o and rearranging terms gives,

$$(2) \quad 1 = q_a + q_r + q_g(1 - \alpha)$$

where:

$q_a = Q_a/Q_o$, the fraction of incident sunlight absorbed in the atmosphere.

$q_r = Q_r/Q_o$, the fraction of incident sunlight reflected to space.

$q_g = Q_g/Q_o$, the transmission of the atmosphere.

$\alpha = Q_s/Q_g$, the surface albedo.

The right-hand term in Eq. (2) is the fractional absorption at the earth's surface and will be denoted as simply q_e . Then,

$$(3) \quad 1 = q_a + q_r + q_e$$

It is apparent from Eq. (3) that the sunlight incident at the top of the atmosphere is divided between two absorption terms: (1) the absorption in the atmosphere, q_a , and (2) the absorption at the earth's surface, q_e , and one reflection term: the reflection of sunlight to space, q_r , by the earth, atmosphere and clouds.

Clearly, the fractional terms are completely specified if the four irradiance values are known and are compatible in time and space. The following section defines the irradiance terms to assure this compatibility.

a. Irradiance at the Upper Boundary

The irradiance at the upper boundary of the atmosphere, Q_o , was calculated from

$$(4) \quad Q_o = I_s (r_m/r)^2 \cos \zeta$$

The solar constant, I_s , was taken as $2.0 \text{ cal/cm}^2 \text{ min}$, r_m and r are the mean and actual earth-sun distances, and ζ is the solar zenith angle at the sub-satellite point.

b. Outward Irradiance at the Upper Boundary

The outward irradiance at the upper boundary was obtained from TIROS IV low-resolution measurements of sunlight reflected to space by the earth, atmosphere and clouds. Although these TIROS sensors respond to sunlight reflected from a relatively large area below the spacecraft (radius of 2890 km),¹ the radiation reaching the sensor is strongly weighted in favor of a relatively small area around the subsatellite point. For example, about 50 percent of the irradiance comes from an area with radius of 734 km, centered at the subsatellite point.

c. Irradiance at the Ground

The irradiance at the ground, Q_g , was calculated from radiation measurements at many surface stations in the region viewed by the satellite. Data were weighted by a factor that was symmetrical about the subsatellite point and varied in the same manner as described in the preceding section for satellite measurements of outward irradiance. Identical geographical weighting is an important consideration of this study, because it is essential that irradiance determined for the upper and lower boundaries of the atmosphere represent identical areas. This is necessary because atmospheric absorption is only a small difference between large irradiance values. The appropriate weighting factor for radiation from a point p on the ground reaching a spherical sensor at height h above the ground has been derived by House [7], as

$$WF_p = (h/d)^2 \cos \phi \quad (5)$$

Here, d is the direct distance from p to the satellite, and ϕ is the zenith angle of the satellite, viewed from point p .

d. Irradiance Reflected at the Ground

The irradiance reflected at the ground, Q_s , was obtained as the product of irradiance at the ground and the surface albedo. Albedo values are representative for an area around the station with a radius of 280 km. The particular radius value was selected in order to include all of the area between surface stations. The values used were the "winter-minimum" albedoes (Fig. 2) for the United States as determined by Kung, *et al.* [10]. Since these are representative of snow-free conditions, it is necessary to correct them if snow exists at a particular time. Using observed daily snow depth, a best estimate of the surface albedo at each station, each day was calculated. The nomogram (Fig. 3) developed by Kung was used for translating snow depth to albedo.

¹ Distance from the subsatellite point to the earth's horizon, as viewed from the satellite.

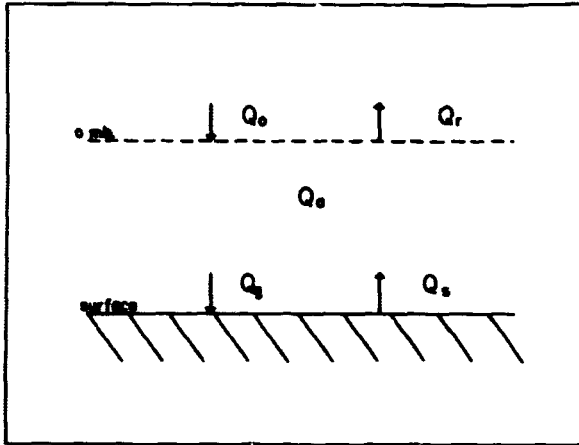


Fig. 1. Symbols for irradiance bounding the atmosphere and absorption of radiation in the atmosphere.

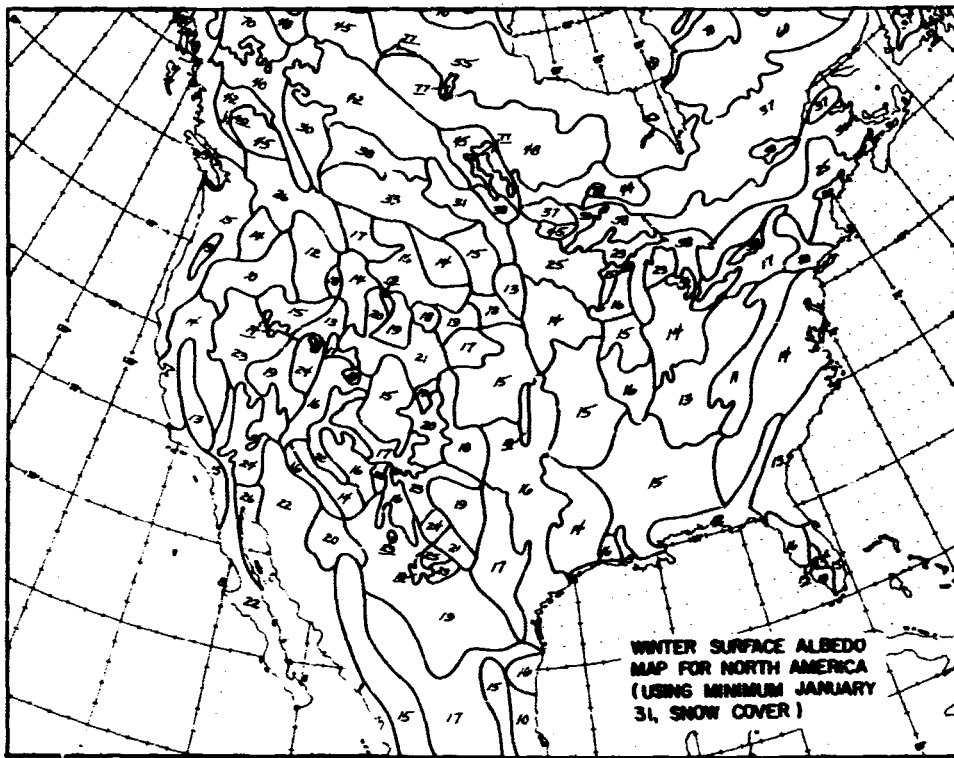


Fig. 2. Winter-minimum albedoes based on minimum snow cover (from Kung, et al. [10]). (Values are percentages)

e. Boundary Condition

A limitation of this study is that outside the surface-station network, it is no longer possible to determine an irradiance at the ground which is representative of the area seen by the satellite. As a result, measurements along the periphery of the network may be in error—particularly where a significant change in cloudiness or surface albedo occurs across the boundary. Inside the boundary, and over most of the continental United States, this is not a problem.

3. MEASUREMENTS

a. Irradiance Values

A total of 775 observations of outward irradiance, Q_r , were obtained by TIROS IV low-resolution radiometers over the United States from February 8 - June 3, 1962. For calculating the partitioning of sunlight, it was required that the other three irradiance terms correspond in time and space with the satellite observation. To do this, the irradiance at the ground was calculated from hourly radiation measurements at surface stations, weighted geographically as previously defined. Hourly surface observations were used for convenience, since the satellite data have no systematic time bias within one hour intervals. The two other irradiance terms were calculated as previously described.

Because of the precession of TIROS IV, daytime observations over the United States are not on a continuous basis, but are for intermittent periods. These periods are shown in Fig. 4. In addition to time bias, there is geographical bias in the sample. This is due to: (1) the orbit inclination of 48.3 degrees which has the effect of increasing the relative frequency of observations in the northern latitudes, and (2) the location of read-out in the eastern United States which has the effect of decreasing the number of observations in that region. Clearly, the data used in this study are biased in time and space. To surmount this problem we have equalized the bias in all variables being studied. Only then, it will be possible to obtain meaningful relationships between them.

b. Optical Pathlength of Atmospheric Water Vapor

Atmospheric water vapor is an effective absorber of sunlight and a variable constituent of the atmosphere. As a result, absorption by water vapor is significantly large, but not geographically uniform. In this paper, the absorption of sunlight as a function of precipitable water is examined in order to make an estimate of its nonuniformity.

A calculation of total precipitable water, u , was made to correspond with each satellite observation. The radiosonde observation closest to the sub-

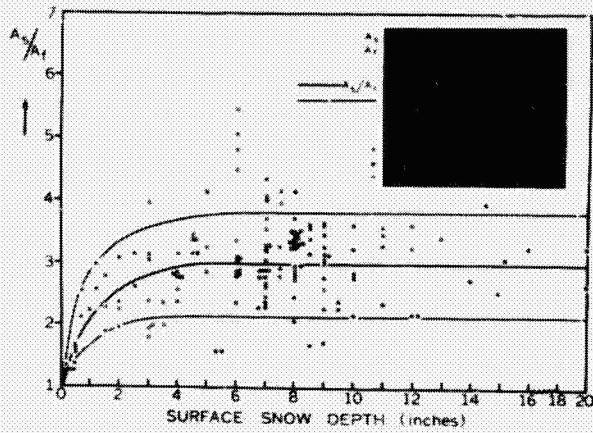


Fig. 3. A factor A_s/A_f for modifying the albedo of snow-free ground as a function of snow depth (from Kung [10]).

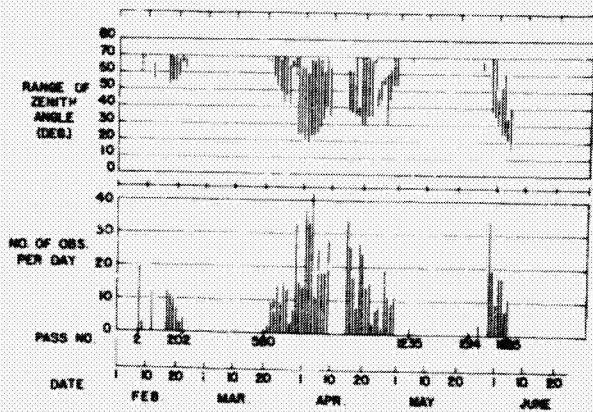


Fig. 4. The number of daytime observations from TIROS IV low resolution radiometers and associated solar zenith angles at times when the satellite was over the continental United States, February-June, 1962.

satellite point, in time and space, was used. The total precipitable water was computed as,

$$(6) \quad u = g^{-1} \int w \, dp$$

where g is the gravitational acceleration at the earth's surface, w is the mixing ratio of water vapor, and p is pressure. The integration was done from the surface to 300 mb.

Over most of the atmosphere, sunlight enters on a slant path rather than vertically. Then, if ζ is the zenith angle of the sun, the optical pathlength, u^* , for sunlight penetrating a clear atmosphere is given as

$$(7) \quad u^* = u \cdot \sec \zeta.$$

4. GEOGRAPHICAL DISTRIBUTION

a. Reflection and Absorption of Sunlight over the United States

The reflection and absorption data were calculated for the hours indicated on Fig. 4. For the period March through May, averages of reflection, absorption and total precipitable water data are shown in Figs. 5 and 6. Spatial smoothing was done by averaging observations within 330 km of fixed grid points over the United States. A 2 by 2 degree latitude-longitude grid was adopted for this purpose. In the southeastern United States where there are sampling limitations, a minimum number of 15 samples was required at a grid-point before the average was calculated. Over the remainder of the United States, the data have been shown up to the border, even though the boundary condition may influence the representativeness of the analysis.

Several relationships between the partitioning terms are significant in Figs. 5 and 6. For example, the patterns of atmospheric absorption and absorption at the ground show similar trends—particularly over the eastern two-thirds of the United States. This suggests that, in comparison to reflection, absorption in the atmosphere has a very dominant effect on the amount of sunlight reaching the ground. It is interesting that neither of these two patterns resemble that of reflection to space. An exception to this is over the Western United States where absorption at the ground appears to be inversely correlated with reflection to space.

A physical interpretation of these results suggests that in areas where the atmospheric water vapor tends to be uniform (e.g., in western U.S.), the variation in atmospheric absorption is correspondingly small. Under these conditions, the reflection term has a dominant effect on the amount of sunlight reaching the ground. On the other hand, in regions where atmospheric water vapor is nonuniform (e.g., in eastern U.S.), the variation in atmospheric absorption is increased, considerably. In fact, it appears to be increased to the extent that water vapor has the dominant effect on the amount of sunlight reaching the ground, rather than the modulating effect of clouds which would otherwise control it.

A striking feature of Figs. 5 and 6 is the similarity between the patterns of total precipitable water and atmospheric absorption—one that would be expected in view of the results of previous work (Gates [2]; Yamamoto [15]; Houghton [6]; and Kimball [9]), among others. The two patterns are remarkably similar over nearly all of the United States, except for the upper Great Lakes region where absorption values are low. This could result from somewhat greater cloudiness in that area. Another explanation could be that surface albedo estimates may not be representative of the surface area seen by the satellite, particularly the snow-covered country to the north. Consideration of a boundary condition of this type would tend to reduce the calculated absorption values for the

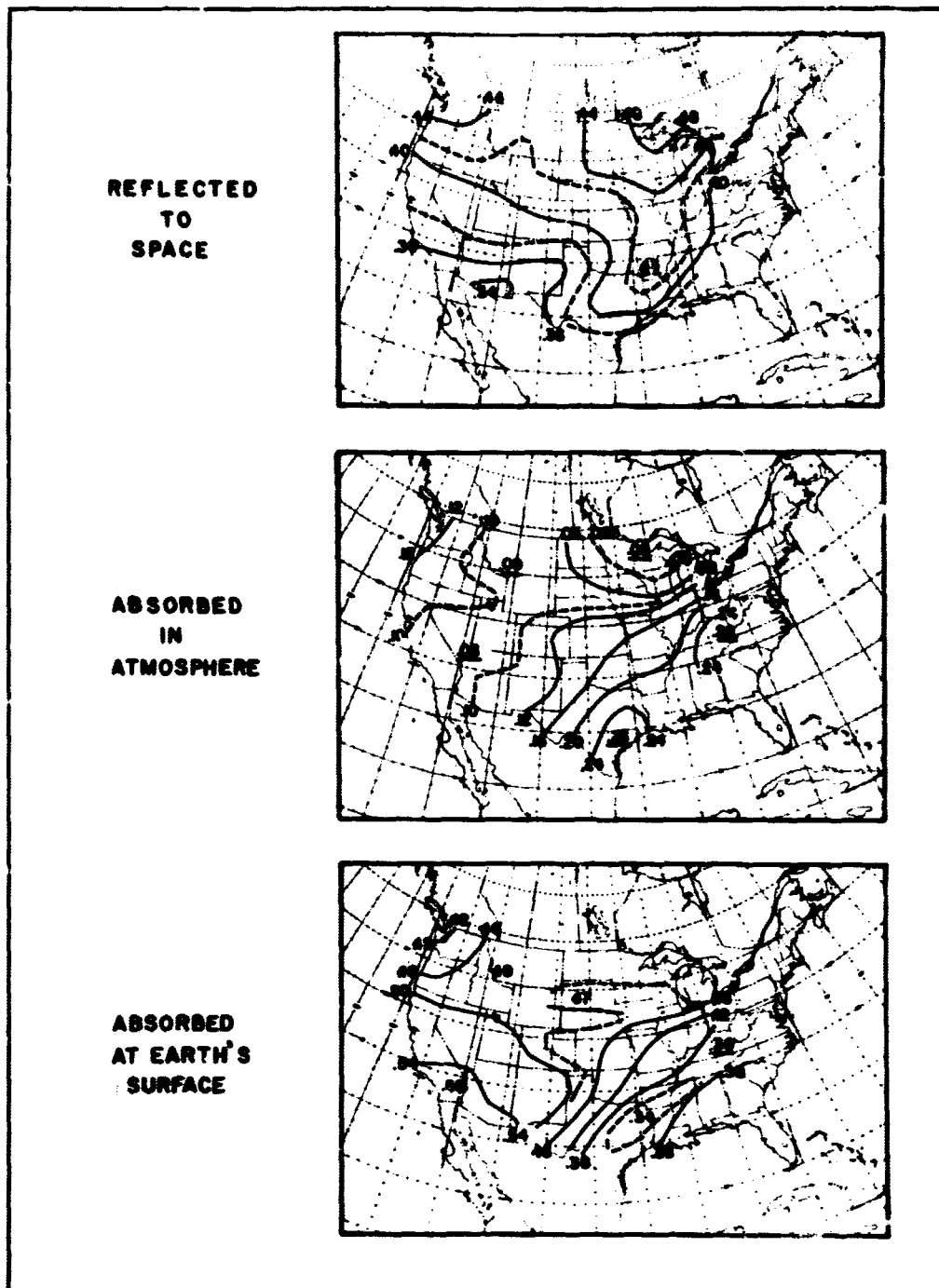


Fig. 5. The reflection and absorption of sunlight during the period March through May, 1962, based on TIROS IV low resolution radiometer and surface radiation data. (Values are fraction of incident sunlight at the top of the atmosphere.)

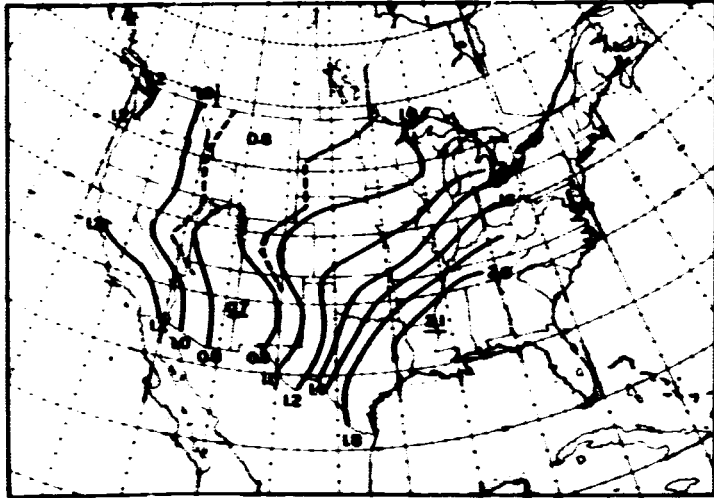


Fig. 6. Total precipitable water (cm) in the atmosphere during the period March through May, 1962. Sampling times correspond to the data illustrated in Fig. 5.

atmosphere. Unfortunately it is not possible to assess the influence of these effects without detailed information on cloudiness associated with the satellite observations.

It is interesting to note in Fig. 5 that absorption in the atmosphere has a considerable variation over the United States, in spite of the smoothing technique used. At the same geographical latitude, absorption varies by a factor of 3 from the minimum values in the Great Basin to the maximum values in southeastern United States. With latitude, it varies by a factor of 7 between the western Great Lakes region and the southeastern United States. It appears that atmospheric absorption has as large a spatial variation as absorption at the ground, and has an even larger variation than the reflection of sunlight to space.

Finally, from the data illustrated in Figs. 5 and 6, overall spatial averages of these terms for the continental United States were derived and summarized in Table 1.

TABLE 1

Average values of partitioning of sunlight over the continental United States during Spring, 1962 (fraction of total incident sunlight)

Reflection to Space, q_r	0.40
Absorbed in Atmosphere, q_a	0.13
Absorbed at ground, q_e	<u>0.47</u>
	1.00
(Total precipitable water	1.19 cm)

Reitan [12] has found that for the period March-May the precipitable water over the entire United States averaged 1.44 cm, based on 11 years of data. When Reitan's data are limited to the area of the present study, the average is 1.39 cm. This indicates the average precipitable water in the present study is low by 0.2 cm, and the fractional absorption of sunlight in the atmosphere is low by about 1 percent in relation to the 11 year period of Reitan.

b. Solar Heating Rate over the United States

The atmospheric absorption values which were determined in this study can be expressed as the amount of heating of an atmospheric column. For the values given in Fig. 5, the resultant heating rate was calculated from

$$(8) \quad \text{Average Heating Rate (}^{\circ}\text{C/day)} = (g \cdot \bar{Q}_0 \cdot q_a) / (10^3 \cdot c_p \cdot \Delta p)$$

\bar{Q}_0 is the average for the period March through May for the United States and Δp was taken as 1000 mb. The results shown in Fig. 7 indicate the maximum warming exceeded 0.8°C/day in the moist belt across the southeastern United States. The minimum warming rate of about 0.35°C/day is found over the northern Great Plains and throughout the western mountain region.

5. ABSORPTION OF SUNLIGHT IN THE ATMOSPHERE

There has been considerable work on absorption of solar radiation in the atmosphere based on laboratory measurements (e.g., Yamamoto [15]; Houghton [6]). These studies were concerned with the absorption in a cloudless atmosphere. Yamamoto, and also Houghton, relate absorption to total precipitable water, for an optical airmass of one (i.e., where the solar zenith angle is zero), as shown in Fig. 8, curves 1 and 2.

The absorption values of the present study have been averaged by class intervals of the natural logarithm of u^* , in order to provide comparable results to those mentioned above. The results are shown in curve 3 of Fig. 8.

The work of Yamamoto and Houghton show the absorption of sunlight in "artificial" atmospheres which depart from the real case because they:

- are cloudless,
- are dustless,
- have fixed vertical distribution of absorbing constituents, and
- have a nonreflecting surface at the lower boundary.

Clearly, the curves in Fig. 8 are not directly comparable. Nevertheless there is significant similarity in the shape of the curves.

The important feature in Fig. 8 is that the absorption of sunlight in an atmosphere with clouds (curve 3) departs from the clear-sky absorption curves

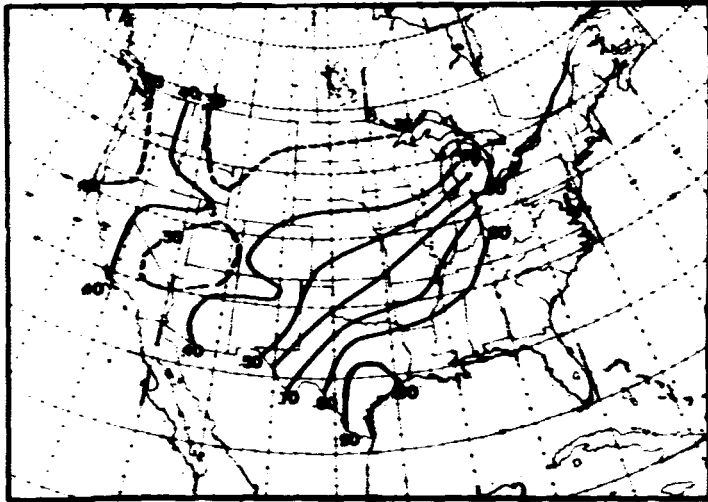


Fig. 7. Atmospheric heating ($^{\circ}\text{C}/\text{day}$) due to absorption of solar radiation in the atmosphere during the period March through May, 1962, based on q_a values of Fig. 5.

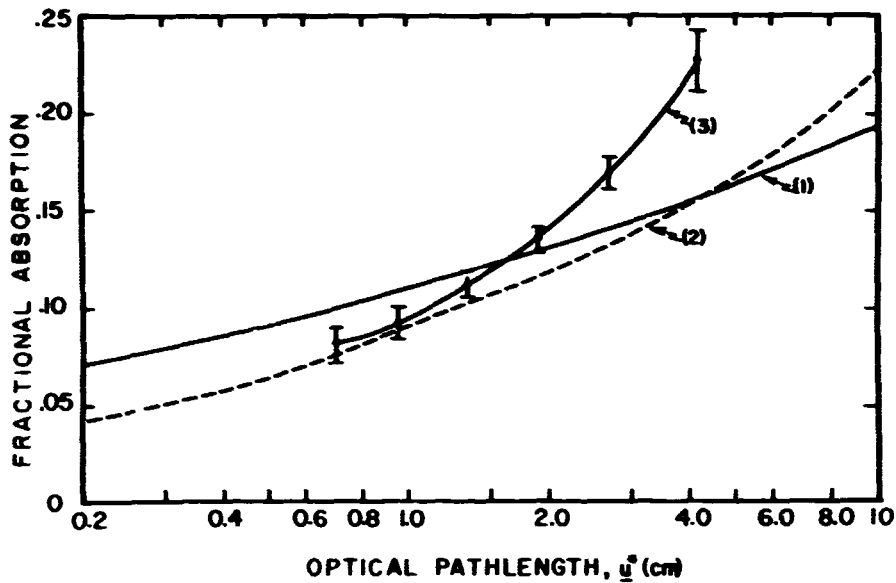


Fig. 8. Absorption of solar radiation in the atmosphere as a function of optical pathlength, u , in cm.

Curve 1 is the absorption in a clear atmosphere due to H_2O , CO_2 and O_2 , from Yamamoto [15].

Curve 2 is the absorption in a clear atmosphere due to H_2O only, from Houghton [6].

Curve 3 is the absorption in the atmosphere over the United States with mixed cloudiness, based on the present study. Brackets indicate the confidence limit of the function values.

(1 and 2) in the region of higher water vapor content. At lower values of water vapor, there is much closer agreement between the curves. Thus, it appears that clear-sky absorption estimates are least applicable in the areas with more moisture (and presumably more cloudiness), and the tendency in these cases is to underestimate the actual absorption that occurs with clouds.

This is particularly important because IR cooling is relatively less in moist, cloudy areas; thus, both the IR and solar radiation have a positive effect on the generation of available potential energy in mid-latitude disturbances. In addition, the solar absorption term is greater than previously thought.

For further studies it is useful to know the function which represents curve 3 (Fig. 8). An approximation was found to be

$$(9) \quad q_a = 0.096 + 0.045(u^*)^{1/2} \cdot \log_e(u^*)$$

The variance of the dependent data from this function is 1.0×10^{-4} .

An example illustrating the use of Eq. (9) has been calculated for 40°N latitude at the time of the vernal equinox. Since both time and position on earth are specified, then the fractional absorption (q_a) and total absorption (Q_a) are simply functions of the optical depth of water vapor. By holding optical depth constant, the fractional and total absorptions are specified as shown in Fig. 9.

The limitations on the use of this example are that: (1) the empirical data obtained over the United States must be used with caution in other areas, e.g., oceanic areas, and (2) optical pathlength is not simply a function of secant of solar zenith angle for atmospheres with clouds, although it may be a good approximation.

REFERENCES

1. A. Angstrom, Atmospheric turbidity, global illumination and planetary albedo of the earth. Tellus, 14, 1962, pp. 435-450.
2. D. M. Gates, Energy Exchange in the Biosphere. Harper and Row Biological Monographs, Harper and Row, New York, N.Y., 1962, 151 pp.
3. A. Danjon, Nouvelles recherches sur la photometrie de la lumiere cendree et l'albedo de la terre. Ann. l'Obs. Strasbourg, 3, 1936, pp. 139-181.
4. J. Dubois, La variation de brillianee de la lumiere cendree de la lune au cours du dernier cycle solarie. L'Astronomie (Paris), 69, 1955, pp. 242-246.
5. S. Fritz, P. Krishna Rao and M. Weinstein, Satellite measurements of reflected solar energy and the energy received at the ground. Journal of the Atmospheric Sciences, 21:2, 1964, pp. 141-151.

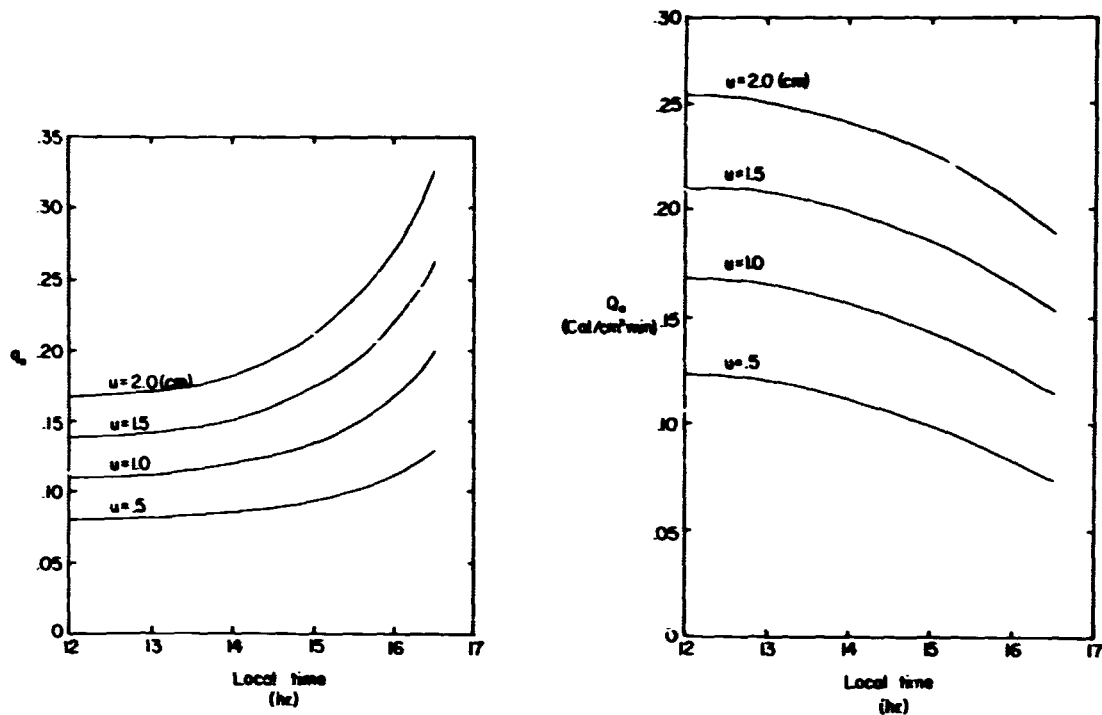


Fig. 9. Fractional absorption (q_a) and total absorption (Q_a) at 40 degrees N. latitude on vernal equinox based on Eq. (9).

6. H. Houghton, On the annual heat balance of the northern hemisphere. Journal of Meteorology, 11:1, 1954, pp. 1-9.
7. F. House, On the interpretation of long-wave radiation data from Explorer VII Satellite, Final Scientific Report, Contract NASw-65, Department of Meteorology, University of Wisconsin, 1968, pp. 150-163.
8. F. House, The radiation balance of the earth from a satellite. Ph. D. thesis, University of Wisconsin, 1965 (unpublished).
9. H. Kimball, Measurements of solar radiation intensity and determination of its depletion by the atmosphere. Monthly Weather Review, 58, 1930, pp. 43-52.
10. E. Kung, R. Bryson and D. Lenschow, Study of a continental surface albedo on the basis of flight measurements and structure of the earth's surface cover over North America. Monthly Weather Review, 92:12, 1964, pp. 543-564.
11. J. London, A study of atmospheric heat balance. Final Report, Contract No. AF19(122)-165, Dept. of Meteorology and Oceanography, New York University, 1957, 99 pp. (OTS No. PB 129551).

12. Reitan, C., Distribution of precipitable water vapor over the continental U.S., Bulletin A.M.S. 41(2), Feb. 1960, pp. 79-87.
13. G. C. Simpson, The distribution of terrestrial radiation. Memoirs of Roy. Meteor. Soc., 3, 23, 1929, pp. 53-78.
14. V. Suomi, The radiation balance of the earth from a satellite, Annals of the IGY, VI, 1958, pp. -340.
15. G. Yamamoto, Direct absorption of solar radiation by Atmospheric Water Vapor, Carbon Dioxide and Molecular Oxygen. Journal of the Atmospheric Sciences, 19:2, 1962, pp. 182-188.

N 69 - 33581

RADIATION ANALYSIS OF A SUBTROPICAL HIGH

by

J. O. Siebers

CONTENTS

	Page
I. INTRODUCTION - THOUGHT EXPERIMENT	126
II. DATA	127
2.1 Radiation Data	127
2.2 Synoptic Data	127
2.3 Additional TIROS IV Data	128
III. PERIOD SELECTION	128
IV. RADIATION LOSS MAPS	129
4.1 Preparation	129
4.2 Discussion of Radiation Loss Maps	130
4.3 Discussion of Quarterly Mean Radiation Loss Map	133
V. MODEL OF SUBTROPICAL HIGH-PRESSURE CELL	135
5.1 Model Construction	135
5.2 Model of Subtropical Anticyclone with respect to Radiation Maximum	136
VI. SYNOPTIC TIME SEQUENCES IN THE VICINITY OF THE RADIATION RIDGE	139
6.1 Stations North of the Radiation Ridge	140
6.2 Stations in the Radiation Ridge	140
6.3 Stations South of the Radiation Ridge	146
6.4 Radiation versus Synoptic Analyses Summary	146
VII. CONCLUSIONS	149
VIII. BIBLIOGRAPHY	150

ABSTRACT:

Long-wave radiation loss maps, based on TIROS IV radiometric measurements of terrestrial radiation are analyzed for the Northern Pacific Ocean during the period 20 March to 1 April 1962. These daily radiation analyses are compared to standard synoptic charts. This comparison shows the association of the maximum ridge of radiation to the subtropical high-pressure belt, and the minimum trough of radiation to the intertropical convergence zone. In this study a model of the subtropical high-pressure cell is constructed with respect to the long-wave radiation maximum. Synoptic time sequences for island stations in the vicinity of the ridge of maximum radiation are analyzed and compared to the daily fluctuations of terrestrial radiation.

I. INTRODUCTION-THOUGHT EXPERIMENT

Approximately 50% of our atmosphere is above that part of the earth which we generally refer to as the tropics; yet, because of a very sparse distribution of meteorological stations, the meteorologist must resort to theory and laboratory models to achieve a better understanding of our atmosphere in this region. Is it now possible in this Age of Satellite Meteorology to supplement or maybe refine these models by proper interpretation of satellite data?

Current knowledge of the meteorological features of the tropic atmosphere tells us that in this region we have a subtropical high-pressure belt characterized by subsiding air from high altitudes, which in part, is responsible for the formation of what is called the trade inversion. This inversion is believed to be at minimal height where the amount of subsiding air is at its maximum. From this location in the eastern sector of the high-pressure system, the height of the inversion increases to the west, south of the pressure ridge, and to the south toward the equator. The strength of the inversion decreases with its increased height, and in the region of the equatorial trough, or ITC, and in the western edge of the high-pressure cell, the inversion is essentially nonexistent and the limiting factor to vertical cloud growth becomes the tropopause.

The meridional distributions of long-wave radiation constructed on the basis of satellite data show that a satellite crossing the tropics in its orbital path measures a radiation maximum in the areas of the subtropical high-pressure belts of both hemispheres and a radiation minimum between these relative maxima. Poleward from these maxima, the satellite radiation show even lower values than in the minimum in the equatorial region.

Could a daily analysis of long-wave radiation show a variation of the radiation values in the east-west direction as well as the already established variation with latitude? If so, can the radiation patterns on a daily basis give

any indication of the synoptic location of the area of lowest height of the trade inversion, thus marking the region of maximum subsidence? Will radiation patterns show any variation on a daily basis, and if so, can they be related to known synoptic features?

A great amount of research has been devoted to the use of satellite pictures over the tropical regions of the oceans for the purpose of detecting, locating, and studying tropical convergent systems of all scales. The purpose of this paper, however, is to analyze satellite radiometric data, obtained from a wide-angle sensor, in the region of the subtropical high-pressure belt in the North Pacific, and to compare these analyses to synoptic analyses. This comparison should answer some of the questions stated above.

II. DATA

2.1 Radiation Data

The long-wave radiation values used for the radiation loss maps were obtained by the Wisconsin Heat Budget Experiment aboard TIROS IV, and are similar to those described by Suomi (1960). The radiation measurements are values of the long-wave emissions from clouds, atmospheric gases (carbon dioxide, water vapor, and ozone), and the earth's surface, integrated over the entire field of view of the spherical sensor. Changes of radiation values along the satellite path are heavily weighted toward the area just beneath the satellite; 50% of the radiation value is coming from an area of 6.6 degree latitude radius, and 9/10 of the radiation value from 33.2% of the total field of view, as stated in above reference.

In the preparation of the radiation loss maps, a small periodic variation was found to exist in the daylight measurements. This variation which amounts to less than 3% of the measured value is attributed to the differential heating and cooling of the sensors as they spin about the satellite spin axis, in and out of the shadow of the satellite. It was smoothed by a weighted mean running in time. The effect of this smoothing is considered tolerable as the object of the radiation loss analysis is to obtain patterns of the long-wave radiation loss, not absolute values of outgoing radiation. The satellite radiometric readings were taken every 30 seconds corresponding to a distance of about 1° of latitude between successive radiation measurements along a given suborbital path. The distance between successive orbits is about 27° longitude at the equator. The effect of this gap will be discussed later.

2.2 Synoptic Data

The synoptic analyses for the surface, 700, 500, 300 and 200 mb levels used in this paper, we obtained as copies of original working charts from the

USWB Honolulu Analysis Center. Additional synoptic data employed in the time sequence analyses was obtained from the Daily Bulletins of Northern Hemisphere Data Tabulations.

2.3 Additional TIROS IV Data

The nephanalyses employed were obtained from the Catalogue of Meteorological Satellite Data-TIROS IV Television Cloud Photography.

III. PERIOD SELECTION

The best period suitable for this project was selected so as to satisfy the following criteria:

- (1) A minimum of 3 successive orbits per day, with radiation measurements over area of interest.
- (2) A minimum of 8 successive days of criterion 1.
- (3) Satellite passes within 6 hours of 0000 GMT, i. e., near local noon in the Pacific Area.

The above criteria were defined in this way because: (1) A minimum of 3 successive orbits are considered necessary to show a representative radiation pattern, (2) A minimum of 8 days was established since this is the time required for the satellite to pass over a given geographical area a second time, and (3) Daylight passes were desired for the availability of TIROS nephanalyses. Daylight passes are also advantageous in that the sequences of radiation data are not interrupted by the transition zone (satellite warming or cooling in its orbital path as it exits or enters the earth's shadow).

In reviewing all orbits of TIROS IV within the lifetime of the Wisconsin Instrument, the period that best met the defined criteria was found to be from 20 March to 1 April, 1962. This period of 13 days had 88 orbits with continuous radiation data. As this period is early in the life of the satellite, any degradation of the radiometer can be assumed small and thus will not influence the results to any serious degree.

IV. RADIATION LOSS MAPS

4.1 Preparation

Long-wave radiation measurements in units of millilangleys per minute were plotted along the suborbital paths from 20° South to 48° North and from 115° West to 105° East on a 1:15 000 000 scaled mercator projection. This is the same base map used for the synoptic charts.

The time between successive orbits was approximately 1 hour and 40 minutes, consequently the distance between successive orbits at the equator was about 27° of longitude. This made the interpolation of isopleths of radiation loss extremely difficult. In order to minimize this handicap and also to acquire a more representative radiation loss pattern, TIROS IV nephanalyses were employed, when available, to supplement the radiation measurements.

The TIROS nephanalyses describe the cloud cover, type and intensity. Cloud cover is given as clear, scattered, broken or overcast. Cloud type is described as stratiform, cumulus, cumulonimbus, or cirrus.

The use of the TIROS nephanalysis as a supplement to the radiation data was inspired by a statement made by Weinstein and Suomi (1961) that where cloud tops are higher and colder, the outgoing radiation is lower, and where the cloud cover is clear to scattered the radiation measurements are higher in relative value. Any cloud present must have a lower temperature than the earth's surface due to the temperature lapse rate in the troposphere. It follows then that the more clouds within the field of view of the sensor, the lower the outgoing radiation measurements. As the satellite radiation reading is heavily weighted for the area just beneath the satellite, the cloud height, intensity and cover under the satellite largely determine the amount of outgoing radiation. Because of this relationship of cloud amount and height to the amount of outgoing radiation, the nephanalyses can give a qualitative estimate of the radiation loss pattern between the plotted suborbital paths of radiation readings.

The latitude of radiation troughs or ridges were easily determined along the satellite suborbital path from the radiometric readings. The orientation of the radiation pattern between the suborbital paths was determined largely from the nephanalysis, using the aforementioned relationship. Radiation troughs were drawn to coincide with areas of broken to overcast cloud areas, with consideration also given to heavy cloud intensity, and to indicated areas of dense cirrus and/or cumulonimbus. Ridges of radiation between the suborbital satellite paths were drawn to coincide with reported areas of clear to scattered clouds. No attempt was made to determine the tops of the clouds displayed in the nephanalyses, as the source of corresponding synoptic data was sparse.

The technique employed in the analysis of the radiation loss maps was similar to the analysis of contours of an upper air constant pressure chart. The use of 24 hour continuity was an invaluable tool in the analyses. All radiation loss maps were prepared independently of the synoptics charts, except for the above mentioned use of TIROS nephanalyses.

4.2 Discussion of Radiation Loss Maps

An example of the daily radiation loss maps is shown in Figure 1. Orbital paths are indicated by dotted lines in this figure. The main patterns of outgoing radiation appearing on the daily maps are: the radiation trough associated with the intertropical convergence zone, the ridge of radiation associated with the subtropical high-pressure belt, and the minor ridges and troughs of radiation associated with the migratory systems moving through the latitudes of the westerlies.

On this particular day the radiation trough associated with the ITC is oriented NE to SW in the Eastern Pacific. It is located at 18°N , 115°W and at about 6°N , 180°W . West of the 180° meridian the trough deviated sharply to the south reaching a minimum position and intensity at about 15°S , 163°E . From this position the trough is oriented to the NW across Indonesia. In the vicinity of Celebes there is a double minimum, and the trough then extends NW across Malaysia.

The east-west radiation maximum ridge in Figure 1 has its most northern position off the coast of Baja, California and shows a relative maximum center in the Eastern Pacific at 20°N , 145°W . Further to the west the ridge weakens in the vicinity of 160°W and reaches its maximum latitude position at 12°N , 165°W . In the Western Pacific the ridge is nearly east-west at about 14°N , with a radiation maximum center at 13°N , 157°E . The ridge then continues toward the Asian Continent showing a weakness over the Philippines and then reintensifying over the Far East Continent. Another ridge of maximum radiation can be seen in the Eastern South Pacific.

The minor radiation ridge and trough patterns to the north of the east-west ridge of maximum radiation are associated with the migratory systems imbedded in the westerlies. The radiation trough off the east coast of Asia is attributed to the convective cloud systems resulting from the instability of the cold continental air moving out to sea over the relatively warm Kuroshio Current. This latter trough varied in intensity during the 13 days, however was always evident in the analyses.

The displacement of these radiation patterns described above for the daily map example are summarized for the 13 daily radiation loss maps in Figure 2. In this figure the dotted lines represent the southern most invasion of the frontal

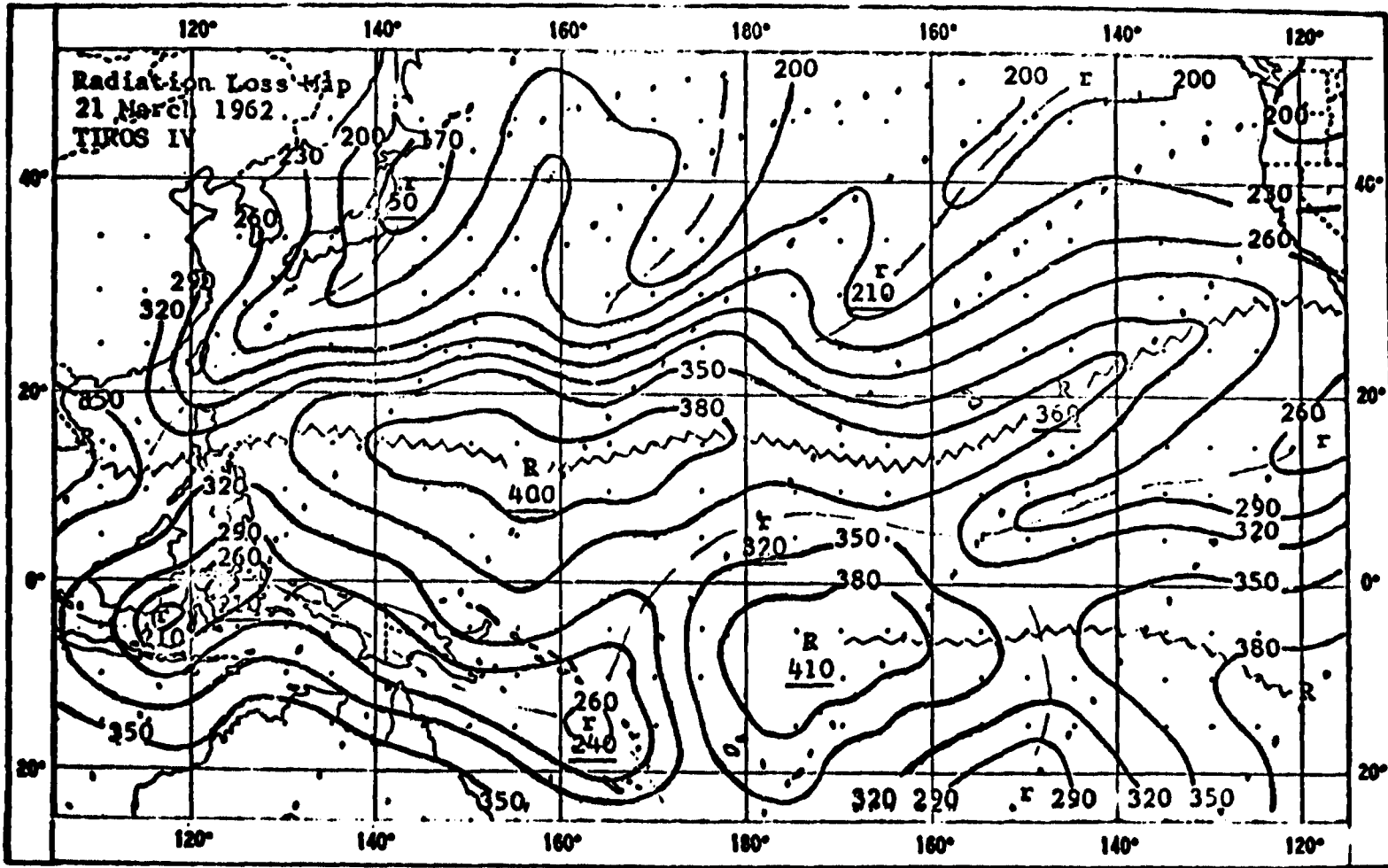


Fig. 1. An Example of Daily Radiation Loss Map. TIROS IV, Wisconsin Heat Budget Radiometer Data.

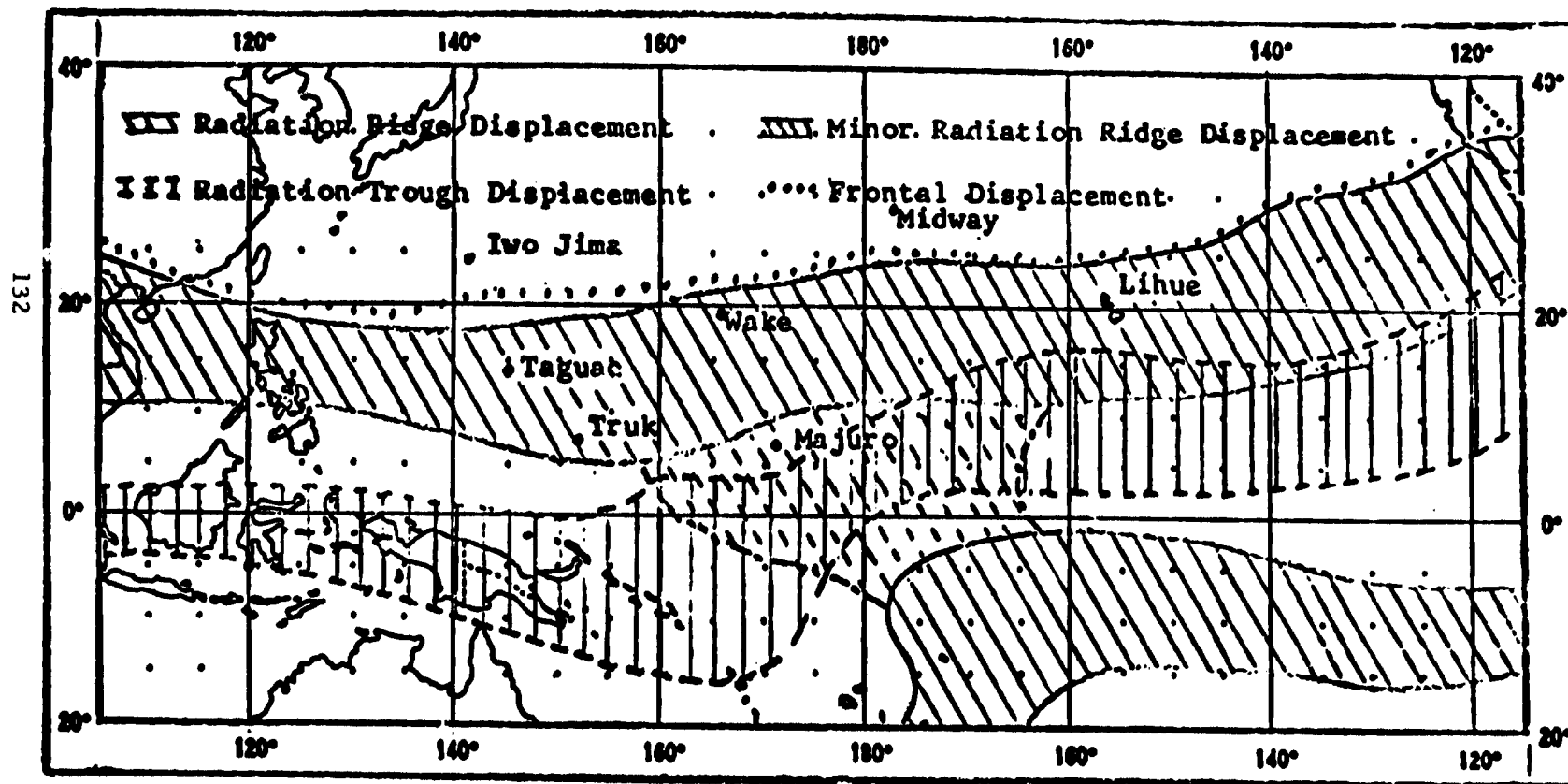


Fig. 2. Displacement Limits of Radiation Ridges and Trough and Fronts During Thirteen Day Period.

systems into the subtropical region during this period. The solid lines represent the northern and southern limit of displacement of the ridge of maximum radiation. In the Northern Pacific the ridge displacement is oriented east-west. In the Southern Pacific the ridge of maximum radiation was only defined in the analyses for the Eastern Pacific. The limit of displacement of the minor ridge between the North and South Pacific regions of maximum radiation in the Central Pacific is shown by the alternating dot-dash line.

The displacement limit of the radiation trough associated with the ITC is shown in Figure 2 by dashed lines. The general pattern and location of this radiation trough on the daily map series agrees well with the climatological location of the ITC for the spring season. The radiation col pattern in the Central Pacific reflects a weakness of the radiation trough and the associated ITC in this region.

Following the daily continuity of the radiation loss map series, it was noted that as a front moved south introducing cloudiness in the westerlies north of the subtropical high cell, the lower long-wave emission from the clouds tend to displace the ridge of radiation maximum to the south. In these areas, the additional appearance of a stronger radiation gradient reflected the presence of greater amounts and heights of cloudiness, and in turn reflected the greater relative intensity of the frontal system. The minor ridges of radiation maximum moving through the westerlies of the temperate latitudes indicate the relatively clear areas associated with the migratory high-pressure cells. When these minor ridges or a relatively weak frontal system, with relative clear areas, are adjacent to the northern periphery of the subtropical high-pressure belt, the ridge of radiation maximum is relocated to the north.

The radiation patterns in the Eastern Pacific were especially difficult to analyze due to the presence of a low-pressure system in the region. This and other synoptic features for this 13 day period will be discussed later.

4.3 Discussion of Quarterly Mean Radiation Loss Map

Figure 3 portrays the average daylight radiation loss values for March, April and May. Radiation values used in the preparation of this map represent mean values of all satellite measurements from the same sensor within areas of 10° of latitude by 10° of longitude. This map was analyzed independent of all synoptic data.

The radiation patterns on the daily map series are similar to those of this mean radiation loss map except for the complex radiation pattern in the Eastern Pacific. This complex pattern of low radiation values on the mean map is due to the variability of the clouds and water vapor associated with the low pressure system in the Eastern Pacific, already mentioned in the preceding section.

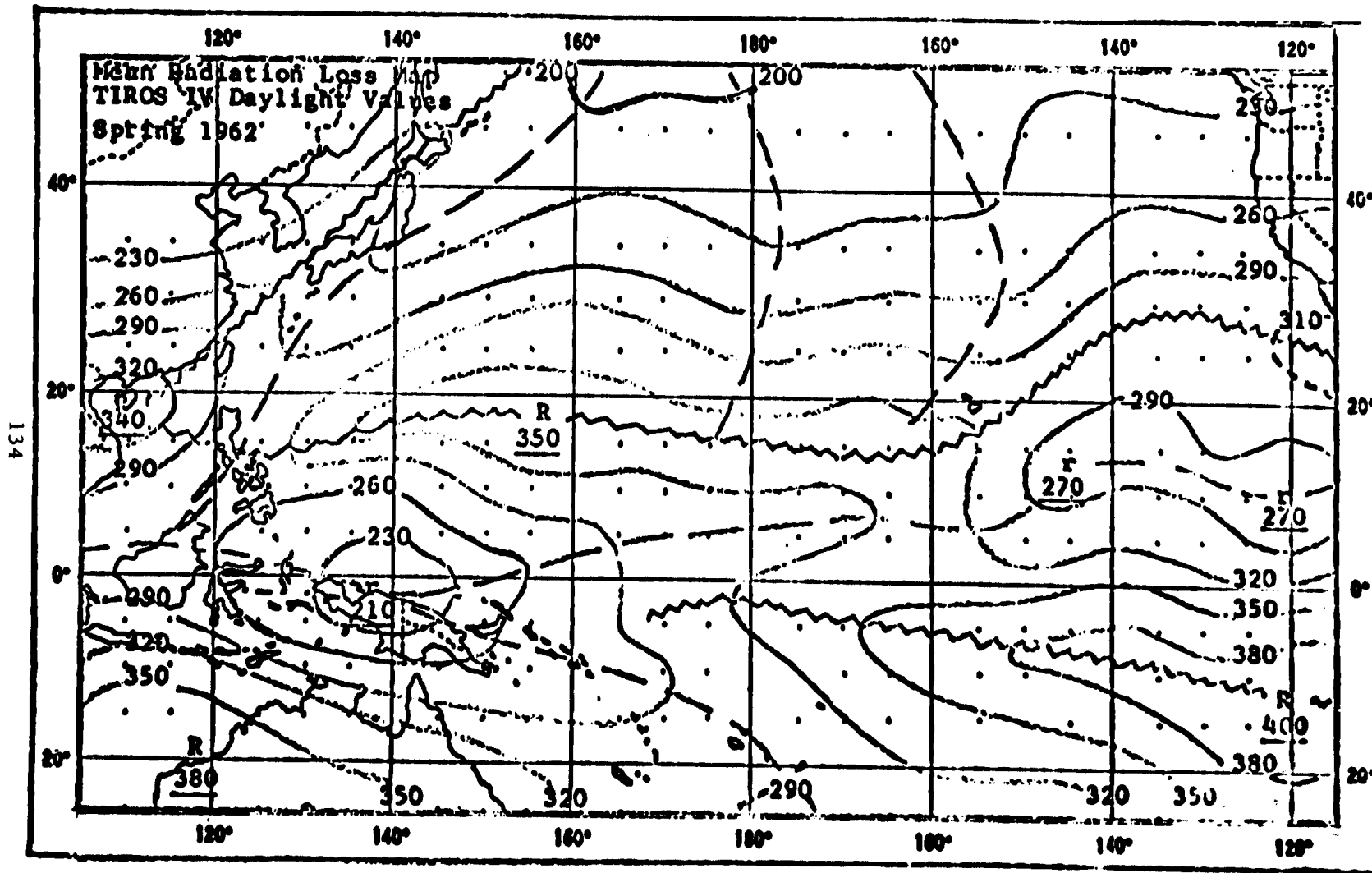


Fig. 3. Mean Daylight Long-wave Radiation Loss Map for March, April and May 1962.

The discontinuity of the ITC in the Central Pacific is again apparent by the radiation col pattern between 160° W and 170° W. The northern displacement of the mean radiation trough in the Western Pacific is explained by the fact that this mean map includes April and May, which is the time that the ITC has already started its motion to the north as indicated by climatological data.

The trough of minimum radiation off the Asian Coast is also evident in the mean radiation pattern. This radiation trough in the mean is attributed to the convective clouds over the Kuroshio Current and the clouds advected in the western sector of the subtropical high, as indicated before.

V. MODEL OF SUBTROPICAL HIGH-PRESSURE CELL

According to Riehl (1954) the trade inversion is formed in the eastern sector of the subtropical high-pressure cell by a broad scale descent of dry air from high altitudes. This inversion then acts as a lid which the lower cumuli enter but rarely penetrate. The height of the trade inversion ascends to the west, south of the pressure ridge, and to the equator. The inversion temperature decreases as the inversion increases with height.

The trade inversion height is a function of the magnitude of the subsidence. In a given synoptic situation the eastern sector of this high-pressure cell is characterized by the strongest subsidence within the cell. Therefore, the height of the inversion must be at a relative minimum in the eastern sector of the subtropical high-pressure cell. Since the inversion is relatively warm when it is at minimal height and since it caps most clouds and water vapor, a terrestrial radiation maximum should be found in this eastern sector of the subtropical high-pressure cell.

5.1 Model Construction

Having 13 days of radiation loss maps for the Pacific Area, and the corresponding standard synoptic level charts, a model of the subtropical high-pressure cell can be constructed. This model can establish the location of the synoptic high-pressure cell with respect to the area of maximum long-wave radiation associated with this area of subsidence.

The vertical and horizontal structure of the subtropical high was determined from the synoptic charts prepared by the USWB Honolulu Analysis Center. In the region of the subtropical high-pressure belt, separate cells were apparent on both the synoptic charts and the radiation loss maps. During this period under consideration the high-pressure cell and the maximum radiation pattern were best defined in the Western North Pacific.

TABLE I

Statistics of Pacific Subtropical Anticyclone Model (20 March to 1 April 1962)

Level	Mean Components of Displacement Vector		Standard Deviation of Vector Components		Number of Cases Defined	Eccentricity of Curve
	X	Y	X	Y		
Surface	- 6.31	15.43	7.93	4.78	17	0.8
700 mb	-10.84	8.70	9.54	3.46	21	0.9
500 mb	-12.53	4.62	9.63	4.40	22	0.9
300 mb	-12.11	3.50	7.66	3.32	17	0.9
200 mb	-11.85	3.06	7.68	4.26	11	0.8

Note: Vector components and standard deviations are expressed in equivalent degrees of latitude, i. e., 1° latitude = 60 nautical miles = 111 kilometers.

Due to sparse data coverage over the ocean, the exact geographical location of the high-pressure feature on the synoptic charts is not always well defined. Table I shows that the number of cases considered for each level varies in the construction of this model. The reason for this variability is that only those cases were used where there was a reasonable amount of confidence in the location of the high-pressure feature.

The horizontal displacement of the synoptic high-pressure features with respect to the associated radiation maximum were determined for each cell. Linear distances from the mercator projection were converted to a rectangular coordinate system scaled in equivalent degrees of latitude (1° = 60 n. m. = 111 km.). Table I shows the resulting statistics of this investigation.

5.2 Model of Subtropical Anticyclone with Respect to Radiation Maximum

Figure 4 illustrates the statistical data in Table I, and portrays the statistical model of the subtropical high-pressure cell with respect to the radiation maximum. In this model the mean displacement for each synoptic level is shown by a vectorial displacement from the long-wave radiation maximum. The ellipse, whose center is at the head of the respective vector, represents the standard deviation about the mean vector position.

The displacement vectors back with increased altitude from the NNW displacement of the surface pressure center to the nearly east-west position of the 200 mb level vector. This model cell shows that the displacement of the

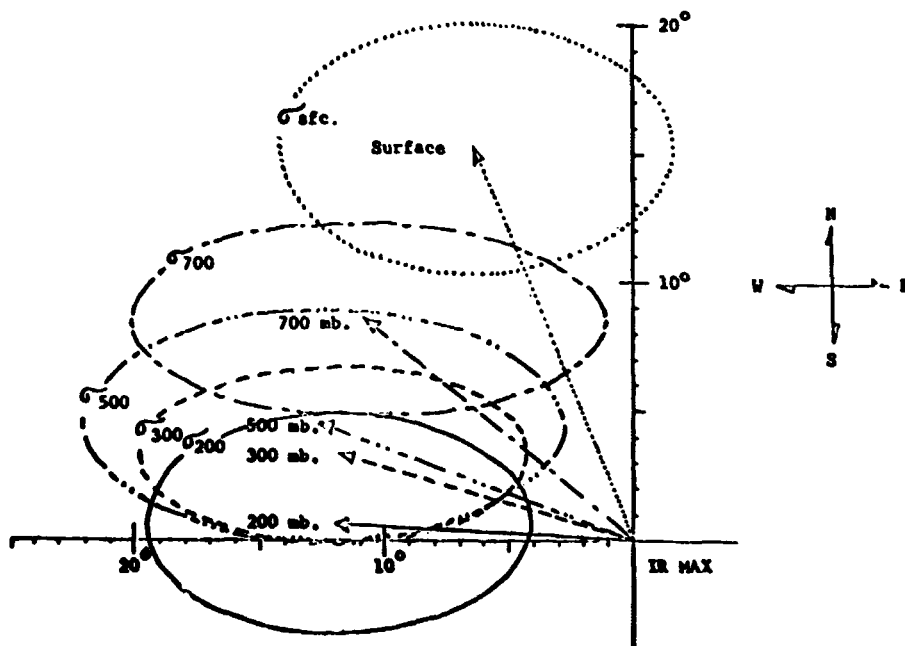
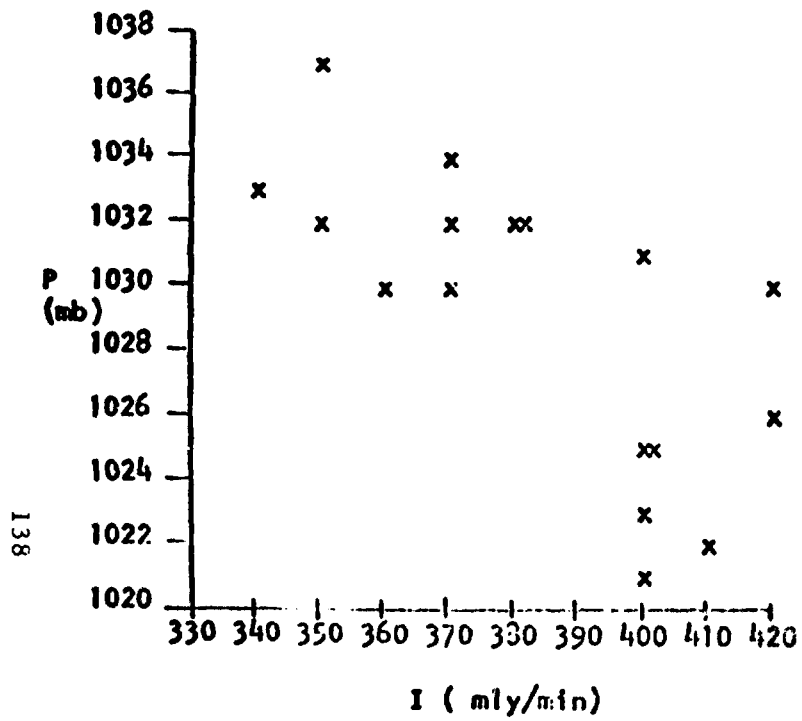


Fig. 4. Model of Pacific Anticyclone with respect to Long-wave radiation Maximum

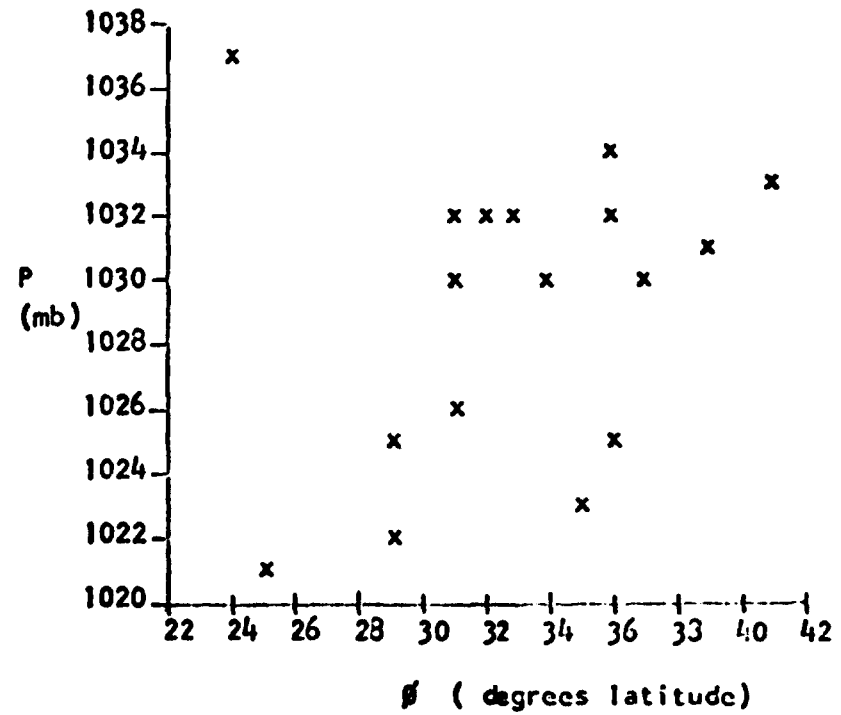
high-pressure cell axis is greatest below the 500 mb level and nearly vertical above. The axis of the cell slopes toward the equator with height. The pressure cell is found in the northwest quadrant with respect to the radiation maximum. The eccentricity of the standard deviation ellipse definitely shows the curves to be elongated in the east-west direction. This orientation of the major axis arises from the fact that the high-pressure ridge of the subtropics is oriented east-west.

An attempt was made to correlate the intensity of the radiation maximum to the intensity of the associated surface high-pressure cell. The scatter diagram shown in Figure 5a shows the relationship of these two variables. This scatter diagram shows a negative correlation. The calculated value was $\gamma_1 = -0.56$. A similar correlation, with a value of $\gamma_2 = -0.52$ was obtained by relating pressure gradients to the radiation field. This negative correlation at least qualitatively, is physically reasonable if we consider that a lower surface intensity of the high-pressure cell indicates a lower vertical development of this cell. Because of this lower vertical development any clouds or moisture advected around or over this cell would then have a higher temperature and would result in a larger long-wave emission.

Figure 5b shows a scatter diagram of the surface pressure intensity to the latitude of the pressure center. A positive correlation is indicated in this diagram, the calculated value being $\gamma_3 = +0.24$. This correlation is



5a. Surface Pressure Intensity (P) versus Radiation Maximum Intensity (I).



5b. Surface Pressure Intensity (P) versus Latitude of Surface Pressure Center (ϕ).

Figure 5. Scatter Diagrams of Surface Pressure Intensity versus Radiation Maximum Intensity and Latitude of Surface Pressure Center.

physically reasonable: when the pressure cell is at a lower altitude it is less developed in the vertical, and is also over a warmer ocean surface, thus resulting in higher long-wave emissions.

Since, however, only 17 cases could be examined in this case study, these correlation coefficients are not significant and may be indicative only of the particular behavior of the systems during this specific period.

VI. SYNOPTIC TIME SEQUENCES IN THE VICINITY OF THE RADIATION RIDGE

The seven island stations designated in Figure 2 were selected for synoptic time sequence analyses on the basis of their location with respect to the radiation ridge, and the availability of synoptic data. These time sequences, shown in Figures 6 through 12, were analyzed for zonal winds and relative humidity for the purpose of investigating the position of the subtropical high with respect to the station, and examining the humidity distribution in these sectors of the pressure cell.

During the period of this case study, the high pressure ridge was characterized by two separate cells. The Western Pacific high was in a better defined stage of vertical development than the Eastern Pacific high due to a low pressure system in the Eastern Pacific. This low pressure system existed as a closed low system for the first three days and then filled; however, a trough aloft persisted in this region for the remainder of the period. A southern extension of this trough aloft was oriented in the low latitudes in a near east-west direction and became adjacent to the ITC in the Central Pacific. The Western Pacific high, and concurrently the ITC, was displaced to the north during the middle of this period.

The stations selected for the time sequence analyses can be classified into three groups on the basis of their location relative to the radiation ridge and expected zonal winds and humidity distributions. The stations to the north of the ridge should display mostly westerly winds, and a variable humidity distribution due to the repeated invasion of frontal systems into their respective areas. The second group which is in the ridge itself should display more frequently easterly winds, and also a lower humidity distribution due to the subsiding air in the pressure ridge. The third group to the south of the radiation ridge can be expected to display even more easterly winds than the second group and should again have a more variable humidity distribution as a result of the perturbations in the easterlies. The humidity pattern of this last group might also be influenced by advected moisture from the region of the ITC.

The time sequences show isopleths of relative humidity as solid lines. The zonal wind regimes are separated by short dashed lines, while the heavy dashed lines indicate the passage of easterly waves or frontal systems at the stations.

The analyses were terminated, near the lower boundary, at the 1000 mb level.

6.1 Stations North of the Radiation Ridge

The time sequence for Midway, Figure 6, shows more days with easterly winds and a more uniform humidity distribution than was expected. The easterly winds, however, can be understood synoptically as the result of the flow between the Western Pacific high to the west and the near stationary low pressure system in the Eastern Pacific during this particular period. The vertical humidity distribution is generally suppressed in the lower 2 kilometers under the influence of the subsiding air.

While Figure 6 does not really show a typical pattern, Figure 7, the time sequence for Iwo Jima, displays what can be considered to be a typical example of the zonal winds and humidity distribution for a station located to the north of the radiation ridge. Advective moisture can be seen aloft on 21, 25, and 27 March, and the moisture associated with a frontal passage is evident on 23 March. A quasi-stationary front in the vicinity of Iwo Jima was shown on the surface analyses obtained from the Honolulu Analysis Center from 25 to 31 March. The presence of this front is indicated on the time sequence by the low level easterly winds during this period.

6.2 Stations in the Radiation Ridge

The time sequences for Lihue, Wake and Taguac are shown in Figures 8, 9 and 10, respectively. The zonal winds on these sequences are as expected and show systematic differences of east versus west winds caused by the movement of the subtropical high axis. Easterly winds extend to greater altitudes on the analyses for Wake and Taguac while the Western Pacific high-pressure cell was displaced to the north. While the time sequences of Taguac and Wake both display, as expected, a general confinement of moisture in the lower layers, the distribution of humidity shown for Wake is considered much more typical for a station located in the radiation ridge. These sequences show that an easterly wave passed Wake on 27 March and Taguac on 29 March, this being the time when the Western Pacific high cell was further north. A classic example of the influence of an easterly wave on the humidity distribution is shown by the Wake analysis.

The greater vertical distribution of humidity over Lihue is due to the convergent flow between the low pressure system to the west and the Eastern Pacific high to the east. Even after the low filled, moisture advection is still quite evident over Lihue. After 26 March, the Eastern Pacific high moved south, and then as expected the moisture was confined in the lower layers of the troposphere, under the influence of subsiding air.

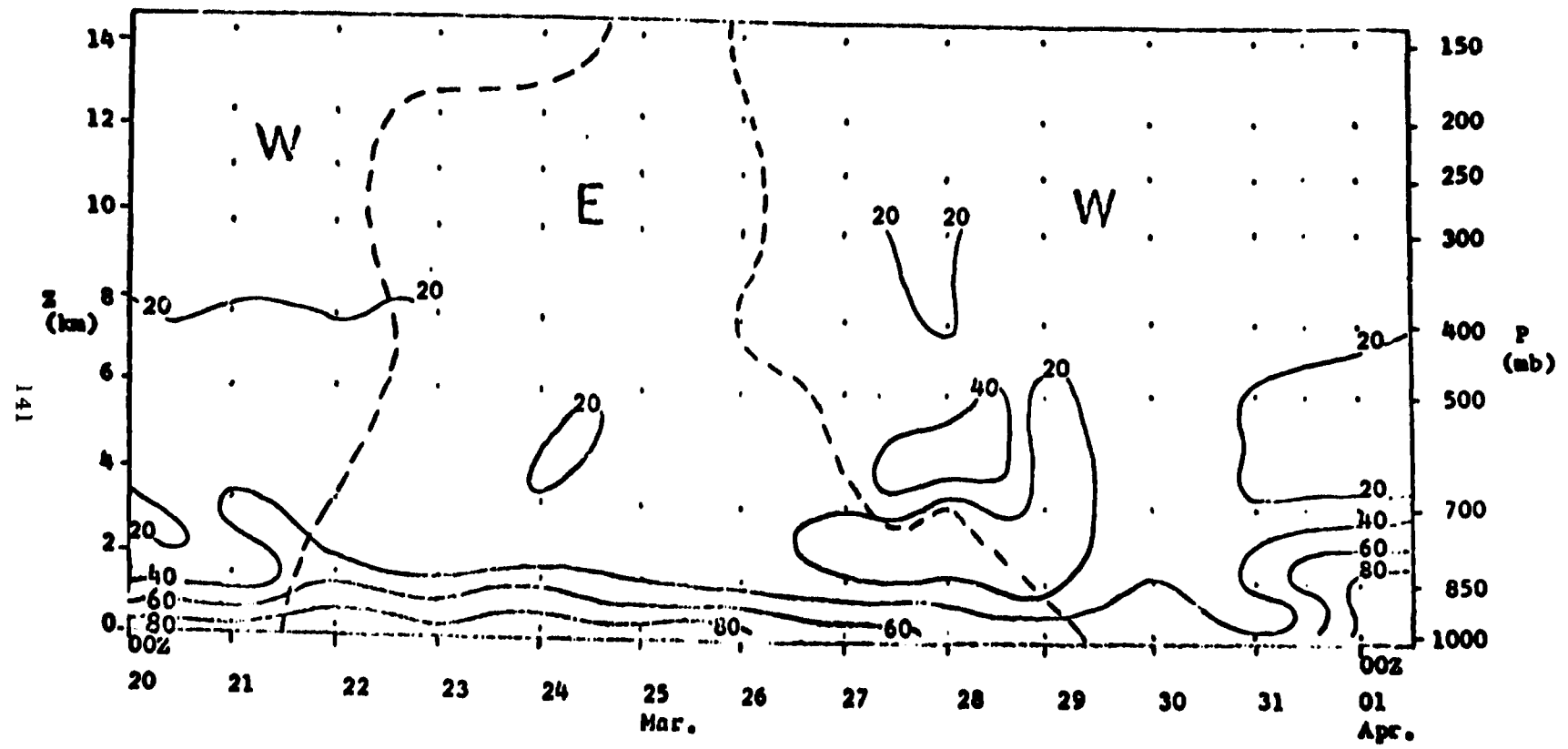


Fig. 6. Time Sequence Showing Relative Humidity Distribution, Zonal Winds, and Surface Observations for Midway.

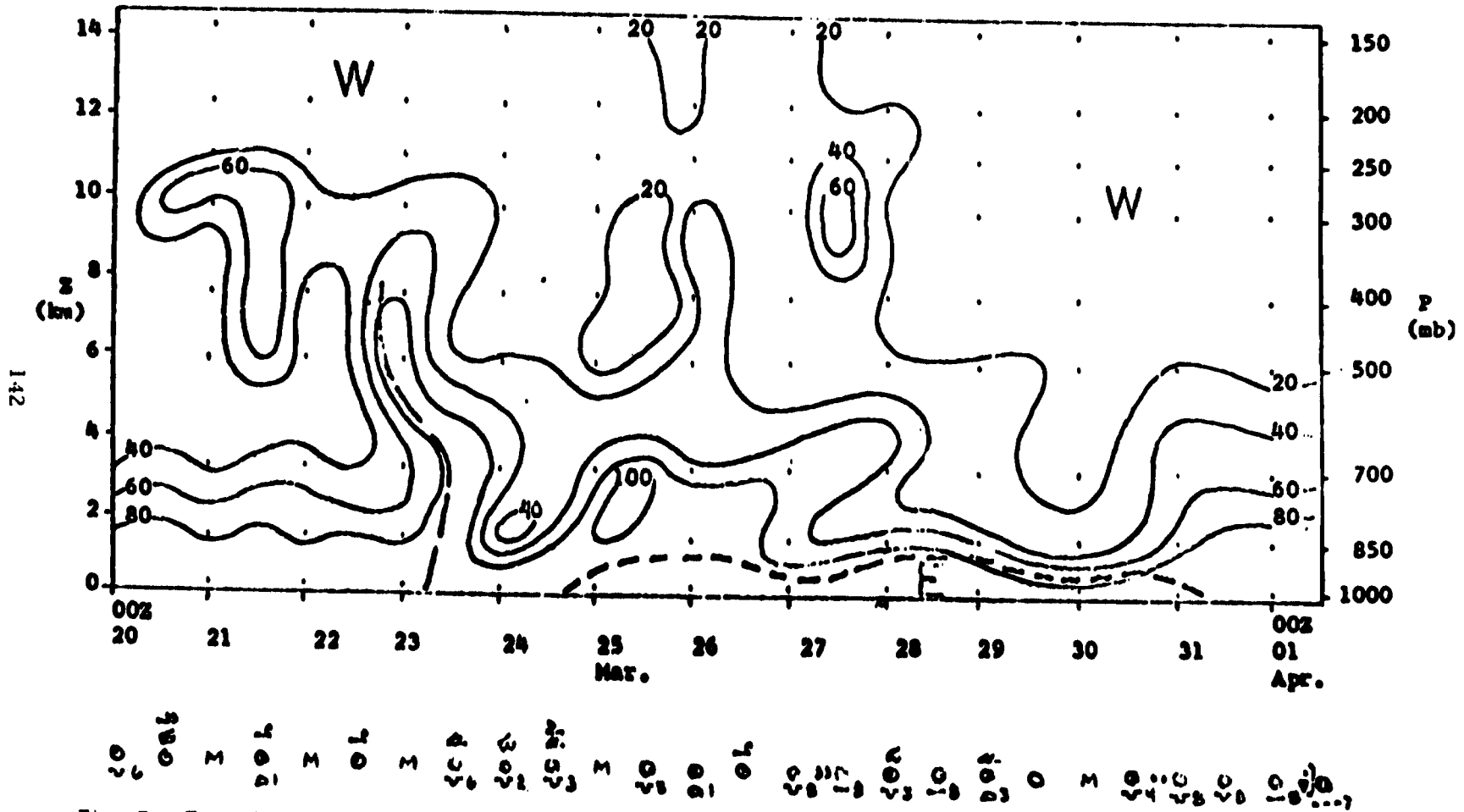


Fig. 7. Time Sequence Showing Relative Humidity Distribution, Zonal Winds, and Surface Observations for Iwo Jima.

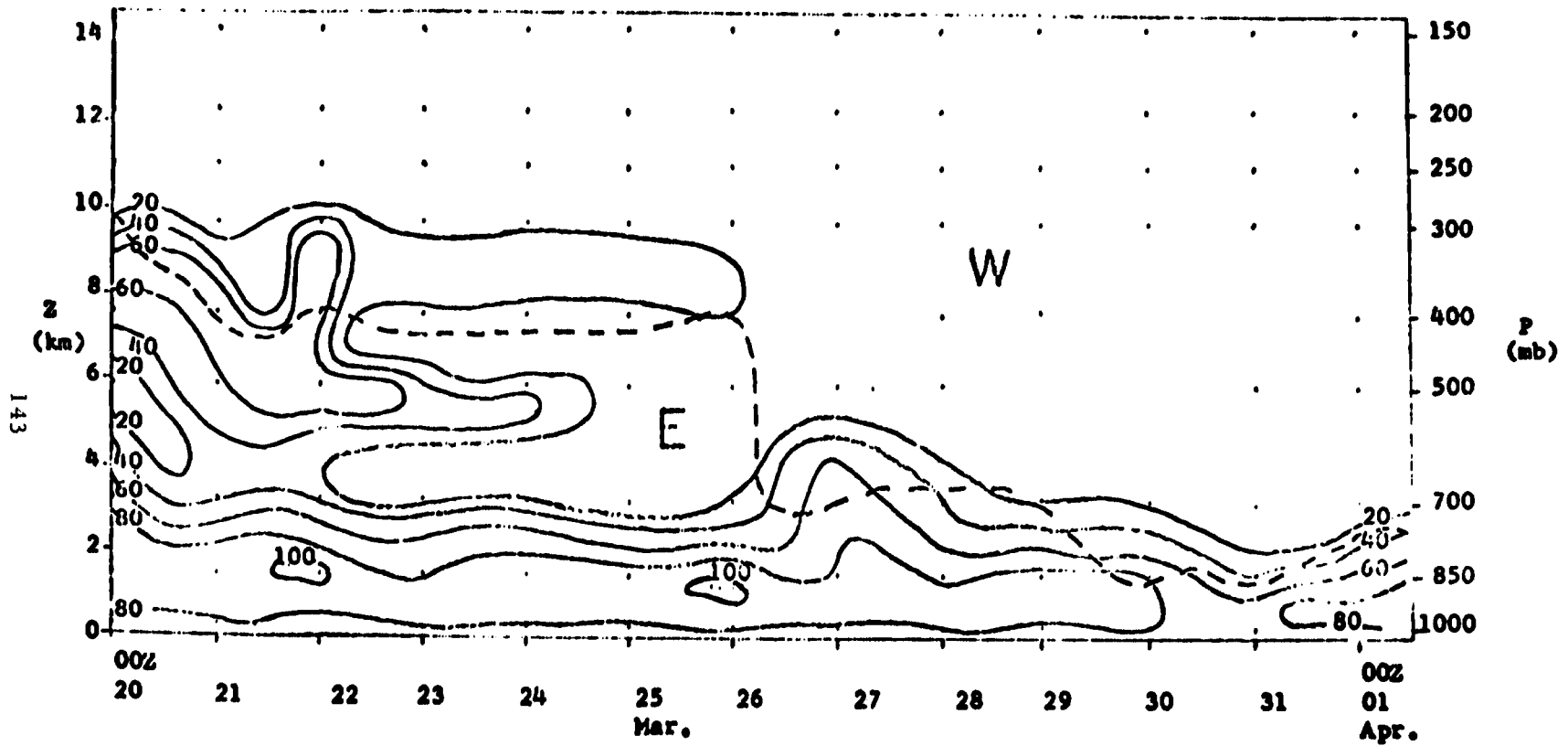


Fig. 8. Time Sequence Showing Relative Humidity Distribution, Zonal Winds, and Surface Observations for Lihue.

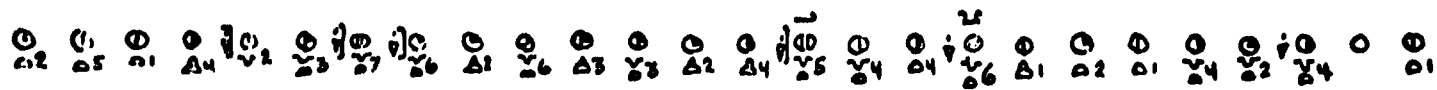
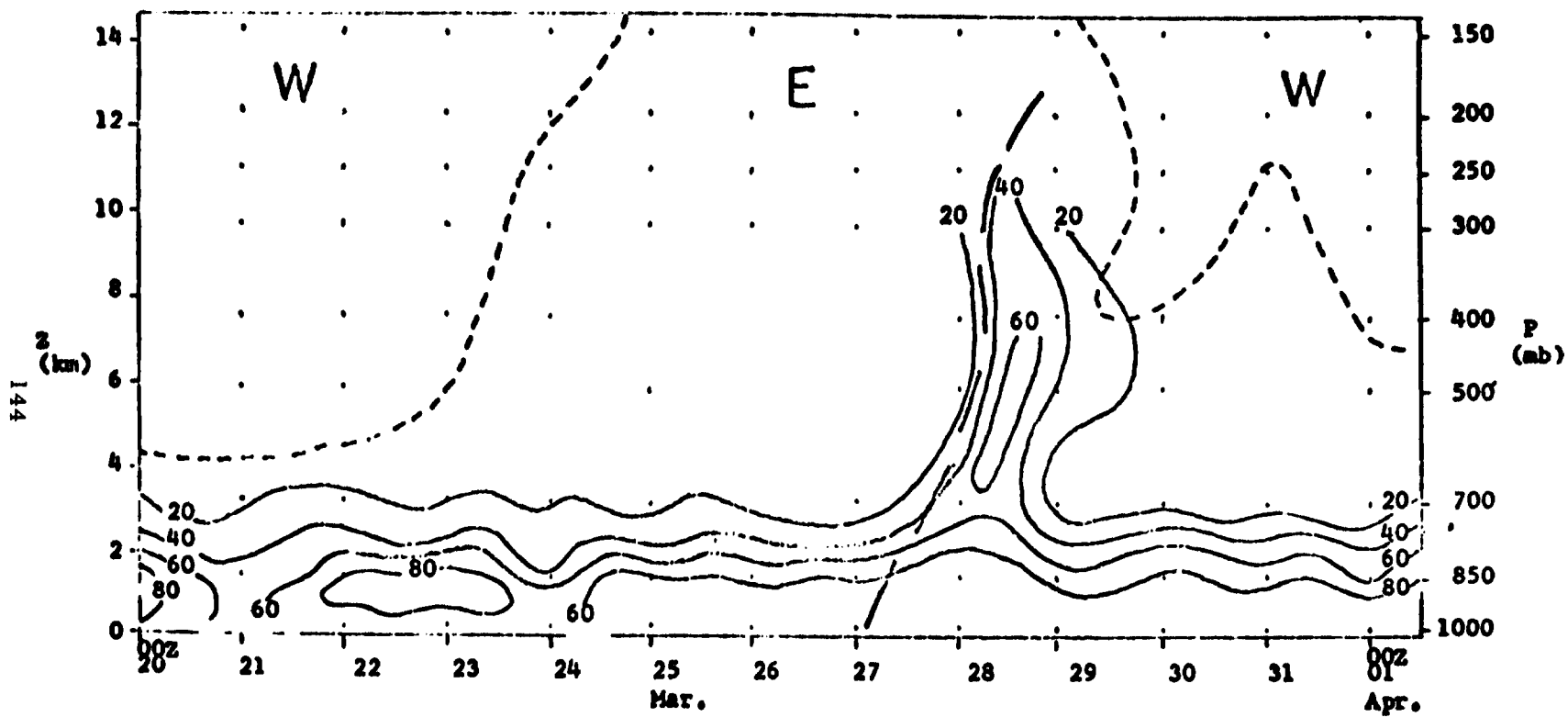


Fig. 9. Time Sequence Showing Relative Humidity Distribution, Zonal Winds, and Surface Observations for Wake.

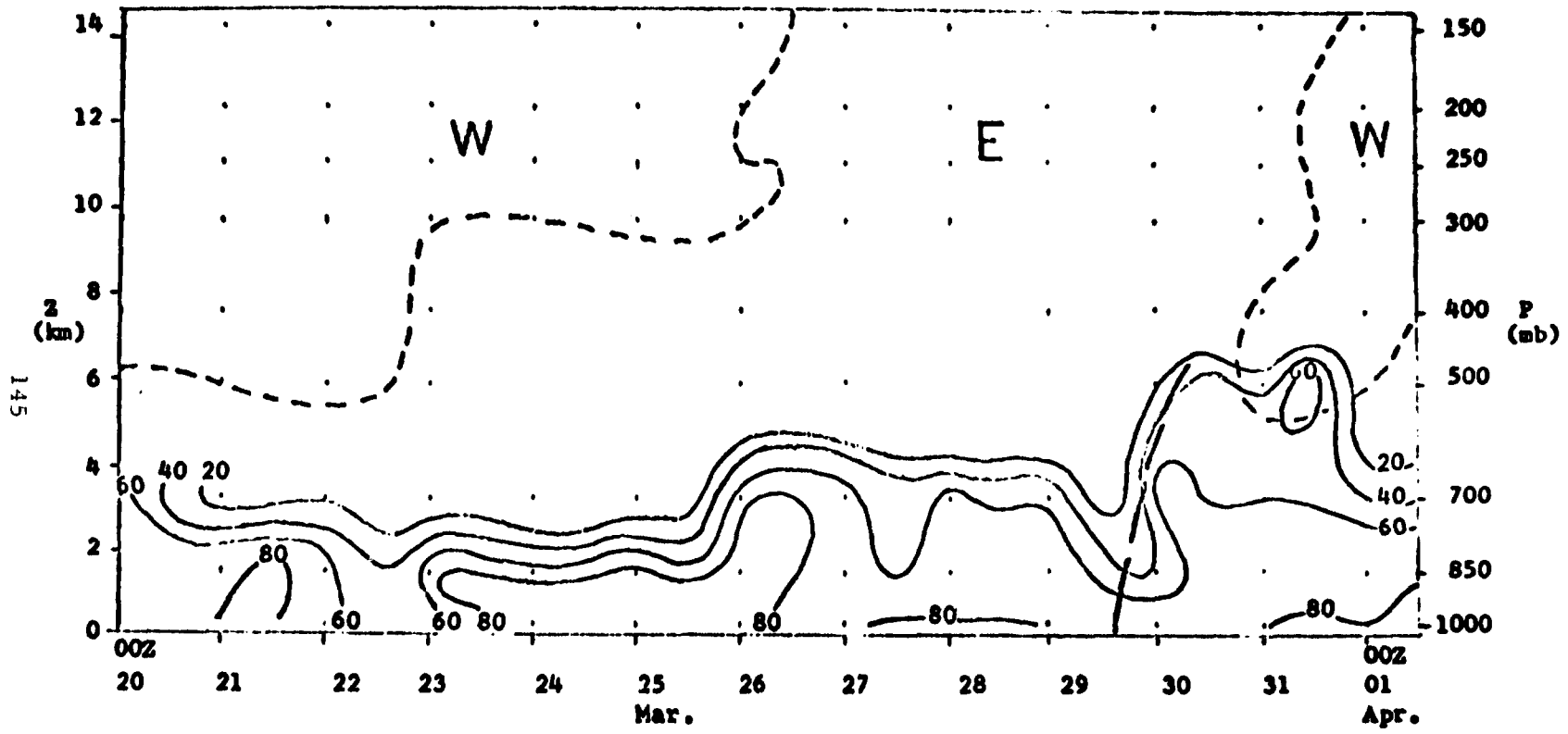


Fig. 10. Time Sequence Showing Relative Humidity Distribution, Zonal Winds, and Surface Observations for Taguac.

6.3 Stations South of the Radiation Ridge

Time sequences for Majuro and Truk are shown in Figures 11 and 12, respectively. Of these two analyses, the one for Truk is considered to be typical for a station south of the subtropical high. Successive easterly perturbations modify the otherwise suppressed humidity distributions as shown on 22 and 27 March. After 28 March, the vertical extent of moisture is highly increased. This is a direct result of the advection of moisture and clouds from the ITC, which was located further north at this time.

The wind field and humidity distribution over Majuro shows the expected pattern only on 20 March. Immediately thereafter, however, and throughout the remainder of the period the zonal winds and humidity distribution are complicated by the northern movement of the ITC and the presence of the trough aloft. In fact, Majuro could be considered, during this time, as rather typical of the behavior of a station close to the ITC.

6.4 Radiation versus Synoptic Analyses Summary

The discussion of the radiation loss maps indicated that large scale features of the atmosphere circulation are associated with distinct patterns of long-wave radiation. The subtropical high pressure belt is associated with the maximum radiation ridge. The intertropical convergence zone is associated with the minimum radiation trough. In the daily map series, and in the time sequence analyses, it was found that these radiation patterns are displaced in the same sense as the associated synoptic pattern.

It was observed in the synoptic time sequence analyses that the main differences between what was expected and what was observed at the stations, chosen for their relative position to the radiation ridge, was due to the daily variations in mesoscale features of the atmosphere. Even in the daily radiation analyses, based on this wide-angle sensor, local mesoscale patterns make sense, and thus these details can be of substantial aid in the analysis of such features on a routine basis. This is especially true since the distance between synoptic meteorological observations in the oceanic region are of the order of hundreds of miles. The best example of the mesoscale capability of the radiation loss maps was a notable increase in the radiation gradient south of the radiation ridge on 28 March over Wake. At this time Wake had its lowest radiation for the entire period.

It is the opinion of the author that with better satellite coverage over the oceanic areas, radiation loss maps prepared on a routine basis will greatly enhance the daily analyses of weather systems in this region, and as a result will provide us with a better understanding of the atmosphere in this vast region.

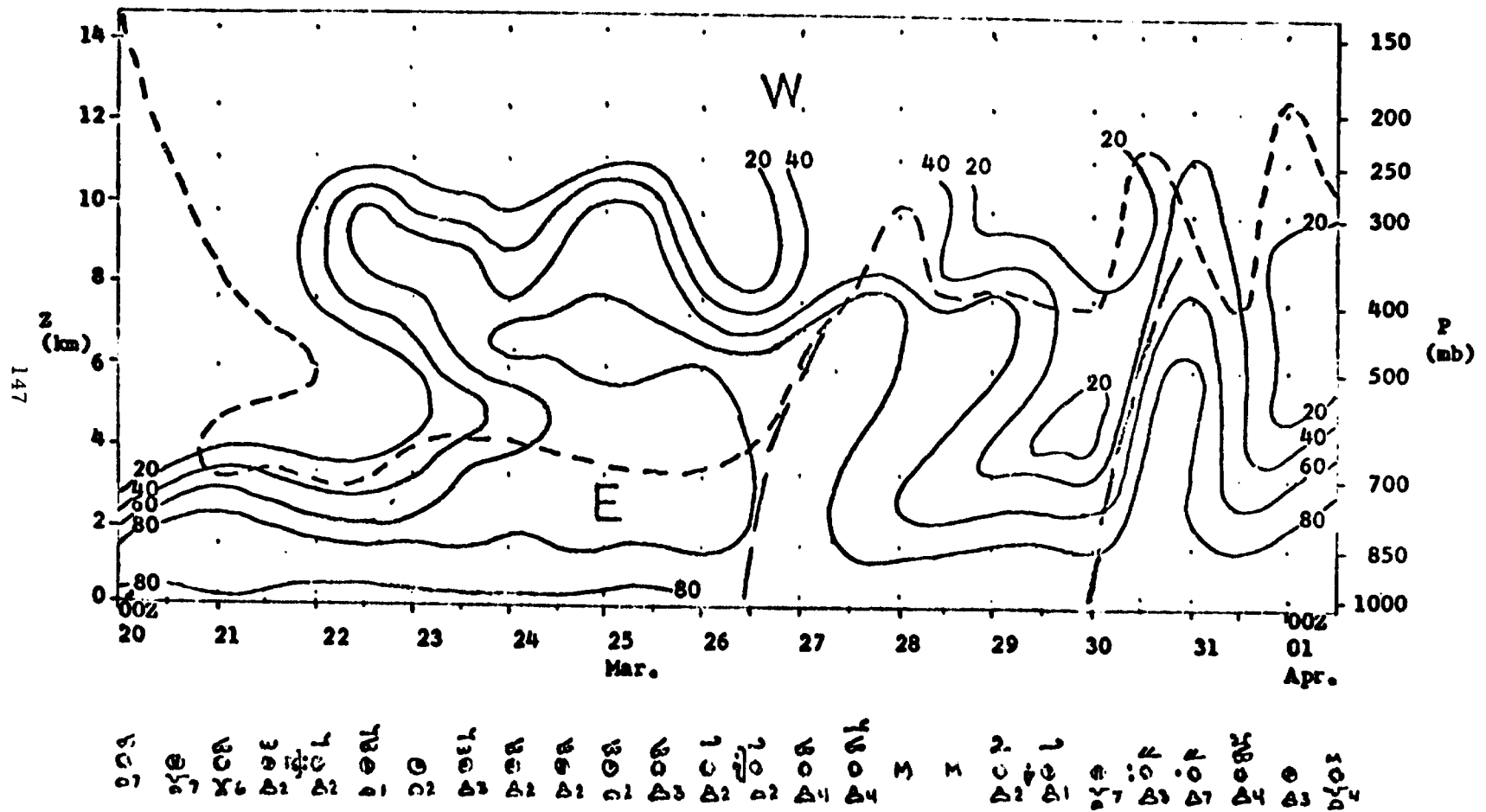


Fig. 11. Time Sequence Showing Relative Humidity Distribution, Zonal Winds, and Surface Observations for Majuro.

VII. CONCLUSIONS

Radiation loss maps can be constructed for the tropical regions on a daily basis by the combined use of satellite radiation measurements and nephel analyses. These maps can then be used to determine the location and movement of large scale synoptic features. In the tropical region a ridge of maximum radiation is associated with the subtropical high pressure cell and a trough of minimum radiation is associated with the intertropical convergence zone. A change in the radiation pattern will be reflected in a corresponding change in the synoptic pressure pattern.

The preparation of mean radiation loss maps are also possible. The patterns on these radiation maps can be used to further confirm the climatological position of large scale synoptic features in what are otherwise sparse data areas.

The model of the subtropical high pressure cell with respect to the observed radiation maximum constructed in this paper confirms the present knowledge of the slope of the pressure cell with height. As the radiation maximum in this model is associated with the trade inversion at its minimal height, this model shows that the trade inversion is lowest in the southeastern sector of the high pressure cell.

The relationship between the surface high pressure intensity and the radiation maximum intensity indicates that the magnitude of the radiation reading is mainly a function of the height, amount and temperature of the clouds within the field of view of the sensor. The comparison of the humidity distribution displayed in the time sequences to the radiation readings for the respective areas also show that each radiation reading is a function of the cloud and moisture distribution in the vertical.

The radiation measurements used in this research are advantageous for the preparation of radiation loss maps because of their dependence on the long-wave emissions from the clouds, atmosphere and earth's surface within the sensors large field of view. A refined correlation of optical depth and these radiation measurements is not feasible.

ACKNOWLEDGMENTS

My sincere thanks and appreciation go to the staff of the Department of Meteorology at the University of Wisconsin for providing my graduate education. In particular I wish to express my thanks to Professor E. W. Wahl for his continued advice and guidance in the preparation of this paper and in my graduate training. My thanks also go to Professor V. E. Suomi for making available the radiation data from his TIROS IV sensor and to Professor R. A. Bryson for his advice in the field of Tropical Meteorology.

Thanks also go to Dr. F. B. House for the original reduction of the radiation data, and to Dr. T. H. Vonder Haar for the preparation of the mean radiation values. I also wish to acknowledge the USWB Honolulu Analysis Center for their prompt response in providing copies of the synoptic chart analyses.

I also acknowledge the United States Air Force for sponsoring my graduate education. This research was partially supported by the National Aeronautics and Space Administration under contract NASw-65.

BIBLIOGRAPHY

Riehl, H., 1954: Tropical Meteorology, McGraw-Hill Book Company, Inc., New York. 380 pp.

Suomi, V. E., 1960: The Thermal Radiation Balance Experiment on Board Explorer VII, Chap. 11 in JUNO II Summary Project Report, vol. III, Explorer VII, NASA, George C. Marshall Space Flight Center, Huntsville, Ala., pp. 247-278.

Weinstein, M., and Suomi, V. E., 1961: Analysis of Satellite Infrared Radiation Measurements on a Synoptic Scale. Monthly Weather Review, 39, pp. 419-428.

N 69 - 33582

ON THE INTERPRETATION OF LONG-WAVE RADIATION DATA
FROM EXPLORER VII SATELLITE

by

F. B. House*

CONTENTS

	Page
INTRODUCTION	151
THEORY OF CALCULATIONS	152
DISCUSSION OF RESULTS	157
BRIEF SUMMARY AND CONCLUSIONS	162

INTRODUCTION

The thermal radiation budget experiment is one of three aboard Explorer VII. Its purpose is to measure the world-wide distribution of incoming and outgoing radiation streams which is basically the source of energy driving the world's weather. Instrumentation for this experiment consists of three hemispheres mounted on mirrors, each having different surface characteristics. One hemisphere is painted black, another white, and the third is polished gold. The black surface is equally sensitive to solar and terrestrial radiation, the white surface is more sensitive to terrestrial radiation than to solar radiation, and the gold surface is more sensitive to solar radiation than to terrestrial radiation.

The purpose of this report is to examine the geometry connected with interpreting the long-wave radiation detected by the white hemisphere. Such characteristics of Explorer VII as the size of the area viewed for given

*Present affiliation, GCA Corporation, Bedford, Massachusetts.

satellite heights and the relative contribution of the radiation detected from different parts of the area are of interest before relating radiation values to meteorological parameters.

The white hemisphere mounted on its mirror has the same properties as an isolated sphere in space, absorbing radiation from the area viewed on the earth and reradiating it over its entire surface. The equilibrium temperature of the sphere depends upon the strength of the radiation currents from the earth. Assuming both the earth and the sphere act as black bodies in the long-wave region of the spectrum, the energy balance equation for the sphere reduces to

$$\beta R_{\uparrow} = 4\pi\sigma T^4 \quad \text{or} \quad R_{\uparrow} = \frac{4\pi}{\beta}\sigma T^4 \quad (1)$$

where β is the solid angle to the earth for a given satellite height, R_{\uparrow} the average flux of radiation leaving the earth from the area in view, σ the Stefan-Boltzman constant, and T the temperature of the sphere. One advantage in using a spherical sensor is that it integrates the radiation over a large segment of the earth; therefore it is possible to draw a composite map using data from consecutive passes even though there is a time difference of one hour and forty minutes between each pass. However, one drawback in using this type of sensor is that the small-scale terrestrial radiation patterns tend to be smoothed. An analysis of this integrating property is the primary investigation of this report.

2. THEORY FOR CALCULATIONS

Figure 1 shows the geometry of the satellite's view of the earth. The satellite is at point X at a height h above the subsatellite point S on the earth's surface. Point C is the center of the earth, and R the mean radius of the earth. The central angle α is the angular distance from the subsatellite point to some point P, α_m the maximum angle to the horizon H. The value of α_m is dependent on the height of the satellite. The following expresses the relation

$$\alpha_m = \arccos \frac{R}{R+h} \quad (2)$$

The relation to determine the solid angle β in the energy balance equation is

$$\beta = 2\pi(1 - \cos \theta_m) \quad (3)$$

where θ_m in Figure 1 is the maximum view angle for a particular satellite height.

The contribution of radiation from each small unit area of the earth varies considerably depending on the position of the area relative to the satellite.

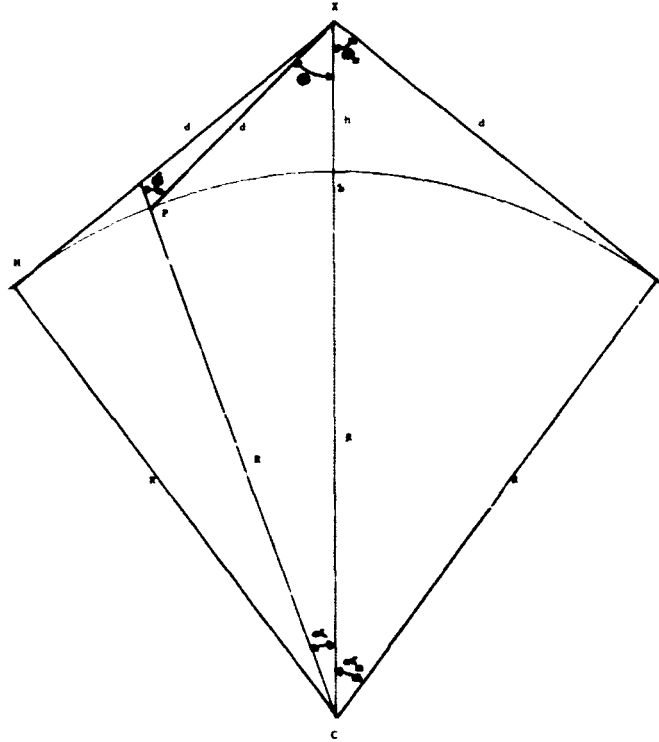


Fig. 1. Geometry of Satellite's View of Earth

A unit area near the subsatellite point contributes the greatest amount, whereas an area near the horizon contributes little to the total radiation detected by the sensor. The weight given the radiation from an area at P, is inversely proportional to the square of the distance from P to X, and directly proportional to the cosine of the zenith angle ϕ of the satellite as observed from P. Let W_p be the weighting factor for the radiation from P.

$$W_p = \frac{\cos \phi}{d^2} \quad (4)$$

Both d and ϕ in (4) are readily calculated.

$$d = [R^2 + (R + h)^2 - 2R(R + h) \cos \alpha]^{1/2} \quad (\text{Law of Cosines})$$

$$\phi = \arcsin \frac{(R + h) \sin \alpha}{d} \quad (\text{Law of Sines})$$

In this report it is assumed that the earth is a uniform black body radiating isotropically at some constant temperature. As stated in equation (1), the flux of radiation leaving the earth is $R\uparrow$ whose magnitude depends on the earth's temperature in accordance with Stefan-Boltzman's relation $R\uparrow = \sigma T^4$. It follows that the contribution of radiation from an area Δ (defined as the effective

radiation R_e) is the product of R_f times the weighting factor at that point.

$$R_e = W_p \cdot R_f = \frac{\cos \phi}{d^2} R_f$$

R_e reaches its maximum value at the subsatellite point where $\phi = 0^\circ$ and $d = h$. Let R_m be the radiation from the subsatellite point.

$$R_m = \frac{\cos 0^\circ}{d^2} R_f = \frac{R_f}{h^2}$$

Next define R_n to be the normalized radiation response equal to the ratio of the effective radiation from any point viewed to that of maximum contribution

$$R_n = \frac{R_e}{R_m} = \frac{\cos \phi / d^2}{1/h^2} \frac{R_f}{R_f}$$

$$R_n = \frac{h^2 \cos \phi}{d^2} \tag{5}$$

Values of R_n compare the effective radiation from any point in view to that from the subsatellite point. They vary in magnitude from 1 at the subsatellite point to 0 at the horizon. A graph of the variation of R_n for two satellite heights appears in Figure 2.

To calculate the total detected radiation from the earth, one must sum the effective radiation from each unit area over the entire field of view. First divide the area in view into a series of small incremental zones of width Δr . (See Figure 3.) The effective radiation from a zone R_z is equal to the product of the zone's area times the radiational flux leaving the earth multiplied by the appropriate weighting factor.

$$R_z = A_z \cdot R_f \cdot W_p$$

From geometry, the area of a zone, A_z , is

$$A_z = 2\pi R \Delta t \tag{6}$$

where Δt is the vertical thickness of the zone. It is of interest to express Δt in terms of distance on the earth's surface. Since Δr is small, consider it to be a straight line. Therefore $\Delta t \simeq \sin \alpha \Delta r$, and $A_z = 2\pi R \sin \alpha \Delta r$. Figure 4 is a plot of the variation in the magnitude of zonal areas as the distance from the subsatellite point increases. The area of a zone can be computed from the graph by multiplying the value of the ordinate for a particular distance from the subsatellite point times the zonal width Δr .

$$A_z = (\text{value} \times \Delta r) \cdot 10^3 \text{ km}^2$$

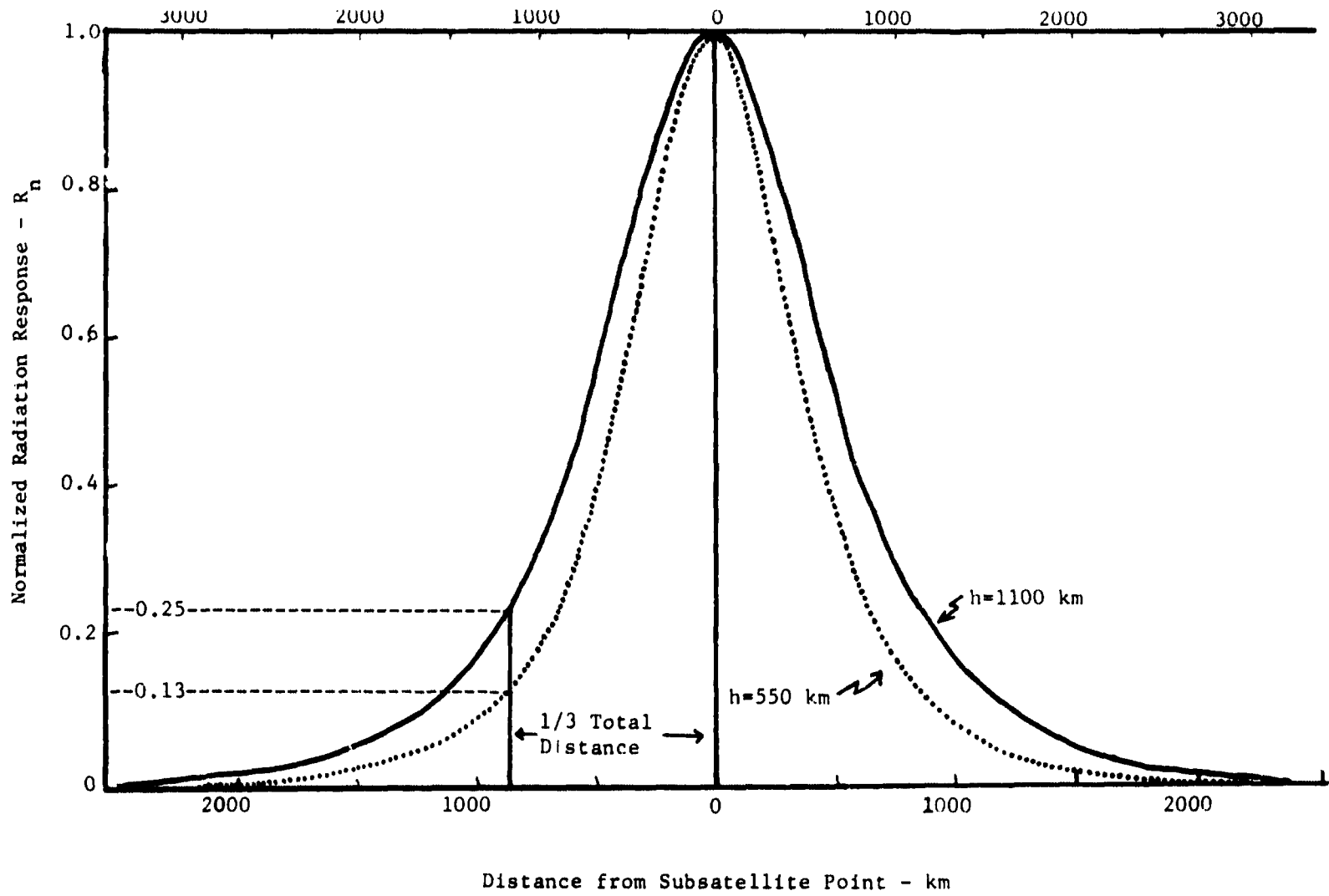


Fig. 2. Variation of normalized radiation response values for two satellite heights.

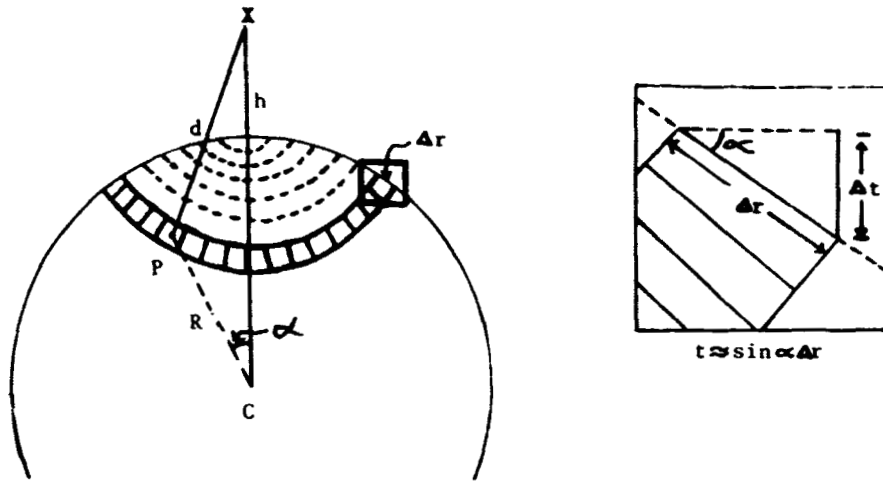


Fig. 3. Geometry of a zone on the earth's surface

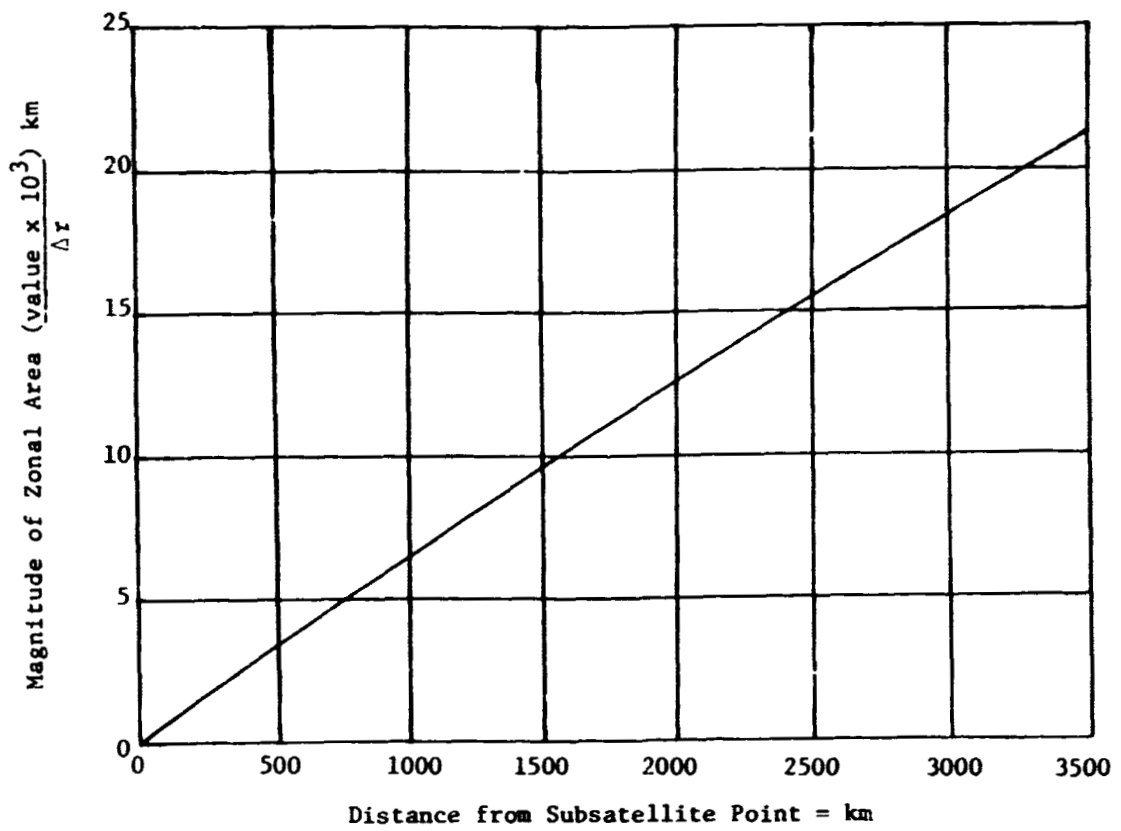


Fig. 4. Variation in the magnitude of zonal areas

The equation for the effective radiation from a zone R_z is

$$R_z = A_z \cdot R \uparrow \cdot W_p = [2\pi R \sin \alpha \frac{\cos \phi}{d^2} \Delta r] \cdot R \uparrow$$

To obtain the total radiation R_T , one must sum the effective radiation from the incremental zones over the entire field of view from the subsatellite point to the horizon.

$$R_T = 2\pi R \cdot R \uparrow \sum_{r=S}^{r=H} \frac{\sin \alpha \cos \phi}{d^2} \Delta r \quad (7)$$

or

$$R_T = 2\pi R \cdot R \uparrow \int_{r=0}^H \frac{\sin \alpha \cos \phi}{d^2} dr$$

A graph of the variation in effective radiation for two satellite heights appears in Figure 5. To obtain the effective radiation from a zone, multiply the values of the ordinate for a particular distance from the subsatellite point times the zonal width.

$$R_z = (\text{value} \cdot \Delta r) \cdot R \uparrow$$

The area under either curve represents the total radiation incident on the sensor for the height in question.

3. DISCUSSION OF RESULTS

In this report calculations were made for two satellite heights, 550 km and 1100 km, which correspond to the height of perigee and apogee respectively above the earth's equatorial radius. Therefore values of normalized radiation response and effective radiation for other heights between perigee and apogee will vary between the sets of curves in Figures 2 and 5.

In Figure 2, the scale of the abscissa for a height of 550 km (dotted line) was expanded to coincide with the scale for the 1100 km height. The curve for the 550 km height drops off more rapidly than the curve for the 1100 km height. For example, compare the values of R_n at a point one-third the total distance from the subsatellite point to the horizon. As indicated in Figure 2, R_n is equal to 0.13 and 0.25 for heights of 550 km and 1100 km, respectively. This indicates that the effective radiation from the subsatellite point at 550 km is 7.7 times as much as that from an area at the 1/3 distance point, and at 1100 km, it is 4.0 times as much. Therefore, for lower satellite heights, one can expect a greater portion of the total radiation to come from an area near the subsatellite point, and as the satellite height increases, the relative import-

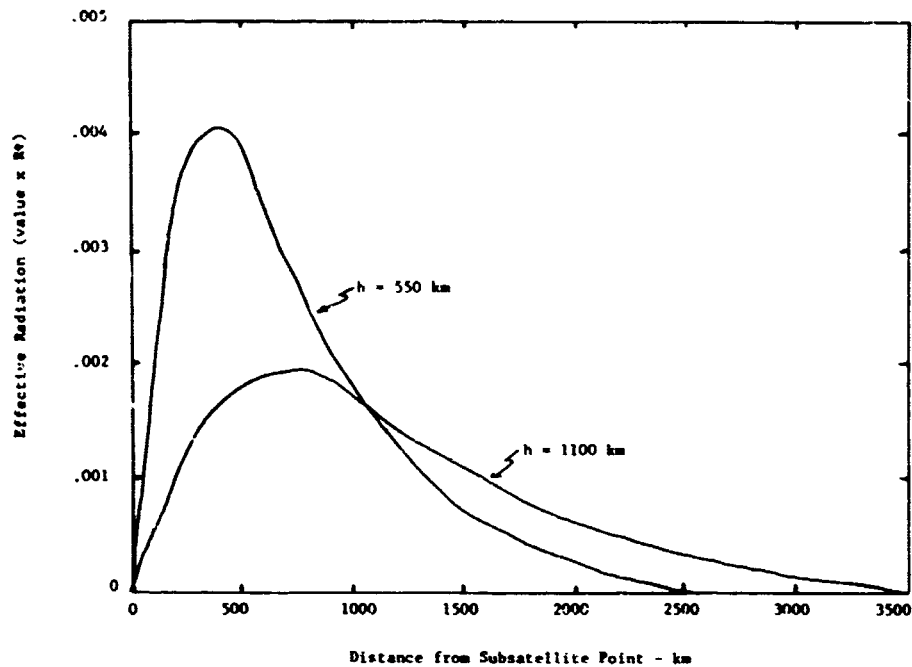


Fig. 5. Variation in the effective radiation for two satellite heights.

ance of the radiation from the subsatellite point decreases. The magnitude of the decrease will be discussed in a later paragraph.

As mentioned before, the area under either curve in Figure 5 represents the total radiation incident on the sensor for that height. The curves were integrated graphically using a planimeter. The total radiation at 550 km was 3.8 $R\uparrow$, and at 1100 km was 3.0 $R\uparrow$. The reason for the decrease in R_T with height is the effect of the inverse square law, i. e., the greater the distance between source and detector, the less the radiation flux detected. In the energy balance equation (1), the radiation from the earth is $\beta R\uparrow$. Computed values for β using equation (3) give values of 3.83 and 3.002 for heights at 550 km and 1100 km, respectively. The computed values agree quite well with the integrated values from the curves.

When interpreting radiation maps, it is of interest to know the total area viewed at a particular data point, and also the approximate size of the areas from which 1/2 and nine-tenths of the total radiation is coming, for example. Define these areas as the 1/2 power and the nine-tenths power response areas. The size of the areas can be determined from the curves in Figure 5. Since the area under each curve represents the total radiation for the given height, the distance from the subsatellite point which corresponds to half the area is the radial distance of the circular area on the earth from which half the radiation is coming. For example, the 1/2 power response areas at 550 km and 1100 km

are at a distance of 589 km and 1000 km, respectively, from the subsatellite point. Other power areas can be computed in this way using the curves.

An easier and more accurate method to determine any power area is as follows. Again the total radiation from the earth is βR^2 . It follows that half the radiation would come from $\frac{1}{2}\beta R^2$, or half the solid angle. In the general case, the X^{th} power area would come from the X^{th} portion of β . From equation (3), $\beta = 2\pi(1 - \cos \theta_m)$, the X^{th} portion of β is $X\beta = 2\pi(1 - \cos \theta_x)$, where θ_x is the view angle for the X^{th} power area. Substituting equation (3) for β ,

$$\begin{aligned}
 X2\pi(1 - \cos \theta_m) &= 2\pi(1 - \cos \theta_x) \\
 \cos \theta_x &= 1 - X(1 - \cos \theta_m) \\
 \theta_x &= \text{arc cos}[1 - X(1 - \cos \theta_m)] \quad (8)
 \end{aligned}$$

From the Laws of Sines and Cosines, one can determine the distance from the subsatellite point for a particular θ_x .

Values of θ_x were computed for every tenth power area for the two heights. The results appear in Table I in terms of distance from the subsatellite point. Figure 6 shows the relative size of the radiation response areas for the two satellite heights using the values computed in Table I. These radiation distributions are the heart of this report. They show graphically the integrating property of the hemispherical sensors aboard Explorer VII. Let us examine them in more detail.

TABLE I

Power Area	Distance from Subsate- lite Point - km		% of Total Area Viewed		Relative Size of Power Areas (A_r)
	h = 550 km	h = 1100 km	h = 550 km	h = 1100 km	h = 550, 1100 km
1/10	189	356	0.58	1.06	3.39
2/10	300	533	1.41	2.38	3.13
3/10	394	678	2.42	3.84	2.95
4/10	489	833	3.74	5.81	2.88
5/10	589	1000	5.49	8.35	2.82
6/10	722	1189	8.01	11.80	2.73
7/10	867	1411	11.75	16.60	2.62
8/10	1067	1700	17.76	24.12	2.52
9/10	1389	2122	30.02	37.36	2.31
10/10	2556	3500	100.00	100.00	1.86

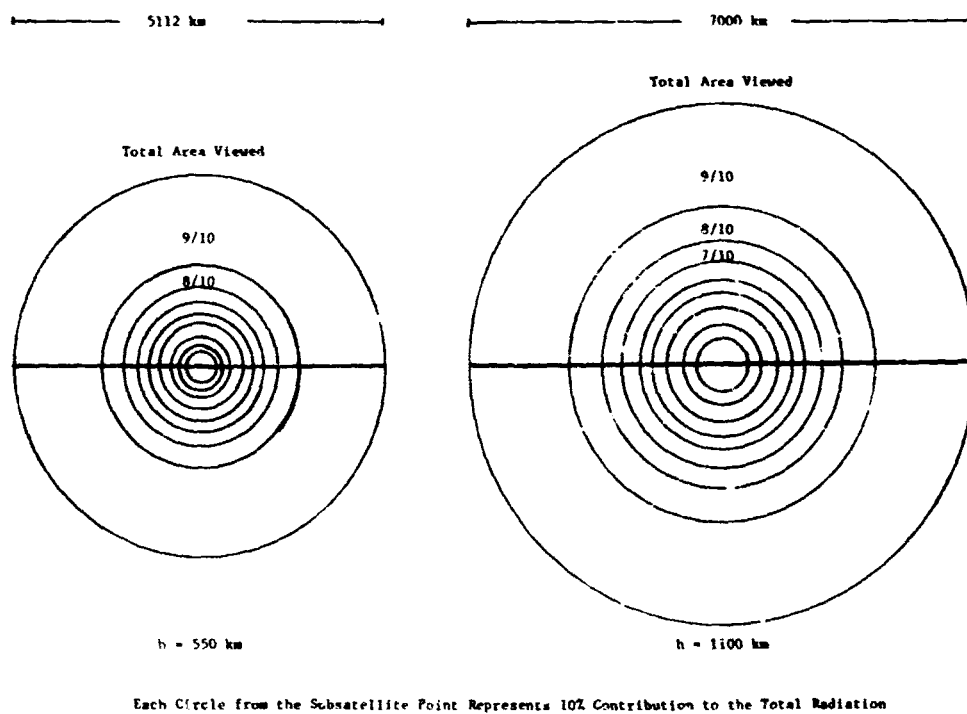


Fig. 6. Relative size of radiation response areas for two satellite heights.

From the discussion of the normalized radiation response curves in Figure 3, it was mentioned that for lower satellite heights, one can expect a greater portion of the total radiation to come from an area near the subsatellite point. Inspection of the relative sizes of the radiation response areas for both heights in Figure 6 indicates this conclusion. Take for example the nine-tenths power response area. For a height of 550 km, nine-tenths of the total radiation is coming from 30.0% of the total viewed area, and for 1100 km, nine-tenths is coming from 37.4% of the viewed area. Computed values for the percent of the total area viewed for each response area appear in Table I. In all cases the value of the percentage is lower for the 550 km height indicating that a greater percent of the total radiation comes from an area near the subsatellite point for lower heights.

The radiation response areas are also an indication of the sensor's resolution. Up to this point, it was assumed that the earth was at a constant temperature; therefore $R\uparrow$ was constant over the entire earth. Assume an idealized case where the radiation from an area the exact size of the five-tenths power response areas is $2R\uparrow$, and the remainder of the area is still $R\uparrow$. The sensor would integrate these values and give an average reading of $1.5 R\uparrow$ for the viewed area. One can see in Figure 6 that the actual size of the five-tenths power response area for 550 km is smaller than for 1100 km. The ratio of the relative size of response areas for two heights can be computed using a form of equation (5).

$$A_r = \frac{A_{z_1}}{A_{z_2}} = \frac{2\pi R t_1}{2\pi R t_2}$$

where A_r is the area ratio, t is the vertical thickness of the zone, and the notation 1 and 2 stand for the two satellite heights. Since the distance from the subsatellite point for the 1/2 power response areas is known, t can be expressed in terms of the central angle.

$$t = R - R \cos \alpha = R(1 - \cos \alpha)$$

$$A_r = \frac{t_1}{t_2} = \frac{R(1 - \cos \alpha_1)}{R(1 - \cos \alpha_2)}$$

$$A_r = \frac{(1 - \cos \alpha_1)}{(1 - \cos \alpha_2)} \quad (9)$$

Computed values of A_r appear in Table I. The value of A_r for the 1/2 power response area is 2.82. This means that it takes an area over two and eight-tenths times as large for 1100 km as it does for 550 km to produce the same fluctuation in the sensors temperature. Therefore, the sensitivity of the sensor to small-scale terrestrial radiation is much better for lower heights. This is especially true as the power area becomes smaller. In Table I, the value of A_r increases to 3.39 for the one-tenth power area.

Nothing has been said about the effect of the earth's atmosphere on the radiation response patterns. Let us consider it in a qualitative manner. One might compare the effect of our atmosphere to the familiar limb darkening of the sun. The sun's edge appears darker than the center because the radiation from the photosphere at the edge travels through a greater optical mass of the sun's atmosphere than that from the center. Therefore the effective black body radiation temperature for the edge is lower.

In the case of the earth, a radiation beam leaving the earth at an angle to the zenith is attenuated more than the vertical beam. This effect accentuates even more the concentration of most of the radiation from an area near the subsatellite point. As the satellite's view angle increases, the attenuation due to the greater optical air mass increases also. An estimation was made of the magnitude of attenuation using an Elsasser chart. For twice the optical depth, (zenith angle of 60°), the decrease is 4 to 5 percent. For radiation from the horizon, the decrease is 15 to 20 percent. Of course, the attenuation will vary with different moisture contents of the atmosphere. The percentages give only an idea of its magnitude. The effect of atmospheric attenuation on the radiation response areas in Figure 6 is to bring the circles closer to the center.

Values were computed for the size of the 1/2 and nine-tenths power response areas and total area viewed for different satellite heights. Figure 7 is a graph of their variation in terms of distance (km) from the subsatellite point. The values were also converted to degrees latitude. See Figure 8. When interpreting radiation maps, it is easier to estimate radiation response areas in terms of degrees latitude.

4. BRIEF SUMMARY AND CONCLUSION

The main impression I wanted to leave with the reader in this report is that even though the sensor aboard Explorer VII is omnidirectional and integrates radiation from the entire field of view, most of the total detected radiation comes from a relatively small area directly below the satellite. For example, if the satellite passes over a storm area, the sensor will definitely detect the variation in the outgoing radiation. If that same storm area is located at a point near the satellite's horizon, the variation in the radiation due to the storm will be hardly noticeable. Therefore a spherical sensor will indicate areas of extensive storminess and also areas of good weather. It was also pointed out in the report that the sensor's resolution improves with lower satellite heights. However, at 1100 km, the resolution is sufficiently adequate to detect variations in the radiation patterns.

Finally, if another satellite is put into orbit with similar sensing equipment as that on Explorer VII, it would be advantageous that it be put into circular orbit at a height around 500 km. Interpretation of radiation data would be

Fig. 7. Variation in the size of radiation response areas (satellite height in km v. radius of area in km).

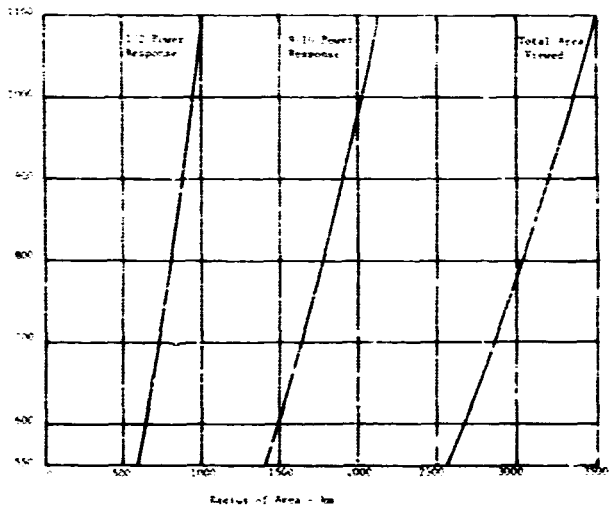
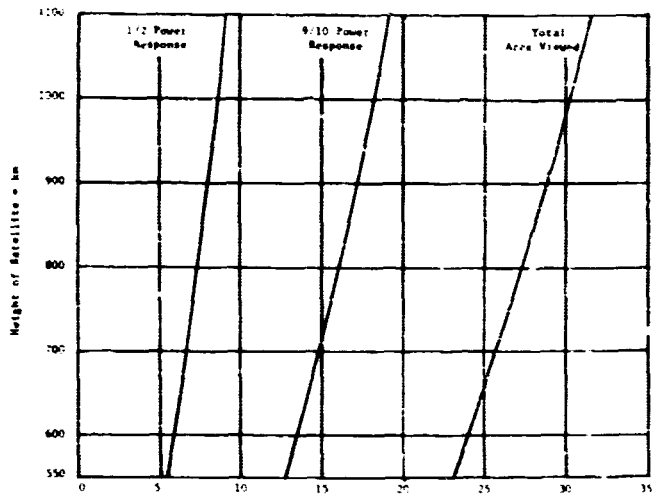


Fig. 8. Variation in the size of radiation response areas (satellite height in km v. radius of area in degrees latitude).

greatly simplified if the satellite orbited at a constant height above the earth's surface. The 500 km height is a compromise between the sensor's resolution and sufficient coverage and smoothing to enable analysis of composite radiation maps.

ABSTRACTS

During the ten years of this contract, many other scientific reports were completed. All of these have been issued in special contract reports or published as theses and/or papers. The following section of this report contains abstracts of some of these papers, with additional comments where appropriate.

1. "Analysis of Satellite Infrared Radiation Measurements on a Synoptic Scale," by M. Weinstein and V. Suomi, Monthly Weather Review; 89:11, 1961.

Abstract

Longwave radiation loss maps, based on Explorer VII measurements of terrestrial radiation at night, are analyzed and compared with composite nephanalyses and frontal analyses. Results indicate a definite relationship between the radiation centers and their corresponding surface low and high pressure centers, their locations, 24-hour intensifications and movements, and the conformity of these movements to the 500-mb geostrophic flow. Some of the potential applications to analysis and forecasting are noted.

This paper presented first results obtained from meteorological satellites. It demonstrated that features of the atmosphere's circulation, marked by associated cloudiness, could be observed and studied using IR measurements from an orbiting satellite. In addition, descriptions of the sensors and orbit of Explorer VII are given.

2. "The Generation of Available Potential Energy Due to Horizontal Variation in Terrestrial Radiation as Measured by the Satellite Explorer VII," by W. C. C. Shen, Ph.D. Thesis. Also, Journal of Atmospheric Science, January 1963.

Abstract

According to radiometer-sonde observations, the net vertical flux divergence of infrared radiation is positively correlated with the outward flux at the top of the atmosphere. Measurements of the latter quantity from the Explorer VII satellite are shown to be

correlated with tropospheric temperature, such that warm air on the average is cooled less than cold air at the same latitude by infrared radiation. Calculations of the generation of eddy available potential energy by this process are presented and shown to be significant.

This work may be considered a pioneer effort in the use of satellite radiation data to study the energetics of the atmosphere. The generation of available potential energy by infrared cooling over a large area was determined as a function of time and for various wave numbers. The average value of the generation was positive. Maximum generation occurs at wave number six. The results of this investigation have been used in several subsequent studies of atmospheric energetics and of the vertical variations of the generation of available potential energy.

3. "An Inflight 'Re-Calibration' of Channel 3 on Tiros IV," by T. H. Vonder Haar and I. Dirmhirn, expanded from MS Thesis, University of Wisconsin, 1964.

Abstract

The reflected shortwave radiation sensor of the scanning radiometer on TIROS IV (Channel 3) degradation is determined by comparing measurements of this medium resolution instrument with those from the University of Wisconsin omnidirectional sensor on the same satellite. This study accounts for the difference in resolution of the two radiometers. More than twenty comparisons were made at different times during the useful life of TIROS IV. The results show that besides a scale correction an additional intensity-dependent factor must be applied to Channel 3 values. This extra term is necessary to correct for electronic degradation and the wavelength-dependency of reflected radiation. Degradation apparently ceases after orbit 650, where the magnitude of the correction factor is near 2.0. These corrections bring the quasi-global summaries of measured albedo to a reasonable value of 33%.

In this work an attempt was made to recalibrate the total reflected solar radiation sensor of NASA's scanning radiometer on TIROS IV by forcing its measurements to agree with those obtained from the Wisconsin sensors on the same satellite. The necessary correction factor determined by this direct comparison is higher than those obtained during a balloon experiment and by theoretical considerations. The resulting correction factor yields reasonable values of reflectance and thus allows the scanning radiometer data to be more usefully applied. The comparison also demonstrated another advantage of including more than one radiation subsystem on meteorological satellites.

4. "The Radiation Balance of the Earth from a Satellite," F. B. House, Ph.D. Thesis, University of Wisconsin, 1965.

Abstract

The measurement of albedo and long-wave radiation by the black omnidirectional sensor on TIROS IV satellite is used to study the radiation balance of the earth. The method used to obtain these results using only a single sensor system is developed. The principal results of this study are:

1. Accurate measurements of the solar and terrestrial radiation streams using a single sensing system are possible, providing the satellite orbit has a precessional period relatively long compared with the movement of weather systems.
2. Previous estimates of the meridional distribution of long-wave radiation agree remarkably well with satellite measurements.
3. Earlier estimates of the planetary albedo are confirmed. However, the meridional distribution of measured albedo value shows lower values in tropical latitudes and higher values at middle and polar latitudes than are indicated by previous estimates.
4. Because of 3 above, satellite measurements of the net radiation distribution with latitude require a larger transport of heat from tropical latitudes than previously estimated.
5. Finally, because separate measurements of solar input to the earth and radiative loss to space were available, the possibility of global radiative equilibrium for a fraction of an annual period is considered.

These zonal averages of albedo, long-wave radiation, and net radiation were obtained by the first totally successful low resolution radiometer experiment. As such, they represent our first look at the earth's radiative budget by sensors whose response apparently remained unchanged after launch. In particular, the albedo values presented in this paper are the most trustworthy of the entire TIROS series.

5. "Experimental Analysis of the TIROS Hemispheric Sensor," by B. B. Sparkman, MS Thesis, University of Wisconsin, 1965.

Abstract

The operation of a TIROS hemispheric infrared sensor is examined in a simulated environment comparable to that of an orbiting radiometer while within the Earth's shadow. Heat flows within the sensor supplementing the signal radiation are examined and a calibration curve derived to minimize these effects. A comparison with an inflight calibration formula is presented.

The laboratory research presented in this paper represents a summary of the most important experiments and calibrations carried out at Wisconsin before the hemispheric radiometers were placed on the TIROS satellites. The construction of the instruments is described in detail. Some of the experiments were used to improve the design of future sensors, such as those now included on ESSA III. Results of the laboratory calibrations compared very well with the inflight calibrations performed after launch. Because it is possible to continually recalibrate inflight the effects of changes in the physical characteristics of the satellite sensors is minimized.

6. "Interrelation of Ionospheric Sporadic E with Thunderstorms and Jet Streams," by T. D. Damon, MS Thesis, University of Wisconsin, 1965.

Abstract

Reports of the occurrence of ionospheric sporadic E clouds from radio amateurs operating on a frequency near fifty megahertz are analyzed on a synoptic scale and compared with the occurrence of thunderstorms and of jet streams. A mechanism is suggested for the observed interrelation between Es and thunderstorms. No definite conclusion is drawn concerning the possible relationship between Es and jet streams.

7. "The Study of Thunderstorms by Radio and Radar Techniques," by L. P. Merritt, MS Thesis, University of Wisconsin, 1966.

Abstract

The general atmospheric electric model is outlined followed by a discussion of fair and disturbed weather electrical and meteorological conditions. Current knowledge of local air mass thunderstorms is then reviewed in some detail. This is followed by a review of past and current research and research techniques as applied to thunderstorms. Recent developments in radio and radar techniques are then considered in terms of their potential usefulness in studying thunderstorms.

8. "The 'Chirp' Digital Radiosonde," by V. E. Suomi, K. J. Hanson, and R. J. Parent, Journal of Applied Meteorology, 6:1, 1967.

Abstract

This paper reports on a digital measurement ("chirp") system which has application for a wide range of meteorological and earth satellite measurements.

The system employs a simple concept in which a voltage pulse, proportional to a sensor voltage, is used to generate a burst of pulses from a voltage controlled oscillator (VCO). A count of the high frequency oscillations which make up the "chirp" provides the digital measurement. The system is adapted to multiple sensor use with a multiplexer.

The system has the advantage in that one has the option of selecting an AC amplifier for low level signals in conjunction with a variety of multiplexers and VCO for the desired measurement. One particular combination of multiplexer and VCO was used to demonstrate its use as a digital radiosonde.

A flight test of the digital radiosonde was obtained. Results clearly show fine structural detail in the temperature profile without any need for subjective interpretation by the operator. Numerous isothermal and inversion layers less than 100 m. in thickness were observed.

The digital radiosonde used conventional (U.S. Weather Bureau) temperature and humidity sensors. Temperature resolution is about 0.1° C and relative humidity is about 0.1 percent. The system resolution is about 0.1 percent.

9. "Theoretical Basis for Low-Resolution Radiometer Measurements from a Satellite," by V. E. Suomi, K. J. Hanson, and T. H. Vonder Haar; Studies in Atmospheric Energetics Based on Aerospace Probings, 1966 Annual Report on WBG-27, Amendment No. 1, for National Environmental Satellite Center of the Environmental Sciences Services Administration, March 1967.

Abstract

This paper is intended to provide the theoretical background for obtaining irradiance values from low-resolution radiometers of the TIROS satellite series. Hemispherical sensors were used on the TIROS series. The theory and notation used in this presentation were developed, in part, by Suomi (1958), Bignelli (1962), and House (1965).

The theory for inflight calibration of the low-resolution radiometers is developed in this paper. Such a calibration is possible from data obtained when the satellite crosses the earth's shadow (usually called the terminator) and the earth shades or unshades the radiometers from the direct sunlight. These inflight calibrations provide information on degradation of the absorbing properties of the sensor surface. The measurements are useful in determining other sensor characteristics as well.

An important feature of this measurement system is that the radiant energy from a specific source which is absorbed by the sensor is used to determine the irradiance from that source, through a known geometrical relationship between the two. The radiation sources are direct solar radiation, reflected solar radiation from the earth, and IR radiation from earth.

Additional Papers

"Satellite Detection of UHF Emissions from Cumulus Clouds," by S. A. Rossby and Saum, presented at International Symposium on Electromagnetic Sensing of Earth from Satellites; March 1965.

"Sferics from Lightning within a Warm Cloud," by S. A. Rossby, Journal of Geophysical Research; 71:16, August 1966.

APPENDIX

List of Figures and Serial Numbers

PRECEDING PAGE BLANK NOT FILMED.

APPENDIX

The following is a list of figures in each of the articles contained in this report and the corresponding photo serial number. Copies of individual photographs may be ordered directly from the University of Wisconsin Space Science and Engineering Center, 1225 West Dayton Street, Madison, Wisconsin 53706, at a charge of one dollar (\$1.00) per print. In ordering photographs the appropriate serial number should be cited.

<u>Figure Number</u>	<u>Title</u>	<u>Serial Number</u>
Article 1		
1	The sun glitter shifts toward west over a calm area in the midst of a rough ocean	70596-C-1
2	The geometry of reflection	74604-C-1
3	The probability space of the two dimensional normal distribution of the waves slope	74602-C-1
4	The linear relation between the waves slope variance and the wind velocity (after Cox and Munk), compared to six points represented by variance calculated from the satellite data, and actual wind measurements	74603-C-1
5	Some of the steps involved in reducing the satellite data, to the standard deviation of the waves slope	74213-C-1
Article 2		
1	Nimbus II MRIR Channel 5 bidirectional reflectance (%) for orbit 468 (June 19, 1966: 1115 to 1123 GMT)	65717-C-1
2	Nimbus II MRIR Channel 5 bidirectional reflectance (%) for orbit 469 (June 19, 1966: 1300 to 1309 GMT)	65715-C-1
3	Nimbus II MRIR Channel 2 infrared temperatures (°C) for orbit 468	65716-C-1

<u>Figure Number</u>	<u>Title</u>	<u>Serial Number</u>
4	Height contours of Greenland in meters with cloud areas shaded	68531-C-1
5	Theoretical bidirectional reflectance (%) as a function of optical thickness (τ') for various observational zenith angles	65718-C-1
6	Variation of bidirectional reflectance as a function of the elevation gradient measured in the direction which bisects the angle between the solar azimuth and MRIR scanning azimuth	68238-C-1
7	Bidirectional reflectance from horizontal Greenland snow surfaces vs. scattering angle	68253-C-1
8	Bidirectional reflectance from cloud areas vs. scattering angle	68252-C-1

Article 3

1	The radiation budget of the earth-atmosphere system	65141-C-1
2	Summary of satellite radiation data (other MRIR observations during 1961 and after June, 1964 were not included in this study)	61802-C-1
3	Simplified viewing geometries of the low and medium resolution TIROS radiation sensors	61803-C-1
4	Diurnal variation of planetary albedo and outgoing longwave radiation based on TIROS IV measurements	65143-C-1
5	Comparison of zonally averaged longwave radiation measurements obtained from LRIR and MRIR sensors during the same time periods	63535-C-1
6	Nomogram showing absolute error in net radiation ($\text{cal} \cdot \text{cm}^{-2} \cdot \text{min}^{-1}$) resulting from albedo and longwave radiation measurement errors	63533-C-1
7	Mean values of outgoing longwave radiation from the earth-atmosphere system (H_L) during Dec. -Jan. -Feb. and Mar. -Apr. -May. Units are $10^{-2} \text{ cal} \cdot \text{cm}^{-2} \cdot \text{min}^{-1}$	65149-C-1

<u>Figure Number</u>	<u>Title</u>	<u>Serial Number</u>
	and regions of $H_L > 0.36 \text{ cal} \cdot \text{cm}^{-2} \cdot \text{min}^{-1}$ are shaded.	
8	Same as figure 7 for June-July-Aug. and Sept.-Oct.-Nov.	65148-C-1
9	Mean values of planetary albedo (A) during Dec.-Jan.-Feb. and Mar.-Apr.-May. Regions of $A < 20\%$ are shaded.	65146-C-1
10	Same as figure 9 for June-July-Aug. and Sept.-Oct.-Nov.	65139-C-1
11	Mean values of the net radiation budget of the earth-atmosphere system (R_{NEA}) during Dec.-Jan.-Feb. and Mar.-Apr.-May. Units are $\text{cal} \cdot \text{cm}^{-2} \cdot \text{min}^{-1}$ and isolines of $R_{NEA} = 0.0$ are double-width.	65147-C-1
12	Same as figure 11 for June-July-Aug. and Sept.-Oct.-Nov.	65145-C
13	Winter-Summer differences in outgoing longwave radiation expressed as JJA minus DJF ($\text{cal} \cdot \text{cm}^{-2} \cdot \text{min}^{-1}$)	63674-C-1
14	Same as figure 13 for net radiation and planetary albedo	65201-C-1
15	Mean annual values of longwave radiation from the earth-atmosphere system (H_L). Units are $10^{-2} \text{ cal} \cdot \text{cm}^{-2} \cdot \text{min}^{-1}$ and regions of $H_L > 0.36$ are shaded.	63056-C-1
16	Mean annual values of planetary albedo (A) in percent. Shaded areas have $A < 20\%$.	62364-C-1
17	Mean annual values of the net radiation budget of the earth-atmosphere system (R_{NEA}). Units are $10^{-2} \text{ cal} \cdot \text{cm}^{-2} \cdot \text{min}^{-1}$.	62637-C-1
18	Mean meridional profiles of the components of the radiation budget of the earth-atmosphere system for each season and the annual case (solid line).	65202-C-1
19	Time-latitude sections showing the seasonal variations of the radiation budget components	65200-C-1
20	Time-latitude sections of planetary albedo, outgoing longwave radiation and the net radiation budget for the period JJA, 1963 to SON, 1965	65144-C-1

<u>Figure Number</u>	<u>Title</u>	<u>Serial Number</u>
21	Radiation budgets of selected latitudinal zones July, 1964 through November, 1965	65203-C-1
22	Global and hemispheric averages of the radiation budget components from June, 1963 to November, 1965. Dashed lines show the mean annual values.	65140-C-1
23	The mean seasonal variation of the radiation budgets of the entire earth and each hemisphere	60511-C-1
24	Major components of the energy budget of the earth-atmosphere system	65142-C-1
25	Seasonal values of the required poleward energy transports by the atmosphere (sensible heat + potential energy) and the oceans. Points above the zero line represent northward transport.	65265-C-1
26	Time-latitude section of the required transport of non-latent energy by the atmosphere and oceans. Units are 10^{19} cal · day ⁻¹ .	65264-C-1
27	Geographical distribution of required divergence of non-latent energy by the atmosphere for the mean annual case. Units are kcal · cm ⁻² · yr ⁻¹ and the major energy exporting regions are shaded.	65263-C-1
28	Poleward transport of non-latent energy derived from the radiation data of the present study and the energy budget values of Sellers (solid line) and Rasool and Prabhakara (unconnected points). Dashed line is from Rasool and Prabhakara.	65266-C-1
29	The total poleward energy transport required by the radiation budget (RT) and the contributions by the oceans (ΔF), the atmosphere's transport of latent heat ($L\Delta C_V$) and sensible heat + potential energy (ΔC).	65262-C-1
A1	Example of parameters computed at each terminator crossing (upper portion) and the variation with time of $(D^* + W^*)$ and $Y = (D^* + W^*)/2r^2 \cos \gamma$	63534-C-1

<u>Figure Number</u>	<u>Title</u>	<u>Serial Number</u>
Article 4		
1	Symbols for irradiance bounding the atmosphere and absorption of radiation in the atmosphere	55398-C-1
2	Winter-minimum albedos based on minimum cover	55396-C-1
3	A factor A_S/A_F for modifying the albedo of snow-free ground as a function of snow depth	55935-C-1
4	The number of daytime observations from TIROS IV low resolution radiometers and associated solar zenith angles at times when the satellite was over the continental United States, February-June, 1962	55399-C-1
5	The reflection and absorption of sunlight during the period March through May, 1962, based on TIROS IV low resolution radiometer and surface radiation data	55392-C-1
6	Total precipitable water (cm) in the atmosphere during the period March through June, 1962. Sampling times correspond to data in Figure 5.	55393-C-1
7	Atmospheric heating ($^{\circ}$ C/day, due to absorption of solar radiation in the atmosphere during the period March through May, 1962, based on q_a values of Figure 5	55397-C-1
8	Absorption of solar radiation in the atmosphere as a function of optical pathlength, u^* , in cm	55910-C-1
Article 5		
1	An example of daily radiation loss map. TIROS IV, Wisconsin heat budget radiometer data.	SSE-259-1
2	Displacement limits of radiation ridges and trough and fronts during thirteen-day period.	SSE-259-2
3	Mean daylight long-wave radiation loss map for March, April and May, 1962	SSE-259-3

<u>Figure Number</u>	<u>Title</u>	<u>Serial Number</u>
4	Model of Pacific Anticyclone with respect to long-wave radiation maximum	SSE-259-4
5	Scatter diagrams of surface pressure intensity vs. radiation maximum intensity and latitude of surface pressure center	SSE-259-5
6	Time sequence showing relative humidity distribution, zonal winds, and surface observations for Midway	SSE-259-6
7	Time sequence showing relative humidity distribution, zonal winds, and surface observations for Iwo Jima	SSE-259-7
8	Time sequence showing relative humidity distribution, zonal winds, and surface observations for Lihue	SSL-259-8
9	Time sequence showing relative humidity distribution, zonal winds, and surface observations for Wake	SSE-259-9
10	Time sequence showing relative humidity distribution, zonal winds, and surface observations for Taguac	SSE-259-10
11	Time sequence showing relative humidity distribution, zonal winds, and surface observations for Majuro	SSE-259-11
12	Time sequence showing relative humidity distribution, zonal winds, and surface observations for Truk	SSE-259-12

Article 6

1	Geometry of satellites' view of earth	SSE-298-1
2	Variation of normalized radiation response values for two satellite heights	SSE-290-2
3	Geometry of a zone on the earth's surface	SSE-290-3
4	Variation in the magnitude of zonal areas	SSE-290-4
5	Variation in the effective radiation for two satellite heights	SSE-290-5

<u>Figure Number</u>	<u>Title</u>	<u>Serial Number</u>
6	Relative size of radiation response areas for two satellite heights	SSE-290-6
7	Variation in the size of radiation response areas (satellite height in km vs. radius of area in km)	SSE-290-7
8	Variation in the size of radiation response areas (satellite height in km vs. radius of area in degrees latitude)	SSE-290-8
Table in this article		SSE-290-9